
Preface

This dissertation is submitted for the degree of Doctor of Philosophy at the University of Leicester. The research described in this dissertation was conducted under the supervision of Dr. Simon Gill in the Department of Engineering and Applied Science from September 2001 to September 2002. This work is to the best of my knowledge original and no part of it has been published previously. Neither this, nor any substantially similar dissertation has been submitted for any degree, diploma or other qualification at this, or any other University. This dissertation contains less than 60,000 words.



**University of
Leicester**

Modelling the Microstructural Evolution of Engineering Materials

Mark G. Cornforth

Thesis submitted to the University of Leicester
in accordance with the requirements for the degree of
Doctor of Philosophy in the Faculty of Engineering

Supervisor: Dr. S. P. A. Gill

Co-Supervisor: Prof. A. C. F. Cocks

University of Leicester Engineering Department
Mechanics of Materials Research Group

Date of Submission: 9th September 2002

Mark G. Cornforth

September 2002.

UMI Number: U166714

All rights reserved

INFORMATION TO ALL USERS

The quality of this reproduction is dependent upon the quality of the copy submitted.

In the unlikely event that the author did not send a complete manuscript and there are missing pages, these will be noted. Also, if material had to be removed, a note will indicate the deletion.



UMI U166714

Published by ProQuest LLC 2013. Copyright in the Dissertation held by the Author.
Microform Edition © ProQuest LLC.

All rights reserved. This work is protected against
unauthorized copying under Title 17, United States Code.



ProQuest LLC
789 East Eisenhower Parkway
P.O. Box 1346
Ann Arbor, MI 48106-1346

Preface

This dissertation is submitted for the degree of Doctor of Philosophy at the University of Leicester. The research described in this dissertation was conducted under the supervision of Dr. Simon Gill in the Department of Engineering, Leicester, between October 1998 and September 2002. This work is to the best of my knowledge original, except where acknowledgement and reference is made to previous work. Neither this, nor any substantially similar dissertation has been submitted for any degree, diploma or other qualification at this, or any other University. This dissertation contains less than 60,000 words.

This thesis is dedicated to the memory of my late father, *Eur. Ing.* A.R. Cornforth *B.Sc.(Hons), C.Eng., M.I.E.E., C.Phys., M.Inst.P., M.Inst.N.D.T.*, who always encouraged and inspired me, and played a major role during my earlier school education. My father passed away before I started University but his fun and laughter will always remain in my thoughts.

Workshops and conferences attended during the period of research:

1. Materials Modelling Laboratory Workshop,
University of Oxford, Oxfordshire. U.K.
1st – 4th September 1999.
2. 14th U.S. National Congress of Theoretical and Applied Mechanics,
Virginia State University, Blacksburg, Virginia. U.S.A.
23rd – 28th June 2002.

Part of this work has been presented in the following publication:

Gill, S.P.A, Cornforth, M.G, & Cocks, A.C.F (2001), Modelling Microstructure Evolution in Engineering Materials, *International Journal of Plasticity*, vol. 17, pp669-690.

Mark Cornforth
September 2002.

Acknowledgements

I would like to thank my research supervisor Dr. Simon Gill for his continued help, support and guidance throughout this period of research and also to Prof. Alan Cocks for introducing me to the field of modelling microstructure evolution. I would also like to acknowledge and thank Prof. Andrew Strang for his help and assistance during a number of valuable discussions.

Financial support from the Engineering and Physical Sciences Research Council (EPSRC) is gratefully acknowledged. Much of the computational processing work was performed using the University of Leicester Mathematical Modelling Centre's supercomputer which was purchased through the EPSRC strategic equipment initiative.

I would also like to extend my thanks and acknowledge the work of Jonathan Richard Shewchuk [1] for his excellent triangulation software, which allowed me to concentrate more thoroughly on other areas of research.

I would finally like to thank the continued motivation and support from my family, close friends and also research colleagues within the University of Leicester Engineering department.

Modelling the Microstructural Evolution of Engineering Materials

Mark G. Cornforth[†]

Mechanics of Materials Research Group,
Department of Engineering, University of Leicester,
Leicester. LE1 7RH. U.K.

Abstract

A continuum variational model has been developed to model the microstructural evolution of a general class of moving boundary precipitate systems within which elastic strain plays a significant role. The variational framework readily allows for the incorporation of a number of different competing kinetic processes and thermodynamic driving forces into a numerical model without geometrical restrictions. The driving forces considered here arise from compositional variations, interfacial energy, phase transformations and changes of elastic stored energy. The kinetic processes are lattice diffusion and interface migration.

The role of elasticity on the evolution of the microstructure is investigated with particular reference to how elastic fields influence the growth morphology of second-phase precipitates. The elasticity is considered in all phases and is assumed to be linear, isotropic but inhomogeneous. The types of elastic effects considered in this analysis arise from the misfit strain between the precipitate and matrix and an externally applied elastic field. The misfit strain has been shown to restrict the morphology of the growing precipitates and alter the equilibrium shape of precipitate particles from that observed in the absence of any elastic fields. In two-particle coarsening, long-range elastic interactions cause considerable particle shape changes.

Non-equilibrium conditions are modelled at the moving interface and mass conservation is satisfied as the interface translates. A static structured underlying grid is coupled with a dynamic unstructured finite element mesh which is adapted to fit the line of the moving boundary. When the finite element mesh is identified as being distorted, compositional data is transferred from one finite element geometry to another by mapping to and from the structured grid. The transfer of information from one finite element geometry to

[†] E-mail: mgc2@le.ac.uk (until 31st December 2002)

markcornforth@yahoo.co.uk

another has been validated with negligible loss of data. The loss of data only occurs due to spatial averaging.

The variational model is initially applied to simulate the microstructure evolution of the InGaAs semiconductor system within a one-dimensional setting in the absence of any moving interfaces. The variational model is then used to study the more complex precipitation kinetics in steels with particular reference to the evolution of a ferrite precipitate embedded within an austenite matrix and the coarsening of $M_{23}C_6$ precipitate particles. Two-dimensional computational results are presented within this context.

Keywords:

Variational calculus, precipitation kinetics, phase transformations, microstructural evolution.

Nomenclature and Abbreviations

a_i	Lattice spacing of component, i
α^p	Number of metal atom sublattice sites within phase, p , in a formula unit
A	Area
\AA	1 Angstrom = 10^{-10} m
b	Phase boundary
c_i	General composition of component, i
$c_e^{[i,j]}$	Composition within element, e , mapped to the centre coordinates of underlying cell, $[i,j]$
c^p	Number of interstitial sublattice sites within phase, p , in a formula unit
d	Degree of freedom
d_{\max}^b	Maximum interface sub-segment length associated with interface boundary, b
D_i	Diffusion coefficient of component, i
D_o	Frequency factor
\dot{D}	Rate of energy dissipation
E	Young's modulus
E_{err}	Quadratic error function
E_a	Activation energy
f_i	Thermodynamic driving force acting on component, i
F	Applied force
g	Gibbs free energy density per unit volume
G	Gibbs free energy density
h^b	Mesh construction point located at a distance in a direction normal to interface boundary, b
h_{\max}	Pre-defined maximum change in length of all localised interface elements
J	Determinant of Jacobian
j	Diffusional flux
J_0, J_1	Bessel functions of the first kind of zero and first order respectively
k	Boltzman's constant

L	Unit of length
\underline{m}_i	Unit vector normal to point, i
M_{in}	Interface mobility coefficient
n	Number of atoms
n_{grid}	Underlying grid resolution
$n_i(\xi, \eta)$	Two-dimensional isoparametric shape function
\underline{n}_i	Unit vector normal to interface boundary segment, i
N_k	Number of components within sublattice, k
N_e	Number of elemental nodes within finite element, e
$N_{[i,j]}$	Number of finite elements covering underlying cell, $[i,j]$
r	Radius
R	Universal gas constant
S	Configurational entropy
t	Time
T	Temperature
$U_{elastic}$	Elastic stored energy
u, v	Displacements in the x and y directions respectively
ν	Poisson's ratio
V	Volume
v_g	Velocity of Gauss point, g
v_n	Interface velocity
$V_e^{[i,j]}$	Volume contribution from element, e , located within cell, $[i,j]$
w	Unit of energy density
w_i	Weighting factor at Gauss point, i
x, y	Global cartesian coordinates
x_i^p	Molar composition of component, i , within phase, p
\bar{x}	Used to denote a dimensionless quantity used in the model (where x is the real numerical value)
y_i^p	Site fraction of component, i , within phase, p
$z_f(s)$	One-dimensional linear interface velocity shape function
ρ	Density

α	Ferrite
γ	Austenite
γ_s	Surface energy
γ_{xy}	Total (engineering) shear strain
σ	Stress
ε	Strain
ε_o	Mis-match (or misfit) strain
\mathcal{D}^{eff}	Effective diffusivity
\mathcal{D}	Lattice diffusivity
μ	Chemical potential
$\mu_e^{[i,j]}$	Volume fraction from element, e , contained within cell $[i,j]$
$\mu_{[i,j]}^e$	Volume fraction from cell, $[i,j]$, located within finite element, e
Π	Variational functional
$\hat{\Pi}$	Constrained functional (with interfacial condition(s))
Ψ	Dissipation potential
ϕ	Rate potential
ψ	Dual potential to ϕ
ψ_{flux}	Rate of energy dissipation due to lattice diffusion
ψ_{in}	Rate of energy dissipation due to interface boundary migration
λ	Lagrange multiplier
ξ, η	Natural or local coordinates within the virtual computational domain
θ	Implicit / explicit time integration scheme constant
τ	Unit of time
β	Minimum angle used during mesh generation
Δt	Time-step
∇	Del-operator
∇^2	Laplacian operator
b.c.c.	Body-centred cubic
f.c.c.	Face-centred cubic
MTDATA	Metallurgical and Thermomechanical Databank

Matrix Notation

$[AB]$	Shape function matrix relating the rate of change of area of each finite element to the corresponding interface nodal velocities
$[B]$	Shape function matrix relating the elastic strains to displacements
$[C]$	Global stiffness matrix
$[D]$	Material stiffness matrix relating stresses to strains
$[E]$	Interface velocity viscosity matrix
$[F]$	Global force matrix
$[F_{ec}]$	Driving force due to a change in elastic stored energy with change in composition
$[F_{ein}]$	Elastic driving force due to the position of the interface boundary
$[F_{pj}]$	Driving force due to a change in phase energy with change in composition
$[F_{pv}]$	Phase energy driving force due to the position of the interface boundary
$[F_{in}]$	Interfacial surface energy driving force on the nodal velocities
$[H^J]$	Shape function matrix relating the rate of change of composition to the elemental fluxes
$[H^x]$	Shape function matrix relating the rate of change of composition to the interface velocities
$[K]$	Diffusive stiffness matrix
$[L]$	Matrix determined from the velocity shape functions and known concentrations either side of the interface boundary
$[M]$	Matrix determined from the geometry of the interface
$[R]$	Elastic force matrix

Subscripts

a	Atomic
b	Interface boundary
c	Composition
d	Defined
e	Finite element
f	Free

<i>g</i>	Gauss point
<i>in</i>	Interface
<i>k</i>	Sublattice component
<i>max</i>	Maximum
<i>min</i>	Minimum
<i>mid</i>	Centrally located
<i>p</i>	Phase identifier
<i>s</i>	Surface boundary
<i>T</i>	Transformation
<i>v</i>	Volumetric
<i>V_a</i>	Vacancies (i.e. unfilled lattice sites)
<i>a</i>	Direction under consideration (<i>x</i> , <i>y</i> or <i>z</i>)

Superscripts

<i>e</i>	Finite element
<i>I</i>	Implicit
<i>mid</i>	Centrally located
<i>p</i>	Phase identifier
<i>t</i>	Interface segment
*	Unknown variable
+/-	Interface element identifier for the right / left side of the interface respectively

Contents Page

	Page No.
Preface	i
Acknowledgements	ii
Abstract	iii
Nomenclature and Abbreviations	v
Chapter 1.0 – Introduction	1
<hr/>	
1.1 – Aims and Objectives	2
1.2 – The Importance of Modelling Elastic Strain	2
1.3 – The General Problem	3
1.4 – Measuring Microstructure Evolution Experimentally	5
1.5 – Methods for Modelling Microstructural Evolution	7
1.5.1 – Analytical Descriptions	8
1.5.2 – Monte Carlo Simulations	9
1.5.3 – The Phase Field Model	10
1.5.4 – The Variational Approach	12
1.6 – Summary	13
Chapter 2.0 – Describing the Microstructure	14
<hr/>	
2.1 – Crystal Atomic Structure	14
2.2 – Strain Associated Phase Changes	15
2.3 – The Phase Diagram	18
2.4 – Summary	19
Chapter 3.0 – Describing Evolution	21
<hr/>	
3.1 – Diffusion in Solids	21
3.2 – Mechanisms of Diffusion	22
3.2.1 – The Interstitial Mechanism	22
3.2.2 – The Vacancy Mechanism	23

3.2.3 – The Substitutional Mechanism	25
3.3 – Lattice Diffusion	25
3.4 – Entropy as a driving force	27
3.5 – Phase Transformations	34
3.5.1 – The Diffusive Transformation	34
3.5.2 – The Displacive Transformation	34
3.5.3 – Interfacial Flux Conditions	35
3.5.4 – Stoichiometric Fluxes	36
3.6 – Summary	37
Chapter 4.0 – The General Model	38

4.1 – Model Description and Diffusional Relationships	38
4.2 – The Variational Formalism	39
4.2.1 – The Variational Principle	39
4.2.2 – The Variational Principle in Geometric Terms	41
4.2.3 – Kinetic Processes	43
(a) Dissipation due to a Material Flux	43
(b) Dissipation due to Interface Migration	44
4.2.4 – Gibbs Free Energy Contributions	45
(a) Interface Surface Energy	45
(b) Chemical Phase Energy	46
(c) Elastic Stored Energy	46
4.2.5 – Constraints on Interface Fluxes	47
4.2.6 – Formulation of the General Functional	48

Chapter 5.0 – Finite Element Discretisation	49
--	-----------

5.1 – Finite Element Modelling	49
5.1.1 – The Problem Description: Degrees of Freedom	51
5.1.2 – Isoparametric Mapping	52
5.2 – The General Solution Process	54
5.2.1 – Determination of the Elastic Field	54

5.2.2 – Determining the Flux Field and Rate of Interface Migration	56
(a) Dissipative Processes	56
(i) Dissipation due to a Lattice Flux	56
(ii) Dissipation due to Interface Boundary Migration	58
(b) Rate of Change of Composition	61
(c) Rate of Change of Gibbs Free Energy	64
(i) Chemical Phase Energy	65
(ii) Elastic Stored Energy	66
(iii) Interface Surface Energy	68
(d) Interface Constraint	69
(e) General Variational Formulation	70
5.2.3 – Updating the Microstructure Description	71
(a) Time Step 1: Limited Change in Composition per Iteration	72
(b) Time Step 2: Limited Interface Movement per Iteration	72
5.3 – The Explicit and Implicit Time Integration Schemes	74
5.3.1 – Background, Stability and Convergence	74
5.3.2 – Implementing the Implicit Integration Scheme	75
5.4 – Iterative Method for the Solution of Unknowns	76
5.5 – Non-Dimensional Analysis	77
Chapter 6.0 – Numerical Implementation	79
<hr/>	
6.1 – Structured Grids	79
6.2 – Unstructured Grids	80
6.3 – Two-Dimensional Mesh Adaption	82
Chapter 7.0 – Numerical Validation	86
<hr/>	
7.1 – Two-Dimensional Finite Element Diffusion due to Entropy	86
7.1.1 – Thermodynamic Driving Force due to Entropy	87
7.1.2 – Computational Finite Element Results	88
7.1.3 – Discussion of Finite Element Results	90
7.2 – Validating the Finite Element Solution	91
<hr/>	

Chapter 8.0 – Substitutional Diffusion with no Interface 94

8.1 – A Real Material System: InGaAs	94
8.2 – The Variational Model	96
8.3 – The InGaAs Phase Separation	97
8.4 – Computational Finite Element Results and Analysis	98
8.5 – Conclusions	102

Chapter 9.0 – Modelling Moving Boundary Problems 103

9.1 – Literature Review	103
9.2 – One-Dimensional Special Interface Element	107
9.3 – Transferring Information across Two-Dimensional Meshes	114
9.3.1 – Mapping to the Underlying Grid from the Finite Element Mesh	115
9.3.2 – Mapping to the Finite Element Mesh from the Underlying Grid	121
(a) Compositional Averaging at the Nodal Points	122
(b) Gauss Point Mapping	123
(c) Linear Regression	124
(d) Volume Fraction Analysis	125
9.3.3 – Testing Data Transfer To and From the Underlying Grid	128
9.3.4 – Validation of the Underlying Grid for Entropic Diffusion	132
9.4 – Flux Field Dependence on Mesh Topology and Geometry	135
9.4.1 – Flux Field Model A: Irregular Mesh Topology	136
9.4.2 – Flux Field Model B: Regular Mesh Topology	137
9.4.3 – Mesh Construction to Ensure a Regular Mesh Topology & Geometry near the Interface	138
(a) Addition of Mesh Construction Points	139
(b) Linear Velocity Field across each Interface Boundary Segment	141
9.5 – Summary	143

Chapter 10.0 – Evolution of a Ferrite Precipitate **144**

10.1 – Physical Background	144
10.2 – The Two Phases: α - and γ -iron	145
10.3 – Solubility of Carbon	148
10.4 – The Transformation Strain	149
10.5 – Comparison with Other Studies	150
10.6 – Description of the Precipitate Model	154
10.7 – The Phase Energy	157
10.8 – Results and Discussion	161
(a) Planar Precipitate Morphology	161
(b) Circular Precipitate Morphology	163
(c) Circular Precipitate Morphology with Applied Uniaxial Tensile Loading	174
10.9 – Summary and Conclusions	178

Chapter 11.0 – Coarsening of $M_{23}C_6$ Precipitates **179**

11.1 – Background into Coarsening	179
11.2 – Literature Review	181
11.3 – Physical Background of $M_{23}C_6$	183
11.4 – Description of the Problem	185
11.5 – The Phase Energy	190
11.5.1 – Phase Energy Dependence on Carbon Composition	191
11.5.2 – Phase Energy Equilibrium Solution	192
11.6 – Elastic Analysis	193
11.6.1 – The Transformation Strain	193
11.6.2 – Material Property Variation with Chromium Composition	194
11.7 – Interfacial Surface Energy	195
11.8 – Results and Discussion	196
11.9 – Comparison with Classical Coarsening Models	206
11.10 – Summary and Conclusions	213

Chapter 12.0 – General Conclusions and Further Work **215**

12.1 – Summary and Conclusions 215

12.2 – Future Work 216

Appendix **221**

A – Elastic Finite Element Derivations 221

A.1 – The Stress-Strain Relationship 221

A.2 – The Relationship between Strain and Displacement 222

A.3 – Elemental Elasticity Matrices 224

A.4 – Stiffness and Transformation Matrix Differentials 224

B – Numerical Integration: Gaussian Quadrature 226

B.1 – One-Dimensional Gaussian Quadrature 226

B.2 – Two-Dimensional Gaussian Quadrature 227

C – General Input Data for 2D Finite Element Mesh Generation 230**D – Derivation and Analysis of the Analytical Solution** 231**E – Material Constants for InGaAs** 233**F – Modelling the Effect of External Loading** 235

F.1 – Modelling an Applied Displacement along the System Boundary 235

F.2 – Modelling an Applied Force along the System Boundary 238

G – Flowcharts for Modelling Microstructure Evolution 241**H – Volumetric Strain Associated with a Ferrite Precipitate Embedded within an Austenite Matrix** 244**I – Data used in the Fe-C Computations** 245**J – Data used in the Fe-Cr-C Computations** 246**K – A Simplified Ostwald Ripening** 248**L – Accompanying PC CD-ROM** 251**References** **252**

Addendum consists of one computer CD-ROM (see Appendix L for more information).

1.0 – Introduction

The manner in which material microstructures evolve both during processing and during their service lifetime can significantly affect material properties and performance. It is therefore advantageous to better understand the evolution of material microstructures so as to enable engineering components to be designed to withstand or avoid suffering any long-term damage, deterioration or potential failure during service.

The modelling of engineering materials is a powerful tool in assisting the design of engineering components and can be used to investigate, elucidate and predict the significant microstructural changes which occur as a material evolves within a given situation. In-depth research and insight into modelling the microstructural evolution of engineering materials is becoming increasingly important and holds great promise for innovation into computational solid mechanics. The modelling of materials has a useful purpose in analysing potential material performance in high stress or high temperature applications and also for studying the effect of applying heat treatment and solid solution strengthening processes to materials. It also proves to be a useful tool for studying material processing and for investigating the degradation processes in materials. Modelling the microstructural evolution of engineering materials is often complex in nature due to the inherent difficulties associated with the modelling of dynamics, instabilities, non-linearities, perturbations, interacting processes, non-equilibrium conditions, moving boundaries, material anisotropy and inhomogeneous material systems. However, although each material system is different in nature and presents its own complexity, assumptions can usually be introduced in order to simplify the analysis and speed up the solution process.

At present there is an international effort concerning the development of quantitative models for predicting the microstructural evolution of materials subject to high stress, high temperature applications and during heat treatment processes. Previous work carried out in this area, such as the development of analytical techniques, is often limited in nature and oversimplifying assumptions are frequently introduced in order to simplify the complexities involved. Such assumptions are often unwarranted in materials systems of interest, and lead to inadequate descriptions of evolving microstructures.

1.1 – Aims and Objectives

The aim of this research work is to develop a general numerical method in order to accurately model the microstructural evolution of engineering materials using a variational approach. The principal objectives of research in this area include the development and utilisation of both current and novel numerical algorithms and computational finite element modelling techniques in order to develop a general variational model to simulate the microstructural evolution of materials. The fundamental variational principle along with the fundamental laws of diffusion theory are jointly incorporated within a finite element framework to form the general model, which couples the different kinetic processes and thermodynamic driving forces associated with microstructure evolution. The general model is then represented and written in the form of computational code which is firstly verified and then utilised to model the subsequent microstructure evolution of real engineering material systems. Real material systems such as the semiconductor InGaAs and precipitate systems such as Fe-C and Fe-Cr-C are investigated since they provide a range of different challenges, complexities and diffusive mechanisms to consider (from substitutional to interstitial to coupled substitutional and interstitial diffusion processes respectively). The variational principle is initially used to model the microstructural evolution of material systems within a one-dimensional setting but this is soon extended and developed to a fully two-dimensional finite element framework.

1.2 – The Importance of Modelling Elastic Strain

One of the features of this research is to model the effect of elastic strain on the evolution of a material microstructure. Elastic strain can have a very strong influence on the microstructural evolution of a particular material [2]. This can be illustrated in Figure 1.1, which shows a micrograph of a Ni-based superalloy [3], in which the microstructure can be considered as that of a matrix material punctuated by the presence of a number of second-phase precipitate particles. The micrograph shows strong spatial correlations between precipitates and a strong preference for a particular shape, where the precipitates tend to be square-like or cuboidal. Elastic interactions cause these features since, unlike other effects influencing the evolution of precipitates, these driving forces act over long distances. The micrograph presented here serves only as an example to illustrate the importance of modelling elastic strain.

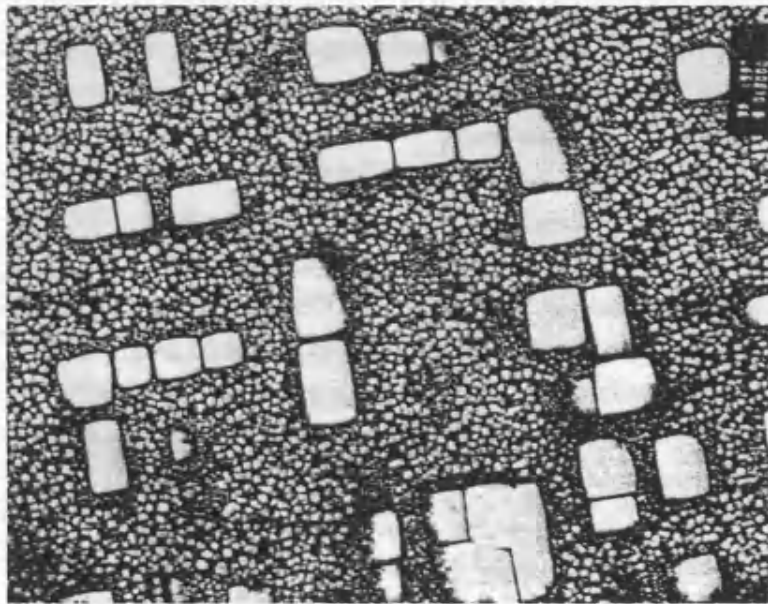


Figure 1.1 – Micrograph of a Ni-based super-alloy illustrating strong spatial correlations between precipitates and a strong preference for a particular shape (Johnson, W.C. and Voorhees, P.W. [3]).

1.3 – The General Problem

The properties of a material depend on the microstructure. A major objective of any material processing route is to produce a microstructure which provides the properties which are appropriate for the design situation being considered. The microstructure can further evolve in service, which can result in a deterioration of the material performance and eventual failure. A major objective of the research being conducted is to develop an understanding of the relationship between microstructure and material behaviour and to determine how the microstructure evolves during processing and in service. General strategies are developed for modelling microstructure evolution which provide a framework for the development of simple analytical procedures and computer software for the detailed simulation of a process.

The general nature of the problem under investigation is shown diagrammatically in Figure 1.2, along with some examples showing the range of physical processes of interest occurring at the micromechanical level. These processes principally include the diffusional rearrangement of matter within the body and the motion of internal interface boundaries separating the different phase regions. It is considered that a given phase can change both its

size and shape with time as a result of diffusive processes that transport mass from one phase to another or from one part of a given phase to another.

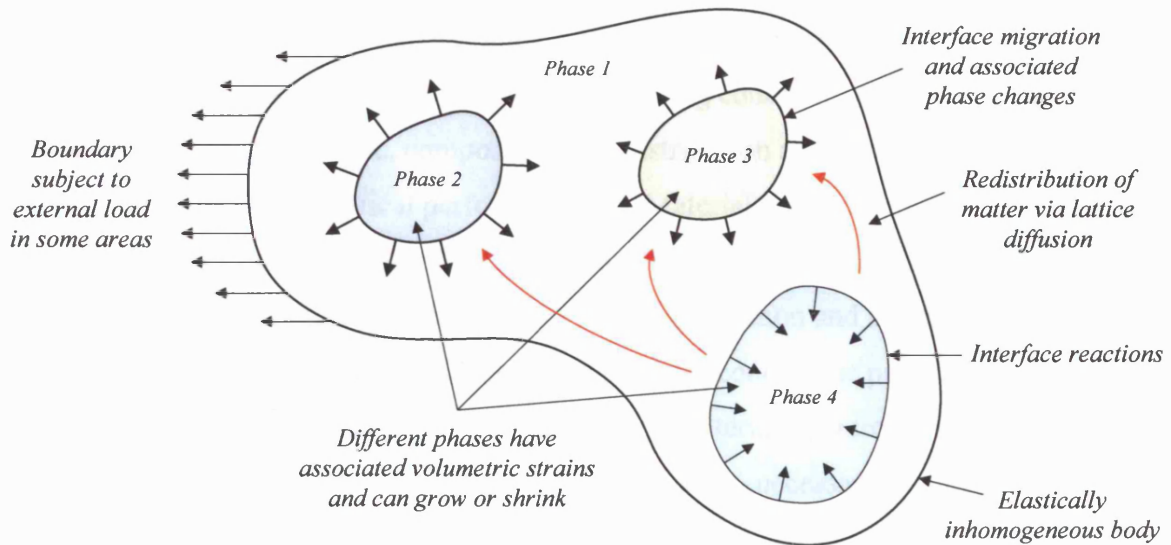


Figure 1.2 – The general situation: A multi-phase elastically inhomogeneous microstructure can evolve by a number of kinetic / dissipative processes: lattice diffusion, the migration of interfaces and / or the rate of operation of any interface reactions.

In multi-phase systems, the evolution of the microstructure is determined by the interaction of the different phases between interface boundaries and the elastic properties of the different phase components. The temperature, which provides thermal energy to the system, and the way in which the different thermodynamic driving forces interact with one another over time determine the evolution path of the material microstructure, thus determining whether a particular phase will nucleate, grow or dissipate.

One of the fundamental difficulties associated with the modelling of materials is how to extract the features of the problem that are important, while at the same time attaining a tolerable level of simplification. The use of a continuum description essentially smears out features associated at the small scale, such as the discrete phenomena that are related to the existence of atoms and replace the kinematic description of materials in terms of atomic positions with field variables. Continuum models have the advantage of reducing the complexity of description of the material system by renouncing non-essential nanoscopic details.

1.4 – Measuring Microstructure Evolution Experimentally

Many engineering materials invariably undergo microstructural changes, not only during material processing and heat treatments but during long-term exposure in service at high temperatures that lead to the degradation of mechanical properties.

In alloy systems, careful control of the processing conditions are required to ensure that the desired precipitate structure, composition and distribution are obtained to achieve optimum mechanical or electrical performance [4]. Material processing is used to alter a given microstructure and usually involves the subjection of a material to either mechanical deformation or heat treatment or both. One of the most common and successful methods of strengthening metals is by creating a fine dispersion of second phase particles, which can be achieved by precipitation. The process of hardening a material by introducing a fine dispersion of particles into a ductile matrix increases the applied stress necessary to move dislocations. The precipitates provide a very strong obstacle to the slip of dislocations in the matrix, and the matrix provides some ductility to the overall alloy. The precipitates should be discontinuous, while the soft ductile matrix should be continuous, such that cracks in the discontinuous brittle precipitates are arrested by the precipitate-matrix interfaces. The precipitate particles should also be small and numerous, increasing the likelihood that they interfere with the slip process, while large quantities of precipitate increase the strength of the alloy. The precipitate particles should also be round, rather than needlelike or sharp-edged, since this is less likely to initiate a crack. These general considerations are used for determining how the characteristics of the matrix and precipitates affect the overall properties of the alloy.

The Al-4% Cu alloy is a classical example of an age hardenable alloy and provides a good example of how the material properties, such as strength and hardness, can be related to the temperature, solute content and precipitate particle spacing. The Cu/Al alloy can be precipitation hardened, in order to attain maximum strength and hardness, by the precipitation of second phase particles at a specified time and temperature. The maximum strength of Cu/Al alloys is achieved by producing a strong uniform closely-spaced dispersion of fine CuAl_2 precipitates within the softer, more ductile matrix. The hardness increases with the percent solute, but decreases as a given precipitate phase coarsens during the continued ageing of the alloy. It is therefore critical that the alloy is precipitation hardened for the correct time and temperature in order to attain optimum mechanical properties.

Experimentally, long time scales are usually required for testing the in service evolution of the mechanical properties of an engineering component which correspond to the evolution of its microstructure. Typical service conditions are usually simulated over time periods of approximately 30,000 hours and the data obtained is then extrapolated to project the safe operational lifespan, mechanical properties and in service performance of the component for time periods of up to 150,000 hours. These predictions include safety factors and attempt to take into account the typical loading history, operating temperatures and stress conditions experienced by the component during its service lifetime. Experimental techniques commonly used to study and characterise a material microstructure at different stages during its service lifetime include destructive testing, where samples are removed from selected areas of the component and then analysed by transmission electron microscopy, and non-destructive testing, which include non-contact methods such as x-ray diffraction and ultrasonic scanning.

We are interested in in-service evolution, particularly the in-service evolution of steels, which represent the most widely used metallic material within the engineering industry. Experimental investigations into how chromium steel microstructures evolve under service conditions have been carried out by Strang et al. [5] [6]. In order to determine the changes in microstructure due to high temperature creep exposure, optical and transmission electron microscopy studies were carried out. From these studies, data was collected based on the size and distribution of minor phases and the chemical composition of components within each phase. Information relating to the composition, size, shape and distribution of second-phase precipitates extracted from such experimental studies is then related to the mechanical properties of the particular material. This process can be carried out at a number of different stages during a material's service lifespan and under a range of operating temperatures in order to investigate the evolution of the phases and how this can be related to the properties and in-service performance of the material. This provides an example of how experimental investigations are carried out and how the evolution of the microstructure can affect the material properties.

It is obviously very expensive and time consuming for industrially based companies to obtain experimental data and several technological advances may have been made to the original component by the time data for microstructural evolution is obtained. For this reason computational analysis is usually favoured and the available experimental data is typically used to validate the models. These models are often based on curve fitting and have little input

from constitutive laws or relevant material properties. Due to the increase in computer power, it is now becoming possible to simulate the evolution of small microstructures, to develop constitutive laws and simple models based on the mechanics and physics of the materials involved. Although considerable time and effort may be required to fully research and develop a computational model to simulate microstructural evolution, recent advances in computer resources and processing power can drastically speed up the solution process. Such models can then be used for improvements in alloy design, to produce greater microstructural stability and mechanical properties during service. These computational models can also be used to predict the safe operational life of high temperature and high stress industrial alloys without having to resort to extensive experimental studies.

1.5 – Methods for Modelling Microstructural Evolution

For a computational model to be a useful tool in the design of a microstructure, it must be based on realistic assumptions regarding the properties and dynamics of the material system of interest. With the advent of high-performance computers and the development of powerful mathematical and numerical methods, models can be formulated to accurately simulate the evolution of a microstructure. As a result, computational models are becoming increasingly able to mimic and predict non-equilibrium microstructural phenomena, such as phase transformations, coarsening, sintering and the morphological evolution of thin films.

This section outlines the principal methods that are widely used to model the microstructural evolution of materials occurring over different characteristic length and time scales. As a summary, the techniques that are widely used for modelling microstructure evolution are listed as follows:

1. Analytical descriptions
2. Monte Carlo simulations
3. Phase field model
4. Variational formulation

Although it is impossible to give an in-depth review of each of the methods considered, a general overview is provided which states the relative advantages and disadvantages associated with each approach.

1.5.1 – Analytical Descriptions

Analytical expressions have widespread use in the field of modelling microstructure evolution and have been used to describe physical processes such as grain growth, nucleation, Ostwald ripening etc [7]. They are usually developed within a continuum framework and are analytically tractable because they enforce restrictions on the way that the composition and geometry of the system evolve. Consider the case of Ostwald ripening [7] – [9], in which larger precipitate particles within the matrix grow at the expense of the smaller ones in order to reduce the total interfacial area. Analysis of the simplified problem of the evolution of two spherical particles leads to the development of a basic equation for particle interaction. This fundamental equation for two particles can be then be used to statistically predict how large systems of multi-sized particles evolve on average. This type of global statistical relationship can then be related to quantities that can be experimentally measured. In the case of Ostwald ripening, the particle interaction law leads to the classical result for the rate of coarsening of precipitates which states that the mean precipitate volume increases linearly with time. This expression is widely used by experimentalists because it is simple and encapsulates the basic physics of a fundamental, relevant process. This rule can then be used to predict the change in a materials property over time beyond the time scale of the experiment. However, some material systems do not exhibit classical Ostwald ripening. Discrepancies can arise because the mechanism for the evolution is different or the precipitates do not remain spherical during coarsening or because compositional phase energy variations, elastic stored energy or more complex phenomena such as plasticity or creep are important. As a result, such an analytical description can lead to a somewhat poor representation of what is actually a far more complex physical process. This is illustrated in more detail in chapter 11, where the classical theory of Ostwald ripening is directly compared against the computational model developed within this thesis. By looking in detail at the complex interaction between two particles in this way, revised interaction rules can be developed to statistically predict how experimentally relevant quantities evolve over time.

In summary, results from analytical expressions are useful in the sense that they provide insights into the qualitative dependence of solutions on particular material and geometric parameters, and sometimes they represent the system behaviour very well. However, due to the complexities associated with modelling the microstructure evolution processes which occur within engineering materials, over-simplifying assumptions are

frequently introduced to analytical expressions in order to reduce the complexity of the system. For this reason, analytical solutions are limited by the fact that they do not allow for the general treatment of a wide range of geometries and are usually restricted to a few specific cases. Despite the useful insight provided by analytical expressions, there are many instances in which the materials and their geometries are sufficiently complex such as to defy analytical descriptions. In many cases, such as modelling moving boundary precipitation kinetics, analytical solutions are generally difficult to obtain and can involve the application of unrealistic assumptions.

1.5.2 – Monte Carlo Simulations

A probabilistic numerical scheme that has widespread use in the consideration of diffusive processes associated with microstructural evolution is the Monte Carlo approach. One is often confronted with problems that have an enormous number of dimensions or a process that involves a path with many possible branch points, each of which is governed by some fundamental probability of occurrence. For each uncertain variable (one that has a range of possible values), one can define the possible values with a probability distribution. Monte Carlo methods are powerful tools for statistically exploring the multiple evolution paths of complex, many-body systems evolving by non-deterministic processes.

In the consideration of diffusive processes, the atomic vibrations do not need to be treated explicitly as they are much more rapid than diffusive events. They can be statistically smoothed using transition state theory such that only the atomic jumps due to diffusion need to be considered. All possible microscopic motions can be readily identified and their activation energies computed. Therefore, a distribution of all competing processes and a quantitative reckoning of their relative states can be established. The evolution of the microstructure can be proceeded by a sequence of Monte Carlo steps, where at each step a member of the distribution of permitted events is randomly selected, weighted by its relative transition rate. As a result, the event changes the configurational state of the system. A typical atomistic Monte Carlo simulation involves the random selection of a particular site for an atom to jump into, and if the net energy of the system is lowered, then the new configuration is accepted, otherwise the new configuration is rejected with a certain probability. In this manner grains and pores may grow and shrink and precipitation can be modelled. The

physical properties of the material are investigated as a function of various parameters, such as grain size, pore distribution, temperature, pressure, etc.

The Monte Carlo method is advantageous in the sense that it can readily incorporate non-linear atomistic interactions and kinetics and it is also usually quite easy to set up a problem and solve it. However, as it is a statistical method the user has to be careful to ensure that the results are valid (particularly at boundaries) and to ensure that the results are statistically significant (by taking the average evolution of many simulations). The latter condition can be very time consuming, particularly for large systems. Also, to obtain a proper relation between real time and Monte Carlo time, the Kinetic Monte Carlo method must be used [10]. This requires all possible events to be assembled into a dynamical hierarchy of transition probabilities at each time step, which can significantly reduce the efficiency of the algorithm.

Sutton and co-workers have recently developed a three-dimensional atomistic Kinetic Monte Carlo approach to modelling evolving microstructures within elastically anisotropic and inhomogeneous systems [11]. In this case, a reduced, local elasticity problem is solved at each time step in order to estimate the long range elastic fields and resulting overall change in energy. To make the computation feasible the number of possible events is highly restricted so that only two mobile vacancies are considered. This is because the number of time steps is significantly higher than that in a deterministic simulation and so the costly calculation of the elastic field at each step becomes prohibitively expensive for systems with more degrees of freedom. This consideration would also make it difficult to investigate other long-range deformation phenomena such as plasticity and creep using Monte Carlo methods. For more background information and detail into the concepts and power behind Monte Carlo simulations, the reader is referred to the work of Krauth [12] and the references contained therein.

1.5.3 – The Phase Field Model

The phase field model treats the system as a whole using a continuous field variable (called the phase or order parameter) to describe the state of the various regions of the system, with the interfacial region being modelled as a diffusive layer. The phase field model involves solving a system of nonlinear coupled partial differential equations and incorporates a wide variety of physical phenomena such as non-equilibrium kinetics and capillarity. One of the

key advantages of the phase field approach is that it eliminates the need of explicitly tracking any interfaces during the course of a simulation, since all that is essentially monitored is one or more field variables through space and time.

In the phase field model, the state of the microstructure can be continuously represented by the order parameter, ϕ . For example, $\phi = 1$, $\phi = 0$ and $0 < \phi < 1$ can represent a precipitate, matrix and interface respectively. The latter is therefore located by the region over which ϕ changes from its precipitate-value to its matrix-value, and the range over which it changes is the width of the interface. In order to overcome difficulties associated with solving free or moving boundary problems, phase-field models employ the diffuse-interface model to simulate microstructural evolution. This is different from the conventional sharp-interface approach and the diffuse-interface field model can describe interfaces and boundaries where the field variables change smoothly from one phase domain to another [13].

In the phase field modelling of solidification, there is no distinction made between the solid, liquid and the interface, since all regions are described in terms of the order parameter. This allows the entire domain to be treated simultaneously. The interface is not tracked but is given implicitly by the chosen value of the order parameter as a function of space and time.

Phase field models are relatively computationally efficient and have been successful at simulating topological transitions and microstructures with a large number of particles, especially during coarsening [14]. Phase field modelling has also been successfully used to model solidification processes [15], grain growth [16] [17], phase separation [18], Ostwald ripening [19] and phase separation coupled with coarsening and refining [20].

Microstructural evolution phenomena such as the nucleation, growth and coarsening of precipitates can be simulated using the phase field approach with a single consistent methodology. Both isothermal aging and heat treatments can be considered and microstructural evolution can be characterised as a function of temperature, alloy composition and internal misfit strain. This method has been used to describe complex multi-phase microstructures with long-range elastic interactions [21]. Analytical linear elastic expressions for the dilation of a small volume are used to calculate the net elastic field by summing over the contributions from all such volumes. However, despite the power and versatility behind the approach, phase field modelling suffers when faced with the concept of modelling non-linear elasticity and plasticity phenomena. Phase field models cannot readily model grain-boundary diffusion and have difficulties in assigning energies associated with interfacial

regions, where the order parameter varies smoothly from its precipitate-value to its matrix-value. It is also difficult to implement complex interfacial conditions between different phase regions. The variational model can readily account for these phenomena, although in this thesis we limit ourselves to the case of linear elastic deformation. This approach is described in the following sub-section.

1.5.4 – The Variational Approach

It is possible to formulate various scientific laws in terms of general principles involving the calculus of variations. These are called variational principles and are usually expressed by stating that some given integral is a maximum or a minimum. One example is Hamilton's principle of least action, of importance in the theory of motion. In this case an integral, called an action integral, is to be minimised. This principle, which leads to Newton's laws of motion as a special case, has also been used as a basis for quantum mechanics. Applications of variational principles also occur in elasticity, aerodynamics, theory of vibrations and other areas in engineering and science.

The variational method employed in this thesis is a global work rate minimisation technique and is essentially a weak integral form of writing solutions to partial differential equations. The widely used Finite Element Method is an example of a variational method. Consequently it is practical to utilise the vast amount of experience obtained with this method in the analysis of the deformation of solids when tackling microstructural evolution problems. The variational principle can hence be used for the solution of typical static problems such as elastic deformation and in less commonly addressed kinetic problems such as diffusion forced by the motion of a remote interface. Hence it can be implemented to model the evolution of material microstructures in a thermodynamically consistent manner, providing a framework for simulating a wide range of physical processes and incorporating any kinetic processes and thermodynamic driving forces. It can also be applied across a wide range of length scales and can be easily implemented in finite element type numerical procedures. However, the development of variational models tends to be time-consuming to implement, particularly for large time-dependent problems, and only allows for the solution of isothermal processes.

Cocks, Gill, Pan, Kucherenko and Suo have extensively applied the variational principle to successfully model a wide range of physical processes, including: the motions of microscopic surfaces [22]; the growth of cracks [23]; the cosintering of particles [23]; the

structural evolution of grains [24] – [27]; void growth in a material subject to creep [28]; the relaxation of epitaxial islands [29]; the evolution of precipitate strengthened materials [30]; phase separation coupled with coarsening and refinement [31]; and the creep response and deformation of engineering materials [23]. This adds strength to the case that this ‘general’ method is very flexible and can look at many problems that other methods cannot.

1.6 – Summary

This chapter describes the general problem under consideration along with a review of the methods commonly used in the field of solid mechanics to model the evolution of material microstructures. Due to the wide applicability of the variational approach to model a variety of complex elasticity phenomena and a range of diffusive mechanisms and processes, the variational approach was selected to model the microstructural evolution of engineering materials, with particular reference to complex moving boundary and precipitate systems. This is the most general and flexible method but also computationally demanding. Therefore it is expected to be developed as a tool for small scale simulations for developing constitutive laws in complex multi-phase multi-component systems.

Within the remainder of this thesis, chapter 2 identifies the information required to characterise the starting microstructure and chapter 3 examines the dynamics of the microstructure and the rate at which a general microstructure can evolve. Chapter 4 describes the general strategy for modelling microstructural evolution at a continuum micromechanical level using the variational approach. Chapters 5 and 6 address the general modelling and numerical strategies of the general solution process incorporating the numerical finite element implementation of the general model. In chapter 7, the computational solution is compared with a known analytical solution in order to validate the numerical code and finite element model. Chapter 8 provides a further benchmark application of the model and simulates the one-dimensional microstructure evolution of the InGaAs semiconductor system. Chapter 9 examines how the general variational model can be used to address issues relating to a general class of moving boundary problems. The variational model is then applied to simulate precipitation and coarsening processes in chapters 10 and 11 respectively. The general conclusions arising from this work are summarised in chapter 12 along with suggestions for further work.

2.0 – Describing the Microstructure

It is important to carefully define and characterise the material microstructure description prior to any computational analysis. This section examines how a microstructure can be described in terms of the composition of each component within each phase domain and by the geometrical shapes of different phases in relation to their interface boundaries. The description of the crystal atomic structure can be related to how internal misfit strains arise as a result of a difference in lattice spacing between different phases. In this thesis, the interface separating each phase is assumed to be coherent such that the elastic fields satisfy continuity conditions across the phase boundary, although this is not a necessary assumption.

2.1 – Crystal Atomic Structure

Following the work of Sundman and Agren [32], a given phase can be considered to consist of a number of different sublattices. For example, in fcc austenite, there are two sublattices:

1. The main fcc lattice sites, which are occupied by vacancies, iron or other metallic substitutional alloying elements such as chromium, nickel or vanadium.
2. The interstitial lattice sites, which are either vacant or occupied by carbon, nitrogen or other interstitial elements.

The fraction of sites occupied by a component, i , within each sublattice is described by the site fraction of that component, y_i , and the summation of the site fractions within each sublattice is defined as being equal to unity. Therefore, for conservation of mass within each sublattice, this can be written in general terms as

$$\sum_{i=1}^{N_k} y_i + y_{va} = 1 \quad (2.1)$$

where N_k is the number of components within sublattice, k , and y_{va} is the site fraction of vacancies, i.e. unfilled lattice sites. Vacancies are necessary for lattice diffusion, but since $y_{va} \ll 1$, the contribution to the mass balance from vacancies can often be ignored.

Within a general class of steels, the site fraction of carbon, y_c^p , within phase, p , can be related to the molar fraction of carbon, x_c^p , through the relation

$$y_c^p = \left(\frac{a^p}{c^p} \right) \left(\frac{x_c^p}{1 - x_c^p} \right) \quad (2.2)$$

where a^p and c^p are used to denote the number of sites on the metal and interstitial sublattices within phase, p in a formula unit. In the case of bcc ferrite, $a^{bcc} = 1$ and $c^{bcc} = 3$, which indicates that three possible interstitial positions exist for one substitutional position occupied by a metal atom.

The local composition is generally described by the molar fraction, x_i^p , of a selected component, i , due to the fact that the site fraction is not generally conserved when the component atoms diffuse from one phase domain to another. However, the site fraction is used in the theoretical analysis to calculate the Gibbs free energy and its derivatives.

2.2 – Strain Associated Phase Changes

Strain associated phase transformations can be described as ‘natural’ changes that occur within engineering materials, where the atoms take up new relative positions under the influence of the elastic strain energy. A phase transformation is used in a general sense to indicate any extensive rearrangement of the atomic structure. For a material, consisting of two different phase regions, A and B , with similar material properties (Young’s modulus, Poisson’s ratio etc), internal stresses will arise as a result of a ‘misfit’ between the different atomic lattices of the phase constituents. When a phase transformation occurs, there is often a change in volume involved in the process. This volumetric or dilatational strain arises due to a change in volume with respect to the original volume. The mismatch strain is calculated based on the different lattice spacings between the two phases and assumes coherency. Taking phase A as the reference configuration, the mismatch (or misfit) strain, ϵ_o , can be defined as

$$\epsilon_o = \frac{a_A - a_B}{a_A}$$

where a_A and a_B are the lattice spacings of phases A and B respectively. Consider the volumetric change of the unit cell of phase constituent A associated with the addition of molar fraction, c , of phase constituent B , as shown in Figure 2.1.

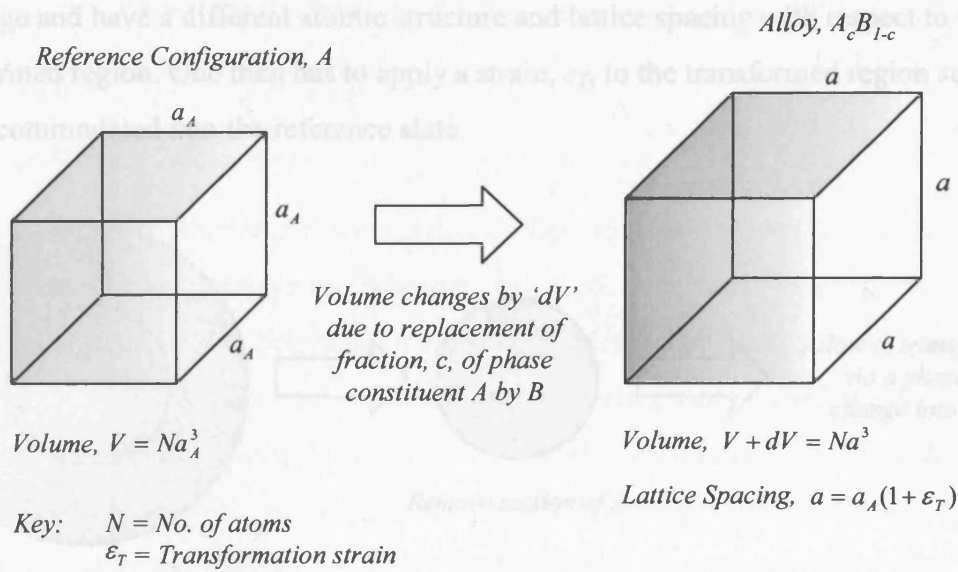


Figure 2.1 – Atomic change of a unit cell of A due to a change in the composition of B.

For simplicity, assume the lattice spacing of the resulting system can be expressed in terms of a linear interpolation of the lattice spacings of each of the constituent phases

$$a = a_A(1 - c) + a_B c = a_A(1 + \epsilon_o c) \quad (2.3)$$

The change in volume associated with the phase change (with respect to the reference configuration) can be expressed as the volumetric strain, ϵ_v , written as

$$\epsilon_v(c) = \frac{dV}{V} = \frac{a^3 - a_A^3}{a_A^3}$$

which can be simplified using equation (2.3) to

$$\begin{aligned} \epsilon_v(c) &= 1 + 3\epsilon_o c + 3\epsilon_o^2 c^2 + \epsilon_o^3 c^3 - 1 \\ &\approx 3\epsilon_o c \text{ for } \epsilon_o \ll 1 \end{aligned} \quad (2.4)$$

Hence, the transformation strain, ϵ_T , is given by

$$\epsilon_T = \epsilon_o c \quad (2.5)$$

A transformation (e.g. a volumetric change) imposed on a region tends to cause complex distortions in both the transformed region and in the surrounding matrix. To demonstrate this, Figure 2.2 shows a conceptual illustration of how a misfitting phase, B, is introduced into the reference phase, A. One initially starts from an unstrained reference state (phase A) and then removes the region where the phase transformation occurs. The removed region is then allowed to transform via a phase change (into B) such that the size and shape of the particle

may change and have a different atomic structure and lattice spacing with respect to the untransformed region. One then has to apply a strain, ϵ_T , to the transformed region such that it can be accommodated into the reference state.

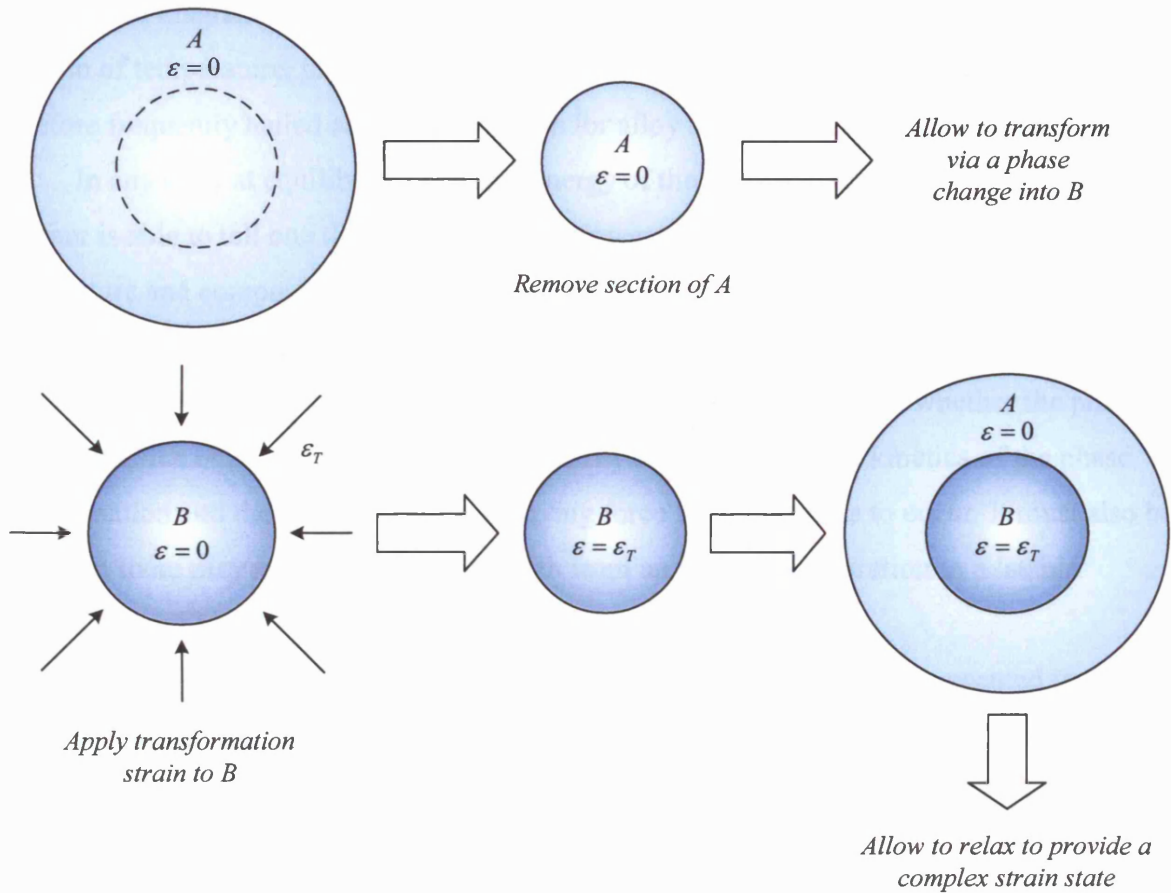


Figure 2.2 – Conceptual illustration of how a misfitting phase, *B* is introduced into a reference phase, *A*.

As the reference state is chosen to correspond to a given lattice spacing, there are always the same total number of atoms per unit reference volume in the reference configuration. This implies that the two descriptions of composition are identical, i.e. volume fraction = atomic fraction. This concept of a global reference state is important because it means that mass is conserved during material transport between phases if the values of the volumetric fluxes are balanced.

It is apparent from Figure 2.2 that the elastic strain field is very complicated, both inside and outside the transformed region. For this reason it is not always possible to obtain an

analytical solution for the elastic fields. As the shape changes become more complex [33], it is necessary to resort to numerical methods.

2.3 – The Phase Diagram

Phase diagrams are visual representations of the equilibrium state of a material as a function of temperature, pressure and concentration of the constituent components. They are therefore frequently hailed as basic blueprints for alloy design, processing and development.

In any alloy at equilibrium, the free energy of the alloy will be a minimum. A phase diagram is able to tell one the equilibrium (i.e. lowest energy) phases at certain conditions of temperature and composition, in the absence of elastic or capillary effects. However, phase diagrams do not give any information about the rate at which a phase transformation takes place, the morphology of the phases (e.g. size, shape and distribution) or whether the phases exist in practice or not. These factors are primarily determined by the kinetics of the phase transformation and the magnitude of the driving force for the process to occur. It must also be noted that there may not necessarily be a path from an initial configuration to a ‘stable’ microstructure [24].

The state of a two-component material at constant pressure can be presented in the well-known graphical form of binary phase diagrams. For three-component materials, an additional dimension is necessary for a complete representation. Therefore, ternary systems are usually presented by a series of sections or projections. For systems with more than three components, the graphical representation of the phase diagram in a useful form becomes not only a challenging task, but may also be hindered by the lack of sufficient experimental information. In this situation, the difficulty of graphically representing systems with many components is irrelevant and phase diagrams can be customised for the materials problem of interest.

A study of the constitution and structure of steels and irons, for example, must first start with the iron-carbon equilibrium phase diagram, shown in Figure 2.3. Many of the basic features of this system influence the behaviour of even the more complex steel alloys. The iron-carbon phase diagram provides a valuable foundation on which to build knowledge of both plain carbon and alloy steels.

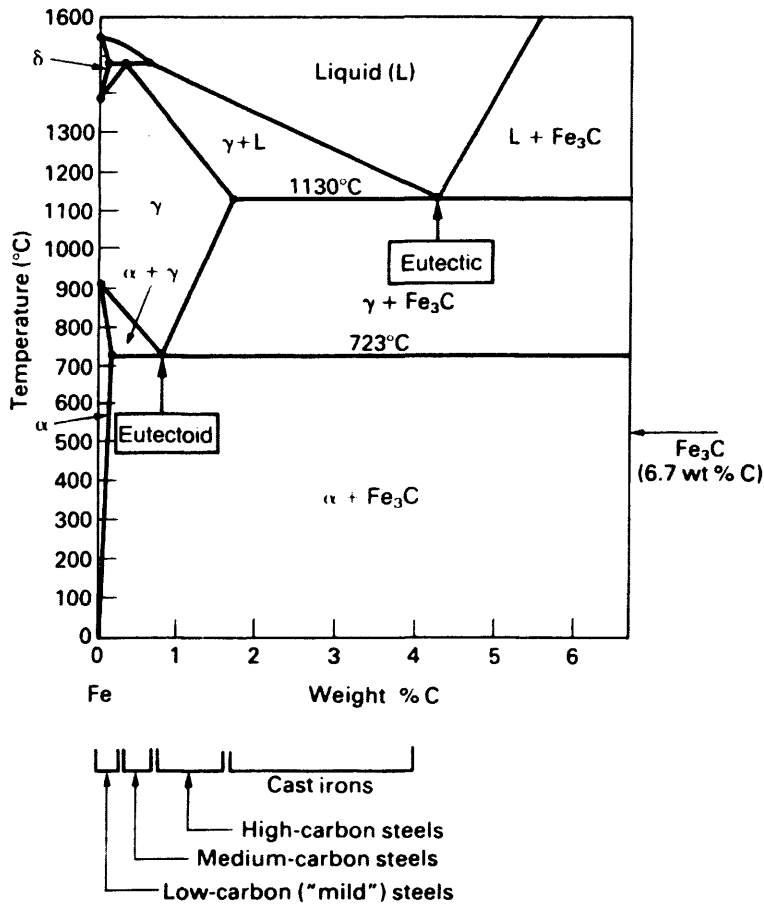


Figure 2.3 – The iron-carbon phase diagram
(Ashby, M.F. & Jones, D.R.H. [34]).

Phase diagrams instruct one's intuition concerning the temporal evolution of certain metastable states. In particular, for the case in which one has a supersaturation of foreign atoms, one is led to expect that if the atoms have sufficient mobility, sooner or later they will find each other out and form new phases, namely precipitates. In multi-component systems, careful control of the processing conditions are required to ensure that the desired precipitate structure, composition and distribution are obtained to achieve the desired material properties for the required service conditions [35].

2.4 – Summary

To fully describe a material microstructure, it is necessary to know the number of phases contained within the microstructure at the particular temperature and condition of interest. It is necessary to know the global composition of each constitutional element (or

sublattice component) at all points across the microstructure along with the relative fractions of each. Information relating to the geometrical positions and associated shapes of the different phases in relation to their interface boundaries is required. It is also necessary to define the lattice spacings of each phase in order to calculate the strains associated with internal solid-solid phase transformations and evaluate material property data in order to perform a complete elastic analysis of the microstructure configuration. It is important that all this information is carefully defined in order to fully characterise the starting material microstructure prior to any computational and theoretical analysis.

The following chapter describes how this information can be used to describe how a material microstructure evolves over time from a defined initial configuration.

3.0 – Describing Evolution

In this chapter, attention is given to describing the dynamics of the microstructure and the rate at which a general microstructure can evolve. This can occur by changing the composition of its phase constituents and / or by translating interface boundaries between different phases. In either case, the unknown system rate variables need to be determined in order for the microstructure to evolve. The different types of diffusive mechanisms along with different phase transformations are discussed within this context.

3.1 – Diffusion in Solids

‘Diffusion’ can be defined as the spontaneous movement and rearrangement of matter, which consequently leads to an equalisation of free energy. Management of diffusion as a means of altering local composition is vital in many fields of engineering such as sintering, diffusion bonding and solid solution strengthening. Although diffusion in solids can be considered as a relatively slow process, it accounts for the microstructural material changes that occur in many temperature-dependent processes such as creep, oxidation, and precipitation. Changes in the structure of materials, which mostly occur by the process of diffusion, and their effect on the physical and mechanical material properties can be explained at an atomic level by the fundamental theory of diffusion.

In solids, the kinetic energy is in the form of atomic vibration, so on the whole little mass actually moves, except when an atom manages to jump from one lattice site to another. This possibility is thermally activated, but few mechanisms for such movement have low enough activation energy to allow a reasonable transport rate. Even when atoms do jump, they jump in random directions so the overall net travel of mass is very small.

Thermodynamics states what the most stable structure is at a given temperature and pressure. However, there is a finite time required to reach that stable structure, i.e. if atoms have to diffuse through a crystal lattice to nucleate a new phase then this takes time. The rate at which a transformation can occur depends on the kinetics. If the kinetics are very slow, the structure may not readily reach the most stable form. If a large number of atoms must diffuse to produce a uniform structure, long times may be required, even at high temperatures.

3.2 – Mechanisms of Diffusion

It is well known that atoms in a crystal continuously oscillate about their equilibrium positions. Occasionally these oscillations become violent enough (for example, if thermal energy is supplied) to allow an atom to change lattice sites. It is these jumps from one site to another which gives rise to diffusion in solids. In this section the principal mechanisms of diffusion are discussed.

3.2.1 – The Interstitial Mechanism

An atom is said to diffuse by an interstitial mechanism when it passes from one interstitial site to one of its neighbouring interstitial sites without permanently displacing any of the main lattice atoms. Figure 3.1 shows the interstitial sites available in the face-centred-cubic (fcc) lattice structure. The main lattice sites within the fcc unit cell reside at the corners and at the centres of each face of the cubic structure.

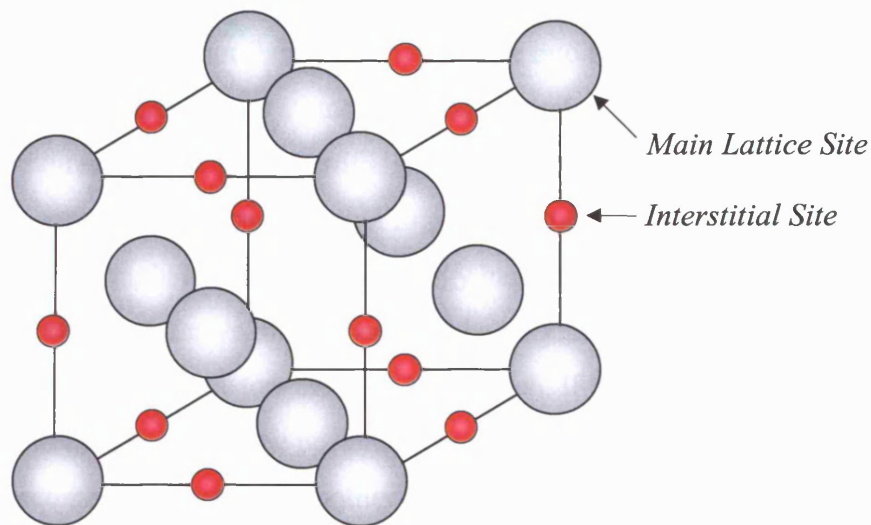


Figure 3.1 – Interstitial sites available within an fcc unit cell
(these sites also form an fcc lattice).

To look at the interstitial diffusive process more closely it is necessary to consider the atomic movements that must occur before a jump can take place. Figure 3.2 shows an interstitial atom in the plane of a group of atoms packed into an fcc cubic lattice.

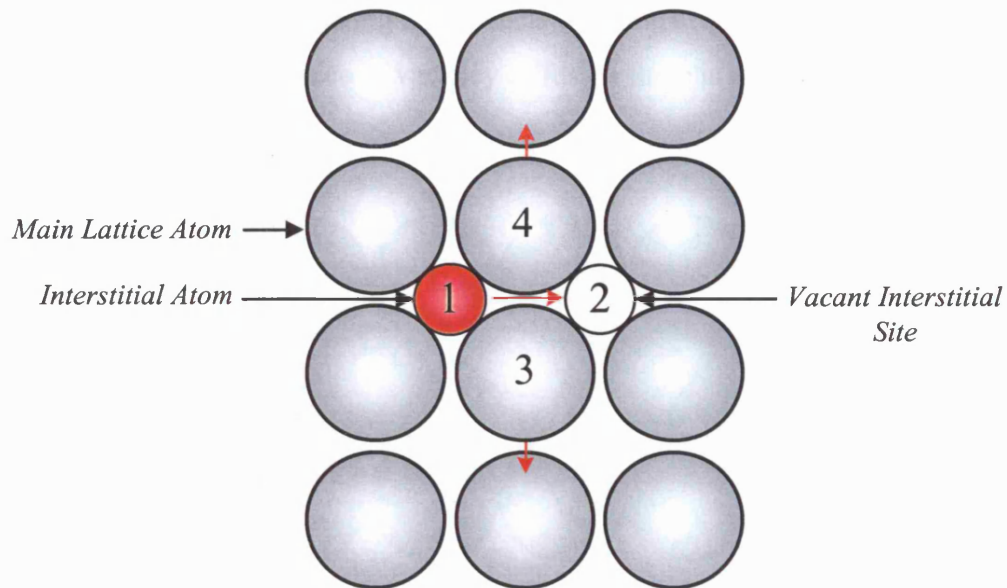


Figure 3.2 – An fcc atomic lattice showing the path of an interstitial atom diffusing by an interstitial mechanism.

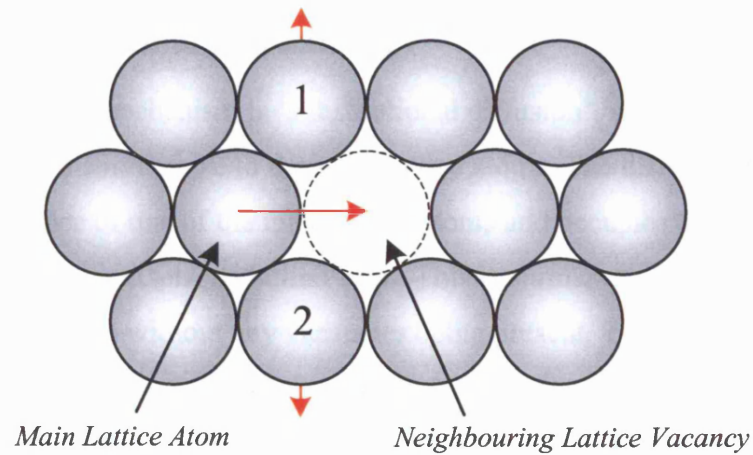
For the interstitial atom (labelled '1') to move into the neighbouring vacant interstitial site (labelled '2') the main lattice atoms (labelled '3' and '4') must move perpendicularly away from the direct path of the interstitially moving atom in order to let it through. However, an appreciable amount of lattice distortion must occur before the interstitial atom can jump, and it is this distortion that constitutes the energy barrier to an interstitial atom changing sites.

The interstitial diffusive mechanism will be dominant in any metallic solid in which the interstitial atoms do not distort the lattice too much. If the diffusing interstitial atom is almost as large as the atoms on the normal lattice site, then the distortion involved in the mechanism becomes too large, and another diffusion mechanism is likely to become dominant. The interstitial mechanism operates within alloys for solute atoms that normally occupy interstitial positions, e.g. carbon in α - and γ -iron.

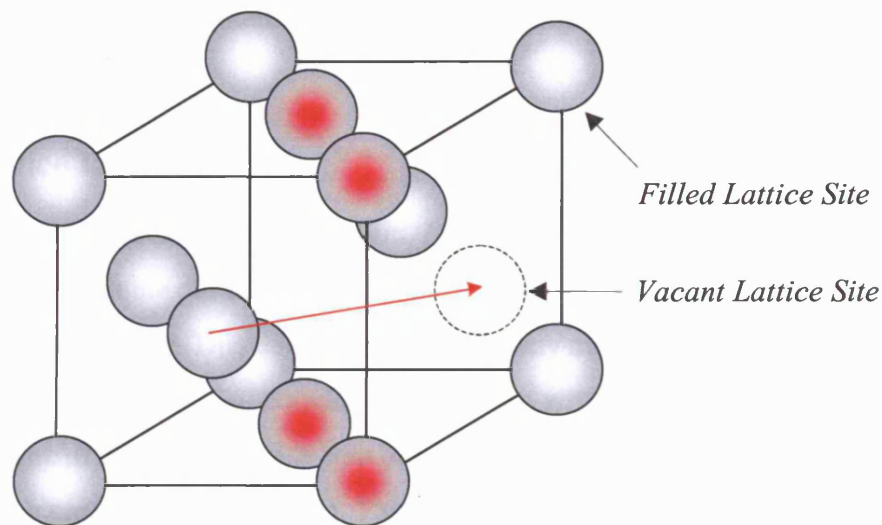
3.2.2 – The Vacancy Mechanism

In all crystals some of the main lattice sites are unoccupied, and these sites are referred to as 'holes' or 'vacancies' within the atomic structure. If one of the lattice atoms in an adjacent site jumps into the vacancy, the atom is said to have diffused by a vacancy mechanism. Figure 3.3(a) and (b) shows two models describing the movement of an atom into

an adjacent vacancy (and thus creating a new vacancy at the original lattice site) within an fcc atomic lattice. During the sequence of vacancy diffusion there is a counter-current flow of atoms and vacancies.



(a)



(b)

Figure 3.3 – Motion of an adjacent atom into a vacancy in an fcc lattice within (a) a close-packed plane of spheres, (b) a unit cell showing the four atoms (indicated by red centres) which have to move before the indicated jump can occur [38].

The distortion associated with moving an atom by vacancy diffusion is usually larger than the distortion created by interstitial diffusion due to the larger energy barrier required to force the atom into its new position. At a given temperature, vacancy diffusion is also considerably slower than interstitial diffusion due to the fact that each interstitial atom always

has several nearest-neighbour sites while the fraction of vacant sites on the main lattice is very small, and each atom must wait an appreciable period until a vacancy becomes available. The vacancy mechanism is a common mechanism of diffusion in fcc metals and alloys [38].

3.2.3 – The Substitutional Mechanism

Another diffusive mechanism is ‘substitutional diffusion’, which occurs when the diffusing atoms are of a similar size to the main lattice atoms. The diffusing atom simply substitutes itself in place of one of the main lattice atoms and occupies the lattice site previously occupied by the displaced lattice atom. This is similar to the vacancy mechanism only the atoms swap places without any vacancies being present. The distortion involved in this mechanism is quite large so this mechanism isn’t so common. As the difference in atomic size, between the diffusing atoms and the main lattice atoms, increases, less substitution will occur (due to the large amount of distortion) and another diffusive mechanism will dominate. Substitutional diffusion is sometimes found to occur amongst metal systems such as InGaAs and Fe-Cr-C.

3.3 – Lattice Diffusion

The diffusional flow, current or flux, j of a material, in a mixture of other species, can be defined as the volume of material passing perpendicularly through a reference surface of unit area during unit time. This definition applies to any mixture regardless of its state. When considering the lattice flux, j_i of component i , one can write the flux as either the volumetric flux, j_{vi} (volume of material crossing unit area per unit time) or the atomic flux, j_{ai} (number of atoms crossing unit area per unit time). The volumes of the phases are transformed to that of a reference phase such that the two flux definitions are equivalent. The two fluxes can be related through the expression

$$j_a = \rho j_v \tag{3.1}$$

where ρ is defined as the number of atoms per unit reference volume. As the reference state is chosen to correspond to a given lattice spacing, there are always the same total number of atoms per unit reference volume in the reference configuration. Hence one can use volumetric or atomic fluxes as they are identical. It is assumed here that the flux and the driving force for component, i can be related through the linear relationship

$$j_i = \mathcal{D}_i^{\text{eff}} f_i \tag{3.2}$$

where \mathcal{D}_i^{eff} is the effective diffusivity of component i , and the driving force on this component, f_i , is related its chemical potential, μ_i , through

$$f_i = -\nabla\mu_i \quad \text{chemical}$$

potential with position, i.e. material always flows down a chemical potential gradient. For material redistribution by diffusion, the chemical potential can be defined as the change in the free energy with change in composition

$$\mu = \frac{\partial g}{\partial c} \quad (3.4)$$

where g is the Gibbs free energy density. The relation between the rate of change of composition and the flux field can be determined from mass conservation. Consider Figure 3.4, which shows a small region of material into which particles of element, A , flow at a rate j_1 and out of which they flow at a rate j_2 . Consideration is given here to a one-dimensional situation in which flow is only considered in the x -direction.

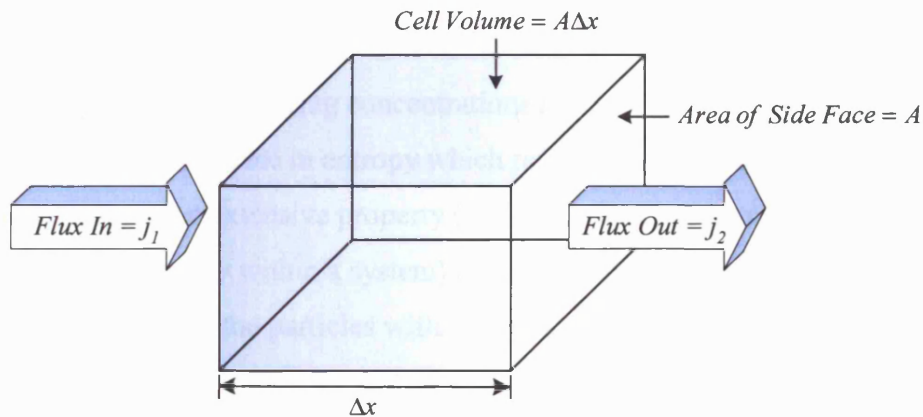


Figure 3.4 – Region of material with a flux inflow of j_1 and a flux outflow of j_2 .

If the flux, j_1 is larger than j_2 , the particles must accumulate within the shaded region, where j_1 and j_2 are both volume of component A flowing per unit area per second. So in time Δt , the volume of component A in the region increases by

$$(j_1 - j_2)A\Delta t$$

The concentration (volume fraction) of A increases by Δc in the same interval of time, so

$$\Delta c A \Delta x = (j_1 - j_2) A \Delta t$$

Cancelling and re-arranging terms on both sides to provide an expression for the rate of increase of concentration provides

$$\frac{\Delta c}{\Delta t} = \frac{(j_1 - j_2)}{\Delta x} \quad (3.5)$$

For infinitesimal increments in Δc and Δt , this can be expressed as

$$\frac{\partial c}{\partial t} = -\frac{\partial j}{\partial x}$$

which can be written in general in three-dimensions for the flux of component, i

$$\dot{c}_i = -\nabla j_i \quad (3.6)$$

where the dot denotes differentiation with respect to time. This expression can be related to the chemical potential through the relation

$$\dot{c}_i = \mathcal{D}_i^{\text{eff}} \nabla f_i = \mathcal{D}_i^{\text{eff}} \nabla^2 \mu_i \quad (3.7)$$

where ∇^2 is the Laplacian operator.

3.4 – Entropy as a driving force

The main interest in diffusion occurs in materials of non-uniform compositions, where the process is one of slowly changing concentrations at all locations across the material. An important concept is the increase in entropy which results from the mixing of two pure components. Entropy is an extensive property (indicating that its magnitude varies from zero to the total amount of energy within a system) and is a measure of the energy that is associated with the state of disorder of the particles within a system. In atomic terms, the total energy is the sum of all the kinetic and potential energies of the constituent atoms, and the entropy is a measure of the degree of disorder, non-uniformity or atomic randomness within the system. The principal deduction from the second law of thermodynamics is that, when an isolated system makes a transition from one state to another, the entropy of the system always increases.

The homogenisation or mixing of components must correspond to an increase in the entropy of the mixture. The configurational entropy is proportional to the number of ways in which atoms in a lattice can be organised, and probability theory states that

$$\Delta S = -R y_i \ln y_i$$

where ΔS is the increase in entropy upon forming a mol of an ideal solution from its pure components, y_i is the site fraction of component i in the mixture, and R is the universal gas constant ($8.314 \text{ Jmol}^{-1}\text{K}^{-1}$).

In general, the free energy per mol associated with entropy can be written as

$$g_{entropy} = -T\Delta S = RT \left(\sum_i^{N_i} y_i \ln y_i + y_{va} \ln y_{va} \right) \quad (3.8)$$

where T is the system temperature in Kelvin. If an ideal solution is obtained upon the addition of two components, A and B , and assuming that the number of vacant lattice sites is small, the concentration of component A can be described by

$$c = y_A = 1 - y_B$$

The entropic free energy per mol of the dual-component system can be expressed as

$$g_{entropy}(c) = RT(c \ln c + (1 - c) \ln(1 - c)) \quad (3.9)$$

This relation is plotted in Figure 3.5, where it can be seen that the entropic free energy is a minimum at $c = 0.5$, where there is an even and uniform mixed distribution of both components A and B . Purely entropic systems are therefore driven to mix completely. The entropic free energy per mol can be easily converted into the entropic free energy per unit volume given the number of mols per unit volume.

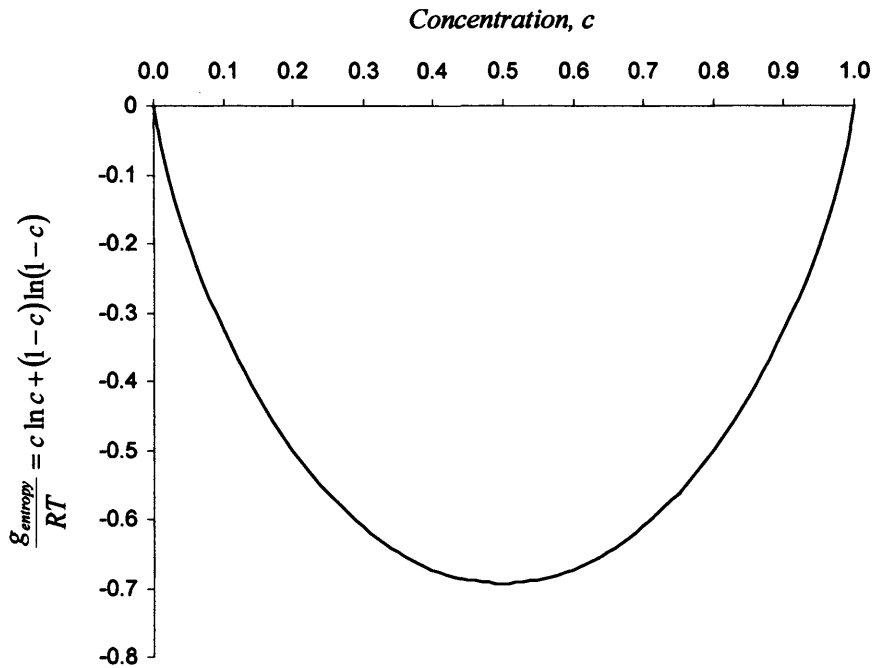


Figure 3.5 – Entropy variation against the site fraction of a single component within a dual component system (ignoring vacancies). The slope of the curve is infinite at the outer limits of $c = 0$ and $c = 1$.

Starting with an abrupt interface between two different species, the change in the concentration profile over time due to entropic diffusion can be expected to follow the trends as shown in Figure 3.6.

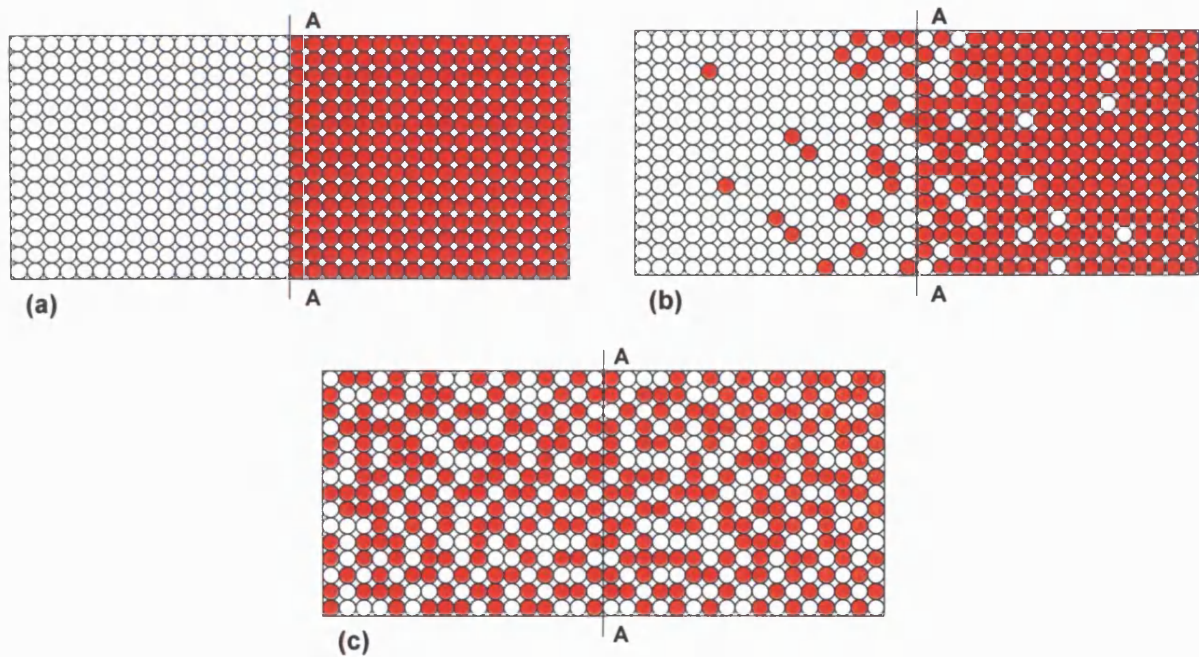


Figure 3.6 – Entropic diffusion of two species across the boundary A-A at the (a) initial state, (b) mid-state, and (c) final (equilibrium) state.

Figure 3.6(a) considers the initial state of an unmixed solution of pure components of red and white atoms located on the right and left planes of the system respectively, separated by an interface plane A-A. The general movement and direction of atoms is highly random and unpredictable in nature, and it is for this reason that entropy does not exist at the atomic level of simulation as it arises naturally due to random thermal exchanges. Continuum models do not specifically model this kind of random event. Therefore entropy is included as an artificial construction to tell the continuum model that if a series of red and white atoms are mixed together within a body, it is statistically highly improbable that the outcome will be that of Figure 3.6(a), but will most likely be similar to the result described within Figure 3.6(c). Entropy therefore drives the process of mixing the red and white atoms, and has the effect of reducing the higher concentrations and raising the lower ones. When uniformity is reached (when no concentration gradient exists) the atomic jump rates across the interface plane can be considered identical in both directions, providing no further net change of concentrations. The system described in Figure 3.6(c) has a higher degree of entropy associated with it compared to the initial unmixed state shown in Figure 3.6(a). During the interesting transient

phase, the differential equations (proposed by Adolf Fick in 1855) can relate concentrations to both time and distance for purely entropic diffusion.

Using equations (3.4) and (3.9), the chemical potential due to entropy can be written as

$$\mu_{entropy} = \frac{\partial g_{entropy}}{\partial c} = RT \ln\left(\frac{c}{1-c}\right)$$

In one-dimensional space, the rate of change of chemical potential due to entropy with position, x , can be described by

$$j = -\mathcal{D}^{eff} \frac{\partial \mu_{entropy}}{\partial x} = -\mathcal{D}^{eff} \frac{\partial \mu_{entropy}}{\partial c} \frac{\partial c}{\partial x} = -\frac{\mathcal{D}^{eff} RT}{c(1-c)} \frac{\partial c}{\partial x}$$

which can be reduced to

$$j_x = -D \frac{\partial c}{\partial x} \tag{3.10}$$

This is known as Fick's first law of diffusion, which asserts the flux of diffusing atoms across a plane to be proportional to their concentration gradient, with the constant of proportionality being a temperature-dependent material property known as the diffusion coefficient, D . The diffusion coefficient, D has the dimension m^2s^{-1} and therefore changes correspondingly with a change in the units of both length and time. The assumption, usually implied by equation (3.10), that D be a constant for a given medium, temperature and pressure is usually only approximately true [35]. The effective diffusivity, $\mathcal{D}^{eff} = \frac{Dc(1-c)}{RT}$ is zero if there are no atoms of component A to diffuse ($c = 0$) or all the atoms are component A ($c = 1$). Fick's first law fits the empirical fact that the flux goes to zero as the material becomes homogeneous, and the negative sign in equation (3.10) ensures that a positive flow of atoms goes in the direction of a falling concentration gradient ($\partial c/\partial x$ negative). It is shown that equation (3.10) is basically a simplification of equation (3.2) for the case of purely entropic diffusion.

Figure 3.7 shows a non-uniform concentration of one species of atom of which there is a net atomic flux in the direction of a falling concentration gradient. There must also be an equal but opposite flux of vacancies, or unoccupied lattice sites, within the structure. Concentration gradients merely change the probabilities of the different species of atoms moving one way or another as they all experience jumps between sites. It must be noted that more than one type of gradient, such as thermal and stress gradients, may dictate a single type of flux and drive the process of diffusion.

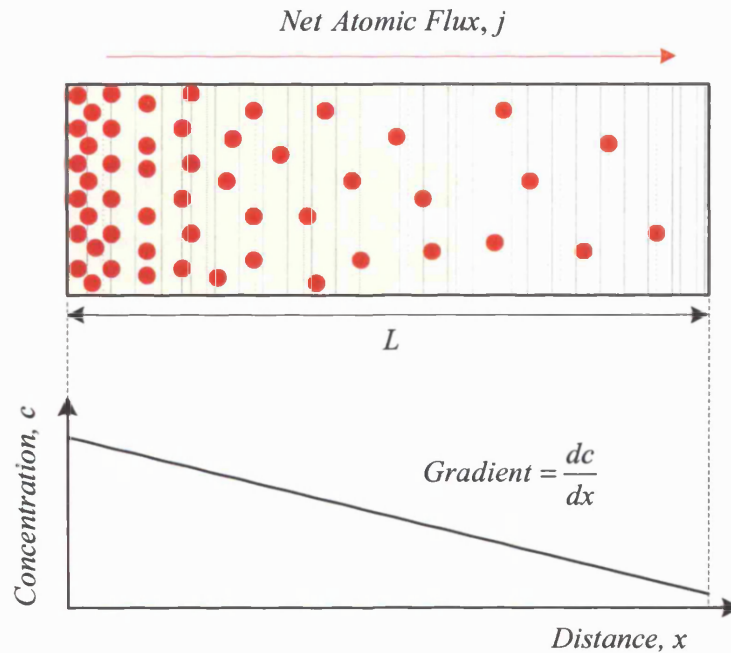


Figure 3.7 – A non-uniform concentration of one species of atom dictates a net atomic flux in the direction of a falling concentration gradient.

The diffusion coefficient, D , can be defined as

$$D = D_o \exp\left(-\frac{E_a}{RT}\right) \quad (3.11)$$

where E_a is the activation energy for the mechanism by which the atoms get from one site to another in the crystal, i.e. the diffusion path. The constant of diffusion, D_o is the material property that converts the mere possibility of jumps (the exponential term) into an effective jump rate. It depends on the atom vibration frequency and the average distance per jump. Figure 3.8 shows the sequence involved when an atom jumps by vacancy diffusion from a main lattice site to a neighboring one, and how the free energy of the entire lattice would vary as the diffusing atom is reversibly moved from configuration (a) to (b) to (c). It is assumed that sufficient thermal energy exists for the energy barrier, E_a , to be crossed allowing the diffusing atom to jump into the neighboring lattice site. Generally less energy is required to move an interstitial atom past the surrounding atoms, and consequently activation energies are lower for interstitial diffusion than for vacancy or substitutional diffusion. Activation energies are usually lower for atoms diffusing through open crystal structures (such as within the bcc unit cell) compared with close-packed crystal structures (such as the fcc unit cell). A small

activation energy increases the diffusion coefficient and flux, since less energy is required to overcome the smaller activation energy barrier.

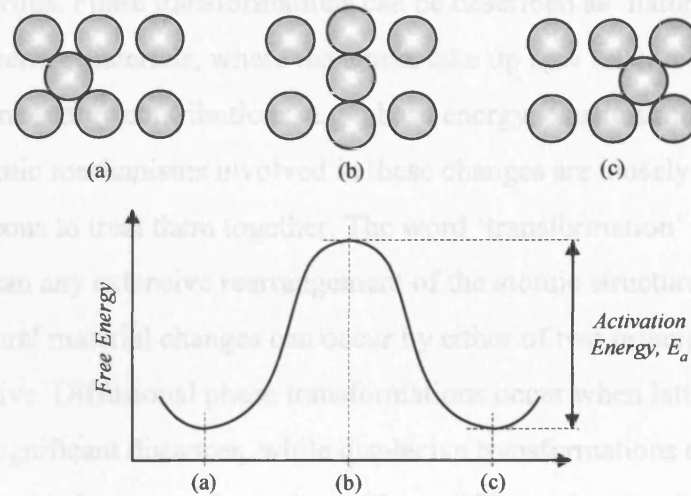


Figure 3.8 – Sequence of configurations showing an atom jumping by vacancy diffusion from one lattice site into a neighbouring one, and the variation in free energy during the process [36].

3.5.1 – The Diffusive Transformation

To model a technical diffusion process an engineer has to determine how the concentration profile varies with time from some initial defined compositional distribution. This involves satisfying mass conservation as defined by Fick's Second Law. Substituting Fick's first law (equation (3.10)) into equation (3.6) gives

$$\frac{\partial c}{\partial t} = D \frac{\partial^2 c}{\partial x^2} \quad (3.12)$$

which is Fick's second law of diffusion, and is a simplified form of equation (3.6) in the case of entropic diffusion only. Fick's second law also assumes that the diffusion coefficient is constant (i.e. independent of position). Experimental determination of diffusional parameters (such as the diffusion coefficient, D) consists of concentration measurements in specimens where controlled entropic diffusion has occurred in a geometry for which equation (3.12) is analytically solvable [37].

3.5 – Phase Transformations

A phase of material can be defined as a region of material that has uniform physical and chemical properties. Phase transformations can be described as ‘natural’ changes that occur within engineering materials, where the atoms take up new relative positions under the influence of different energy contributions, e.g. phase energy, elastic strain energy, surface energy etc. The atomic mechanisms involved in these changes are closely related and it is therefore advantageous to treat them together. The word ‘transformation’ will be used in a general sense to mean any extensive rearrangement of the atomic structure.

Microstructural material changes can occur by either of two principal mechanisms: diffusive or displacive. Diffusional phase transformations occur when lattice components are redistributed over significant distances, while displacive transformations occur as a result of a sudden change in atomic lattice configuration with no diffusion involved. Phase transformations occur at interfaces between phase regions. In order to numerically model such phenomena, interfacial conditions need to be taken into account. Such interfacial conditions may require a particular stoichiometry of components within one or more of the phases.

3.5.1 – The Diffusive Transformation

Diffusive changes require the diffusion of atoms through the material, and most structural changes that occur in practice occur by a diffusive mechanism. A net flux exists whenever a concentration gradient is present within the material and the diffusing atoms move from one lattice site to another under the influence of a driving force. Because of the surrounding atoms, the activation energy is large and the rate of diffusion is relatively slow. In order for a diffusional transformation to occur there must be a finite time available for the atoms to diffuse across the atomic lattice.

3.5.2 – The Displacive Transformation

Sometimes there may be insufficient time for diffusion to occur, even though very large driving forces for transformation can be obtained, so there is a critical point where the old structure spontaneously deforms into the new structure by a displacive transformation. A displacive transformation is one where the parent is deformed into the product without any diffusion taking place. The lattice of the parent is sheared into the new structure. Displacive transformations can be regarded as a mechanical deformation that also changes the nature of

the crystal lattice. Displacive transformations occur very rapidly and simply involve the minor “shuffling” of atoms about their original lattice positions.

3.5.3 – Interfacial Flux Conditions

For mass to be conserved as matter diffuses across an interface and as the interface translates in a direction normal to the interface boundary, an interfacial condition needs to be enforced. Consider the situation illustrated in Figure 3.9(a) where a sharp interface boundary separates two phases, 1 and 2, of uniform local composition, c_A and c_B respectively. The interface displaces by an amount, Δx_{in} during an interval of time, Δt , as shown in Figure 3.9(b). This displacement is accompanied by a change in composition as c_B changes to c_A within the interfacial region.

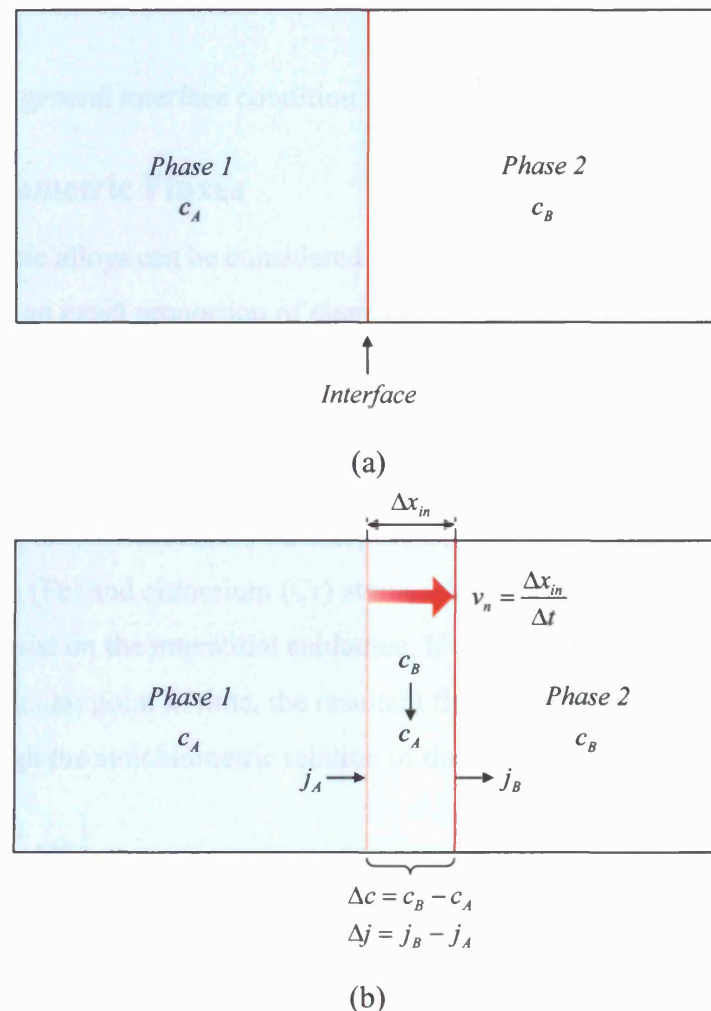


Figure 3.9 – An interface separating two phases (a) initially at time, $t = 0$ and (b) after the interface has displaced by an amount, Δx_{in} during an interval of time, Δt .

From Figure 3.9, the interface condition can be derived by considering Fick's second law of diffusion (equation (3.6)) within one-dimensional space, such that

$$\dot{c}_{in} \Delta x_{in} = j_A - j_B = -\Delta j$$

where \dot{c}_{in} is the rate of change of composition across the interfacial region, which can be expressed as

$$\dot{c}_{in} = \frac{(c_B - c_A)}{\Delta t} = \frac{\Delta c}{\Delta t}$$

Substituting this into the above expression gives

$$\Delta c \frac{\Delta x_{in}}{\Delta t} = -\Delta j$$

or

$$\Delta c v_n + \Delta j = 0 \tag{3.13}$$

which provides the general interface condition necessary for mass conservation.

3.5.4 – Stoichiometric Fluxes

Stoichiometric alloys can be considered as material systems in which their constitution is constructed from an exact proportion of elements to make the pure chemical compound. If, for example, a compound is made up of three separate elements, and the atomic fluxes of two of the elements is known at a particular point, then the unknown atomic flux of the remaining element can be readily determined by knowing their exact stoichiometric relation.

Considering the stoichiometric carbide, $M_{23}C_6$, where M primarily represents a combination of iron (Fe) and chromium (Cr) atoms which exist on the main sublattice, and the carbon (C) atoms exist on the interstitial sublattice. If the lattice fluxes of iron and chromium are known at a particular point in time, the resultant flux of the interstitial carbon atoms can be calculated through the stoichiometric relation of the components, i.e.

$$j_C = \frac{6}{23}(j_{Fe} + j_{Cr})$$

such as to maintain the component ratio of $M_{23}C_6$. Consideration must also be given to the fact that different element ratios within a microstructure can give rise to variations in mechanical properties from the tensile strength, yield strength, hardness and toughness to the creep, oxidation and corrosion resistance across a range of different temperatures.

3.6 – Summary

Having fully characterised the starting material microstructure in terms of the composition of the relevant sublattice components and location of the phase boundaries, it is then possible to describe the rate of change of the microstructure over time (i.e. the kinetics of evolution). To fully describe the rate of evolution of a general material microstructure, it is necessary to know the rate of change of composition, \dot{c} , of the relevant sublattice components at all points across the microstructure along with the velocities associated with all phase boundaries, v_n . Equations (3.6) and (3.13) state that these quantities are known given the flux field, so this is the unknown field to be determined.

4.0 – The General Model

The manner of evolution of a material microstructure by mass redistribution is determined by the kinetic process by which the mass transport takes place and by the thermodynamic driving forces for evolution. Modelling the evolution process in real engineering materials can be difficult as a range of mechanisms and driving forces exist and the geometry of the microstructure is usually complex. The variational principle outlined here presents a framework in which any number of competing mechanisms and driving forces can be readily incorporated into a numerical model of any geometrical complexity.

This section describes the general strategy for modelling microstructural evolution at a continuum micromechanical level. The approach is based on a fundamental variational principle which considers the competition between all kinetic dissipative processes that are driven by a number of thermodynamic driving forces. The variational principle is described and formulated in its general form, which can be used to aid the development of computational simulation procedures. In subsequent chapters of this thesis, the general model is utilised to illustrate its power and versatility by modelling a number of complex real material systems.

4.1 – Model Description and Diffusional Relationships

Consideration is given to the development of a thermodynamically consistent model in which thermal fluctuation effects can be neglected. Within this context, it is natural to consider an isothermal model. From the theory of thermodynamics, the potential for describing an isothermal situation is the Gibbs free energy.

In single-phase material systems, the diffusional rearrangement of matter can be examined by relating the lattice flux to the concentration gradient using Fick's first law of diffusion (equation (3.10)) [38]. Diffusional re-arrangement of material occurs to reduce the Gibbs free energy of the body. In simple single phase systems, the free energy is determined by the composition and this approach is appropriate. In multi-phase systems, the properties of an interface between different phases and the elastic interaction between the different components and phases can play an important role in determining the evolution of the microstructure. Considering a range of dissipative kinetic processes and the way in which a number of different thermodynamic driving forces interact with one another over time

determines the subsequent evolution of the microstructure, thus determining whether a particular phase will nucleate, grow or dissipate at the expense of another.

By developing a general thermodynamically consistent variational model, it is possible to accurately simulate the competition between the rate of energy dissipation and rate of change of Gibbs free energy across a range of material systems. The development and application of such a general model would allow the evolution of a variety of complex single and multi-phase material systems to be analysed and investigated over a range of different microstructure starting configurations, geometries, temperatures, length scales and under the influence of a range of different thermodynamic driving forces. By solving a set of governing system equations that control the process of microstructural evolution, both structural changes and the changes in material properties can be investigated over time.

4.2 – The Variational Formalism

4.2.1 – The Variational Principle

The variational principle allows the general features of the structure of constitutive laws for the microscopic response to be identified which consider the competition between the different mechanisms of a particular diffusive process. If the thermodynamic driving forces and kinetic dissipative processes are known along with the microscopic constitutive laws for the mechanisms involved, the response of the system can be analysed using a continuum variational approach.

The variational principle can be applied to static systems, in order to determine the final equilibrium state, and also to dynamic systems, in order to determine the kinetics of evolution. Here, the main interest and complexity arises in the latter case, where the variational functional is written in terms of the rate of change of energy within the system in order to determine the unknown system rate variables.

In this case the variational functional can be written as

$$\Pi = \Psi + \dot{G} \quad (4.1)$$

where Ψ is a dissipation potential and represents the rate of energy dissipation, and \dot{G} is the rate of change of Gibbs free energy. The rate of change of Gibbs free energy is the thermodynamic driving force for the system to evolve and the dissipation potential represents

the kinetic processes (irreversible) on which this driving force does work. The only restriction to the use of this variational principle is the fact that the process must be isothermal. For a full derivation see Cocks et al. [23].

In situations where the range of assumed fields is limited, it is assumed that the most appropriate field, i.e. that which is closest to the exact field, is that which provides the minimum value of the functional Π within the assumed set of fields. The exact field of unknown rate variables (e.g. lattice flux, interface velocities etc.) therefore provides a stationary value of the functional, i.e. at $\partial\Pi = 0$. The variational principle essentially states that the correct evolution path of a system at any instant in time is given by the minimum value of the variational functional. The assumed solution, however, must satisfy mass conservation.

Sun et al. [24] have demonstrated that the common assumption that a microstructure will evolve in a direction which maximises the change in Gibbs free energy is not always correct. One of the advantages of using the variational functional is that it is not necessary to either specify the exact form of the constitutive laws nor precisely determine all the contributions to the chemical potential at every point. These terms are naturally included into the variational principle and the exact solution also satisfies all the necessary internal equilibrium requirements.

Typical examples of the range of kinetic and dissipative processes along with thermodynamic driving forces contributing to the variational functional of equation (4.1) are listed in Table 4.1.

<i>Kinetic/ Dissipative Mechanisms</i>	<i>Contributions to the Gibbs Free Energy</i>
<i>Lattice diffusion</i>	<i>Chemical phase energy</i>
<i>Interface reactions</i>	<i>Compositional gradients</i>
<i>Interface migration</i>	<i>Elastic strain energy</i>
<i>Surface diffusion</i>	<i>Interface / surface energy</i>
<i>Non-linear viscous behaviour</i>	<i>Potential energy of applied load(s)</i>

Table 4.1 – A range of kinetic / dissipative processes and thermodynamic driving forces (contributing to the variational functional) can influence the evolution of a material microstructure.

There is no unique starting configuration for the analysis of physical processes within which these mechanisms operate and which fully take into account the interactions between the different mechanisms and driving forces, but any procedure must be thermodynamically consistent and allow the relative importance of all competing mechanisms of a particular process to be identified [23]. In many practical situations it proves appropriate to express the variational principle in dimensionless form, which is performed by identifying the appropriate dimensionless quantities relevant to the particular physical problem.

4.2.2 – The Variational Principle in Geometric Terms

Suo [22] has demonstrated how the variational principle can be employed to analyse a wide range of problems in which the behaviour is expressed in terms of a limited number of geometric parameters. Considering a hypothetical surface profile landscape to describe the Gibbs free energy as a function of the generalised degrees of freedom within a general system, it is possible to visualise the effect of the variational method in geometric terms. It can be considered that the valleys on this energy landscape represent a state of thermodynamic equilibrium and everywhere else represents a state of non-equilibrium. Thermodynamics states that a system will evolve in order to reduce the total Gibbs free energy, so a system can

evolve by following an evolution path, represented by a descending curve on the energy landscape. Starting from an initial arbitrary non-equilibrium configuration on the energy landscape, an infinite number of descending curves, i.e. evolution paths, exist. From this simple analysis, it can be seen that thermodynamics alone does not dictate the evolution path, nor does it select one final equilibrium state among several available equilibrium states. The evolution path is consequently determined by the coupling of the different kinetic processes and thermodynamic driving forces associated with microstructure evolution, which are both integrated into the variational functional.

The variational principle states that the correct evolution path for the system at any instant in time is given by the stationary value of the variational functional

$$\frac{\partial \Pi}{\partial d} = 0 \quad (4.2)$$

where d represents the degree of freedom. For illustrative purposes, a general system is described by a single degree of freedom, where the free energy is a function of the degree of freedom and can generally be represented by the curve shown in Figure 4.1.

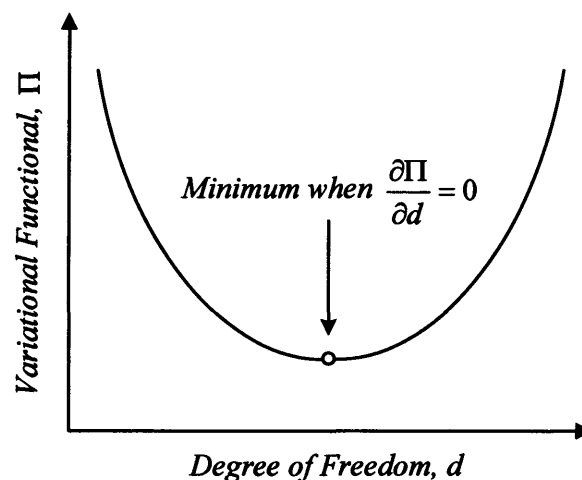


Figure 4.1 – Diffusional rearrangement of material will follow an evolution path which provides a minimum value of the variational functional.

Thermodynamics states that if the system is in a state of non-equilibrium, it will follow the curve such that it evolves towards a state of equilibrium, where the functional is found to be a minimum. For a single degree of freedom system, therefore, the thermodynamics dictates the evolution path of the microstructure and its equilibrium state, and the kinetics determines

the rate of evolution and how quickly the final state of thermodynamic equilibrium is attained. However, for systems with more than one degree of freedom, there may be more than one evolution path that a microstructure can follow. In this case, it is both the thermodynamics and kinetics that determines the path and the final state, and the kinetics play a more significant role than just determining the rate of evolution [24].

4.2.3 – Kinetic Processes

The rate of energy dissipation for material rearrangement due to lattice diffusion, \dot{D} can be expressed as

$$\dot{D} = -\dot{f}j = \phi + \psi \quad (4.3)$$

where ϕ is a rate potential and ψ is the dual potential to ϕ . These are defined by

$$\phi = \frac{1}{2} \mathcal{D}^{eff} f^2 \quad (4.4)$$

$$\psi = \frac{1}{2} \frac{j^2}{\mathcal{D}^{eff}} \quad (4.5)$$

where j is the material flux and f is the driving force for the diffusive mechanism.

The flux is related to the rate potential through the relation

$$j = \frac{\partial \phi}{\partial f} = \mathcal{D}^{eff} f$$

and the driving force is related to the dual potential through

$$f = \frac{\partial \psi}{\partial j} = \frac{j}{\mathcal{D}^{eff}} \quad (4.6)$$

The dissipation potential contained in equation (4.1) can be defined as

$$\Psi = \sum_{\text{processes } \nu} \int \psi dV \quad (4.7)$$

where the summation is performed over all kinetic and dissipative processes within the body and V is the domain over which a particular process operates.

(a) Dissipation due to a Material Flux

The rate of energy dissipation due to lattice diffusion can be written in potential form in terms of the material flux and effective diffusivity

$$\psi_{flux} = \frac{1}{2} \int_V \frac{j^2}{\mathcal{D}^{eff}} dV \quad (4.8)$$

This can be expressed in its general form as

$$\psi_{flux} = \frac{1}{2} \sum_p \sum_k \sum_\alpha \int_{V_p} \frac{j_{k\alpha}^2}{\mathcal{D}_{kp}^{eff}} dV \quad (4.9)$$

where p denotes the phase, k denotes the sublattice component and α denotes the direction under consideration (x , y or z). The flux, j , can be used to denote contributions from surface, grain boundary or lattice flux, depending on the nature of the system. In the case of either a surface or grain boundary flux field, the integral needs to be evaluated over the area of the surface or grain boundary respectively.

(b) Dissipation due to Interface Migration

The resultant growth of a particular phase at the expense of another due to a displacive phase transformation will be limited by the mobility of the interface. The kinetic process that needs to be considered in this context is that due to the interface boundary migration. The interface velocity in the direction normal to the interface surface, v_n , is related to the effective mobility coefficient of the interface, M_{in} , and the interface driving force, f_{in} , through the linear relation

$$v_n = M_{in} f_{in} \quad (4.10)$$

which is analogous to the way in which the lattice flux is related to the effective diffusivity and lattice driving force.

The rate of energy dissipation due to interface boundary migration can be written in terms of the interface velocity and effective mobility of the interface

$$\psi_{in} = \frac{1}{2} \int_A \frac{v_n^2}{M_{in}} dA \quad (4.11)$$

where A is the surface area of the interface. This represents the dissipation potential for atomic rearrangement during a phase transformation. During a diffusive phase transformation, the contribution from this dissipation (viscosity) term will be small but will have the effect of improving the stability of interface movement. However, this will become the dominant term whenever the active phase transformation mechanism is displacive.

Equation (4.11) can be generally written as

$$\psi_{in} = \frac{1}{2} \sum_b \int_{A_b} \frac{v_n^2}{M_{in}^b} dA \quad (4.12)$$

where the summation is performed over all phase boundaries, b .

4.2.4 – Gibbs Free Energy Contributions

The driving forces considered here derive from the reduction in interfacial energy, the reduction in compositional (or phase) energy and the reduction in elastic stored energy of the system

$$\dot{G} = \frac{d}{dt} (G_{surface} + G_{phase} + U_{elastic}) = \dot{G}_{surface} + \dot{G}_{phase} + \dot{U}_{elastic}$$

where $\dot{G}_{surface}$ is the rate of change of interfacial energy, \dot{G}_{phase} is the rate of change of compositional (phase) free energy and $\dot{U}_{elastic}$ is the rate of change of elastic stored energy.

(a) Interface Surface Energy

Interfaces in solids include surfaces such as phase boundaries, grain boundaries, domain walls and bi-material interfaces. The energy of an interface is represented by a material constant, γ_s which is the energy per unit area of surface (Jm^{-2}) or force per unit length (Nm^{-1}), i.e. a surface tension. Surface tension is of the order of $1 Jm^{-2}$ for most solids. Within this analysis, γ_s is assumed to be independent of surface orientation or strain.

The surface energy of a free surface can be represented by

$$G_{surface} = \int_{A_s} \gamma_s dA \quad (4.13)$$

where A_s is the area of the surface under consideration. If the surface tension is constant, this expression can be reduced to

$$G_{surface} = \gamma_s A_s \quad (4.14)$$

Equation (4.13) can be presented in its general anisotropic form as

$$G_{surface} = \sum_b \int_{A_b} \gamma_b dA \quad (4.15)$$

where γ_b is the interface surface energy of phase boundary, b . Thermodynamics requires that an interface will move in a direction that reduces the free energy. Since the surface tension is positive, a surface will evolve in order to minimise its total surface area.

Considering an interface separating two phases of defined composition, the interface will move as a result of atoms leaving one phase, crossing the interface and attaching themselves to the other phase. In this case, one phase will grow at the expense of the other. However, the interface energy alone is not usually sufficient to determine the evolution of a particular phase within a multi-phase system. Other effects such as the chemical phase energy density and elastic strain energy also play important roles.

(b) Chemical Phase Energy

The chemical phase energy includes the potential energy (energy due to bonds between atoms), thermal energy (thermal vibrations / heat content) and also entropy, which all constitute the internal energy of the phase and can be described by

$$G_{phase} = \int_{V_p} g_p(c, T) dV \quad (4.16)$$

where $g_p(c, T)$ is the chemical energy density of phase p , and is a function dependent on both constitution and temperature. The chemical phase energy function is usually determined through the use of phase diagrams in conjunction with thermodynamic assessment experiments under controlled temperatures and conditions. The set of parameter values describing the Gibbs phase energy density of each phase are then determined via computer optimisation techniques. Many such functions are available for different materials in the ThermoCalc database (www.met.kth.se/tc/) as well as others.

Equation (4.16) can be expressed in its general form as

$$G_{phase} = \sum_p \int_{V_p} g_p(c, T) dV \quad (4.17)$$

where the summation is performed over each phase, p , within the body.

(c) Elastic Stored Energy

The elastic stored energy of a general body can be described by

$$U_{elastic} = \frac{1}{2} \int_V \sigma_{ij} \epsilon_{ij} dV \quad (4.18)$$

where σ_{ij} and ϵ_{ij} are the total stress and strain at a particular point respectively. Einstein suffix notation has been adopted with i or $j = x, y$ or z , e.g.

$$\sigma_{ij} \epsilon_{ij} = \sigma_{xx} \epsilon_{xx} + \sigma_{yy} \epsilon_{yy} + \sigma_{zz} \epsilon_{zz} + 2(\tau_{xy} \epsilon_{xy} + \tau_{xz} \epsilon_{xz} + \tau_{yz} \epsilon_{yz})$$

For a linear elastic material, $\sigma_{ij} = D_{ijkl} \varepsilon_{kl}$, where D_{ijkl} is the elastic stiffness tensor and i, j, k and l are x, y or z .

Hence equation (4.18) can be written in its general form as

$$U_{elastic} = \frac{1}{2} \sum_p \int_{V_p} \varepsilon_{ij} D_{ijkl}^p \varepsilon_{kl} dV \quad (4.19)$$

which represents the total elastic stored energy summed over all phases in the general body.

If, as discussed in section 2.2, there is a transformation strain associated with a particular phase within a general body, the elastic stored energy can be expressed as

$$U_{elastic} = \frac{1}{2} \sum_p \int_{V_p} (\varepsilon_{ij} - \varepsilon_{ij}^{pT}) D_{ijkl}^p (\varepsilon_{kl} - \varepsilon_{kl}^{pT}) dV \quad (4.20)$$

where ε_{ij}^{pT} is the transformation strain for phase p . In this analysis, one phase is chosen as the reference phase, so that its transformation strain is zero and the transformation strain associated with the remaining phases within the body are calculated with respect to this.

4.2.5 – Constraints on Interface Fluxes

As discussed in section 3.5.3, the flux must be continuous everywhere apart from at the interface where, from equation (3.13), the following condition needs to be satisfied

$$\Delta j_\alpha n_\alpha = -\Delta c v_n$$

where suffix notation has again been used to imply $\Delta j_\alpha n_\alpha = \Delta j_x n_x + \Delta j_y n_y + \Delta j_z n_z$, which denotes the flux difference across the interface in a direction normal to the interface. This constraint can be implemented into the variational functional through a distribution of Lagrange multipliers, λ , by introducing a constrained functional

$$\hat{\Pi} = \Pi + \int_A \lambda \{ \Delta j_\alpha n_\alpha + \Delta c v_n \} dA \quad (4.21)$$

which can generally be presented as

$$\hat{\Pi} = \Pi + \sum_b \int_A \lambda \{ \Delta j_b + \Delta c v_n \} dA \quad (4.22)$$

where Π is the functional of equation (4.1). Equation (4.22) represents the constraint imposed on an interface within a general multi-phase body, where the fluxes are assumed to be non-stoichiometric. If non-stoichiometric fluxes are considered, such as within the carbide precipitate, $M_{23}C_6$, then it proves necessary to impose additional constraints (through the use

of extra Lagrange multipliers) on the fluxes in order to maintain the correct ratio and balance of elements within the multi-phase alloy. Further details of this are put aside until later.

4.2.6 – Formulation of the General Functional

The variational functional can be presented in its very general form for the dissipative processes and thermodynamic driving forces considered by combining equations (4.9), (4.12), (4.15), (4.19), (4.17) and (4.22) into the general functional of equation (4.1) to give

$$\hat{\Pi} = \frac{1}{2} \sum_p \sum_k \sum_\alpha \int \frac{j_{k\alpha}^2}{\mathcal{D}_{pk}^{eff}} dV + \frac{1}{2} \sum_b \int \frac{v_n^2}{M_{in}^b} dA + \frac{d}{dt} \left[\sum_b \int \gamma_b dA + \sum_p \int g_p dV + \frac{1}{2} \sum_p \int \sigma_{ij} \varepsilon_{ij} dV \right] + \sum_b \int \lambda \{ \Delta j_\alpha n_\alpha + \Delta c v_n \} dA \quad (4.23)$$

The exact flux pattern, interface velocities and distribution of Lagrange multipliers is that which provides a stationary value of the functional $\hat{\Pi}$. Equation (4.23) has been written in such a way that it can be readily used to model the microstructure evolution of a general body consisting of p phase regions, b interface boundaries and k sublattice components.

The procedures described in this section can be employed to analyse a wide range of situations involving the nucleation and growth of different phases within a multi-phase body. Now that the general model has been fully described and formulated for a general multi-component multi-phase system, one is now in a position to implement the variational functional into a finite element framework, the purpose of the following chapter.

5.0 – Finite Element Discretisation

This chapter describes the numerical finite element implementation of the general model described in the previous chapter.

5.1 – Finite Element Modelling

The recent advancement of numerical mathematics and increase in computer resources and processing power has revolutionised many areas of science and engineering over the last decade, and solid mechanics has been one of the many fields to benefit from its impact. In solid mechanics, the finite element method is most commonly used to solve elasticity problems. It is a variational method, and, within this line of work is needed to calculate the quasi-static elastic field of a microstructure and also calculate the kinetic flux field using a special variational functional. These problems are coupled and therefore it seems natural to express both the static and kinetic problems in terms of the finite element method.

All physical phenomena encountered in engineering mechanics are modelled by expressions involving differential equations, and usually the problem presented is too complicated to be solved by classical analytical methods. The finite element method is a numerical approach by which general differential equations can be solved in an approximate manner. The differential equation(s) which describe the physical problem considered are assumed to hold over a certain region, which may be one, two or three-dimensional. It is a characteristic feature of the finite element method that instead of seeking approximations that hold directly over the entire region, the region is divided into smaller sections, so-called ‘finite elements’, and the approximation is then carried out over each individual element. This elemental approximation is usually a polynomial expression, which numerically represents the manner in which the variable changes over the finite element. The approximation assumes that the variable is known at the elemental nodal points, located at the boundary of each element (and sometimes within it). The precise manner in which the variable changes between its values at the nodal points is expressed by the specific approximation, which may be linear, quadratic or cubic etc. For instance, even though the variable varies in a highly non-linear fashion over the entire region, it may be a fair approximation to assume that the variable varies in a linear fashion over each element.

Once the type of approximation (or shape function), which is to be applied over each element, has been selected, the corresponding behaviour of each element can then be determined. This can be performed because the approximation made over each element is fairly simple. Having determined the behaviour over all elements, the elements can then be ‘assembled’ or combined together to form the entire region, which provides an approximate solution for the behaviour of the entire body.

The finite element method is a numerical approach that results in the establishment of systems of equations often involving many unknowns. The original problem, in principle, has infinitely many unknowns, i.e. degrees of freedom, and is replaced by a problem with a finite number of unknowns. In general, it is obvious that the more unknowns, the more accurate the approximate solution. A system with a finite number of unknowns is called a ‘discrete system’ in contrast to the original ‘continuous system’ with an infinite number of unknowns. The finite element method can be applied to arbitrary differential equations, and moreover, arbitrary geometries of bodies consisting of arbitrary materials can be analysed.

The finite element method can be summarised in the following basic steps:

1. Definition of finite element type and establishment of shape function relations (approximation must at least include terms corresponding to an arbitrary linear polynomial).
2. Definition of geometry followed by division (meshing) of regions into finite elements. Defining degrees of freedom at nodes ensures continuity of displacement.
3. Definition of system boundary conditions.
4. Formulation of the variational functional. The system of equations is constructed for the whole structure by ‘assembling’ the contributions from each finite element.
5. Solution of the system of equations by minimising the functional with respect to the degrees of freedom.

5.1.1 – The Problem Description: Degrees of Freedom

In general, an analytical description of a system is not possible and a discrete representation of the structure has to be employed (see Figure 5.1). This naturally implies that the number of possible evolution paths for the structure is restricted. However, by increasing the number of degrees of freedom of the discretisation, the number of available paths can be increased for a potentially more accurate solution.

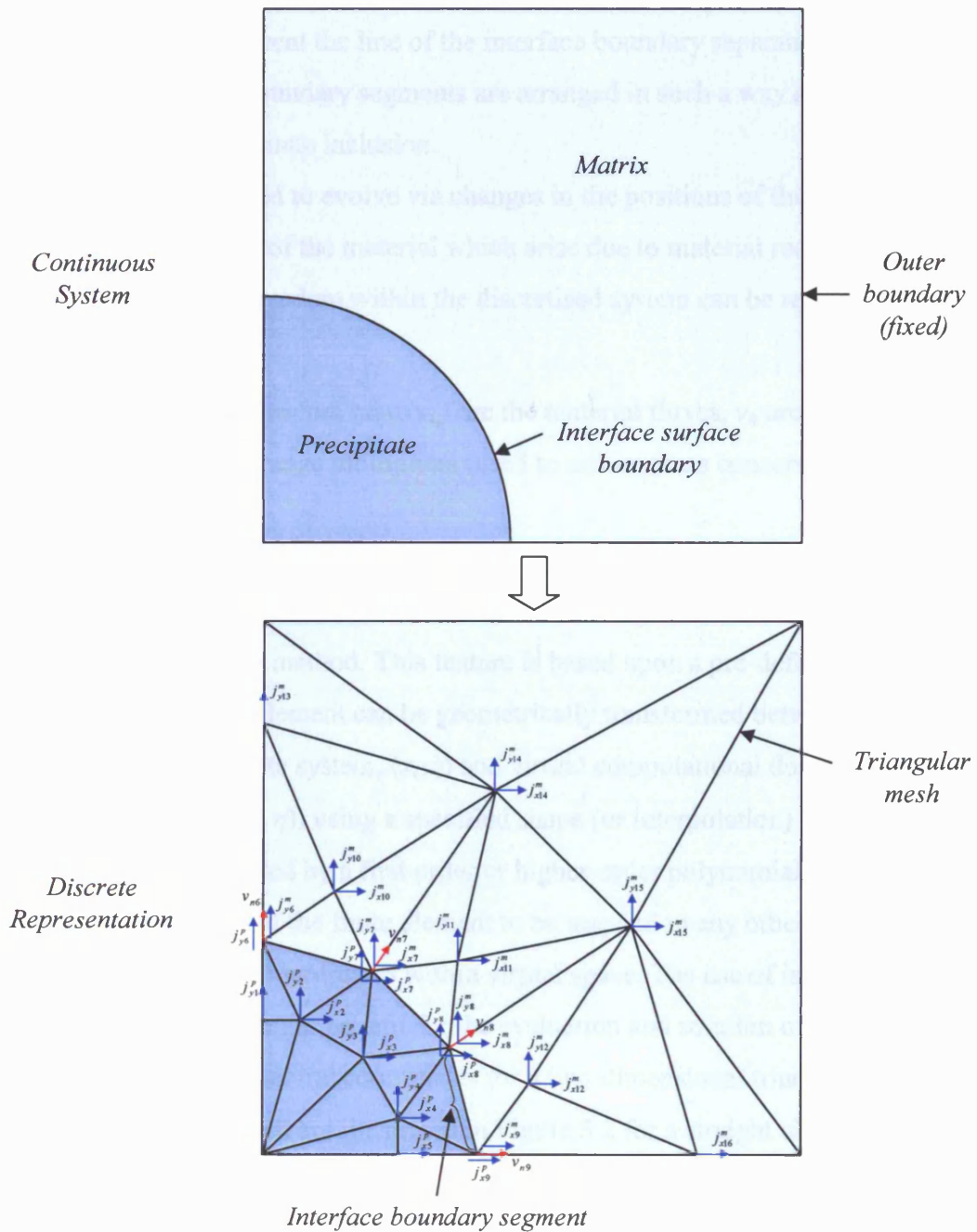


Figure 5.1 – An example of the discrete representation of a continuous system.

Figure 5.1 shows an example of a continuous precipitate / matrix system, in which each phase region is discretised into a number of three-noded straight-sided triangular finite elements. The outer nodes of the discrete system are constrained in such a way as to retain the shape of the outer system boundaries. In the discrete representation, the sharp interface boundary is modelled by an assembly of edges of discrete finite elements, and at a given instant in time, the system consists of a number of ‘interface boundary segments’ that are connected together to represent the line of the interface boundary separating the matrix and precipitate. The interface boundary segments are arranged in such a way as to retain the circular nature of the precipitate inclusion.

The system is allowed to evolve via changes in the positions of the interface and changes in the composition of the material which arise due to material redistribution. It will be shown that the degrees of freedom within the discretised system can be represented by

$$[d] = \{j, v_n, \lambda\} \quad (5.1)$$

where $[d]$ is the degree of freedom matrix, j are the material fluxes, v_n are the interfacial velocities and λ are the Lagrange multipliers (used to ensure mass conservation).

5.1.2 – Isoparametric Mapping

The ability to handle distorted and non-uniform computational domains is an important feature of the finite element method. This feature is based upon a pre-defined mapping method whereby the finite element can be geometrically transformed between the physical domain (cartesian co-ordinate system, (x, y)) and virtual computational domain (natural or local co-ordinate system, (ξ, η)) using a specified shape (or interpolation) function. The shape function is usually represented by a first order or higher-order polynomial, allowing values defined at the nodal points of the finite element to be mapped to any other point within the finite element with defined coordinates within virtual space. The use of isoparametric mapping therefore has particular benefit for the evaluation and solution of integral and differential equations. The natural coordinates for a two-dimensional triangular finite element are taken to be ξ and η , which are illustrated in Figure 5.2 for a straight sided six-noded finite element.

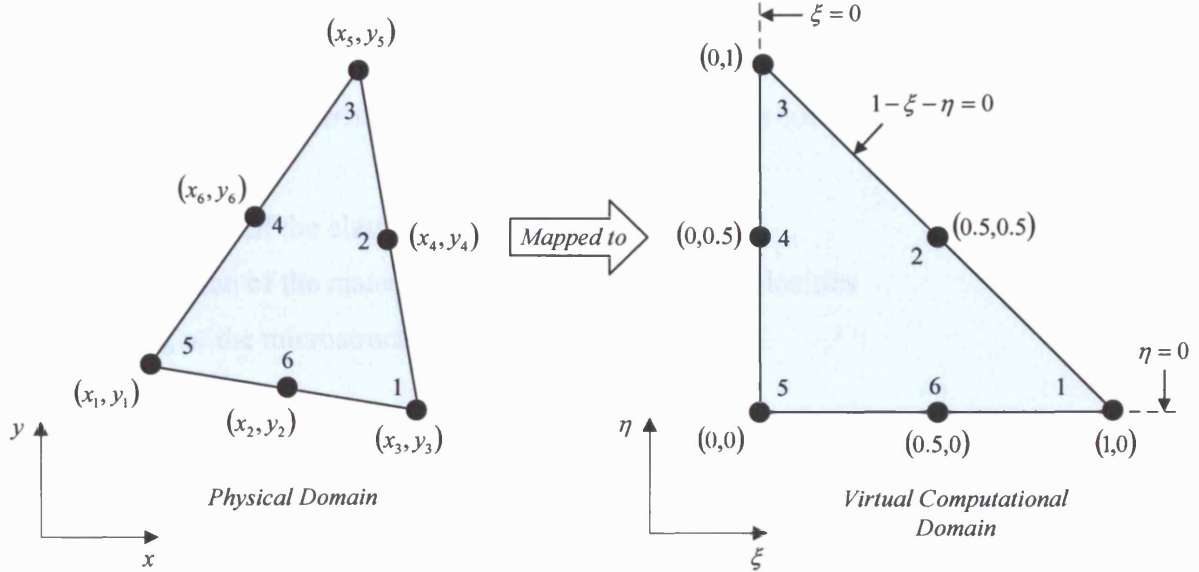


Figure 5.2 – Mapping the physical domain onto the virtual computational domain for a six-noded quadratic-type finite element with straight sides.

The natural coordinates for the two-dimensional finite element shown in Figure 5.2 vary such that $0 \leq \xi \leq +1$, $0 \leq \eta \leq +1$ and $\xi + \eta \leq +1$, and are purposely set-up in this way to facilitate the use of standard Gauss integration formulas.

The shape function across a general isoparametric finite element can be used to determine the value of an arbitrary function, z , at defined coordinates within virtual computational space by knowing the values of the function at the elemental nodal points. Considering the isoparametric finite element shown in Figure 5.2, the value of the arbitrary function, z at virtual coordinates (ξ, η) , can be calculated through the relation

$$z = \sum_{i=1}^{N_e} n_i(\xi, \eta) z_i \quad (5.2)$$

where the summation is carried out over N_e elemental nodes, $n_i(\xi, \eta)$ is the shape function and z_i is the value of z at nodal point i . See Appendix B for a full definition of the three-noded linear and six-noded quadratic two-dimensional shape functions.

5.2 – The General Solution Process

The solution process and numerical implementation of the general model, described in the previous chapter, consists of three main stages which are outlined as follows:

1. Determination of the elastic field
2. Determination of the material flux field and interface velocities
3. Updating of the microstructure description

The rate of evolution of the microstructure is determined for the microstructure configuration and the above processes can be repeated until an equilibrium microstructure is obtained. The three stages outlined above are described in detail within the following subsections of this chapter.

5.2.1 – Determination of the Elastic Field

It is assumed that the displacement field is continuous across the interface and this renders the interface coherent, i.e. the two phases neither slip nor separate at the interface. If it is known how the horizontal and vertical displacements (u and v) within a two-dimensional element vary with position (x and y), the elastic strains and stresses can be determined. The elastic displacement field within a two-dimensional finite element can be described by

$$\begin{aligned} u &= n_i(\xi, \eta)u_i \\ v &= n_i(\xi, \eta)v_i \end{aligned} \tag{5.3}$$

where u and v are the displacements at (ξ, η) , and u_i and v_i are the displacements at nodal point i . In this two-dimensional analysis, two types of isoparametric triangular elements are considered and are shown in Figure 5.3.

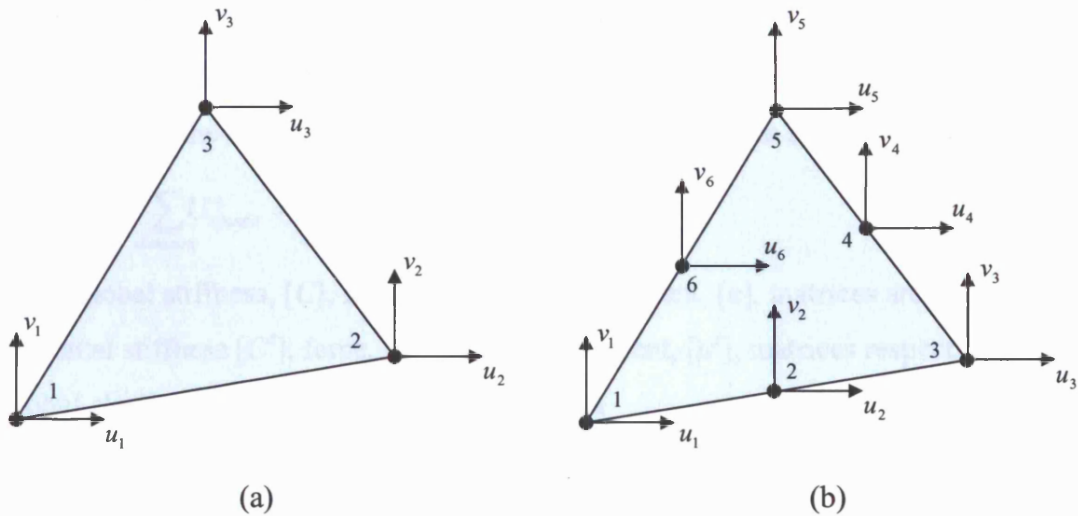


Figure 5.3 – The displacement field across a two-dimensional (a) three-noded linear and (b) six-noded quadratic type finite element.

Considering an elastically deformed element, subject to a transformation strain, ε_T , one can write the elastic stored energy of the element, $U_{elastic}^e$, in terms of the nodal displacements of the element, $[u^e]$, as

$$\begin{aligned}
 U_{elastic}^e &= \frac{1}{2} \int_{V^e} [\sigma]^T [\varepsilon - \varepsilon_T] dV \\
 &= \frac{1}{2} \int_{V^e} [\varepsilon - \varepsilon_T]^T [D] [\varepsilon - \varepsilon_T] dV \\
 &= \frac{1}{2} [u^e]^T [C^e] [u^e] - [u^e]^T [R^e] + \frac{1}{2} U_o^e
 \end{aligned} \tag{5.4}$$

where $[\varepsilon_T]$ is the transformation strain matrix and V^e is the elemental volume (area). The stresses are related to the strains through the relation, $[\sigma] = [D][\varepsilon]$, where $[D]$ is the material stiffness matrix (see Appendix A.1). The elemental matrices $[C^e]$, $[R^e]$ and U_o^e are determined from the material parameters, element geometry, composition and defined shape functions and are expressed as

$$\begin{aligned}
 [C^e] &= \int_{V^e} [B^e]^T [D] [B^e] dV \\
 [R^e] &= \int_{V^e} [\varepsilon_T]^T [D] [B^e] dV \\
 U_o^e &= \int_{V^e} [\varepsilon_T]^T [D] [\varepsilon_T] dV
 \end{aligned} \tag{5.5}$$

where $[B^e]$ is the shape function matrix relating the elastic strains to displacements such that $[\varepsilon] = [B^e][u^e]$ (see Appendix A.2).

One can assemble the elemental matrices to find the global elastic stored energy

$$U_{elastic} = \sum_{elements} U_{elastic}^e = \frac{1}{2}[u]^T[C][u] - [u]^T[R] + \frac{1}{2}U_o \quad (5.6)$$

where the global stiffness, $[C]$, force, $[R]$, and displacement, $[u]$, matrices are assembled from the elemental stiffness $[C^e]$, force, $[R^e]$, and displacement, $[u^e]$, matrices respectively.

The global elastic stored energy is a minimum when

$$\frac{\partial U_{elastic}}{\partial [u]^T} = 0$$

which leads to

$$[C][u] = [R]$$

So the displacements can be determined from

$$[u] = [C]^{-1}[R] \quad (5.7)$$

The displacement matrix, $[u]$, can therefore be computationally calculated from equation (5.7). Having found the nodal displacements, the true stresses, strains and global elastic stored energy can then be readily calculated.

From this analysis, it can be seen that the elastic field variables can be solved at any time for any defined finite element geometry and are computed independently of the flux field and interface velocity migration process (described in the following sub-section). However, for elastically driven diffusion, it is necessary to know the elastic field.

5.2.2 – Determining the Flux Field and Rate of Interface Migration

(a) Dissipative Processes

The two sources of energy dissipation considered in this analysis are due to lattice diffusion and interface boundary migration.

(i) Dissipation due to a Lattice Flux

The same finite element mesh and shape functions used to calculate the elastic displacement field, $[u]$, are used to calculate the lattice flux field, $[j]$, which can be described across the type of two-dimensional finite elements shown in Figure 5.4 by

$$j_{pk\alpha} = n_i(\xi, \eta) j_{pk\alpha i} \quad (5.8)$$

where p denotes the phase, k denotes the sublattice component, α denotes the direction under consideration and the right hand side denotes the summation over all elemental nodes, i , in element e .

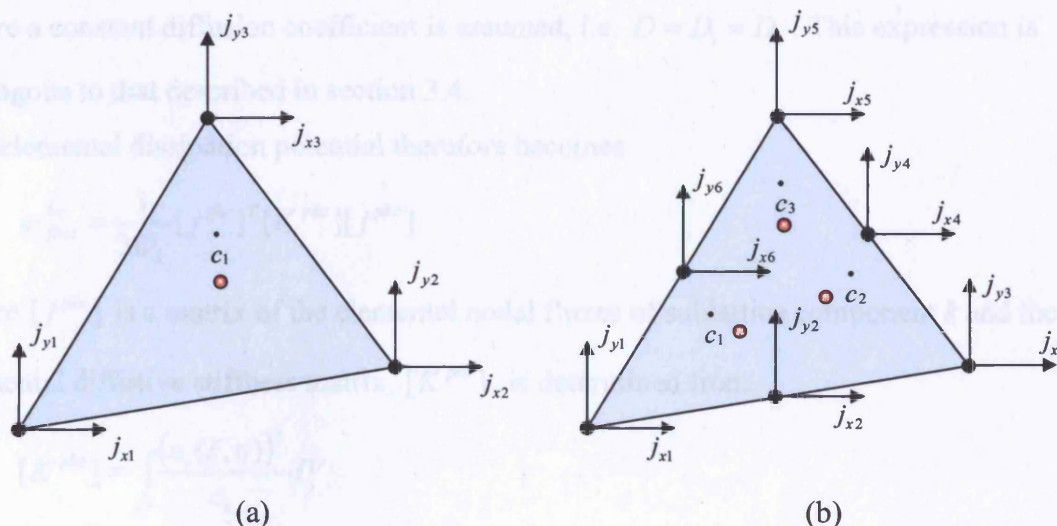


Figure 5.4 – The lattice flux field across a two-dimensional (a) three-noded linear and (b) six-noded quadratic type finite element. The rate of change of composition is evaluated at the elemental Gauss points.

From equation (4.9), the elemental dissipation potential for sublattice component k is therefore

$$\dot{\psi}_{flux}^{ke} = \frac{1}{2} \sum_{\alpha} \int_{V^e} \frac{(n_i(\xi, \eta) j_{k\alpha i})^2}{\mathcal{D}_k^{eff}} dV \quad (5.9)$$

The effective diffusivity is related to the composition of sublattice component k through the linear relation

$$\mathcal{D}_k^{eff} = \mathcal{D}_k c_k$$

where the lattice diffusivity, \mathcal{D}_k , is defined by $\mathcal{D}_k = \frac{D_k}{RT}$ and is assumed constant (D_k is the diffusion coefficient of sublattice component k). For a two component system (where $c = c_1$ and $c_2 \approx 1 - c$), the effective diffusivities for each sublattice component can be described by

$$\mathcal{D}_1^{eff} = \frac{D_1 c}{RT} \quad \mathcal{D}_2^{eff} = \frac{D_2 (1 - c)}{RT}$$

These can be combined to give an overall effective diffusivity such that

$$\frac{1}{\mathcal{D}^{\text{eff}}} = \frac{1}{\mathcal{D}_1^{\text{eff}}} + \frac{1}{\mathcal{D}_2^{\text{eff}}}$$

$$\mathcal{D}^{\text{eff}} = \frac{Dc(1-c)}{RT}$$

where a constant diffusion coefficient is assumed, i.e. $D = D_1 = D_2$. This expression is analogous to that described in section 3.4.

The elemental dissipation potential therefore becomes

$$\psi_{\text{flux}}^{ke} = \frac{1}{2\mathcal{D}_k} [j^{pke}]^T [K^{pke}] [j^{pke}]$$

where $[j^{pke}]$ is a matrix of the elemental nodal fluxes of sublattice component k and the elemental diffusive stiffness matrix, $[K^{pke}]$, is determined from

$$[K^{pke}] = \int_{V^e} \frac{(n_i(\xi, \eta))^2}{c_k} dV$$

The elemental diffusive stiffness matrix, $[K^{pke}]$, can be numerically evaluated using Gaussian quadrature (see Appendix B).

The total dissipation due to sublattice component, k , is therefore

$$\psi_{\text{flux}}^k = \frac{1}{2\mathcal{D}_k} \sum_{\text{elements}, e} [j^{ke}]^T [K^{ke}] [j^{ke}] = \frac{1}{2\mathcal{D}_k} [j^k]^T [K^k] [j^k]$$

where $[j^k]$ and $[K^k]$ are the global flux and diffusive stiffness matrices for sublattice component k . The total dissipation potential due to a lattice flux is simply

$$\psi_{\text{flux}} = \sum_{\substack{\text{components} \\ \& \text{ sublattices}, k}} \psi_{\text{flux}}^k = \frac{1}{2\mathcal{D}} [j]^T [K] [j] \quad (5.9)$$

where $[j]$ and $[K]$ are the global flux and diffusive stiffness matrices for all components and \mathcal{D} is a lattice diffusivity constant.

(ii) Dissipation due to Interface Boundary Migration

An interface boundary migrates with velocity, v_n , by the process of breaking atoms from one phase and attaching them to the other phase. In the finite element discretisation described in Figure 5.1 the mesh is constructed such that the sides of a series of elements lie along the interface forming interface boundary segments. The velocity degrees of freedom

associated with the motion of the interface are introduced at the nodes along the interface. To derive the dissipation potential associated with interface migration, one only needs to consider one interface segment as shown in Figure 5.5.

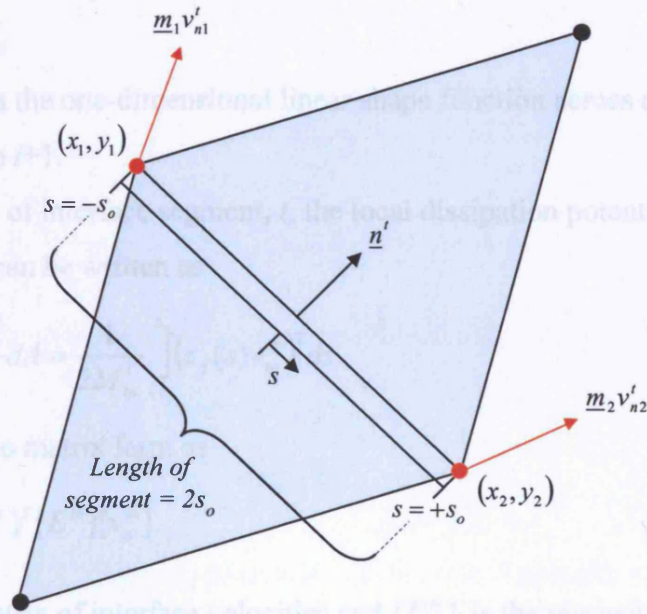


Figure 5.5 – An interface boundary segment, t , constructed from the edges of two adjacent three-noded linear type finite elements.

The interface velocity field across interface segment, t , can be described by the linear interpolation function

$$v_n^t(s) = v_{n1}^t \underline{m}_1 \cdot \underline{n}^t \frac{(s_o - s)}{2s_o} + v_{n2}^t \underline{m}_2 \cdot \underline{n}^t \frac{(s_o + s)}{2s_o} \quad (5.10)$$

where s is the position of interest along the interface boundary segment between the outer nodes, \underline{n}^t is the normal unit vector to boundary segment t , and \underline{m}_i is the normal unit vector at boundary node i , determined from

$$\underline{m}_i = \frac{\frac{1}{2}(\underline{n}^t + \underline{n}^{t+1})}{\left| \frac{1}{2}(\underline{n}^t + \underline{n}^{t+1}) \right|}$$

where boundary point, i , is located between the two connecting boundary segments, t and $t + 1$. The dot between vectors, \underline{n} and \underline{m} , in equation (5.10) denotes the scalar product. The

interface segment is flat so if six-noded finite elements are used, equation (5.10) still holds but the interface velocity of the mid-node, $v_{mid}^t = (v_{ni}^t + v_{n(i+1)}^t)/2$, is given by the interface velocity of the two end nodes.

Equation (5.10) can be generally expressed as

$$v_n^t(s) = z_j(s)v_{nj}^t \quad (5.11)$$

where $z_j(s)$ represents the one-dimensional linear shape function across each interface segment and j ranges from i to $i+1$.

For finite element, e , of interface segment, t , the local dissipation potential due to interface boundary migration can be written as

$$\psi_{in}^{te} = \frac{1}{2} \int_{A'} \frac{(v_n^{te})^2}{M_{in}^t} dA = \frac{1}{2M_{in}^t} \int_{-s_o}^{s_o} (z_j(s)v_{nj}^{te})^2 ds$$

which can be cast into matrix form as

$$\psi_{in}^{te} = \frac{1}{2M_{in}^t} [v_n^{te}]^T [E^{te}] [v_n^{te}] \quad (5.12)$$

where $[v_n^{te}]$ is the matrix of interface velocities and $[E^{te}]$ is the viscosity matrix associated with element, e , of interface segment, t , which is defined by

$$[E^{te}] = s_o \begin{bmatrix} \frac{2}{3} & \frac{1}{3} \\ \frac{1}{3} & \frac{2}{3} \end{bmatrix} \quad (5.13)$$

Equation (5.13) holds for six-noded finite elements provided that the interface mid-node is constrained in such a way that each interface sub-segment remains flat.

One can assemble the segment matrices to determine the global dissipation potential due to interface boundary migration

$$\psi_{in} = \frac{1}{2} \sum_t \sum_e \frac{[v_n^{te}]^T [E^{te}] [v_n^{te}]}{M_{in}^t} = \frac{1}{2M_{in}} [v_n]^T [E] [v_n] \quad (5.14)$$

where $[v_n]$ and $[E]$ are the global interface velocity and global viscosity matrices respectively and M_{in} is a reference mobility.

(b) Rate of Change of Composition

The rate of change of composition can be related to the lattice flux field through the two-dimensional Fick's relation (equation (3.6)) written as

$$\frac{dc_k}{dt} = - \left(\frac{\partial j_{kx}}{\partial x} + \frac{\partial j_{ky}}{\partial y} \right) \quad \forall(x, y)$$

We satisfy this point-wise condition globally over each whole element rather than at each point in the element, so that

$$\int_{V^e} \frac{dc_k}{dt} dV^e = - \int_{V^e} \left(\frac{\partial j_{kx}}{\partial x} + \frac{\partial j_{ky}}{\partial y} \right) dV^e$$

This expression for the rate of change of composition can be evaluated using Gaussian quadrature

$$\int_0^{1-\eta} \int_0^\eta \frac{dc_k}{dt} J d\xi d\eta = - \int_0^{1-\eta} \int_0^\eta \left(\frac{\partial j_{kx}}{\partial x} + \frac{\partial j_{ky}}{\partial y} \right) J d\xi d\eta$$

where J is the determinant of the Jacobian and is defined in Appendix A.2.

This expression can be written in elemental matrix form as

$$[\dot{c}_{ke}] = [H_{ke}^j]^T [j_{ke}] \quad (5.15)$$

where $[\dot{c}_{ke}]$ is the matrix for the rate of change of composition of sublattice component k within element, e , and $[H_{ke}^j]$ is the elemental shape function matrix relating the rate of change of composition within the element to the elemental fluxes of sublattice component k (the superscript j simply indicates that the matrix is associated with the fluxes and is not an index). Globally, one can assemble such matrices over all elements and sublattice components to give

$$[\dot{c}] = [H^j]^T [j] \quad (5.16)$$

where $[\dot{c}]$ is the matrix containing the rates of change of composition of all sublattice components at all elemental Gauss points and $[H^j]$ is the global shape function matrix relating the rate of change of composition to the lattice fluxes, $[j]$, defined at the elemental nodal points.

A finite element mesh adaption technique is developed and implemented in order to allow the mesh to be locally updated as the interface traverses through the system. Using mesh adaption it is possible to update the position of the elemental nodes located along the

interface, provided that the finite elements local to the interface do not become too distorted and the solution is affected. This problem is addressed in detail in chapter 9. If the mesh is adapted local to the line of the interface, the elemental nodal points located along the interface will move in accordance with the calculated velocity of the interfacial nodes and the selected iterative time step. The geometry of the interface elements will therefore change, indicating that the respective positions of the elemental Gauss points will also change along with the associated rate of change of composition stored at these points.

In a moving reference frame (such as that near the phase interfaces) the composition at a Gauss point g , $c_g(x, t)$ is a function of time and position such that

$$\frac{dc_g}{dt} = \frac{\partial c_g}{\partial t} + v_{gx} \frac{\partial c_g}{\partial x} + v_{gy} \frac{\partial c_g}{\partial y} \quad (5.17)$$

where $\frac{dc_g}{dt}$ is the material time derivative, $\frac{\partial c_g}{\partial t}$ is the rate of change of composition at Gauss point g , and v_{gx} and v_{gy} are the velocities of Gauss point g in the x and y directions respectively.

For three-noded (first order) finite elements, no compositional gradients exist

within the finite elements, i.e. $\frac{\partial c_g}{\partial x} = \frac{\partial c_g}{\partial y} = 0$, so the latter terms within equation (5.17) only

become important for six-noded quadratic or higher order type finite elements. For six-noded type finite elements, the composition defined at the elemental Gauss points can be related to the composition at any point within the element (with defined local coordinates ξ and η) through the relation

$$c(\xi, \eta) = m_j(\xi, \eta)c_j \quad (5.18)$$

where the shape function, m_j , relates the composition defined within the virtual computational domain to the composition defined within the physical domain. For a six-noded finite element, the shape function, m_j , can be defined by

$$\begin{aligned} m_1(\xi, \eta) &= \frac{(6\xi - 1)}{3} \\ m_2(\xi, \eta) &= \frac{(6\eta - 1)}{3} \\ m_3(\xi, \eta) &= \frac{(5 - 6(\xi + \eta))}{3} \end{aligned}$$

From equations (5.18) and (A.9) (see Appendix A.2), one can find the compositional gradients and Gauss point velocity components so that one can write, using equation (5.16) to define

$$\frac{\partial c_g}{\partial t} \quad (5.20)$$

$$[\dot{c}_g] = [H^j]^T [j] + [H^x]^T [v_n] \quad (5.19)$$

where $[H^x]$ is a global shape function matrix relating the rate of change of composition to the interface velocities, and the superscript x indicates it is associated with changes in the interface position.

The Gauss points move in the direction of the normal, \underline{n}^t , to interface segment, t , so the velocity of the Gauss points, v_g , within the interface elements can be determined by interpolation of the velocities at the elemental corner nodal points. From Figure 5.6 it can be seen that the motion of the Gauss points is principally in the direction normal to the interface, $\underline{n} = [n_x, n_y]$ (there is a slight tangential component when $\underline{m} \neq \underline{n}$ as the element gets wider / thinner which is ignored), so one can generally write $v_g \underline{n} = [v_{gx}, v_{gy}]$.

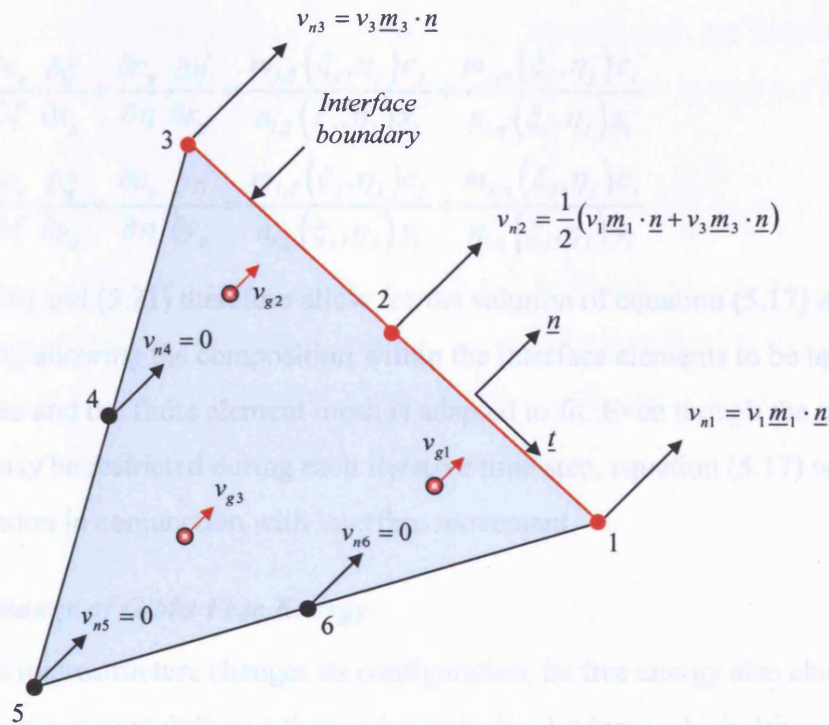


Figure 5.6 – A six-noded finite element located local to the interface, whose geometry and composition change as the interface nodes move and the finite element mesh is adapted.

The velocities of the Gauss points can be determined from the nodal velocities defined at the corners of the finite element through the expression

$$v_g(\xi, \eta) = n_i(\xi, \eta)v_{ni} \quad (5.20)$$

For six-noded quadratic type finite elements, the composition defined at the elemental Gauss points can be related to the composition at any points within the finite element (with defined coordinates ξ and η) using the relation defined by equation (5.18).

The x and y coordinates of the Gauss points can be determined from

$$\begin{aligned} x_{gj} &= n_i(\xi_j, \eta_j)x_i \\ y_{gj} &= n_i(\xi_j, \eta_j)y_i \end{aligned}$$

where the Gauss points are located at (ξ_j, η_j) . Therefore from equation (5.17), $\frac{\partial c_g}{\partial x}$ and $\frac{\partial c_g}{\partial y}$

depend on the direction of motion of the Gauss points, i.e. resolved in a direction normal to the interface segment, such that

$$\frac{\partial c_g}{\partial x_{gn}} = \frac{\partial c_g}{\partial x_g} n_x \quad \frac{\partial c_j}{\partial y_{gn}} = \frac{\partial c_g}{\partial y_g} n_y \quad (5.21)$$

where

$$\begin{aligned} \frac{\partial c_g}{\partial x_g} &= \frac{\partial c_g}{\partial \xi} \frac{\partial \xi}{\partial x_g} + \frac{\partial c_g}{\partial \eta} \frac{\partial \eta}{\partial x_g} = \frac{m_{j,\xi}(\xi_j, \eta_j)c_j}{n_{i,\xi}(\xi_j, \eta_j)x_i} + \frac{m_{j,\eta}(\xi_j, \eta_j)c_j}{n_{i,\eta}(\xi_j, \eta_j)x_i} \\ \frac{\partial c_g}{\partial y_g} &= \frac{\partial c_g}{\partial \xi} \frac{\partial \xi}{\partial y_g} + \frac{\partial c_g}{\partial \eta} \frac{\partial \eta}{\partial y_g} = \frac{m_{j,\xi}(\xi_j, \eta_j)c_j}{n_{i,\xi}(\xi_j, \eta_j)y_i} + \frac{m_{j,\eta}(\xi_j, \eta_j)c_j}{n_{i,\eta}(\xi_j, \eta_j)y_i} \end{aligned}$$

Equations (5.20) and (5.21) therefore allow for the solution of equation (5.17) and hence equation (5.19), allowing the composition within the interface elements to be updated as the interface moves and the finite element mesh is adapted to fit. Even though the movement of the interface may be restricted during each iterative time step, equation (5.17) will aid general mass conservation in conjunction with interface movement.

(c) Rate of Change of Gibbs Free Energy

When a microstructure changes its configuration, its free energy also changes. The free energy change of a system defines a thermodynamic driving force which drives the configurational change of the structure. The total global thermodynamic driving force matrix

is assembled from all individual elemental thermodynamic driving force contributions due to the chemical phase energy, interface energy and elastic stored energy respectively.

It is important to be able to predict the probable outcome of the system under the influence of individual thermodynamic driving forces. This is carried out by considering the theoretical dependence of the driving force on factors such as the composition and the position of the interface boundary. However, when more than one driving force is considered it is more difficult to predict the likely evolution of the microstructure and computational modelling becomes a necessity.

(i) *Chemical Phase Energy*

At a given temperature the phase energy of equation (4.17) becomes

$$G_{phase} = \sum_{elements,e} \int_{V_e} g(c^e) dV = \sum_{elements,e} \int_0^{1-\eta} \int_0^{1-\eta} g(c^e) J^e d\xi d\eta$$

The derivative of this expression is given by

$$\dot{G}_{phase} = \sum_{elements,e} \int_0^{1-\eta} \int_0^{1-\eta} \frac{dg(c^e)}{dc^e} \frac{dc^e}{dt} J^e d\xi d\eta + \sum_{elements,e} \int_0^{1-\eta} \int_0^{1-\eta} g(c^e) \frac{dJ^e}{dt} d\xi d\eta$$

where the integral is approximated by Gaussian integration although $g(c^e)$ is non-linear.

Hence, using equation (5.19), the rate of change of chemical phase energy can be expressed in matrix form as

$$\dot{G}_{phase} = -[j]^T [H^j] [F_{pj}] - [v_n]^T ([H^x] [F_{pj}] + [F_{pv}]) \quad (5.22)$$

where $[F_{pj}]$ and $[F_{pv}]$ represent the driving forces due to a change in chemical phase energy with change in composition and change in the position of the interface boundary respectively.

The rate of change of the determinant of Jacobian can be evaluated from equation (A.10) (see Appendix A.2) such that

$$\frac{dJ^e}{dt} = N_{ij} \left(\dot{x}_i y_j + x_i \dot{y}_j \right) = [AB^e] [v_n]$$

where $[AB]$ is a shape function matrix relating the rate of change of area of each finite element to the corresponding interface nodal velocities. The rate of change of the Jacobian will be non-zero for finite elements located local to the interface that have at least one node along the line of the interface boundary. The rate of change of elemental area is related to the rate of change of the determinant of the Jacobian through the relation

$$\dot{A}^e = \int_0^1 \int_0^1 \dot{J}^e d\xi d\eta = \frac{1}{2} \dot{J}^e$$

As the interface moves and the elemental interface nodes are adapted, there will be a change in elemental area associated with the finite elements with at least one or more nodes located on the interface, as shown in Figure 5.7.

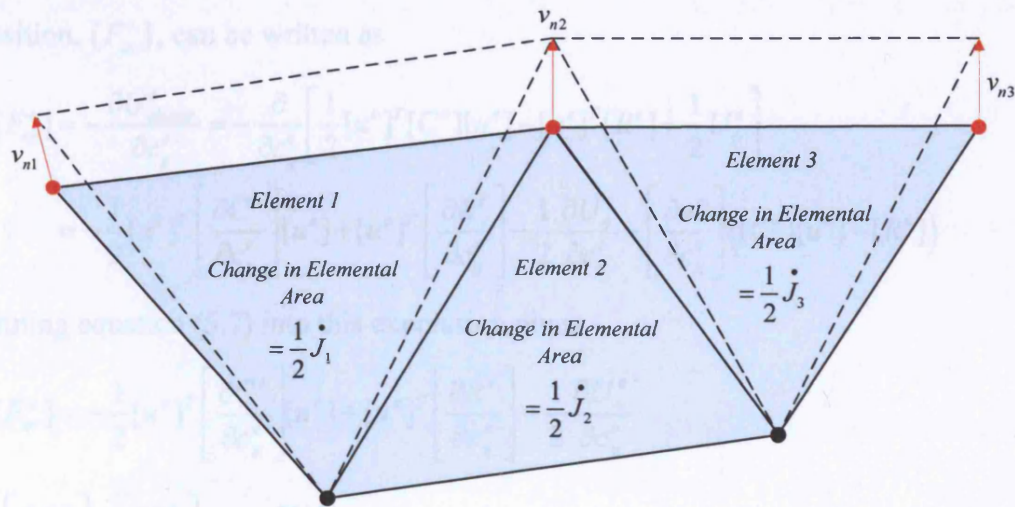


Figure 5.7 – Three adjacent finite elements and their relative change in area as the interface nodes move with velocity, v_{ni} and the elemental nodes are adapted.

(ii) *Elastic Stored Energy*

The elastic stored energy in an element, $U_{elastic}^e$, depends on the compositional values at the elemental Gauss points, c_g^e , (these define the transformation strain and elastic properties in the element) and the positions of the nodes that lie on the interfacial boundary (if any), x_{in}^t , (these define the shape and volume of each phase).

The rate of change of elastic stored energy within an element, e , can therefore be written as

$$\dot{U}_{elastic}^e = \frac{d}{dt} (U_{elastic}^e(c_g^e, x_{in}^t)) = \sum_g \frac{\partial U_{elastic}^e}{\partial c_g^e} \dot{c}_g^e + \sum_t \frac{\partial U_{elastic}^e}{\partial x_{in}^t} \dot{x}_{in}^t \quad (5.23)$$

where the summations are performed over all Gauss points, g , and interface boundary sub-segments, t , associated with finite element, e .

Equation (5.23) can be conveniently written in matrix form as

$$\dot{U}_{elastic}^e = - \left([\dot{c}_g^e] [F_{ec}^e] + [\dot{x}_{in}^t]^T [F_{ein}^e] \right) \quad (5.24)$$

where $[F_{ec}^e]$ denotes the elemental elastic driving force due to a change in elastic stored energy with change in composition and $[F_{ein}^e]$ represents the elemental elastic driving force due to the position of the interface (derived from the elastic distortion of the near interface elements).

The elemental elastic driving force due to a change in elastic stored energy with change in composition, $[F_{ec}^e]$, can be written as

$$\begin{aligned} [F_{ec}^e] &= -\frac{\partial U_{elastic}^e}{\partial c_g^e} = -\frac{\partial}{\partial c_g^e} \left[\frac{1}{2} [u^e]^T [C^e] [u^e] - [u^e]^T [R^e] + \frac{1}{2} U_o^e \right] \\ &= -\frac{1}{2} [u^e]^T \left[\frac{\partial C^e}{\partial c_g^e} \right] [u^e] + [u^e]^T \left[\frac{\partial R^e}{\partial c_g^e} \right] - \frac{1}{2} \frac{\partial U_o^e}{\partial c_g^e} - \left[\frac{\partial u^e}{\partial c_g^e} \right] ([C^e][u^e] - [R^e]) \end{aligned}$$

Substituting equation (5.7) into this expression gives

$$[F_{ec}^e] = -\frac{1}{2} [u^e]^T \left[\frac{\partial C^e}{\partial c_g^e} \right] [u^e] + [u^e]^T \left[\frac{\partial R^e}{\partial c_g^e} \right] - \frac{1}{2} \frac{\partial U_o^e}{\partial c_g^e} \quad (5.25)$$

where $\left[\frac{\partial C^e}{\partial c_g^e} \right]$, $\left[\frac{\partial R^e}{\partial c_g^e} \right]$ and $\frac{\partial U_o^e}{\partial c_g^e}$ are defined by

$$\begin{aligned} \left[\frac{\partial C^e}{\partial c_g^e} \right] &= \int_{V^e} [B^e]^T \left[\frac{\partial D}{\partial c_g^e} \right] [B^e] \partial V \\ \left[\frac{\partial R^e}{\partial c_g^e} \right] &= \int_{V^e} [B^e]^T \left[\frac{\partial D}{\partial c_g^e} \right] [\varepsilon_T] \partial V + \int_{V^e} [B^e]^T [D] \left[\frac{\partial \varepsilon_T}{\partial c_g^e} \right] \partial V \\ \frac{\partial U_o^e}{\partial c_g^e} &= 2 \int_{V^e} \left[\frac{\partial \varepsilon_T}{\partial c_g^e} \right]^T [D] [\varepsilon_T] \partial V + \int_{V^e} [\varepsilon_T]^T \left[\frac{\partial D}{\partial c_g^e} \right] [\varepsilon_T] \partial V \end{aligned}$$

The derivative of the elastic strain energy with respect to the positions of the nodes that lie on the interfacial boundary, $[F_{ein}^e]$, can be described by

$$\begin{aligned} [F_{ein}^e] &= -\frac{\partial U_{elastic}^e}{\partial x_{in}^t} = -\frac{\partial}{\partial x_{in}^t} \left[\frac{1}{2} [u^e]^T [C^e] [u^e] - [u^e]^T [R^e] + \frac{1}{2} U_o^e \right] \\ &= -\left[\frac{\partial u^e}{\partial x_{in}^t} \right]^T ([C^e][u^e] - [R^e]) - \frac{1}{2} [u^e]^T \left[\frac{\partial C^e}{\partial x_{in}^t} \right] [u^e] + [u^e]^T \left[\frac{\partial R^e}{\partial x_{in}^t} \right] - \frac{1}{2} \frac{\partial U_o^e}{\partial x_{in}^t} \end{aligned}$$

Substituting equation (5.7) into this expression gives

$$[F_{ein}^e] = -\frac{1}{2} [u^e]^T \left[\frac{\partial C^e}{\partial x_{in}^t} \right] [u^e] + [u^e]^T \left[\frac{\partial R^e}{\partial x_{in}^t} \right] - \frac{1}{2} \frac{\partial U_o^e}{\partial x_{in}^t} \quad (5.26)$$

In order to evaluate this contribution it is necessary to determine the differentials of the stiffness and transformation matrices, which are defined in Appendix A.4. The elastic driving forces defined within equations (5.25) and (5.26) can be evaluated knowing the elemental displacement field, $[u^e]$, which is given by the finite element elasticity solution of equation (5.7).

One can assemble the elemental matrices to determine the total rate of change of elastic stored energy such that

$$\dot{U}_{elastic} = - \sum_{elements,e} \left([c_g^e][F_{ec}^e] + [x_{in}^e]^T [F_{ein}^e] \right)$$

where the summation is performed over all elements, e . Using equation (5.19) this can be conveniently expressed in global form as

$$\dot{U}_{elastic} = -[j]^T [H^j][F_{ec}] - [v_n]^T ([H^x][F_{ec}] + [F_{ein}]) \quad (5.27)$$

where the global driving forces due to the change in elastic stored energy with composition and interface position are given by $[F_{ec}]$ and $[F_{ein}]$ respectively.

(iii) Interface Surface Energy

The rate of change of interfacial energy can be represented by

$$\dot{G}_{surface} = \frac{d}{dt} \int_{A_s} \gamma_s dA = \gamma_s \dot{A}_s \quad (5.28)$$

Here it is assumed for simplicity that the interfacial energy is isotropic (γ_s does not depend on the local interface normal, \underline{n}), and although interfacial energies can vary significantly from one crystal face to the next across a range of microstructures, it is assumed that this variability can be suppressed without losing the essential features of the process being carried out.

Consider the interface boundary segment shown in Figure 5.5. Using Pythagoras' theorem, the area (i.e. length) of the interface boundary segment can be expressed as

$$A_{in} = 2s_o = \sqrt{(x_{i+1} - x_i)^2 + (y_{i+1} - y_i)^2}$$

Differentiating this expression with respect to time gives

$$\dot{A}_{in} = \frac{(x_{i+1} - x_i)(\dot{x}_{i+1} - \dot{x}_i) + (y_{i+1} - y_i)(\dot{y}_{i+1} - \dot{y}_i)}{2s_o}$$

where the velocities of the interfacial nodes are resolved in a direction normal to each point such that

$$\begin{aligned} \dot{x}_i &= m_{xi} v_{ni} & \dot{x}_{i+1} &= m_{x(i+1)} v_{n(i+1)} \\ \dot{y}_i &= m_{yi} v_{ni} & \dot{y}_{i+1} &= m_{y(i+1)} v_{n(i+1)} \end{aligned}$$

This implies that the rate of change of area of the interface segment is

$$\dot{A}_{in} = \frac{(x_{i+1} - x_i)(m_{x(i+1)} v_{n(i+1)} - m_{xi} v_{ni}) + (y_{i+1} - y_i)(m_{y(i+1)} v_{n(i+1)} - m_{yi} v_{ni})}{2s_o} \quad (5.29)$$

Assembling all contributions from each interface boundary segment, equation (4.13) can be expressed in general matrix form as

$$\dot{G}_{surface} = -[v_n]^T [F_{in}] \quad (5.30)$$

where $[F_{in}]$ represents the thermodynamic interfacial driving force acting on the velocities along the line of the interface.

(d) Interface Constraint

When meshing the body it is ensured that the interface lies along the edges of a series of elements and these edges move as the interface translates. At a given instant in time the composition is known at all elemental Gauss points across the finite element mesh. Its value is constant within the linear three noded triangular element of Figure 5.4(a) and varies linearly within the quadratic six noded triangular element of Figure 5.4(b).

Additional degrees of freedom are provided by the interface velocity at the interfacial nodes and the interface constraint of equation (4.22) is taken into account through a series of Lagrange multipliers applied along the line of the interface. The discontinuity in the flux field at the interface is taken into account through the Lagrange multipliers with four fluxes defined at each interfacial node (two in each direction) as opposed to two fluxes at each node (one in each direction) within a continuous flux field. In order to apply the interface constraint at all nodes along the interface, it is necessary to determine the difference in concentration across the interface, Δc , at each interfacial nodal point. This is calculated by considering only the finite elements that share an edge with the interface boundary. For six-noded quadratic type finite elements, the composition defined at the elemental Gauss points can be related to the composition at any point within the finite element using equation (5.18). Using this relation, the composition stored at the three Gauss points can be mapped to the elemental nodes (of

defined ζ and η coordinates). The contribution from finite elements with only one node touching an interface boundary point is second order and hence this contribution is assumed to be negligible. Where an interface node is shared by more than one edge-sharing interface element (everywhere apart from at the boundaries of the simulation), the compositional values are averaged.

The Lagrangian term of equation (4.22) can therefore be expressed in matrix form as

$$\int_A \lambda \{ \Delta j_\alpha n_\alpha + \Delta c v_n \} dA = [\lambda]^T \{ [M][j] + [L][v_n] \} \quad (5.31)$$

where $[\lambda]$ is the matrix of Lagrange multipliers, $[M]$ is determined from the geometry of the interface, $[v_n]$ is the matrix of unknown velocities and $[L]$ is determined from the velocity shape functions and known concentrations either side of the boundary.

(e) General Variational Formulation

The general dissipation potential and rate of change of Gibbs' free energy can be expressed in terms of the degree of freedom matrix as

$$\Psi = \frac{1}{2} [d]^T [C] [d] \quad \dot{G} = -[d]^T [F] \quad (5.32)$$

where $[d]$ is the degree of freedom matrix of nodal fluxes, interface velocities and Lagrange multipliers and is defined by

$$[d]^T = [j \quad ; \quad v_n \quad ; \quad \lambda]$$

The generalised global stiffness and force matrices ($[C]$ and $[F]$ respectively) are defined by the system geometry and material parameters. The global stiffness matrix, $[C]$, incorporates the $[K]$, $[E]$, $[M]$ and $[L]$ matrices contained within equations (5.9), (5.14) and (5.31). The global force matrix, $[F]$, incorporates the driving force matrices, $[F_{pj}]$, $[F_{pv}]$, $[F_{ec}]$, $[F_{ein}]$ and $[F_{in}]$ contained within equations (5.22), (5.27) and (5.30).

Hence the variational functional can be written as

$$\hat{\Pi} = \frac{1}{2} \begin{bmatrix} j \\ v_n \\ \lambda \end{bmatrix}^T \begin{bmatrix} K/\mathcal{D} & 0 & M/2 \\ 0 & E/M_{in} & L/2 \\ M/2 & L/2 & 0 \end{bmatrix} \begin{bmatrix} j \\ v_n \\ \lambda \end{bmatrix} - \begin{bmatrix} j \\ v_n \\ \lambda \end{bmatrix}^T \begin{bmatrix} [H^j][F_{pj} + F_{ec}] \\ [F_{pv} + F_{ein} + F_{in}] + [H^x][F_{pj} + F_{ec}] \\ 0 \end{bmatrix} \quad (5.33)$$

or

$$\hat{\Pi} = \frac{1}{2}[d]^T[C][d] - [d]^T[F]$$

The stationary value for the functional satisfies

$$\frac{\partial \hat{\Pi}}{\partial [d]^T} = [C][d] - [F] = 0$$

such that

$$[d] = [C]^{-1}[F] \tag{5.34}$$

The matrices on the right hand side of equation (5.34) are known given the current geometry and compositional field of the microstructure and hence the degree of freedom matrix can be numerically calculated. The nodal velocities encapsulated in it can then be used to update the geometry of the interface boundary, and both the nodal fluxes and interface velocities can be used to update the constitution of the microstructure by using a suitable time step. The process can then be repeated. By solving the fundamental problem given by equation (5.34) it is hence possible to determine the subsequent evolution of the microstructure by integrating the lattice flux and interface velocity rates over the desired time interval. However, for elastically driven diffusion and interface migration, it is necessary to know the elastic field (given by equation (5.7)).

The variational microstructural model considered here relies on thermodynamic and kinetic parameters that must be determined externally. Parameters for the classes of microstructural evolution considered in this analysis include the free energies of stable and metastable phases, interfacial surface energies, lattice spacings, material property data and their dependence on local composition, self- and inter-diffusivities of components within individual phases and interface mobilities, all of which are derived from experimental investigations.

5.2.3 – Updating the Microstructure Description

The nodal fluxes and interface velocities can be used to determine the rate of change of composition at the elemental Gauss points (using equation (5.19)) and the composition across the finite element mesh can then be globally updated accordingly by selecting a suitable time step, Δt , so that

$$c_g(t + \Delta t) = c_g(t) + \frac{dc_g(t)}{dt} \Delta t \tag{5.35}$$

The interface nodal velocities can also be used to update the interface boundary description (position of the points located along the interface boundary) through

$$\begin{aligned}x_i(t + \Delta t) &= x_i(t) + v_{ni} m_{xi} \Delta t \\y_i(t + \Delta t) &= y_i(t) + v_{ni} m_{yi} \Delta t\end{aligned}\tag{5.36}$$

The time step can be calculated by limiting the change in composition or degree of interface movement per iteration. Each of these two methods are considered below.

(a) Time Step 1: Limited Change in Composition per Iteration

The time step can be calculated using a pre-defined maximum change in composition per iteration, Δc_{max} , and the maximum rate of change of composition for the current iteration, \dot{c}_{max} , through

$$\Delta t_1 = \frac{\Delta c_{max}}{\dot{c}_{max}}\tag{5.37}$$

where Δc_{max} is usually defined as being between 0.1 to 1.0% of the initial maximum change in composition defined across the microstructure (usually at phase boundaries).

(b) Time Step 2: Limited Interface Movement per Iteration

The time step can also be calculated based on a pre-defined maximum change in length of the interface elements, h_{max} .

5.3 – The Explicit and Implicit Time Integration Schemes

There are essentially two families of numerical integration schemes that can be used in computational analysis and are often referred to as being explicit or implicit. When a direct computation of the dependent variables is required, the dependent variables are defined by adapted sets of equations, which are then solved to obtain the solution. The numerical solution is said to be 'explicit' if the dependent variables are advanced a solution through a sequence of steps from an initial state to a final converged state.

5.3.1 – Explicit Schemes, Stability and Convergence

The primary reason for using explicit time integration is to allow for larger time steps. A simple explicit scheme will advance the solution through a sequence of steps from an initial state to a final converged state. The primary reason for using explicit time integration is to allow for larger time steps. A simple explicit scheme will advance the solution through a sequence of steps from an initial state to a final converged state.

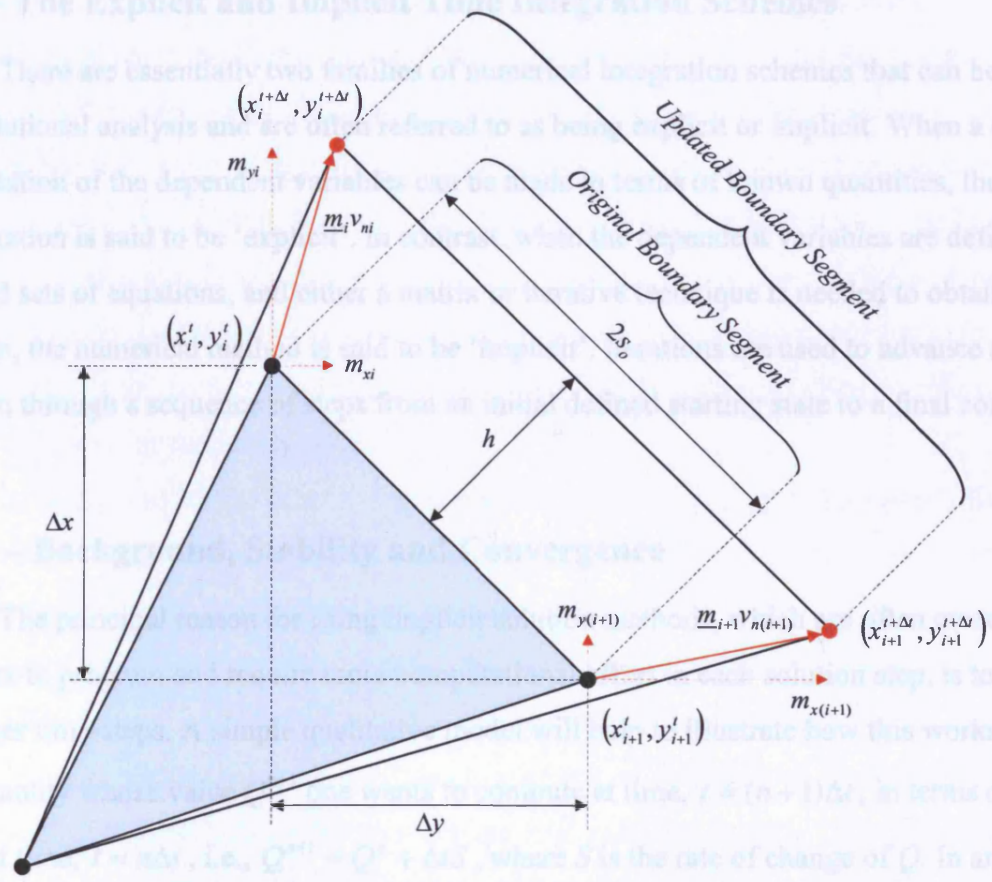


Figure 5.8 – Controlled extension of an interface element from time, ‘ t ’ to ‘ $t + \Delta t$ ’ (interface movement is exaggerated to illustrate the approach).

To first order, the relative rate of extension of the interface element shown in Figure 5.8 can be calculated from equation (5.29), and the time step can then be calculated from

$$\Delta t_2 = \frac{h_{\max}}{\dot{A}_{in}} \tag{5.38}$$

where h_{\max} is selected to control the maximum permissible extension of an interface element, which is typically selected such that $h_{\max} = 0.1\%$.

The microstructure description (global composition and location of the interface boundary) can be updated accordingly from the smallest explicit time step of Δt_1 and Δt_2 defined by equations (5.37) and (5.38) respectively. In some circumstances, an implicit time integration scheme can be implemented in order to increase the stability and speed of the solution process. This is addressed in the following section.

5.3 – The Explicit and Implicit Time Integration Schemes

There are essentially two families of numerical integration schemes that can be used in computational analysis and are often referred to as being explicit or implicit. When a direct computation of the dependent variables can be made in terms of known quantities, the computation is said to be ‘explicit’. In contrast, when the dependent variables are defined by coupled sets of equations, and either a matrix or iterative technique is needed to obtain the solution, the numerical method is said to be ‘implicit’. Iterations are used to advance a solution through a sequence of steps from an initial defined starting state to a final converged state.

5.3.1 – Background, Stability and Convergence

The principal reason for using implicit solution methods, which are often more complex to program and require more computational effort in each solution step, is to allow for larger time-steps. A simple qualitative model will help to illustrate how this works. Let Q be a quantity whose value Q^{n+1} one wants to compute at time, $t = (n + 1)\Delta t$, in terms of its value at time, $t = n\Delta t$, i.e., $Q^{n+1} = Q^n + \Delta t S$, where S is the rate of change of Q . In an explicit numerical method, S would be evaluated in terms of known quantities at the previous time step, n . An implicit method, in contrast, would evaluate some or all of the terms in S in terms of unknown quantities at the new time step, $n + 1$. Since new quantities then appear on both the left and right side of the Q -equation, it is said to be an implicit definition of the new $n + 1$ values. Usually a matrix or iterative solution must be used to compute the new quantities.

Numerical stability is related to the behaviour of the solution as the time-step, Δt , is increased. If the solution remains well behaved for arbitrarily large values of the time step, the method is said to be unconditionally stable. This situation never occurs with explicit methods, which are always conditionally stable. It is easy to see this by dividing the Q -equation by Δt and then letting Δt approach infinity. In this limit there are no $n+1$ terms remaining in the equation so no solution exists for Q^{n+1} , indicating that there must be some limit on the size of the time step for there to be a solution. In an implicit formulation, a solution for the unknowns at level $n + 1$ may be obtained for any size time step. Of course, the solution for very large times may not be realistic unless the implicit formulation has been very carefully constructed.

In the case of the explicit formulation of the diffusive problem, the matrix of the unknown variables at the new time is a square stiffness matrix, while the right-hand side of the system is dependent only on the variables at the previous times. This therefore leads to a trivial matrix inversion and hence to a solution with a minimal number of arithmetic operations for each time step. However, this advantage is counter-balanced by the fact that stability and convergence conditions impose severe restrictions on the maximum admissible time step. While this might not be a limitation for the physical problem, it leads to the necessity of a large number of steps in order to reach the final state solution corresponding to a physical time-independent problem.

In an implicit formulation, the matrix to be inverted is a modified square stiffness matrix where more than one set of variables are unknown at the same time level. In most cases, however, the structure of the matrix will be rather simple, allowing simple algorithms for the solution of the system at each time step, although the number of operations required will be higher when compared with explicit methods. This is compensated by the fact that the implicit method places less stability-related limitations on the time step, and hence a smaller number of iterations will be needed to reach the final equilibrium state. This means that the calculation time can be decreased, if required, without affecting the stability of the solution.

5.3.2 – Implementing the Implicit Integration Scheme

For an explicit time integration scheme, the global composition and interface boundary description are updated using

$$\begin{aligned} [c(t + \Delta t)] &= [c(t)] + [\dot{c}(t)]\Delta t \\ [x(t + \Delta t)] &= [x(t)] + [v_n(t)]\Delta t \end{aligned} \quad (5.39)$$

which uses the compositional and interface boundary values calculated at the previous time level, i.e. $c(t)$ and $v_n(t)$. In order to implement an implicit time integration scheme, equation (5.39) can be replaced by

$$\begin{aligned} [c(t + \Delta t)] &= [c(t)] + \left[(1 - \theta)[\dot{c}(t)] + \theta[\dot{c}(t + \Delta t)] \right] \Delta t \\ [x(t + \Delta t)] &= [x(t)] + \left[(1 - \theta)[v_n(t)] + \theta[v_n(t + \Delta t)] \right] \Delta t \end{aligned} \quad (5.40)$$

where θ is a constant within the range, $0 \leq \theta \leq 1$. If $\theta = 0$, the integration scheme acts fully explicit (and becomes identical to that of equation (5.39)), but if $\theta = 1$ then the scheme becomes fully implicit and essentially makes use of improved values of the interface velocities

and the rates of change of composition. In order to implement the implicit time integration scheme, extra information needs to be calculated in terms of the thermodynamic driving forces.

From equation (5.32), one can write the variational functional as

$$\begin{aligned}\hat{\Pi} &= \frac{1}{2}[d]^T[C][d] - [d]^T \left\{ [F] + \theta \left(\left[\frac{\partial F}{\partial c_g} \right] [\dot{c}] + \left[\frac{\partial F}{\partial x_{in}} \right] [v_n] \right) \right\} \\ &= \frac{1}{2}[d]^T[C'] [d] - [d]^T [F]\end{aligned}\quad (5.41)$$

where the modified global stiffness matrix can be written as

$$[C'] = [C] - 2\theta \begin{bmatrix} \left[\frac{\partial F}{\partial c_g} \right] [H^J]^T \\ \left[\frac{\partial F}{\partial x_{in}} \right] + \left[\frac{\partial F}{\partial c_g} \right] [H^x]^T \\ 0 \end{bmatrix}$$

The derivatives of the force matrices are calculated using finite differences as the algebraic derivatives are cumbersome. The derivative of the elastic stored energy driving force requires a large number of simultaneous linear equations to be solved for each nodal force derivative, and this is extremely expensive in computer time. As the implicit corrections are small in this case, these elastic terms are neglected for the implicit time integration analysis.

5.4 – Iterative Method for the Solution of Unknowns

The discretised finite element integrals for the solution of unknowns for both the elasticity (equation (5.7)) and the coupled diffusion and moving boundary problem (equation (5.34)) take the form of the general linear system equation

$$[A][x] = [b] \quad (5.42)$$

where $[x]$ represents the nodal displacements, $[u]$, for the elasticity problem and the general degree of freedom matrix, $[d]$, for the coupled diffusion and moving boundary problem. In both cases, the matrix, $[A]$, is a square symmetric matrix, which is positive definite (contains non-zero values on the leading diagonal) for the elasticity problem and non-positive definite for the diffusion and interface migration problem. In general, the unknowns within equation (5.42) cannot be readily computed by a full matrix solver since, although exact, the size of

matrix, $[A]$ can soon exceed the availability of conventional computer memory as the resolution of the finite element mesh is increased. Equation (5.42) is therefore computed using a sparse matrix iterative linear system solver (since the matrix, $[A]$ is sparse), which has a reasonably fast solution convergence rate and is computationally efficient (since only non-zero values are stored along with their position within the square matrix).

For the elasticity problem the preconditioned conjugate gradient method is used to solve for nodal displacements, while the Lanczos method is used to solve for the lattice fluxes and respective interface velocities.

5.5 – Non-Dimensional Analysis

For the description of multi-component diffusion and interface boundary migration to be as general as possible, it is necessary to seek an expression to the general variational functional that can be expressed in terms of dimensionless variables. Non-dimensional analysis is performed to simplify the act of comparing equation variables that are considered to be numerically similar. This is achieved by replacing each of the dimensional variables by the product of a constant reference parameter and a non-dimensional component. The dimensionless quantities are essentially dimensionless ratios comparing one quantity with another of the same kind and their numerical values are independent of the system of units employed. In order to ensure equal scaling of all terms included in the variational functional, non-dimensional analysis is therefore carried out.

The following system of units are introduced:

$\{\tau\}$ – unit of time

$\{L\}$ – unit of length

$\{w\}$ – unit of volumetric energy density

where the exact specification of the characteristic length, $\{L\}$, depends on the problem under consideration. All quantities used in the variational functional are written in terms of these dimensionless quantities such that

$$\begin{aligned}
 j &= \bar{j} \cdot \{L\} \{\tau\}^{-1} \\
 t &= \bar{t} \cdot \{\tau\} \\
 v_n &= \bar{v}_n \cdot \{L\} \{\tau\}^{-1} & [H] &= [\bar{H}] \cdot \{L\}^2 \\
 g &= \bar{g} \cdot \{w\} & [K] &= [\bar{K}] \cdot \{L\}^2 \\
 \gamma_s &= \bar{\gamma}_s \cdot \{w\} \{L\}^{-1} & [E] &= [\bar{E}] \cdot \{L\} \\
 V &= \bar{V} \cdot \{L\}^2
 \end{aligned}$$

where x can be defined as the real numerical value and \bar{x} is the dimensionless quantity used in the model. Non-dimensionalising all terms within the variational functional of equation (5.33) gives

$$\hat{\Pi} = \frac{1}{2} \begin{bmatrix} \bar{j} \\ \bar{v}_n \\ \lambda \end{bmatrix}^T \begin{bmatrix} \frac{\bar{K}}{\mathcal{D}} \frac{\{L\}^4}{\{\tau\}^2} & 0 & \frac{M}{2} \\ 0 & \frac{\bar{E}}{M_{in}} \frac{\{L\}^3}{\{\tau\}^2} & \frac{L}{2} \\ \frac{M}{2} & \frac{L}{2} & 0 \end{bmatrix} \begin{bmatrix} \bar{j} \\ \bar{v}_n \\ \lambda \end{bmatrix} - \begin{bmatrix} \bar{j} \\ \bar{v}_n \\ \lambda \end{bmatrix}^T \begin{bmatrix} [\bar{H}_j][\bar{F}_{pj} + \bar{F}_{ec}] \frac{\{w\} \{L\}^2}{\{\tau\}} \\ ([\bar{F}_{pv} + \bar{F}_{cin} + \bar{F}_{in}] + [\bar{H}_x][\bar{F}_{pj} + \bar{F}_{ec}]) \frac{\{w\} \{L\}^2}{\{\tau\}} \\ 0 \end{bmatrix}$$

Let, $\bar{\Pi} = \frac{\hat{\Pi} \{\tau\}}{\{w\} \{L\}^2}$, so

$$\bar{\Pi} = \frac{1}{2} \begin{bmatrix} \bar{j} \\ \bar{v}_n \\ \lambda \end{bmatrix}^T \begin{bmatrix} \frac{\bar{K}}{\mathcal{D}} & 0 & \frac{M}{2} \\ 0 & \frac{\bar{E}}{M_{in}} & \frac{L}{2} \\ \frac{M}{2} & \frac{L}{2} & 0 \end{bmatrix} \begin{bmatrix} \bar{j} \\ \bar{v}_n \\ \lambda \end{bmatrix} - \begin{bmatrix} \bar{j} \\ \bar{v}_n \\ \lambda \end{bmatrix}^T \begin{bmatrix} [\bar{H}_j]^T [\bar{F}_{pj} + \bar{F}_{ec}] \\ [\bar{F}_{pv} + \bar{F}_{cin} + \bar{F}_{in}] + [\bar{H}_x][\bar{F}_{pj} + \bar{F}_{ec}] \\ 0 \end{bmatrix}$$

$$\bar{\Pi} = \frac{1}{2} [\bar{d}]^T [\bar{C}] [\bar{d}] - [\bar{d}]^T [\bar{F}] \tag{5.43}$$

where

$$\bar{\mathcal{D}} = \mathcal{D} \frac{\{w\} \{\tau\}}{\{L\}^2} \quad \bar{M}_{in} = M_{in} \frac{\{w\} \{\tau\}}{\{L\}} \tag{5.44}$$

The variational functional is now completely non-dimensional, allowing all terms within the variational functional to be independent of the system of units employed and have a similar order of scaling.

6.0 – Numerical Implementation

This chapter describes the general structured and unstructured grids which can be generated during the finite element discretisation process and describes the mesh adaption technique used for modelling moving boundary-type problems.

6.1 – Structured Grids

Structured meshes are comprised of an assembly of regular cells, where all the cells have a fixed number of neighbouring cells that are arranged in a cartesian co-ordinate system. The regular cells are numbered consecutively along the orthogonal axes of the coordinate system, with equal spacing defined between each cell. A structured grid means that the elements are well ordered and a simple scheme can be used to label elements and identify neighbours.

All of the major discretisation methods available can be performed based on structured grids without too much difficulty and can be implemented in a computationally efficient manner. However, a disadvantage of using structured domains is that it is not well suited to the solution of highly complex geometries and, for this reason, it may not always be possible to generate an acceptable grid. One solution to this problem is to further sub-divide the domain into smaller regions and generate a grid for each region, which is known as generating 'multi-grids'. The grids can then be re-combined to give the required global solution. Structured grids can suffer from highly skewed cells when trying to model curved or irregular surfaces. The skewed cells have disproportionate dimensions with one axis being several times larger than the other, which can produce inaccuracies in the solution. The simplest structured grid is generated from a square box by subdividing it into a set of regular elements whose faces are parallel to the faces of the box as shown in Figure 6.1.

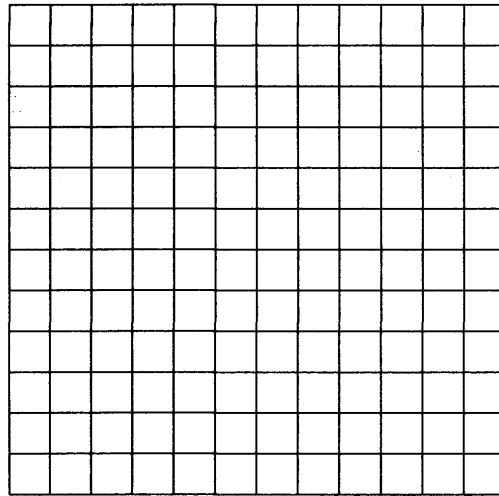


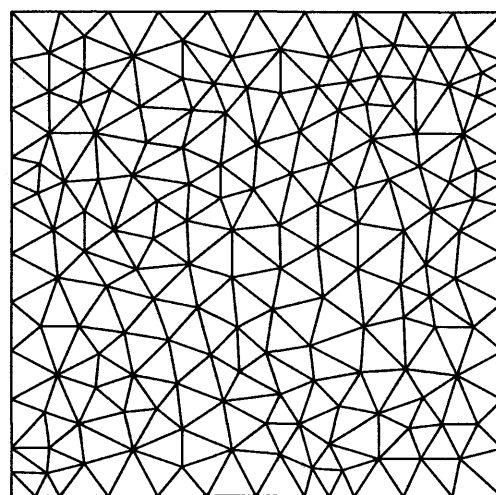
Figure 6.1 – Example of a structured grid of a regular domain.

Regular meshes are efficient in terms of both computation and storage and are mainly used in finite difference discretisations. However, it is not always possible to create high-quality structured meshes for complex domains, and in such cases unstructured meshes must be used.

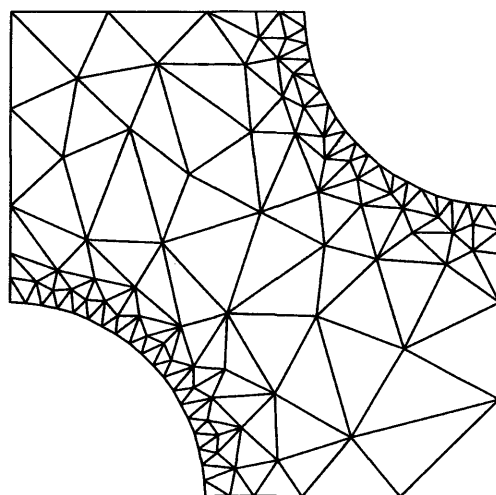
6.2 – Unstructured Grids

An unstructured grid differs from a structured grid in the sense that there is no inherent structure based on an underlying co-ordinate system. An unstructured grid can consist of triangular, quadrilateral, hexagonal or octagonal elements in two-dimensions, or tetragonal or cubical elements in three-dimensions. In unstructured grids, elements can be joined in any manner and do not necessarily have a constant number of neighbouring elements, so special lists must be kept in order to identify neighbouring elements. There is no concept of directionality to an unstructured grid, so therefore methods applicable to a structured grid system cannot be used. Unstructured grids have the advantage of generality in that they can be made to conform to almost any desired geometry. Unstructured grids require more information to be stored and recovered than structured grids (e.g. the neighbour connectivity list), which incurs a memory and computation cost. Figure 6.2 shows an example of an unstructured mesh of a regular and irregular domain.

Unstructured grids are typically generated using *Delaunay* triangulation based techniques [1]. A Delaunay triangulation of a point set is a triangulation whose vertices are the point set, having the property that no point in the point set falls in the interior of the circumcircle (circle that passes through all three vertices) of any triangle in the triangulation. A conforming Delaunay triangulation is a true Delaunay triangulation in which each segment may have been sub-divided into several edges by the insertion of additional points. These inserted points are necessary to allow the segments to exist in the mesh while maintaining the Delaunay property.



(a)



(b)

Figure 6.2 – Example of an unstructured mesh of (a) a regular domain and (b) an irregular domain.

In summary, the best choice for a grid system depends on several factors such as: convenience in generation; memory requirements; numerical accuracy; flexibility to conform to complex geometries and flexibility for localised regions of high or low resolution. Even when automatic grid generators are employed, there are requirements for users to supply data to control the number and type of elements, their connectivity, aspect ratios and other essential features. In general, the generation of a geometry conforming grid can consume a significant amount of time and effort.

The C program 'Triangle' [1] is used for two-dimensional quality mesh generation and construction of Delaunay triangulations for all two-dimensional finite element simulations considered in this thesis. See Appendix C for a general description of the data required to generate a two-dimensional finite element mesh.

6.3 – Two-Dimensional Mesh Adaption

The mesh adaption technique is a powerful tool which alleviates some of the complexities relating to the modelling of moving boundary type systems. Although mesh adaption does not address the crucial time-consuming issues of geometry set up, it automates the process of adjusting the mesh to fit the geometric characteristics of the problem. Local mesh adaption can be easily applied to unstructured grids due to their inherent flexibility and are ideal for problems involving moving bodies. However, it is desirable that no very large or small angles are generated in order to minimise the distortion of the finite element mesh. Through mesh adaption, changes of the position of the interface with time do not always require complete regeneration of the finite element mesh. As the interface traverses through the system, the finite element mesh is adapted to fit the new geometry of the interface points, but in order to ensure that the interface elements do not become too distorted, upper and lower angle constraints are placed on these finite elements.

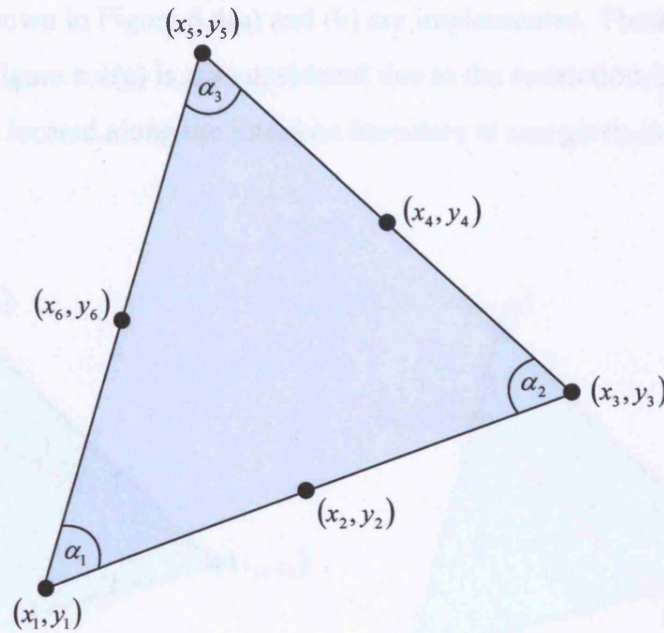


Figure 6.3 – The angles, α_1 , α_2 and α_3 are calculated to ensure that the finite element, located local to the interface boundary, does not become too distorted such that the solution is affected.

Considering Figure 6.3, the angles α_1 , α_2 and α_3 are required to be above a certain value to ensure that the distortion of the interface elements is not excessive. Babuska and Aziz [39] show that the accuracy of the finite element solution degrades as the maximum angle approaches 180° . To maintain the quality of the finite element solution, mesh adaption is not performed where all angles, α , lie within the range $20.0^\circ < \alpha < 160.0^\circ$. These upper and lower angle constraints were selected through consideration that the finite element mesh is typically generated using a minimum meshing angle of approximately 25.0° . If an angle is found to exist outside this range, then one or more near interface elements are identified as being distorted, the composition is mapped to a structured underlying grid and the finite element mesh is regenerated. The composition is then mapped back to the new finite element mesh from the underlying grid, and the process of mesh adaption then continues. More details regarding this are provided in section 9.3.

The unstructured finite element mesh is generated using a triangulation algorithm [1], which is used to generate either first or second order triangular elements, which are then used for the basis of elemental adaption. During mesh adaption, the elemental nodes located along the interface boundary are only permitted to move, and the single and two node element

adaptation methods shown in Figure 6.4(a) and (b) are implemented. Three noded finite element adaptation shown in Figure 6.4(c) is not considered due to the restriction that only one finite element edge can be located along the interface boundary at any given instant in time.

series of four one-dimensional finite elements as shown in Figure 6.5. The nodal strain values can be averaged across the mesh such as to provide a smooth continuous strain field. The finite element can be regenerated and refined if the strain is to be a large difference between the continuous and discontinuous fields at a particular point or area within the finite element.

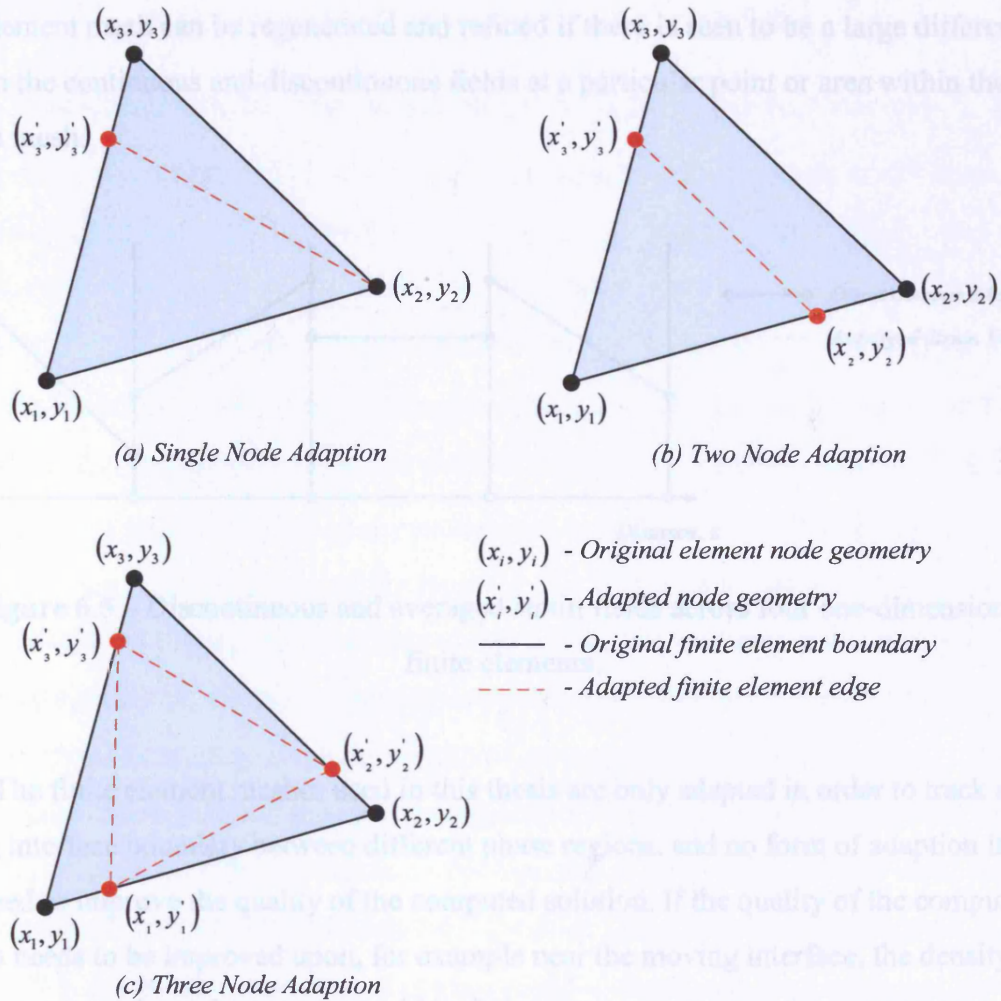


Figure 6.4 – Finite element nodal adaption techniques.

7.0 – Numerical Validation

An unstructured finite element mesh can also be adaptively refined in order to ensure or improve the quality of a computed solution. Consider the discontinuous strain field across a series of four one-dimensional finite elements as shown in Figure 6.5. The nodal strain values can be averaged across the mesh such as to provide a smooth continuous strain field. The finite element mesh can be regenerated and refined if there is seen to be a large difference between the continuous and discontinuous fields at a particular point or area within the finite element mesh.

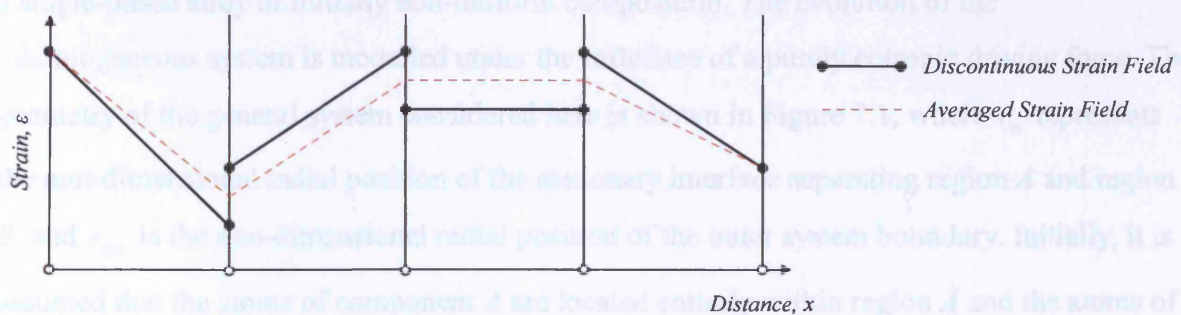


Figure 6.5 – Discontinuous and averaged strain fields across four one-dimensional finite elements.

The finite element meshes used in this thesis are only adapted in order to track a moving interface boundary between different phase regions, and no form of adaption is performed to improve the quality of the computed solution. If the quality of the computational solution needs to be improved upon, for example near the moving interface, the density of the finite element mesh can be increased within this region.

7.0 – Numerical Validation

This section provides a bench-test for the model described in the previous sections of this thesis. The computational solution is compared with a known analytical solution in order to validate the numerical code and finite element model, and to attempt to illustrate the potential capabilities and innovative approach integrated into the model.

7.1 – Two-Dimensional Finite Element Diffusion due to Entropy

In order to validate the general numerical model, attention is given to diffusion within a single-phase alloy of initially non-uniform composition. The evolution of the inhomogeneous system is modelled under the influence of a purely entropic driving force. The geometry of the general system considered here is shown in Figure 7.1, where r_{in} represents the non-dimensional radial position of the stationary interface separating region A and region B , and r_{sys} is the non-dimensional radial position of the outer system boundary. Initially, it is assumed that the atoms of component A are located entirely within region A and the atoms of component B are located entirely within region B . An equilibrium concentration of vacancies is assumed within both regions. It must be noted that whenever the atoms of A diffuse from region A into region B , there is an equal and opposite flux of atoms of component B such that

$$j = j_A = -j_B$$

For simplicity, the diffusional flux of component A only need be considered and the site fraction, c , is taken to be the site fraction of component A from which the site fraction of component B can be readily determined, i.e. $c_B \approx 1 - c$. The state shown in Figure 7.1 is the state at which the system is considered to have a well-ordered atomic arrangement and its lowest degree of entropy.

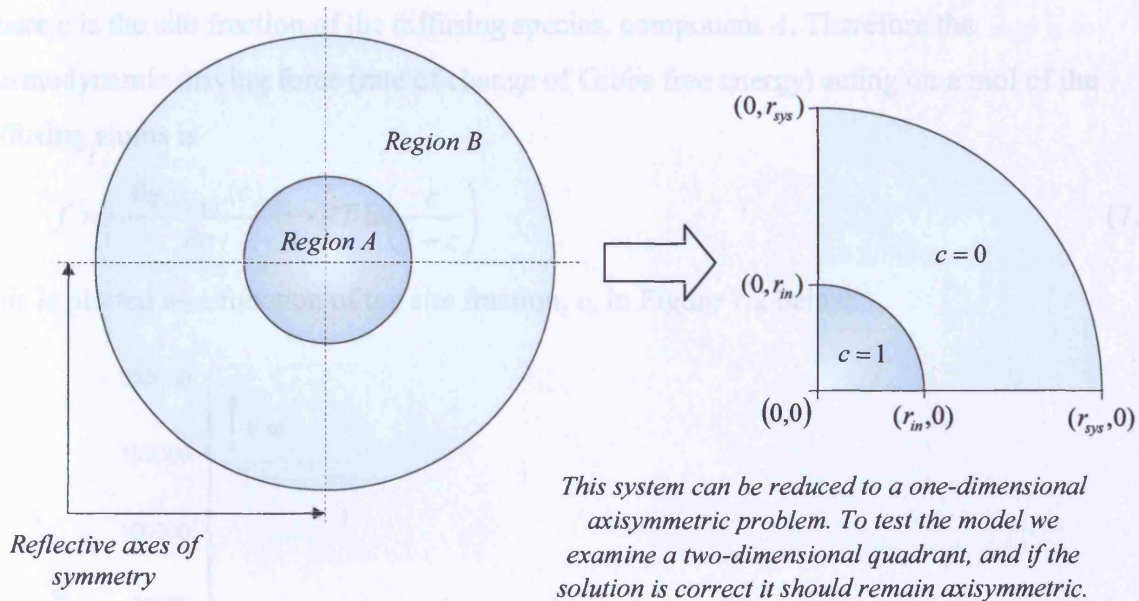


Figure 7.1 – Investigating the entropic evolution of a single phase alloy of initially non-uniform composition.

In order to correctly set up the two-dimensional finite element mesh for the system shown in Figure 7.1, it is necessary to make use of any existing axes of symmetry in order to reduce computational time and resources. It is assumed that the system is two-fold symmetric, which implies that only a single quadrant of the system need be considered. Within the quadrant, the boundaries of symmetry are constrained such that there is no flux field in the direction normal to the system boundaries.

7.1.1 – Thermodynamic Driving Force due to Entropy

A system will evolve in order to achieve a state of thermodynamic equilibrium, a state in which the properties do not change with time. For a purely entropic system in a state of thermodynamic equilibrium of known atomic configuration, the entropy is greater than that of any other state with the same energy. At such a state, with given pressure and temperature, the Gibbs free energy is smaller than that of any other state with the same pressure and temperature.

The entropic contribution to the Gibbs free energy per unit volume of the system shown in Figure 7.1 can be described by equation (3.9), written as

$$g_{entropy}(c) = RT(c \ln c + (1 - c) \ln(1 - c))$$

where c is the site fraction of the diffusing species, component A . Therefore the thermodynamic driving force (rate of change of Gibbs free energy) acting on a mol of the diffusing atoms is

$$f = -\frac{\partial g_{entropy}(c)}{\partial c} = -RT \ln\left(\frac{c}{1-c}\right) \quad (7.1)$$

This is plotted as a function of the site fraction, c , in Figure 7.2 below.

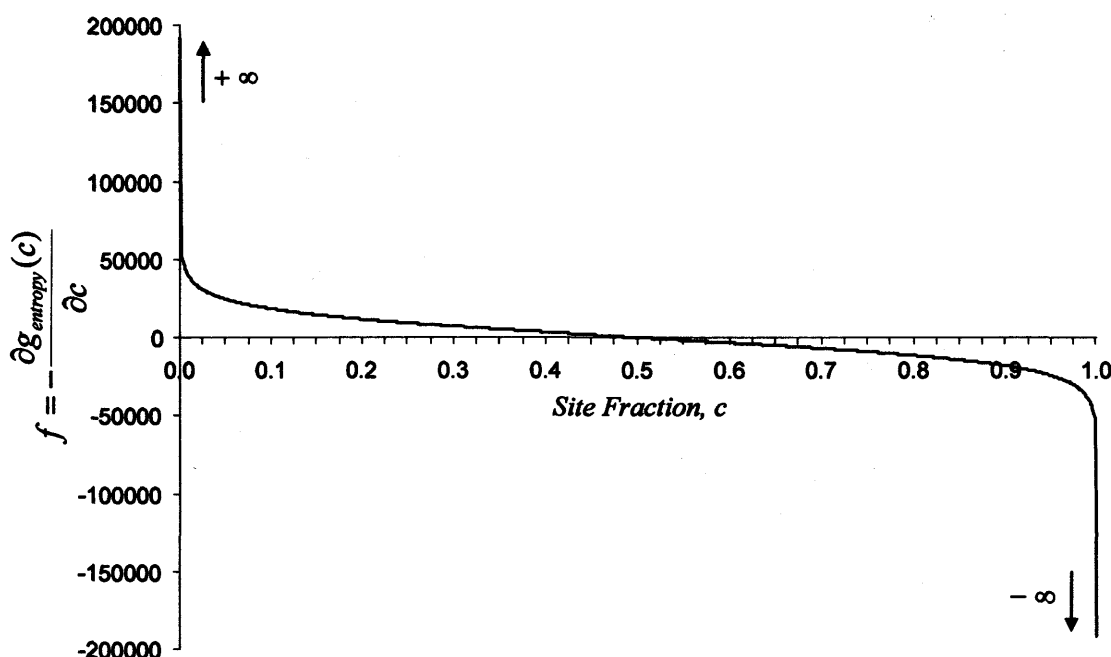


Figure 7.2 – Graph showing how the variation of the driving force due to entropy with site fraction at a temperature of 1000K.

It can be seen that as the site fraction approaches zero or unity, the thermodynamic driving force becomes infinite. This provides a large entropic driving force for the atoms to diffuse away from these compositional states and ensures that the site fraction remains between zero and one. Initially, $c = 1$ and $c = 0$ within regions A and B respectively, so it was necessary to truncate the driving force f such that it is not infinite.

7.1.2 – Computational Finite Element Results

The resultant entropic evolution of the microstructure can be modelled by the composition defined at the elemental Gauss points. The lattice flux field was modelled by a quadratic interpolation function over a mesh of 1,577 six-noded quadratic-type finite elements. The resultant evolution of the microstructure under the influence of entropy is

shown in Figure 7.3. An explicit time integration scheme was used and the time step was calculated based on a maximum change in composition per iteration of 0.1%.

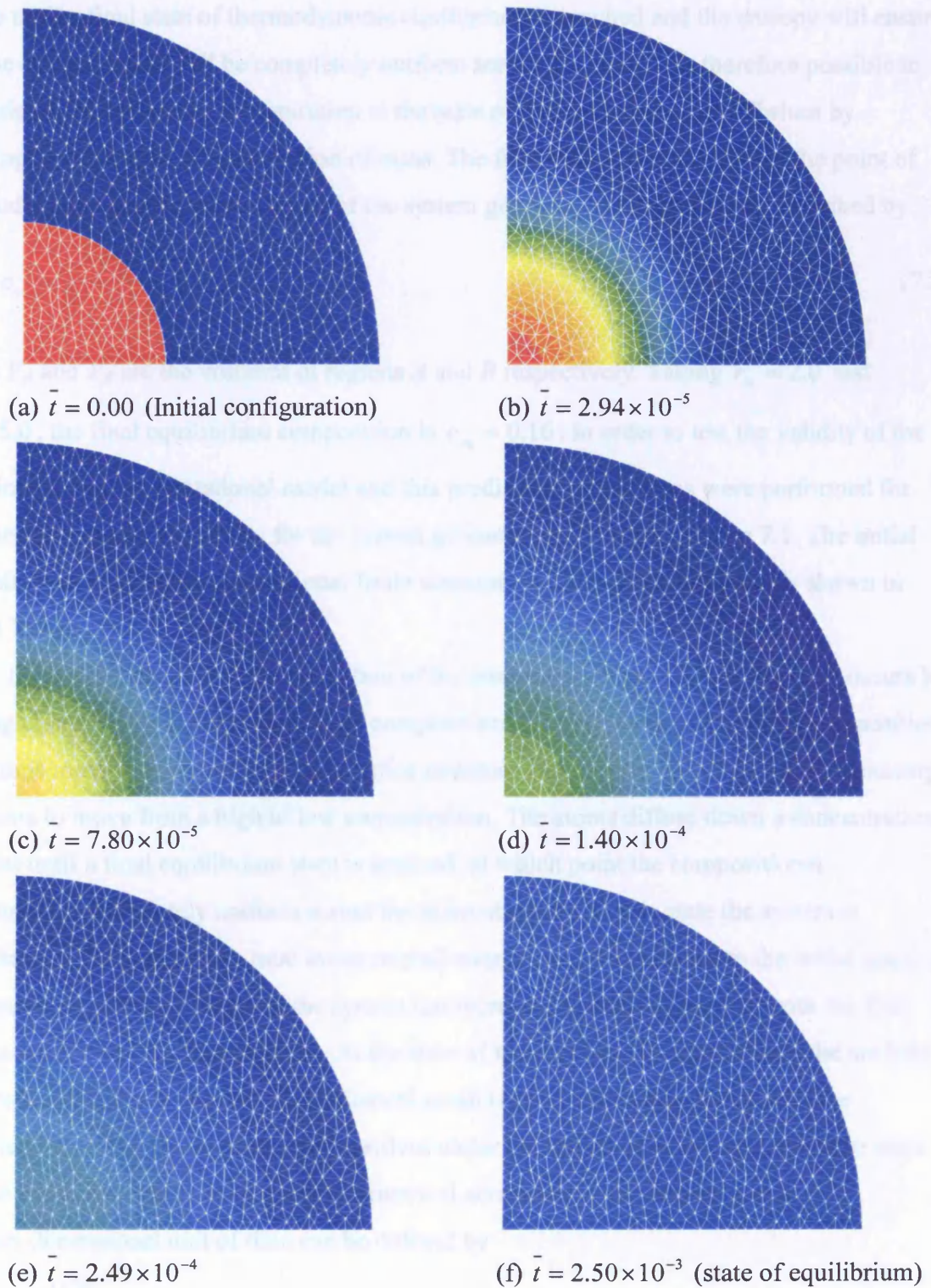


Figure 7.3 – Evolution of the microstructure due to entropic driving forces with the composition defined across a fixed mesh of 1,577 six-noded finite elements.

7.1.3 – Discussion of Finite Element Results

Mass must be conserved at all times during the process of diffusion. A system will evolve until a final state of thermodynamic equilibrium is reached and the entropy will ensure that the concentration will be completely uniform across the body. It is therefore possible to theoretically calculate the concentration at the state of thermodynamic equilibrium by applying the principle of conservation of mass. The final compositional state at the point of thermodynamic equilibrium in terms of the system geometry can therefore be described by

$$c_{eq} = \frac{V_A}{(V_A + V_B)} = \frac{\overline{r}_{in}^{-2}}{\overline{r}_{sys}^{-2}} \quad (7.2)$$

where V_A and V_B are the volumes of regions A and B respectively. Taking $\overline{r}_{in} = 2.0$ and $\overline{r}_{sys} = 5.0$, the final equilibrium composition is $c_{eq} = 0.16$. In order to test the validity of the two-dimensional computational model and this prediction, simulations were performed for diffusion purely due to entropy for the system geometry described by Figure 7.1. The initial geometry was meshed by conventional finite element meshing procedures and is shown in Figure 7.3(a).

Figure 7.3 shows that the relaxation of the concentration gradient in the alloy occurs by moving atoms out of the regions of high composition and into the regions of low composition. The atoms move around within a rigid lattice structure and there is initially a net flux causing the atoms to move from a high to low concentration. The atoms diffuse down a concentration gradient until a final equilibrium state is attained, at which point the compositional distribution is completely uniform across the microstructure. In this state the system is considered to have attained a total lower overall energy state with respect to the initial starting configuration, and the entropy of the system has increased in good agreement with the first and second laws of thermodynamics. At the state of thermodynamic equilibrium, the uniform compositional value across the finite element mesh is in excellent agreement with the predicted value. As the microstructure evolves under the influence of entropy, it can be seen that the compositional field remains symmetrical across the finite element mesh.

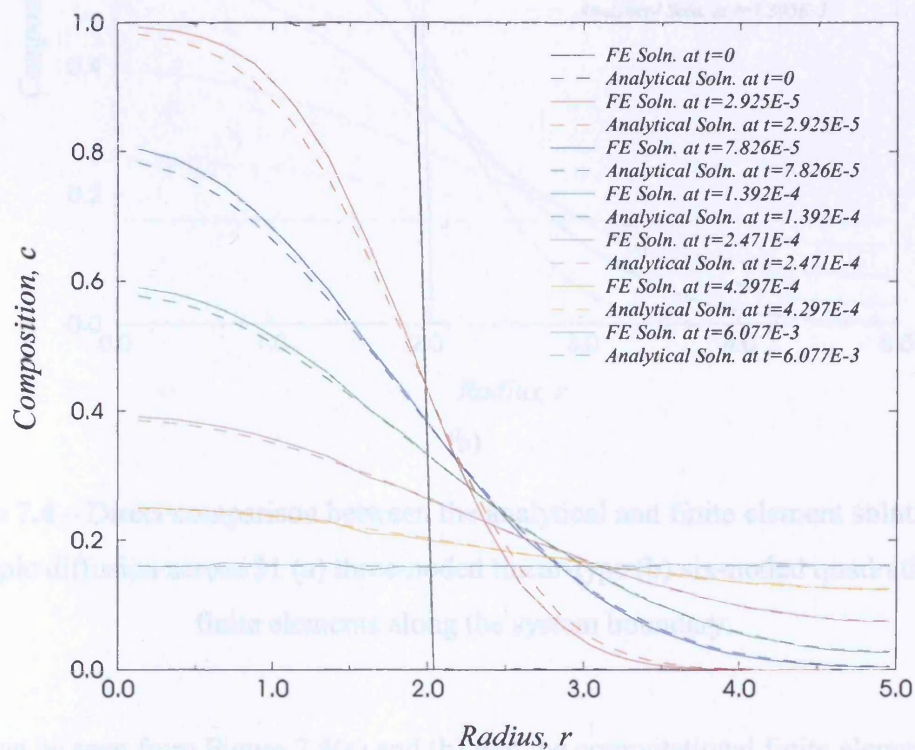
The non-dimensional unit of time can be defined by

$$\tau = \frac{\{L\}^2}{\{w\}D}$$

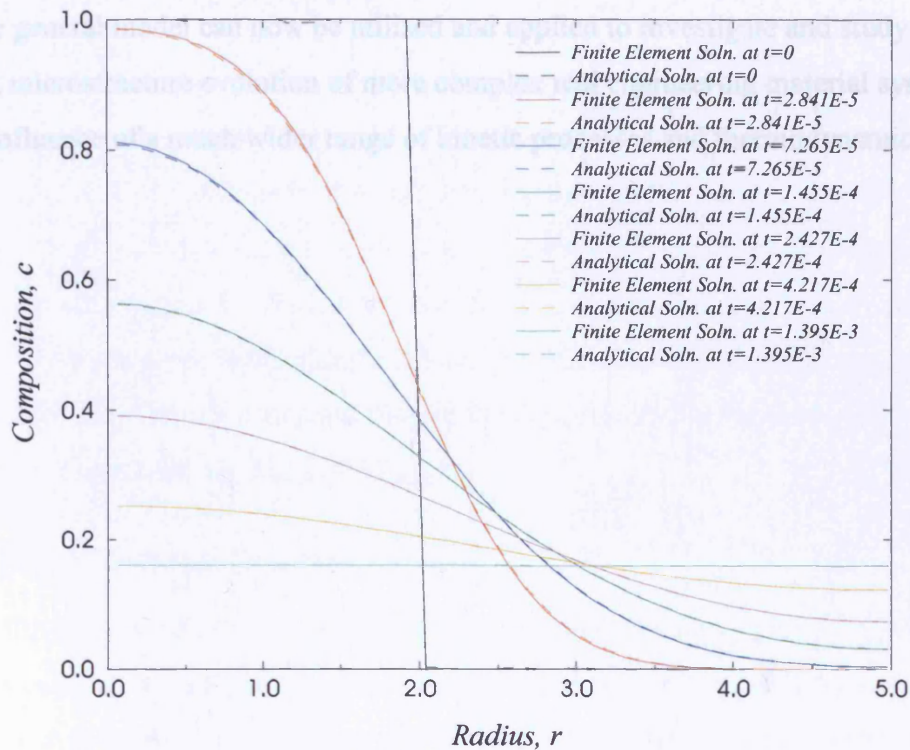
where the non-dimensional diffusivity is taken to be unity (see section 5.5).

7.2 – Validating the Finite Element Solution

In order to test the validity of the two-dimensional computational model, the finite element solution for diffusion purely due to entropy was directly compared with the analytical solution (derived in Appendix D). The three-noded and six-noded finite element results for the evolution of an initial step change in composition due to entropy are compared with the analytical results as shown in Figure 7.4(a) and (b) respectively.



(a)



(b)

Figure 7.4 – Direct comparison between the analytical and finite element solutions for entropic diffusion across 31 (a) three-noded linear-type (b) six-noded quadratic-type finite elements along the system boundary.

It can be seen from Figure 7.4(a) and (b) that the computational finite element solution follows the exact analytical solution very closely, especially when a higher order shape function is selected. A more accurate finite element solution could be obtained by further reducing the time step per iteration, or by implementing an implicit time integration scheme into the two-dimensional model, which would considerably aid the speed of solution generation. Figure 7.4(a) and (b) therefore validate the general model (without a moving boundary) behind the finite element solution for entropic diffusion within the two-dimensional system of Figure 7.1. The initial ripples that can be observed in the analytical solution at time $t = 0$ are due to approximating an infinite series (see equation (D.2) in Appendix D) by a finite number of terms.

The general model can now be utilised and applied to investigate and study the subsequent microstructure evolution of more complex real engineering material systems, under the influence of a much wider range of kinetic processes and thermodynamic driving forces.

8.0 – Substitutional Diffusion with no Interface

In this section, the general model is used to simulate the microstructure evolution of the InGaAs III-V semiconductor system. The InGaAs system is of interest due to the fact that it consists of a single phase, possesses a high mismatch strain (for an InAs inclusion within a GaAs matrix ($\text{In}_c\text{Ga}_{1-c}\text{As}$), $\varepsilon_T(c) = 6.7c\%$), and there are only two relevant components to consider in the substitutional diffusive process (Indium, In and Gallium, Ga). In this case, particular attention is given to the effect of elastic strain on the diffusional rearrangement of material in the body. There are no phase boundaries to consider but the elastic stored energy is a function of composition, i.e. $U_{elastic} = U_{elastic}(c)$.

8.1 – A Real Material System: InGaAs

The InGaAs system is a commonly used semiconductor alloy, which is primarily used in the semiconductor industry in many optoelectronic devices. Although InAs and GaAs are predicted not to intermix, it is found in these devices that substantial inter-diffusion occurs between them. This is thought to happen to relieve the large internal strains that are present in such devices, which affects the electronic properties of the device. The electronic properties of the material are strain dependent and hence devices can be strain engineered in this fashion. However, the material system will naturally wish to evolve to relax this strain if there is a process by which it can do so. It is this relaxation process, which is not normally beneficial to the device, which is considered here. Further understanding of the effect of strain on the inter-diffusion of InAs and GaAs is of particular interest.

The InGaAs system has a zincblende structure, in which one face-centred cubic (fcc) lattice is entirely occupied by Arsenide atoms and a mixture of Indium and Gallium atoms occupies the other fcc lattice. The InGaAs structure is illustrated in Figure 8.1. In the analysis, it is assumed that all the main lattice sites are filled, i.e. there are no filled interstitial sites, and the diffusive mechanism is a substitutional one. The species diffuse on their separate fcc lattices, so the only lattice of interest, therefore, is the InGa lattice as the composition of the As lattice does not change. The state of the alloy can therefore be represented by a single state variable, c , taken to be the fraction of Indium atoms in the InGa fcc sublattice.

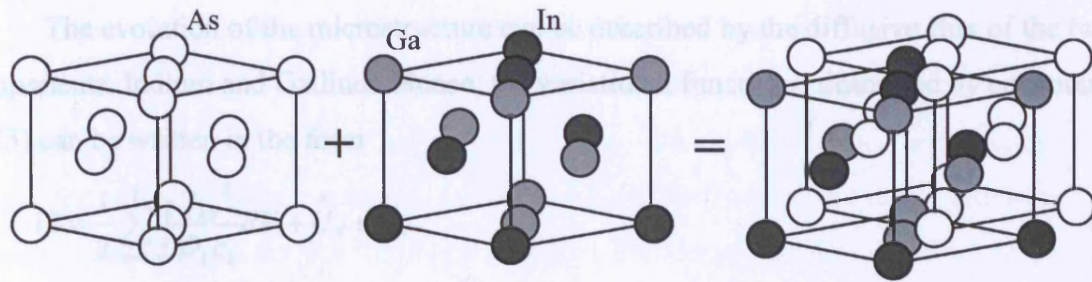


Figure 8.1 – The zincblende structure of InGaAs consisting of two interpenetrating fcc lattices.

The spherically symmetric problem of a small spherical particle of InAs embedded in a GaAs matrix is considered as shown in Figure 8.2. The abrupt interface between the particle and the matrix is taken to be coherent such that the particle composed of the larger InAs crystal lattice is in compression. The system shown in Figure 8.2 can be reduced to a one-dimensional axisymmetric problem.

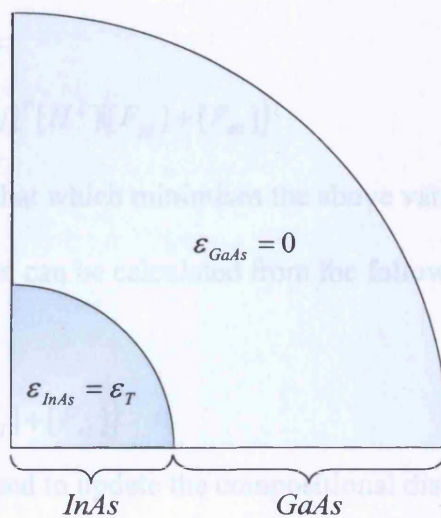


Figure 8.2 – Modelling a small spherical particle of InAs (subject to a transformation strain, ϵ_T) embedded in a GaAs matrix.

8.2 – The Variational Model

The evolution of the microstructure can be described by the diffusive flux of the two components, Indium and Gallium. Hence, the variational functional described by equation (4.23) can be written in the form

$$\Pi = \frac{1}{2} \sum_{k=1}^2 \int_V \frac{j_{k\alpha}^2}{\mathcal{D}_k c_k} dV + \dot{U}_e + \dot{G}_c \quad (8.1)$$

where \dot{G}_c is the rate of change of phase energy and \dot{U}_e is the rate of change of elastic stored energy. This is essentially the same problem as considered in the previous chapter, but with elastic stored energy and a more complicated expression for the compositional phase energy. For simplicity, it is assumed that the vacancy concentration is small and constant such that the composition of the system can simply be represented by a single state variable, $c = c_{In}$ such that $c_{Ga} \approx 1 - c$, and $j_\alpha = j_{In \alpha} = -j_{Ga \alpha}$. A constant lattice diffusivity is also assumed such that $\mathcal{D} = \mathcal{D}_{In} = \mathcal{D}_{Ga}$ and equation (8.1) can be simplified to

$$\Pi = \frac{1}{2} \int_V \frac{j_\alpha^2}{\mathcal{D}c(1-c)} dV + \dot{U}_e + \dot{G}_c \quad (8.2)$$

and written in matrix form as

$$\Pi = \frac{1}{2\mathcal{D}} [j]^T [K] [j] - [j]^T [H^j] ([F_{pj}] + [F_{ec}])$$

The actual flux field will be that which minimises the above variational functional such that,

$\frac{\partial \Pi}{\partial [j]^T} = 0$. Thus the flux field can be calculated from the following system of simultaneous

linear equations

$$[j] = 2\mathcal{D}[K]^{-1}[H^j]([F_{pj}] + [F_{ec}]) \quad (8.3)$$

which can consequently be used to update the compositional distribution using a suitable time integration scheme. For the system under consideration, it is assumed that the geometry remains unchanged and that the only variable is the Indium composition, which is a function of the position in the body. The body is meshed uniformly and one-dimensional type finite elements were used.

8.3 – The InGaAs Phase Separation

Below a critical temperature, this material system is characterised by a phase separation in which two differently composed InGaAs alloys are observed to exist. The origin behind this phase separation has been investigated by Mohri [40] who has proposed that it occurs due to the difference in natural lattice spacing of the In and Ga atoms as they are constrained to fit into the same fcc lattice structure. If allowed to relax, an fcc unit cell would distort under these conditions. Mohri has derived an internal elastic energy contribution due to the constraint on the crystalline structure (this should not be confused with the bulk elastic energy discussed in sections 4.2.4(c) and 5.2.2(c)(ii)). The calculated phase energy driving force (the chemical potential), $\frac{\partial G_c}{\partial c}$, as a function of composition is shown with and without the Mohri internal energy contribution in Figure 8.3 at a temperature of 250°C. Below about 500°C a phase separation is expected to occur.

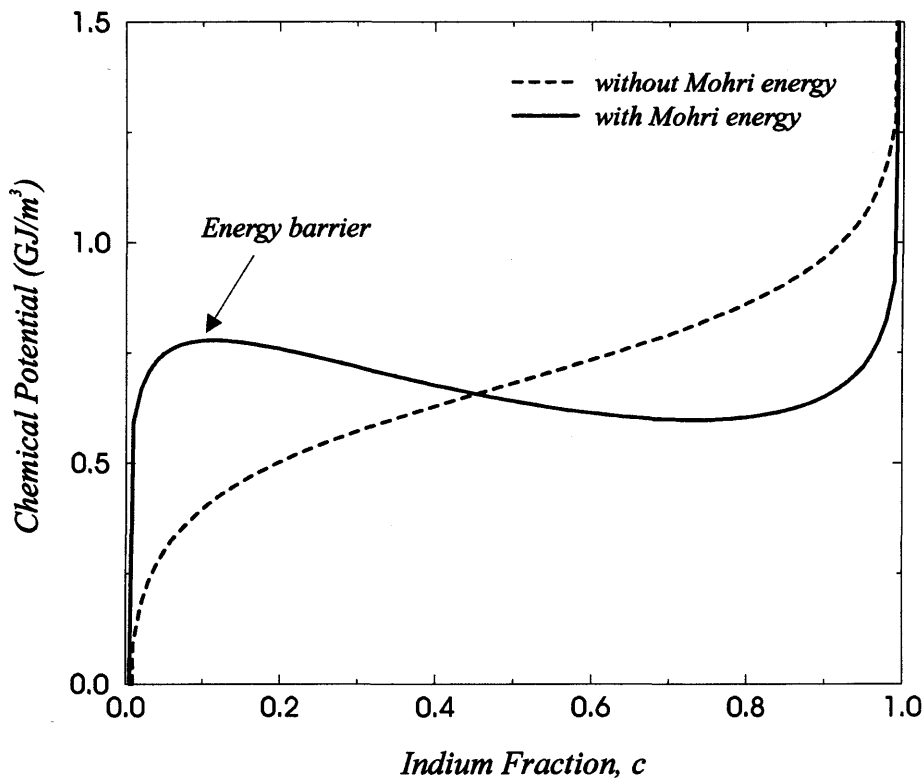


Figure 8.3 – Graph showing the relationship between the chemical potential and the Indium composition for an $\text{In}_c\text{Ga}_{1-c}\text{As}$ alloy at a temperature of 250°C. The theoretically derived Mohri internal energy contribution is the origin of the observed phase separation at this temperature.

It is clear from Figure 8.3 that for the case without the Mohri internal energy, the entropy terms will drive the phases to mix completely to produce a homogeneous alloy. However, with the Mohri energy penalty for mixing, there is a definite energy barrier to be crossed for mixing to occur. This energy barrier is proposed to be the origin of the phase separation and restricts the solubility of the InAs and GaAs.

8.4 – Computational Finite Element Results and Analysis

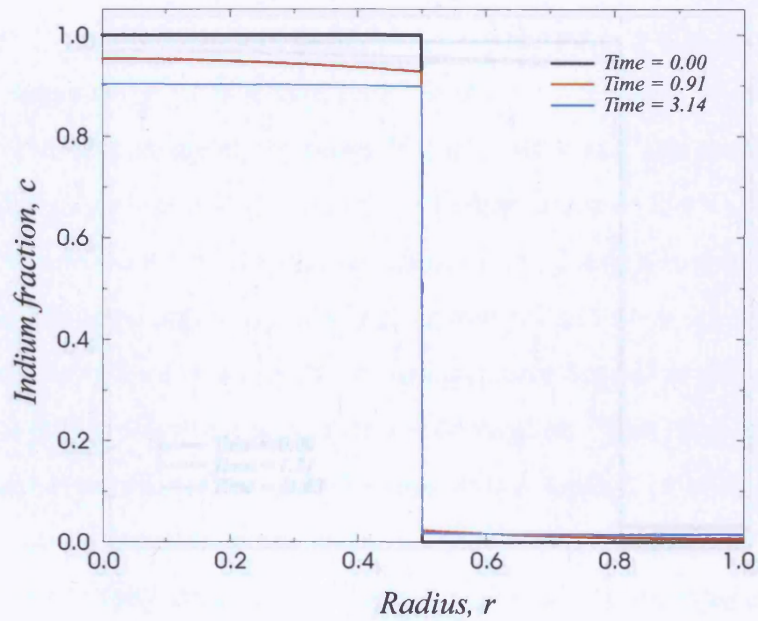
It is of interest to investigate the effect of the material microstructure on the evolution of this material system. The nodal displacements and lattice flux field were calculated as described in chapter 5, with the position of the outer system boundaries fixed and assuming zero surface flux normal to the system boundaries. The radial distance and time were non-dimensionalised with respect to the radius of the boundary, R , and the characteristic time,

$\tau = \sqrt{\frac{10^9 R^5}{D}}$. Different energy contributions (phase energy density and elastic stored energy)

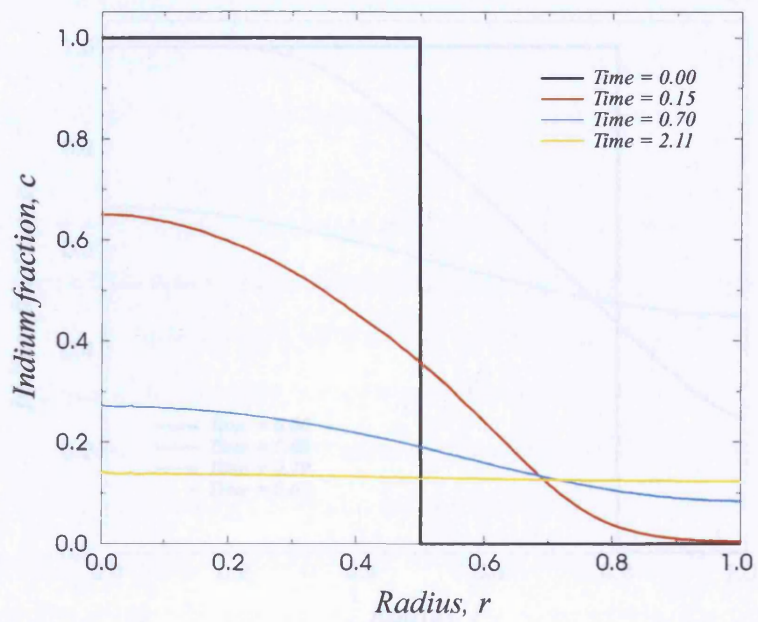
were incorporated into the computational model to investigate the individual contribution from each driving force on the net process of diffusional rearrangement and microstructural evolution of $\text{In}_c\text{Ga}_{1-c}\text{As}$.

The graphs shown in Figure 8.4(a) and (b), and Figure 8.5(a) and (b) show a representation of the finite element compositional results obtained for the $\text{In}_c\text{Ga}_{1-c}\text{As}$ spherical system at a temperature of 250°C for two different initial InAs volume fractions. In all cases the Mohri internal energy is included in the calculations.

The results were generated using a second order implicit time integration scheme with no mis-match strain applied (see Figure 8.4(a) and Figure 8.5(a)) and with mis-match strain applied, such that $\epsilon_T(c) = 6.7c\%$ (see Figure 8.4(b) and Figure 8.5(b)). The material parameters used in this analysis are given in Appendix E. The analysis was performed using 50 one-dimensional three-noded quadratic spherically symmetric finite elements in order to calculate the elastic displacement and lattice flux fields.



(a)



(b)

Figure 8.4 – A graph to show the evolution of a spherically symmetric InAs particle in a GaAs matrix at 250°C (a) without the bulk elastic energy driving force (b) with the bulk elastic energy driving force (12.5% initial InAs volume fraction).

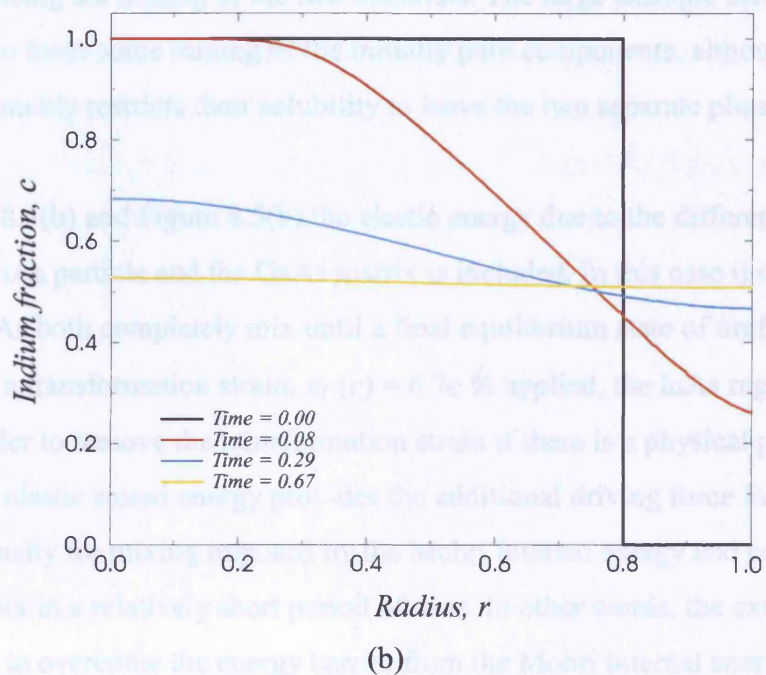
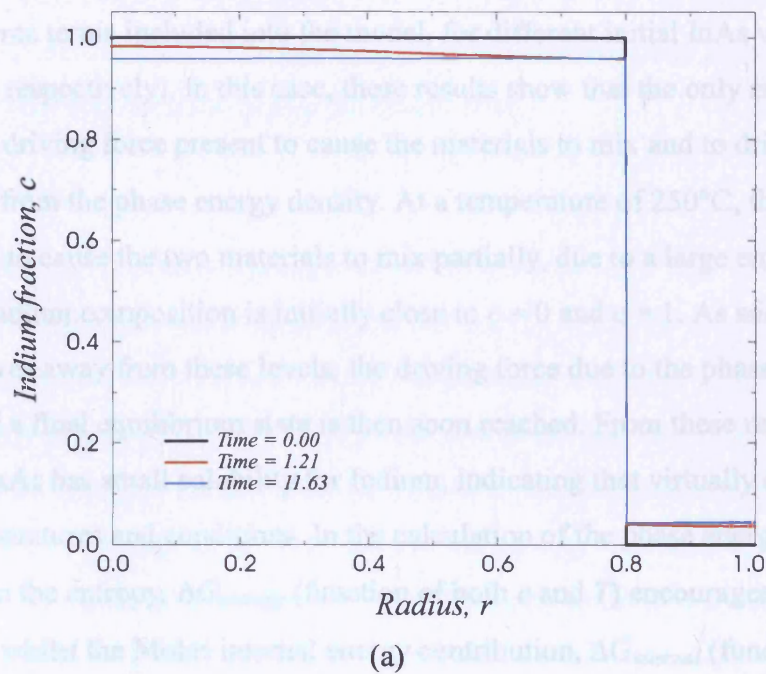


Figure 8.5 – A graph to show the evolution of a spherically symmetric InAs particle in a GaAs matrix at 250°C (a) without the bulk elastic energy driving force (b) with the bulk elastic energy driving force (50% initial InAs volume fraction).

Figure 8.4(a) and Figure 8.5(a) show the evolution of the system without any bulk elastic driving force terms included into the model, for different initial InAs volume fractions (12.5% and 50% respectively). In this case, these results show that the only energy contribution and driving force present to cause the materials to mix and to drive the process of evolution is that from the phase energy density. At a temperature of 250°C, the phase energy is only sufficient to cause the two materials to mix partially, due to a large entropic driving force when the indium composition is initially close to $c = 0$ and $c = 1$. As soon as the Indium composition moves away from these levels, the driving force due to the phase energy reduces considerably and a final equilibrium state is then soon reached. From these results it can be stated that the GaAs has small solubility for Indium, indicating that virtually no mixing occurs under these temperatures and conditions. In the calculation of the phase energy density, the contribution from the entropy, $\Delta G_{entropy}$ (function of both c and T) encourages the two materials to mix whilst the Mohri internal energy contribution, $\Delta G_{internal}$ (function of c) has the effect of opposing the mixing of the two materials. The large entropic driving forces are initially present to force some mixing of the initially pure components, although the Mohri internal energy quickly restricts their solubility to leave the two separate phases in equilibrium.

In Figure 8.4(b) and Figure 8.5(b) the elastic energy due to the difference in the lattice spacings of the InAs particle and the GaAs matrix is included. In this case it can be seen that the InAs and GaAs both completely mix until a final equilibrium state of uniform composition is attained. With a transformation strain, $\epsilon_T(c) = 6.7c\%$ applied, the InAs region will initially try to relax in order to remove the transformation strain if there is a physical process by which it can do so. The elastic stored energy provides the additional driving force for the system to overcome the penalty for mixing imposed by the Mohri internal energy and causes the two components to mix in a relatively short period of time. In other words, the extra energy required in order to overcome the energy barrier from the Mohri internal energy is provided by the elastic stored energy. During the evolution process, the phase energy will initially dominate due to the presence of a large entropic driving force (as with no mis-match strain applied), but the contribution from the elastic strain energy allows the two materials to completely mix and evolve to a lower overall energy state.

It was found that the implicit integration scheme provided greater accuracy and stability such that larger time steps could be used. The explicit method required a much smaller time step in order to provide a reasonably accurate solution and therefore required more overall iterations to reach the final equilibrium state.

8.5 – Conclusions

In the analysis of this simple problem, it can be observed how important it is to properly model the different contributions to the free energy of the system. If one component is omitted, then significant errors can arise in the simulation of the microstructural evolution process. It can be proven theoretically that the final compositional state always has a lower overall energy than that of the initial state, but the model provides an accurate representation of how the composition changes over time showing the path by which the system evolves, which is important. Consideration of the only start and finish equilibrium states is not enough as one needs to demonstrate that there is a path by which a system can go from one energy state to the other.

The same variational approach developed here [2] has been also applied within a two-dimensional setting by Gill et al. [29] to model the evolution of epitaxially strained InAs islands grown on a GaAs substrate for the situation in which surface diffusion dominates, where the island relaxes by changing its shape, and also where lattice diffusion dominates, where the island relaxes by changing its compositional profile.

9.0 – Modelling Moving Boundary Problems

This section examines how the general variational model is used to model issues relating to a general class of moving boundary problems.

The solution of moving boundary problems with phase changes is of special interest due to the inherent difficulties associated with modelling the discontinuity of otherwise continuous variables (e.g. the flux field and composition) at the moving interface and modelling the location of the moving boundary with respect to both space and time. The ability to model an interface between different phase regions with dissimilar material properties and characteristics is of considerable technical interest.

This chapter describes how the general model was initially applied and developed to model the evolution of a precipitate within a one-dimensional finite element setting. However, due to limitations placed on this model, further modifications and extensions were made to allow for the numerical modelling of the evolution of precipitate type systems within two-dimensional space. Within this finite element framework, novel numerical modifications include the mapping of the composition from an unstructured mesh of standard space-time two-dimensional finite elements to a structured underlying grid. This allowed the finite element mesh to be re-generated when necessary and the composition can then mapped back to the new unstructured finite element geometry.

9.1 – Literature Review

The study of moving boundary problems arising in solid-state diffusion processes has become a highly popular subject in recent years due to its extensive application to a large number of problems of practical importance [41][42]. Many computational models consider very specific cases and introduce assumptions that are only usually applicable to a particular material and physical process under consideration. Many of these models employ analytical techniques and consequently introduce drastically simplifying assumptions in order to achieve tractable results. Analytical solutions to moving boundary problems are usually restricted to a few particular cases, mainly due to the number of complexities associated with such problems, and solutions to one-dimensional problems are only usually available [43]. As each problem presents its own complexity, recourse is generally made to numerical methods.

In heat-transfer, the ‘Stefan problem’ is often used to describe free boundary problems associated with phase transformations. In this case, the problem is named after J. Stefan [44][45], who studied the melting of the polar ice cap in the 1890s. In this case, the boundaries are phase boundaries between ice and water that change in response to the heat supplied from convective fluid currents. Whatever the name, the presence of a free or moving boundary introduces serious complications for any type of analysis. For all but the simplest of problems, it is necessary to resort to numerical solutions. Even then, free surfaces require the introduction of special methods to define their location, their movement and their influence on a flow.

Most numerical methods formulated for such problems are usually only applicable for a single moving boundary between two adjacent phases [46]. Methods chosen to tackle moving boundary problems are usually either finite difference or finite element methods. The finite element method has the advantage that it has the ability to handle more complex geometries, but is considered to be more time consuming to implement compared with finite difference techniques. The finite difference approach is considered to be more flexible and simpler to both formulate and program, and for these reasons, the finite difference approach is usually favoured and more widely used. An advantage of using the finite element method comes from the fact that it has the strong ability to model linear elastic, non-linear elastic as well as complex plasticity phenomena. For this reason it is widely found in many commercial software packages (such as ABAQUS) for the solution of deformation and fracture problems.

Bonnerot and Jamet [47] used the finite element method to study multi-phase moving boundary problems within one-dimensional space. In their analysis they applied a modified and extended form of their third-order accuracy discontinuous finite element method [48]. On application to a moving boundary problem, they adopted a curved triangular finite element for each appearing or disappearing phase, whilst curved trapezoidal finite elements were applied elsewhere. Despite the accuracy and convergence speed of this method, it is not applicable to modelling higher dimensional moving boundary problems.

A description of various numerical methods with useful bibliography may be found in the surveys of Crank [46] and Furzeland [49]. Furzeland compared methods used for modelling moving boundary problems in terms of their accuracy, ability to handle complex problems, computational efficiency and ease of programming. The conclusion from this work was that no one method fulfilled all these criteria. The work of Poirier and Salcudean [50]

compared different numerical schemes applied to different physical problems. The conclusion from this work was that the best numerical approach primarily depends on the nature of the problem under consideration. For a greater insight, review and comparison between many of the numerical finite difference schemes currently available for solving moving boundary problems, the reader is referred to the work of Zerroukat [51] and the references contained therein.

Applying the finite element method to modelling moving boundary problems in two or three-dimensional space immediately imposes computational problems. When the interface boundary or boundaries move, the mesh usually distorts to some degree, and large distortions tend to reduce the accuracy of the simulation. After the interface has travelled some distance the distortion becomes too great, and either the entire domain or the region around each phase needs to be remeshed. Johnson and Tezduyar [52][53], Mittal and Tezduyar [54] and Tezduyar et al. [55] have developed efficient algorithms for moving particles and a moving finite element mesh. Triangular finite elements were used to discretise the phase surrounding the particles and special narrow elements were used near each particle to track the moving boundary. The elements near each particle deform as the particle moves through the mesh, and remeshing is therefore necessary as the particles move through the mesh. However, remeshing and checking the mesh for distortion prove to be a computationally intensive process if carried out at each time step. Consequently, remeshing is performed at specified time steps, which increases the potential for increased error if too much distortion occurs between remeshing. This technique is most suitable for slowly deforming spatial domains, which is the case here.

Hu et al. [56] describe a method for the simulation of moving fluid particles in two-dimensions using unstructured finite element meshes. They remesh at every time step, generating a new mesh that bears no straightforward relationship to the previous mesh. This then requires the regeneration of element-connectivity information, which is necessary for the finite element method to know how the solution interacts between adjacent elements. A stable time integration scheme is employed where, at each time step, the positions of the particles are updated, the computational domain is remeshed, the solution at the previous time is mapped onto the new mesh and the unknown variables are solved across the new mesh respectively. The difficulties they address are remeshing at each time step and the interpolation of the solution onto the new mesh. It appears that this method is very computationally intensive but better suited to modelling computational domains that move more drastically with time.

Unverdi and Tryggvason [57] consider the motion of bubbles within a fluid and use a regular finite difference grid onto which they overlay an unstructured mesh to represent the particle surface. This method essentially attempts to couple the flexibility of the finite difference method with the ability of the finite element method to handle more complex geometries.

In recent years, the boundary element method has emerged as an alternative to both finite element and finite difference methods. The boundary element method has the advantage that a two-dimensional problem can essentially be reduced to a one-dimensional problem, since only the boundary of each element is considered during evaluation of integral equations. This method is applicable to many problems, particularly those with variable and extended domains since only the discretisation of the boundary is necessary [58]. The boundary element method has the ability to compute linear elasticity problems very quickly and proves to be good for investigating irregular and highly perturbed boundary shapes. The boundary element method cannot handle non-linear elasticity and plasticity phenomena and struggles when the material properties, such as Young's modulus and transformation strain, vary both spatially and with compositional gradients across the microstructure. This approach has been successfully applied by Jou [59] and Jou et al. [60] [61] to model the evolution of precipitates and coarsening of particles under the influence of elastic fields. This method has also been applied to model other moving boundary and phase change problems such as solidification [62] [63].

Many models that have been previously developed over the years for modelling moving boundary systems usually introduce simplifying assumptions and consider quite specific cases. Through a literature review there appears to be a lack of 'general' models capable of modelling complex elasticity phenomena coupled with both diffusion and moving boundary mechanisms. With this in mind, the finite element method is formulated in the next section of this chapter and applied to model the moving problem between two phases within an elastically inhomogeneous material system. The method is developed and tested within one-dimensional space before it is implemented and used to model higher dimensional problems.

9.2 – One-Dimensional Special Interface Element

Initially, a one-dimensional implementation of the variational formalism described in chapter 5 was undertaken. This allowed various modelling issues to be addressed and different options to be tried and tested before moving onto higher dimensional simulations. This section is presented as an experimental development exercise and describes how the general model can be applied to model a moving boundary between two different phase regions within a one-dimensional finite element framework.

The initial approach to solving this problem was to model the displacement field, flux field and composition using a fixed structured mesh of standard regularly spaced one-dimensional finite elements. The flux and compositional discontinuities present within the finite element containing the moving interface can be modelled using a special interface element incorporating discontinuous interpolation. Since the finite element mesh remains fixed throughout the processing period, no re-meshing is required and it is therefore not necessary to map information across finite element meshes.

An alternative to this approach was to model the displacement field, flux field and carbon composition using an unstructured finite element mesh. As before, the element containing the boundary can be treated as a special interface element capable of modelling the discontinuity at the sharp interface. As the moving interface boundary approaches an outer finite element node, within the current finite element, such that no further interface boundary movement is possible, the finite element mesh can be regenerated. Information would then need to be transferred from the old mesh to the new finite element mesh for the simulation to continue. On generation of the new finite element mesh, control measures can be placed on the location of the finite elements such as to maximise the movement of the interface boundary and to minimise the frequency of future re-meshes.

The initial fixed mesh approach was selected due to its simplicity, ease of numerical implementation and to avoid additional complexities associated with mapping information across different mesh geometries. To apply this approach to model microstructural evolution within a multi-phase moving interface system, it is necessary to develop a methodology to model the non-equilibrium conditions (i.e. flux and concentration discontinuities) at the sharp interface. Consider the regular three-noded quadratic-type one-dimensional finite element shown in Figure 9.1.

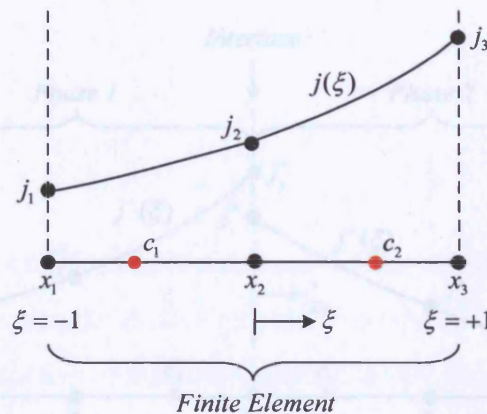


Figure 9.1 – Representation of the flux field and composition across a three-noded quadratic-type one-dimensional finite element.

The flux field across this element can be expressed as

$$j(\xi) = n_i(\xi)j_i$$

where $i = 1, 2, 3$ and $-1 \leq \xi \leq +1$ is a local coordinate variable. The flux field is considered continuous everywhere across each phase domain apart from at the interface where a discontinuity exists. A discontinuous interpolation of the lattice flux field within the finite element containing the moving interface can be introduced in order to account for this discontinuity. The finite element containing the moving interface boundary can be divided at the interface and treated as two regular variable-sized finite elements. The flux field across each of these sub-elements can be modelled using the flux field relation as described above with two discontinuous flux values defined at the interface. An example of such an interface element can be graphically represented as shown in Figure 9.2, where the variables associated within each sub-element phase region are represented by the + and – superscripts.

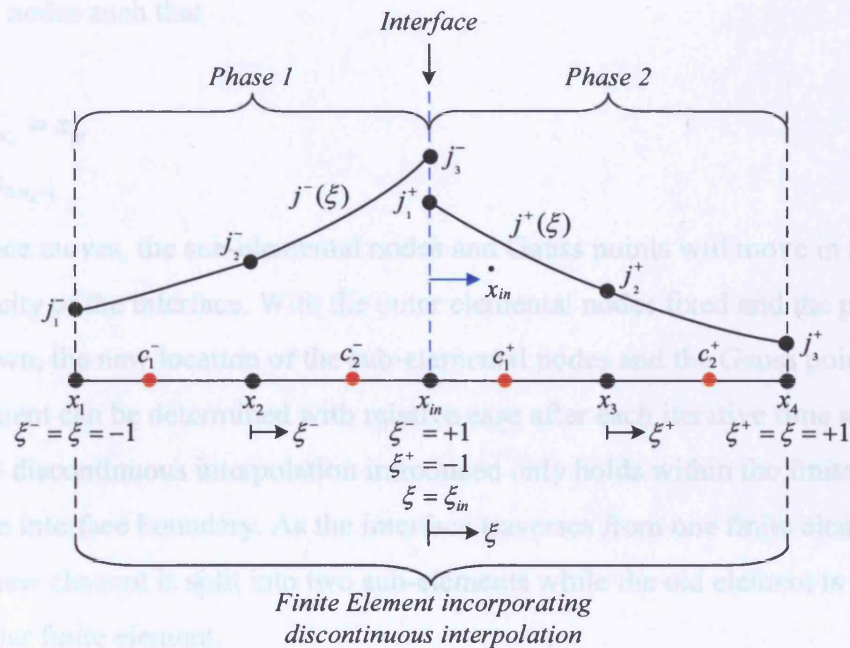


Figure 9.2 – Modelling a discontinuity in the flux field at a variable interface position across a one-dimensional finite element.

The flux field across the interface element can be represented by

$$j(\xi) = \begin{cases} j^-(\xi^-) & \xi \leq \xi_{in} \\ j^+(\xi^+) & \xi > \xi_{in} \end{cases} \quad (9.1)$$

where

$$\xi_{in} = \frac{2x_{in} - (x_1 + x_4)}{(x_4 - x_1)} \quad (9.2)$$

Local co-ordinate variables, ξ^- and ξ^+ , are introduced on each side of the interface element, such that $-1 \leq \xi^- \leq +1$ and $-1 \leq \xi^+ \leq +1$, so the flux field within each interface sub-element can be described by

$$\begin{aligned} j^-(\xi^-) &= n_i(\xi^-)j_i^- \\ j^+(\xi^+) &= n_i(\xi^+)j_i^+ \end{aligned} \quad (9.3)$$

Similarly, the variation in position on each side of the interface can be expressed as

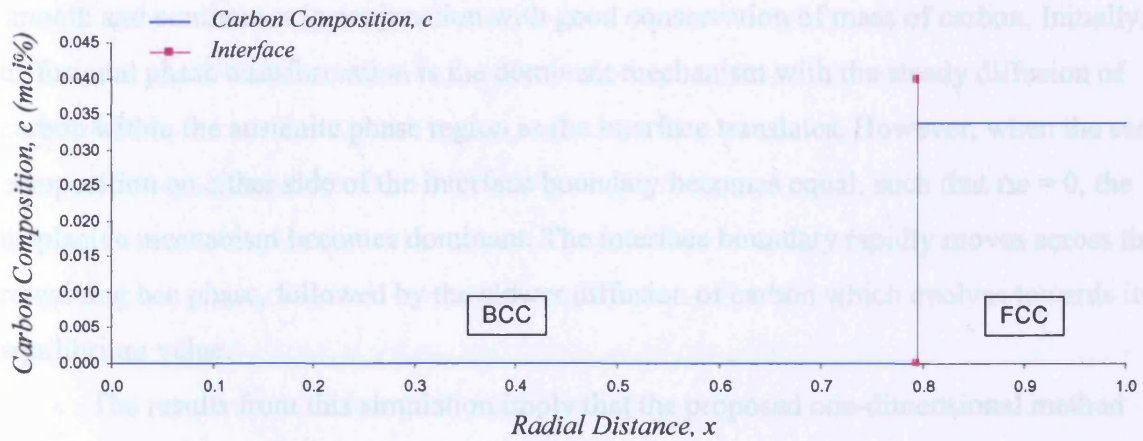
$$\begin{aligned} x^-(\xi^-) &= n_i(\xi^-)x_i^- \\ x^+(\xi^+) &= n_i(\xi^+)x_i^+ \end{aligned}$$

In a one-dimensional finite element with N_e elemental nodal points, the interface element will have ' $2N_e - 1$ ' nodes such that

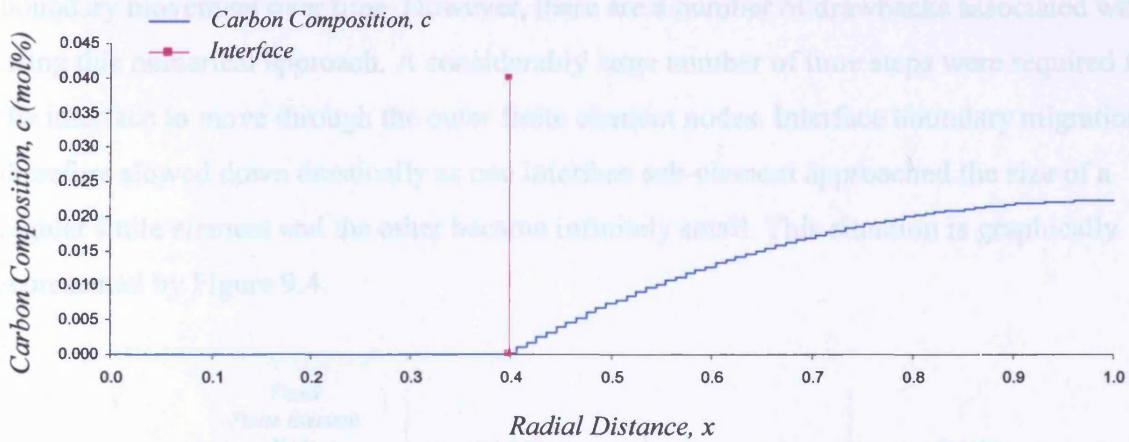
$$\begin{aligned}x_1^- &= x_1 \\x_1^+ &= x_{N_e}^- = x_{in} \\x_{N_e}^+ &= x_{2N_e-1}\end{aligned}$$

As the interface moves, the sub-elemental nodes and Gauss points will move in accordance with the velocity of the interface. With the outer elemental nodes fixed and the position of the interface known, the new location of the sub-elemental nodes and the Gauss points within each sub-element can be determined with relative ease after each iterative time step. It must be noted that the discontinuous interpolation introduced only holds within the finite element containing the interface boundary. As the interface traverses from one finite element into another, the new element is split into two sub-elements while the old element is restored to that of a regular finite element.

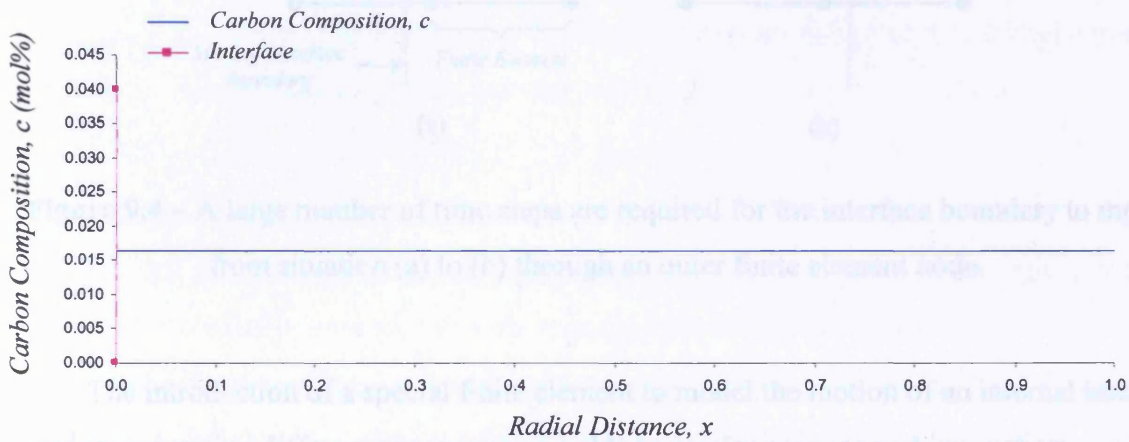
The one-dimensional model described here was implemented and used to model the microstructural evolution of a spherical Fe-C system (which is described in more detail in chapter 10) composed of two different phases, ferrite (bcc) and austenite (fcc), separated by a sharp interface. Figure 9.3 shows the compositional configuration of interstitial carbon during three different stages of this one-dimensional experimental simulation. The finite element mesh consists of 100 linear-type finite elements with a 50% bcc to 50% fcc initial volume ratio. For simplicity of illustration, the energy of the interface between the two phases is not included and the elastic properties of both phases are assumed to be identical. The diffusivity of carbon in the ferrite phase is found to be approximately 20 times that in the austenite phase.



(a)



(b)



(c)

Figure 9.3 – Microstructural evolution of the one-dimensional spherical Fe-C system: (a) the initial configuration, (b) after 14,000 iterations and (c) at equilibrium.

The results from this one-dimensional simulation show that interface motion is both smooth and continuous in conjunction with good conservation of mass of carbon. Initially, the diffusional phase transformation is the dominant mechanism with the steady diffusion of carbon within the austenite phase region as the interface translates. However, when the carbon composition on either side of the interface boundary becomes equal, such that $\Delta c = 0$, the displacive mechanism becomes dominant. The interface boundary rapidly moves across the remaining bcc phase, followed by the slower diffusion of carbon which evolves towards its equilibrium value.

The results from this simulation imply that the proposed one-dimensional method works quite well and can accurately model the change in composition coupled with interface boundary movement over time. However, there are a number of drawbacks associated with using this numerical approach. A considerably large number of time steps were required for the interface to move through the outer finite element nodes. Interface boundary migration therefore slowed down drastically as one interface sub-element approached the size of a regular finite element and the other became infinitely small. This situation is graphically represented by Figure 9.4.

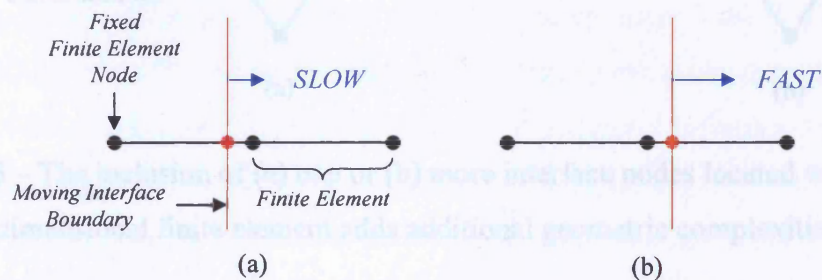


Figure 9.4 – A large number of time steps are required for the interface boundary to move from situation (a) to (b) through an outer finite element node.

The introduction of a special finite element to model the motion of an internal interface boundary separating different phase regions holds particular promise and innovation. However, considering the dimensional geometric capabilities of a one-dimensional model, limitations are placed on modelling the change in shape and size of the interface over time as a result of complex elastic fields and diffusive processes that can transport mass from one phase to another. Limitations are imposed on modelling material anisotropies, complex

unsymmetrical and distorted geometries and on the application of multi-directional driving forces and external loading. Despite the useful insight provided by one-dimensional models, there are many instances in which the geometries are sufficiently complex such as to defy a simplified representation of what is essentially a complex higher dimensional problem.

The one-dimensional model with a special interface element can be theoretically implemented into higher dimensional space but geometric complications can arise as the interface boundary and line of discontinuity moves directly through the finite elements. Further complexities arise when more than one interface node is arbitrarily located within these finite elements, as shown in Figure 9.5(b). This situation imposes severe numerical problems and challenges associated with modelling the elastic and flux fields within these finite elements with the additional complexity of a discontinuity at the interface.

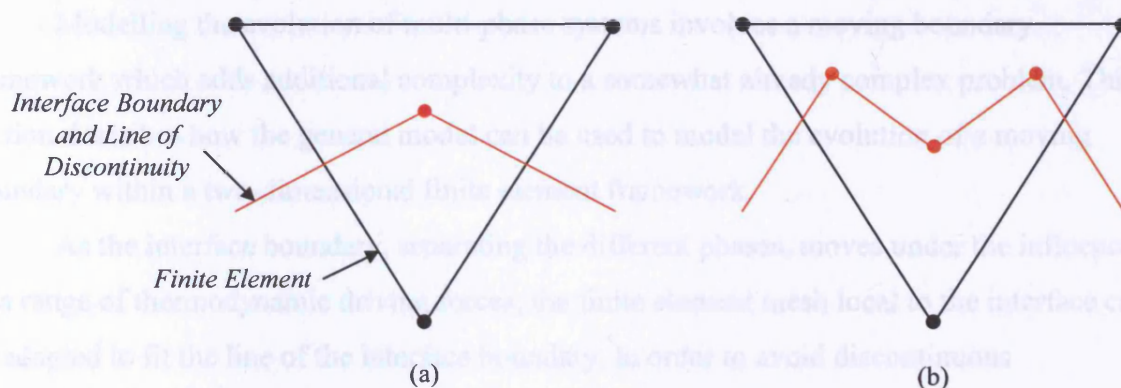


Figure 9.5 – The inclusion of (a) one or (b) more interface nodes located within a two-dimensional finite element adds additional geometric complexities.

When the region under analysis is two or three dimensional, the definition of a special element with a discontinuity in its shape functions becomes more difficult. Therefore, due to the geometric restrictions associated with extending the current working one-dimensional model into higher dimensional space, the alternate approach of adapting the finite element mesh local to the line of the interface and regenerating the mesh is now addressed. In this case, the finite element mesh is regenerated when no further interface boundary movement is possible (such that the finite element mesh, local to the interface, does not become too distorted and the solution is affected) and information is then transferred between different finite element geometries.

The following section of this chapter describes how the numerical method and ideas formulated from this simple one-dimensional experimental moving boundary system can now be extended to model a moving boundary problem in two-dimensional space. A two-dimensional model is considered since this removes some of the geometric complexity of working in three-dimensional space and the results have the benefit of being easier to visualise and interpret. A novel numerical method of transferring information across different two-dimensional unstructured finite element geometries is introduced and discussed in considerable detail. A higher dimensional model will have the advantage of allowing effects due to material property anisotropies, remote uniaxial and combined loading and multi-phase nucleation and interactions to be fully modelled.

9.3 – Transferring Information across Two-Dimensional Meshes

Modelling the evolution of multi-phase systems involves a moving boundary framework which adds additional complexity to a somewhat already complex problem. This section describes how the general model can be used to model the evolution of a moving boundary within a two-dimensional finite element framework.

As the interface boundary, separating the different phases, moves under the influence of a range of thermodynamic driving forces, the finite element mesh local to the interface can be adapted to fit the line of the interface boundary. In order to avoid discontinuous interpolation of the moving interface within elements, the system is adapted (subject to no critical elemental angle constraints being violated) after each iteration in order for the edges of the finite elements local to the interface to lie along the interface boundary. However, the system will need to be re-meshed occasionally in order to prevent these finite elements from becoming too distorted such as to restrict further interface movement and affect the finite element solution through the local distortion of the mesh. The compositional data is stored at the elemental Gauss points and after the finite element mesh is re-generated, the elemental Gauss points will occupy different coordinates, making it extremely difficult to determine the new compositional distribution by interpolating from the compositional data stored across the previous finite element mesh.

In order to get around this problem it is proposed to implement an underlying structured square grid, whose geometry and resolution is pre-defined and remains fixed throughout the processing period. When a system re-mesh is required, the compositional data

across the finite element mesh can be mapped to the underlying grid with a single compositional value stored within each square cell of the grid. The finite element mesh can be re-generated when required and the composition at the Gauss points across the new finite element mesh can be determined by mapping the compositional data back from the underlying grid. The underlying grid is therefore simply used as a medium for the transfer of compositional data from one finite element geometry to another by essentially writing data from one mesh geometry and then lifting and relating the necessary grid values to the new finite element geometry. It is expected that one will always get some local redistribution of material during mapping due to averaging, so it is important to regenerate the finite element mesh as infrequently as possible. However, the number of times the finite element mesh will need to be regenerated will depend on both the physical system of interest and on the density of the mesh local to the interfacial region. If the density around the interfacial region is high, this will not only incur a computational processing cost but the interface boundary will not have to move far for the mesh to become distorted. This therefore implies that the density of the finite element mesh, particularly around the moving interface boundaries, has to be carefully chosen such that the solution is accurate, with results being obtained within an acceptable time frame.

The mapping techniques considered for the process of mapping data from an unstructured finite element mesh to a structured underlying grid and vice versa are fully described and discussed in the following sub-sections. The accuracy of data transfer is then tested and the mapping method is then validated by using a suitable example.

9.3.1 – Mapping to the Underlying Grid from the Finite Element Mesh

The composition defined within each finite element can be mapped to the corresponding underlying cells that cover the finite element using the process of “volume fraction” analysis. This method involves the calculation of the volume fraction contribution from each underlying cell that is located within each triangular finite element. The composition within each underlying cell can then be calculated knowing the composition within the finite element(s) covering the underlying cell and the volume fraction contribution from the finite element(s). As an example, consider the situation where a compositional cell overlaps six three-noded triangular finite elements as shown in Figure 9.6.

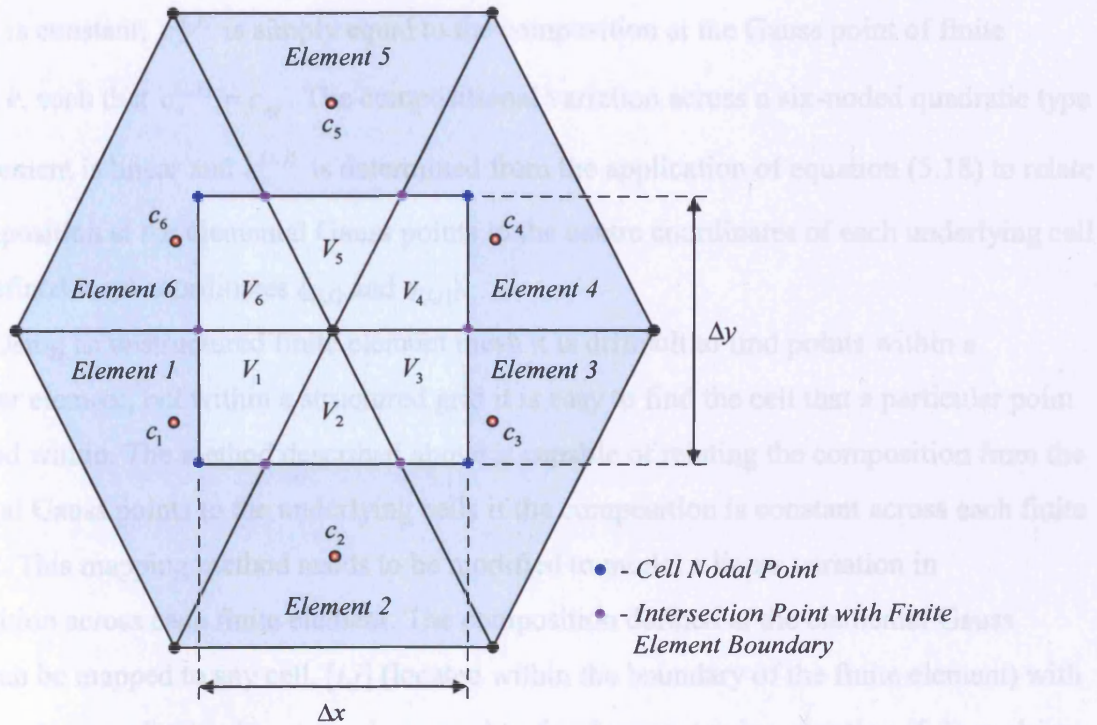


Figure 9.6 – Six three-noded triangular finite elements overlap a single underlying cell.

Using a linear interpolation function to describe the lattice flux field across each finite element, the composition is constant within each finite element. For a quadratic interpolation function, the composition varies linearly across each finite element.

The total volume of an underlying cell, $[i,j]$, can be expressed as

$$V_{[i,j]} = \sum_{e=1}^{N_{[i,j]}} V_e^{[i,j]} = \Delta x \cdot \Delta y \quad (9.4)$$

where $N_{[i,j]}$ represents the number of finite elements covering underlying cell, $[i,j]$, and $V_e^{[i,j]}$ is the volume contribution from element, e , located within cell $[i,j]$.

The composition, $c_{[i,j]}$, within the underlying cell, $[i,j]$, shown in Figure 9.6, can be written as

$$c_{[i,j]} = \left(\frac{V_1 c_1 + V_2 c_2 + V_3 c_3 + V_4 c_4 + V_5 c_5 + V_6 c_6}{V_1 + V_2 + V_3 + V_4 + V_5 + V_6} \right) = \sum_{e=1}^{N_{[i,j]}} \mu_e^{[i,j]} c_e^{[i,j]} \quad (9.5)$$

where $\mu_e^{[i,j]} = \frac{V_e^{[i,j]}}{V_{[i,j]}}$ is the volume fraction contribution from element, e , contained within cell, $[i,j]$ and $c_e^{[i,j]}$ is the composition within element e , mapped to the centre coordinates of underlying cell $[i,j]$. Since the compositional variation across a three-noded linear type finite

element is constant, $c_e^{[i,j]}$ is simply equal to the composition at the Gauss point of finite element e , such that $c_e^{[i,j]} = c_{eg}$. The compositional variation across a six-noded quadratic type finite element is linear and $c_e^{[i,j]}$ is determined from the application of equation (5.18) to relate the composition at the elemental Gauss points to the centre coordinates of each underlying cell (with defined local coordinates $\xi_{[i,j]}$ and $\eta_{[i,j]}$).

Using an unstructured finite element mesh it is difficult to find points within a particular element, but within a structured grid it is easy to find the cell that a particular point is located within. The method described above is capable of relating the composition from the elemental Gauss points to the underlying cells if the composition is constant across each finite element. This mapping method needs to be modified to model a linear variation in composition across each finite element. The composition defined at the elemental Gauss points can be mapped to any cell, $[i,j]$ (located within the boundary of the finite element) with known centre coordinates $(x_{[i,j]}, y_{[i,j]})$ mapped to ξ and η space using equation (5.2) as shown in Figure 9.7.

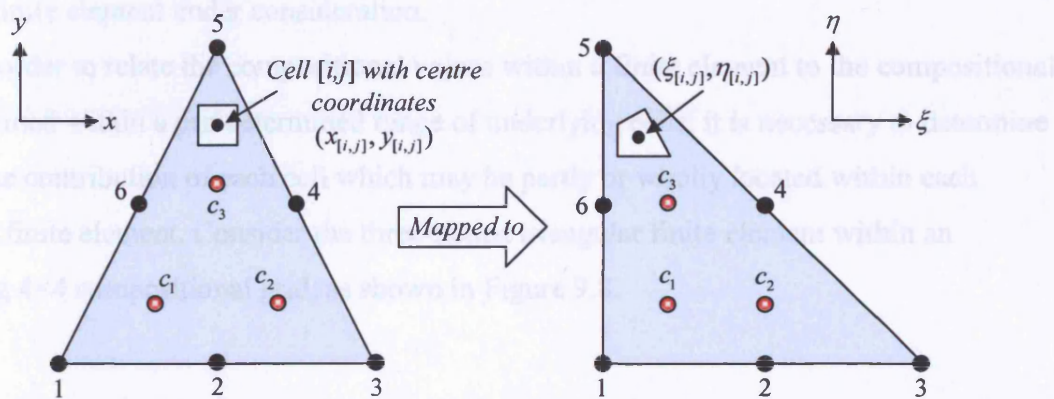


Figure 9.7 – Mapping the composition stored at the element Gauss points to the underlying cell geometry.

In order to determine whether an underlying cell point, or other specified point, with known coordinates (x,y) is located within the boundary of a finite element of known geometry, it is necessary to translate the global x and y cell point coordinates into (ξ,η) space. The local ξ and η values can be calculated for any point with coordinates (x,y) through the selected elemental shape function.

Taking the linear elemental shape function as an example

$$x(\xi, \eta) = x_1(1 - \xi - \eta) + x_2\xi + x_3\eta$$

$$y(\xi, \eta) = y_1(1 - \xi - \eta) + y_2\xi + y_3\eta$$

one has

$$\xi_{[i,j]} = \frac{(y_{[i,j]} - y_1)(x_3 - x_1) - (y_3 - y_1)(x_{[i,j]} - x_1)}{(y_2 - y_1)(x_3 - x_1) - (y_3 - y_1)(x_2 - x_1)} \quad (9.6)$$

$$\eta_{[i,j]} = \frac{(y_2 - y_1)(x_{[i,j]} - x_1) - (y_{[i,j]} - y_1)(x_2 - x_1)}{(y_2 - y_1)(x_3 - x_1) - (y_3 - y_1)(x_2 - x_1)} \quad (9.7)$$

A particular cell can be confirmed as being located within the boundary of a triangular finite element if any arbitrary point along the boundary of the underlying cell satisfies all three of the following conditions:

1. $0 \leq \xi_{[i,j]} \leq +1$
2. $0 \leq \eta_{[i,j]} \leq +1$
3. $\xi_{[i,j]} + \eta_{[i,j]} \leq +1$

If all of the three conditions are satisfied then the cell will have a volume fraction contribution from the finite element under consideration.

In order to relate the compositional values within a finite element to the compositional values defined within a pre-determined range of underlying cells, it is necessary to determine the volume contribution of each cell which may be partly or wholly located within each triangular finite element. Consider the three-noded triangular finite element within an underlying 4×4 compositional grid, as shown in Figure 9.8.

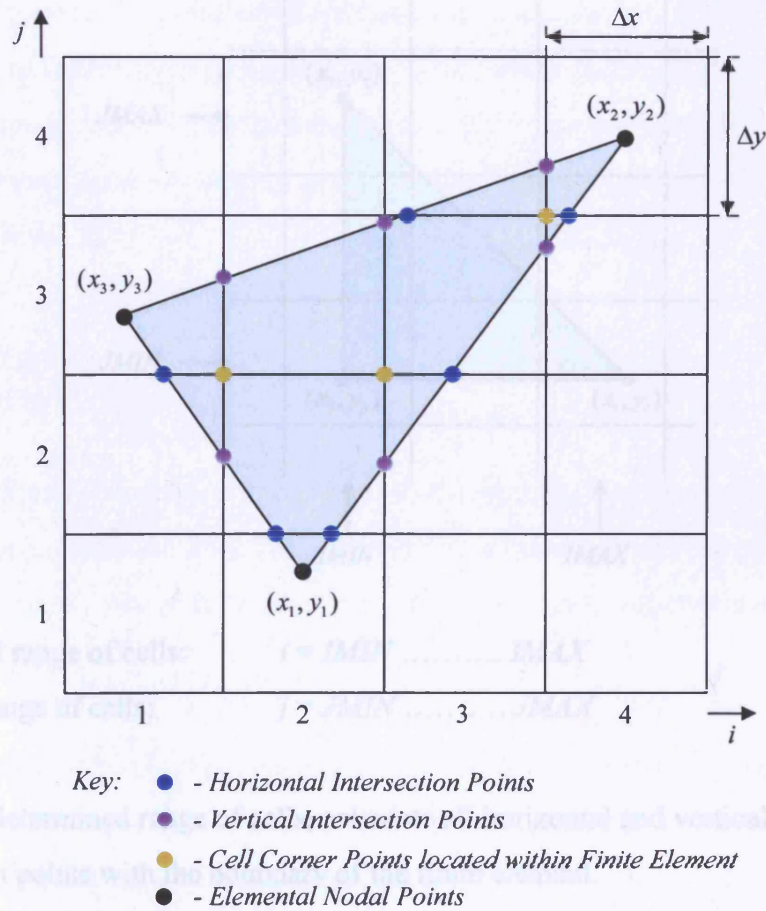


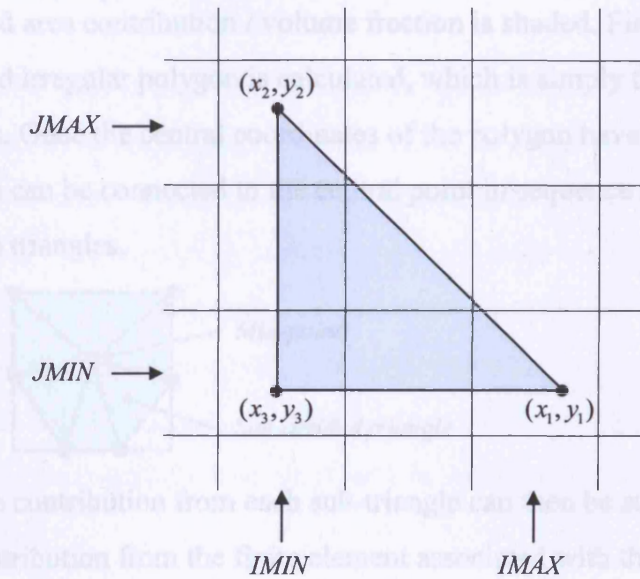
Figure 9.8 – A three-noded triangular finite element located within a 4×4 structured underlying grid.

For each finite element the following steps are performed:

1. Determine the underlying cell that each outer elemental nodal point is located within, i.e. a nodal point with coordinates (x, y) is located within cell

$\left(INT\left(\frac{x}{\Delta x}\right) + 1, INT\left(\frac{y}{\Delta y}\right) + 1 \right)$ (where INT is a rounded down integer). Then determine the range of horizontal and vertical underlying cells covering the finite element.

Consider the following example:

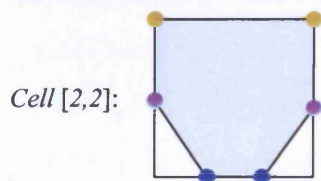


Horizontal range of cells: $i = IMIN \dots\dots\dots IMAX$

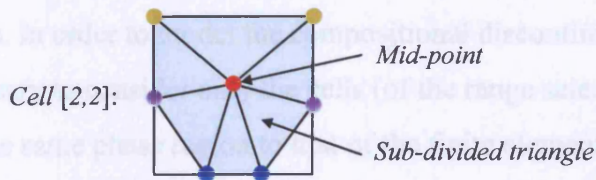
Vertical range of cells: $j = JMIN \dots\dots\dots JMAX$

2. Using the determined range of cells, calculate all horizontal and vertical underlying grid intersection points with the boundary of the finite element.

3. For each underlying cell within the range, determine the intersection points, internal cell corner points and triangle nodal points that lie on or within the outer boundaries of the selected cell.
 - (a) If two of these points or less lie within the cell, there is no area contribution associated with the finite element from this particular cell.
 - (b) If three points lie within the cell, these points form a simple triangle and the volume fraction can be easily calculated.
 - (c) If more than three points lie within the cell, then the cell needs to be further sub-divided into triangular sections. For example, consider cell [2,2] from Figure 9.8, which contains four grid intersection points (two vertical and two horizontal) and two internal cell corner points.



The required area contribution / volume fraction is shaded. Firstly, the mid-point of the six-sided irregular polygon is calculated, which is simply the average of the six outer points. Once the central coordinates of the polygon have been calculated, the outer points can be connected to the central point in sequence to form a series of sub-divided triangles.



The volume contribution from each sub-triangle can then be summed to provide the volume contribution from the finite element associated with this particular cell. The total volume fraction for each cell should sum to unity, otherwise mass will not be conserved.

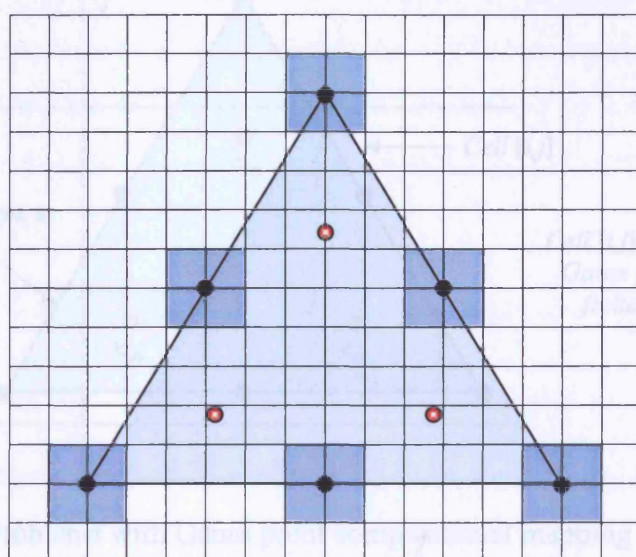
4. Once the volume fraction has been calculated for each underlying cell located within each finite element, it is possible to map the composition defined across the finite element mesh to the underlying grid using equation (9.5).

9.3.2 – Mapping to the Finite Element Mesh from the Underlying Grid

Once the composition has been successfully mapped to the underlying grid and the system has been re-meshed with the updated interface boundary geometry, it is then necessary to relate the compositional values stored across the underlying grid back to the new finite element mesh. It is therefore necessary to develop an accurate and consistent mapping technique in order to map the compositional values across the underlying structured grid to the Gauss point(s) within each finite element. Due to the fact that one is essentially mapping a typically large number of compositional grid values to a much smaller number of Gauss points, there are more mapping techniques that can be considered here compared to mesh to grid mapping. With this in mind, the following underlying grid to finite element mesh mapping approaches are introduced and discussed.

(a) Compositional Averaging at the Nodal Points

By selecting a range of compositional cells that are located within the vicinity of the elemental nodal points, the composition can be calculated at the nodal points by averaging over a range of selected cells. The compositional values can then be determined at the elemental Gauss points by interpolating between the nodal values using suitable interpolation functions. In order to model the compositional discontinuity at the interfacial nodes, it would be necessary to consider only the cells (of the range selected around the node) that are located within the same phase region to that of the finite element under consideration. This approach can be theoretically implemented for both three and six-noded finite elements and is illustrated in Figure 9.9.



- Key:
- - Elemental nodal point
 - ⊙ - Elemental Gauss point
 - - Compositional cells considered for nodal compositional averaging

Figure 9.9 – Nodal compositional averaging.

However, this method will be limited when a relatively coarse underlying grid is implemented and inaccuracies could occur at the interfacial nodes where only the cells located within the same phase region need to be considered. To avoid complexities associated with selecting cells within a designated phase region near interface boundaries, consideration was therefore given to other underlying grid to finite element mesh mapping techniques.

(b) Gauss Point Mapping

The composition at the elemental Gauss points can be determined by taking the compositional value of the underlying cell that the Gauss point is located within. Knowing the coordinates of each elemental Gauss point, it is relatively easy to determine the underlying cell that the Gauss point is located within. This method can essentially be used for both linear and quadratic flux interpolation functions. In the case of the quadratic flux shape function, using a fine unstructured finite element mesh and a coarse structured underlying grid may cause inaccurate compositional Gauss values to be mapped from the underlying grid. This situation can be graphically illustrated by Figure 9.10 below.

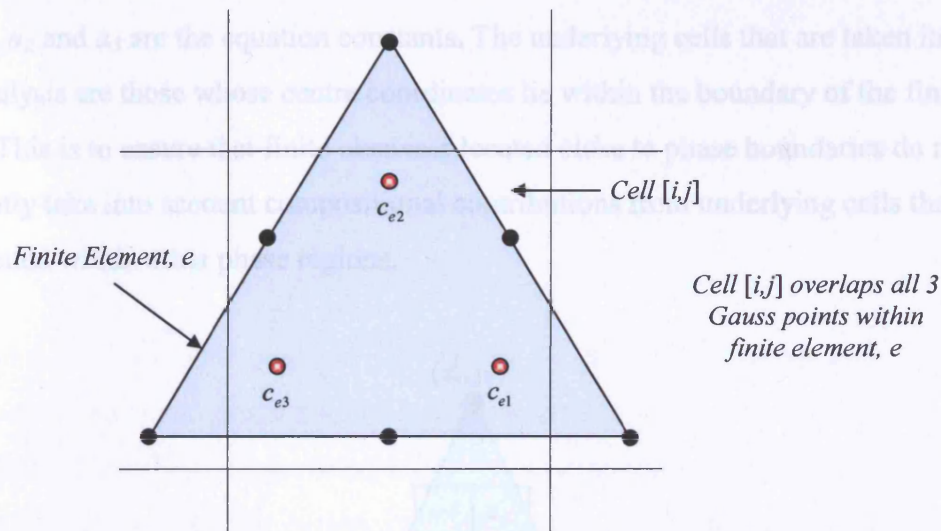


Figure 9.10 – Problems with Gauss point compositional mapping using a relatively coarse underlying grid.

In the situation shown in Figure 9.10 for finite element, e ,

$$c_{e1} = c_{e2} = c_{e3} = c_{[i,j]}$$

However, this problem can be avoided by implementing a fine underlying grid such that the compositional gradient within each finite element can be better represented. Ideally, for the smallest six-noded finite element defined across the mesh, the underlying grid resolution should be selected such that the three Gauss point values are all taken from different underlying cells.

(c) Linear Regression

The linear regression model involves the prediction of the average value of one variable (the dependent variable, y) as a linear function of another variable (the independent variable, x), based over N values of data. Simple regression is essentially a method of determining the best linear surface to fit the data provided. This method can be used to determine the function for the variation in composition across a finite element using the compositional values stored at the underlying grid points.

The linear regression equation for the compositional variation across a two-dimensional finite element (such as that shown in Figure 9.11) can be expressed as

$$c(\xi, \eta) = \alpha_1 \xi + \alpha_2 \eta + \alpha_3 \tag{9.8}$$

where α_1 , α_2 and α_3 are the equation constants. The underlying cells that are taken into account in this analysis are those whose centre coordinates lie within the boundary of the finite element. This is to ensure that finite elements located close to phase boundaries do not significantly take into account compositional contributions from underlying cells that are partly located within other phase regions.

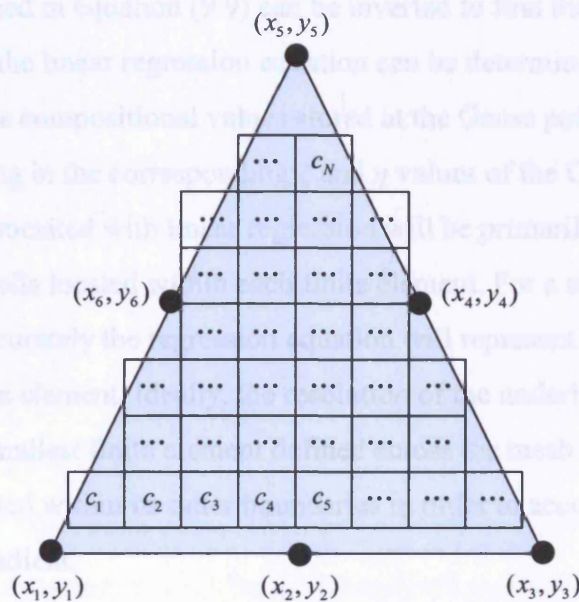


Figure 9.11 – The linear compositional variation across a two-dimensional quadratic-type finite element can be determined from the underlying cells by using linear regression.

Introduce a quadratic error function, E_{err} , such that

$$E_{err} = \sum_{i=1}^N (c_i - c(\xi_i, \eta_i))^2$$

Choosing α_1 , α_2 and α_3 such that the error function is minimised, i.e. $\frac{\partial E_{err}}{\partial \alpha_1} = 0$, $\frac{\partial E_{err}}{\partial \alpha_2} = 0$ and

$\frac{\partial E_{err}}{\partial \alpha_3} = 0$ gives

$$\begin{bmatrix} c_1 \\ c_2 \\ c_3 \end{bmatrix} = \begin{bmatrix} x_1 & x_2 & N \\ x_4 & x_3 & x_1 \\ x_3 & x_5 & x_2 \end{bmatrix} \begin{bmatrix} \alpha_1 \\ \alpha_2 \\ \alpha_3 \end{bmatrix} \quad (9.9)$$

where

$$\begin{aligned} c_1 &= \sum_{i=1}^N c_i & x_1 &= \sum_{i=1}^N \xi_i & x_4 &= \sum_{i=1}^N \xi_i^2 \\ c_2 &= \sum_{i=1}^N c_i \xi_i & x_2 &= \sum_{i=1}^N \eta_i & x_5 &= \sum_{i=1}^N \eta_i^2 \\ c_3 &= \sum_{i=1}^N c_i \eta_i & x_3 &= \sum_{i=1}^N \xi_i \eta_i \end{aligned}$$

The square matrix defined in equation (9.9) can be inverted to find the equation constants, α_i . Once these are known, the linear regression equation can be determined for the finite element from equation (9.8). The compositional values stored at the Gauss points can then be calculated by substituting in the corresponding ξ and η values of the Gauss points.

The accuracy associated with linear regression will be primarily dependent on the number of underlying cells located within each finite element. For a six-noded finite element, this will dictate how accurately the regression equation will represent the linear compositional gradient across the finite element. Ideally, the resolution of the underlying grid should be selected such that the smallest finite element defined across the mesh has the required number of underlying cells located within its outer boundaries in order to accurately reconstruct the linear compositional gradient.

(d) Volume Fraction Analysis

The linear regression and averaging mapping techniques are quick and efficient methods for mapping the composition from a relatively fine underlying grid back to the finite element mesh after the system has been re-meshed. However, these mapping techniques are

subject to error whenever a coarse underlying grid is selected such that no cell is completely located within the boundary of a finite element, as illustrated in Figure 9.12.

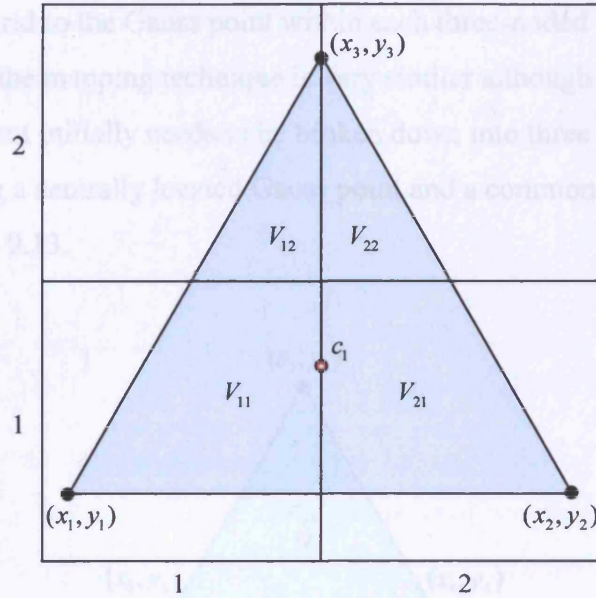


Figure 9.12 – A three-noded two-dimensional triangular finite element located within a 2×2 structured underlying grid.

It is therefore proposed to map the composition back to the Gauss point(s) within the finite element using volume fraction analysis, which is essentially the reverse method to that used to map the composition from the Gauss points to the underlying grid (see section 9.3.1). The area of a general finite element can be represented by

$$V_e = \sum_{i=i_{\min}^e}^{i_{\max}^e} \sum_{j=j_{\min}^e}^{j_{\max}^e} V_e^{[i,j]} = \frac{1}{2} J_e \quad (9.10)$$

where J_e is the determinant of the Jacobian for finite element, e , i_{\min}^e and i_{\max}^e represent the range of horizontal cells and j_{\min}^e and j_{\max}^e represent the range of vertical cells covering element, e , and $V_e^{[i,j]}$ is the volume contribution from element e , located within cell $[i,j]$ (defined in section 9.3.1). Following equation (9.5), the composition, c_g^e , at Gauss point, g , within finite element, e , is

$$c_g^e = \sum_{i=i_{\min}^e}^{i_{\max}^e} \sum_{j=j_{\min}^e}^{j_{\max}^e} \mu_{[i,j]}^e c_{[i,j]} \quad (9.11)$$

where $\mu_{[i,j]}^e = \frac{V_e^{[i,j]}}{V_e}$ is the volume fraction from cell $[i,j]$, located within finite element e .

The method discussed above is directly applicable for mapping the compositional data stored across the underlying grid to the Gauss point within each three-noded finite element. For six-noded finite elements, the mapping technique is very similar although slightly more complex. In this case, each element initially needs to be broken down into three separate sections, with each section containing a centrally located Gauss point and a common elemental mid-point, as shown below in Figure 9.13.

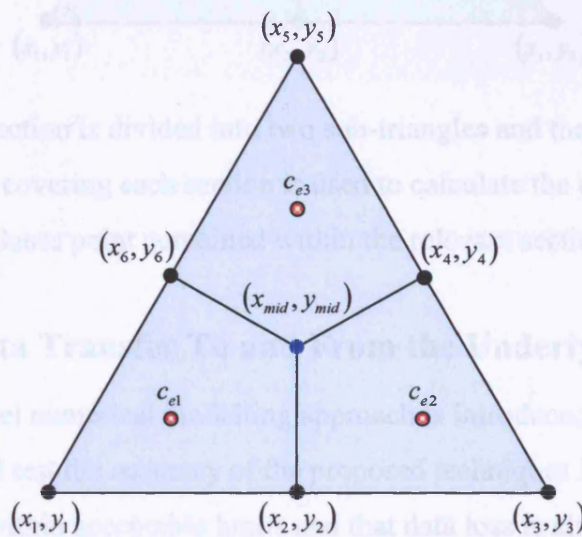


Figure 9.13 – A six-noded finite element split into three equal sections, with a single Gauss point contained with each section.

Each section therefore comprises of one corner nodal point, two nodal mid-points and the common element mid-point. Each section is then divided into two sub-triangles as shown in Figure 9.14, and the volume fractions are individually calculated (with respect to one third of the area of the finite element, i.e. the area of each section) for both sub-triangles within each section. The cell compositions and volume fractions are then used to map the composition to the corresponding Gauss point located within each section of the finite element through application of equation (9.11).

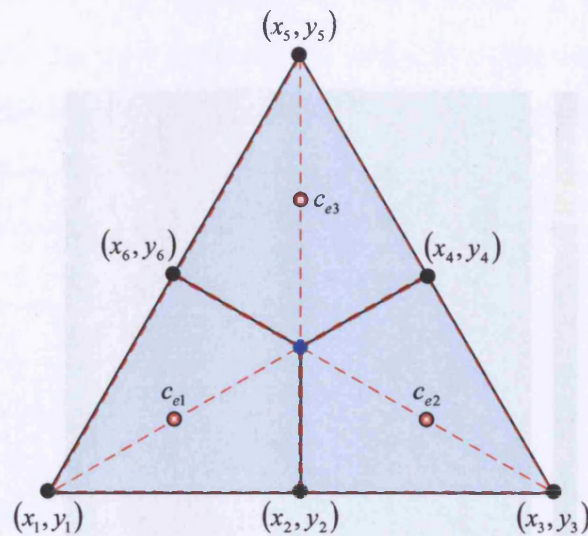


Figure 9.14 – Each section is divided into two sub-triangles and the volume fraction of the underlying cells covering each section is used to calculate the composition at the Gauss point contained within the relevant section.

9.3.3 – Testing Data Transfer To and From the Underlying Grid

Whenever a novel numerical modelling approach is introduced, it is always necessary to formally validate and test the accuracy of the proposed techniques in order to ensure that numerical accuracy is within acceptable limits and that data loss is always kept to a minimum. Data transfer from the finite element mesh to an underlying grid of defined resolution and vice versa using the mapping techniques (that have been considered within this chapter) is investigated with regards to the numerical error and time associated with the mapping process.

A sine wave function is defined across a finite element mesh of 1,024 six-noded two-dimensional finite elements as shown in Figure 9.15. The data stored at the Gauss points across the finite element mesh is mapped to a structured underlying grid using volume fraction analysis, and the data across the grid is then mapped back to an identical finite element mesh. An error check is carried out between the original sine wave data and the reconstructed data mapped back to the finite element mesh. This process is outlined in Figure 9.16 and is examined for three different underlying grid to finite element mesh mapping techniques (Gauss point, linear regression and volume fraction mapping). All of these methods are shown to vary in terms of both numerical accuracy and computational processing time taken during the mapping process.

The results from the numerical mapping test are shown in Table 9.3, Figure 9.17 and Figure 9.18. The first column of the table shows the mesh size and the corresponding processing time taken during the mapping process. Two test cases are shown in the table.

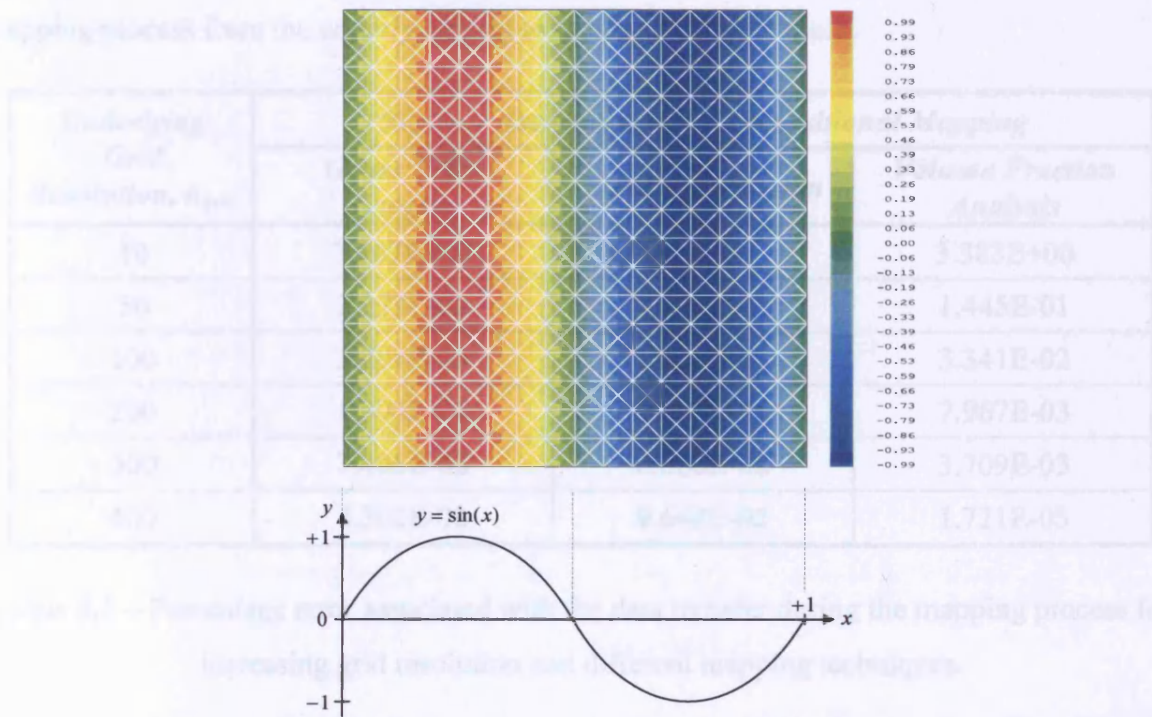


Figure 9.15 – Sine wave data stored across a finite element mesh of 1,024 six-noded quadratic-type finite elements.

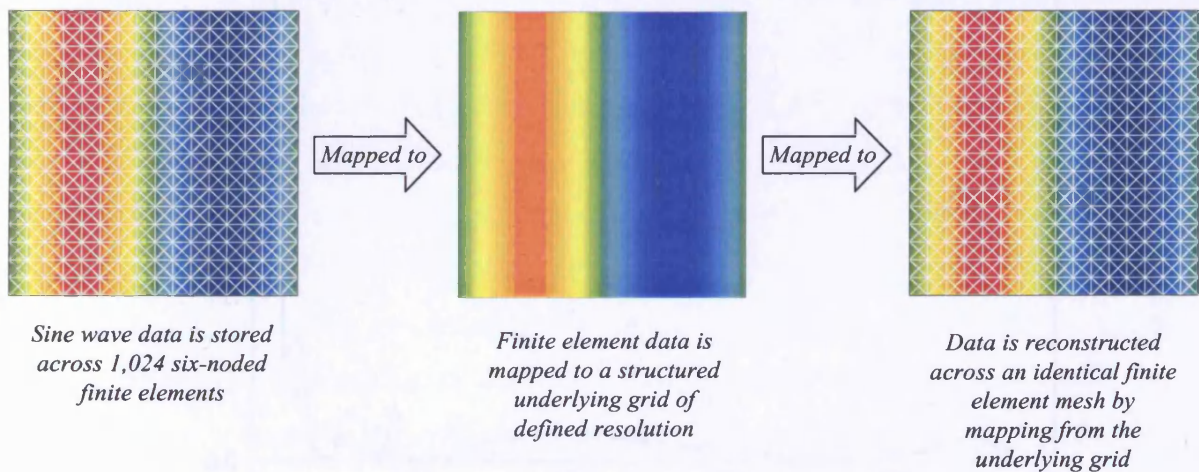


Figure 9.16 – Procedure for testing the accuracy of data transfer to and from a structured underlying grid.

The results from the numerical mapping test are shown in Table 9.1, Figure 9.17 and Figure 9.18 in terms of the numerical error and computational processing time taken during the mapping process from the underlying grid to the finite element mesh.

<i>Underlying Grid Resolution, n_{grid}</i>	<i>% Error Associated with Compositional Mapping</i>		
	<i>Gauss Point Mapping</i>	<i>Linear Regression</i>	<i>Volume Fraction Analysis</i>
10	3.967E+00	N/A	3.383E+00
50	2.273E-02	7.222E-02	1.445E-01
100	3.798E-03	1.224E-02	3.341E-02
200	1.996E-01	7.498E-02	7.967E-03
300	7.495E-02	6.886E-02	3.709E-03
400	4.302E-02	9.648E-02	1.721E-03

Table 9.1 – Percentage error associated with the data transfer during the mapping process for increasing grid resolution and different mapping techniques.

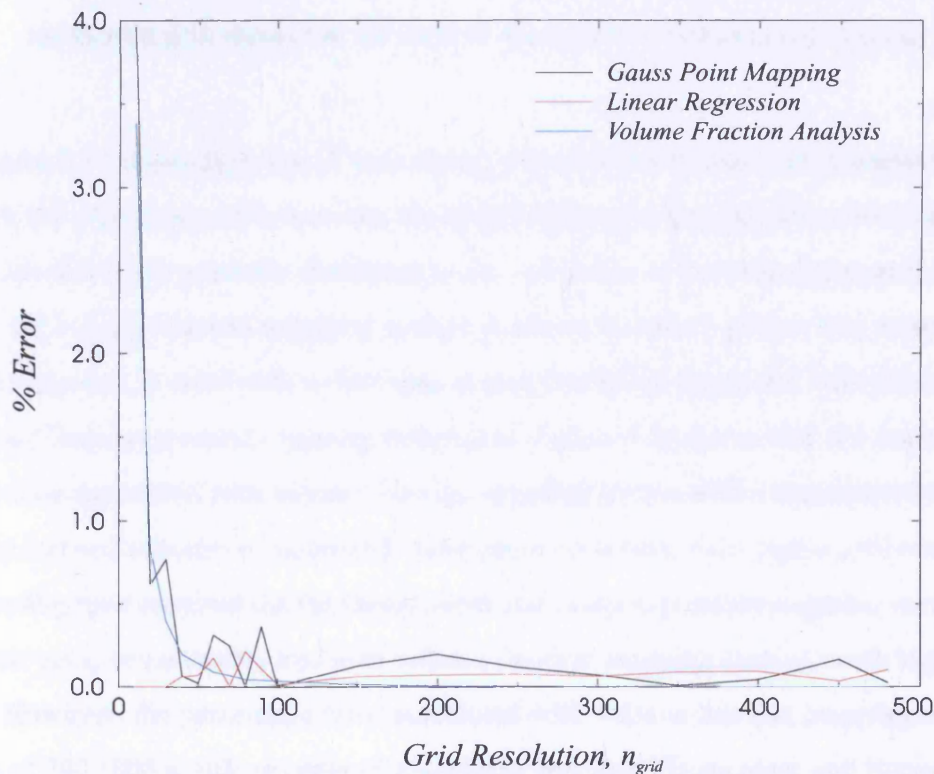


Figure 9.17 – Graph showing the percentage error associated with the mapping process for increasing grid resolution for each of the different mapping techniques.

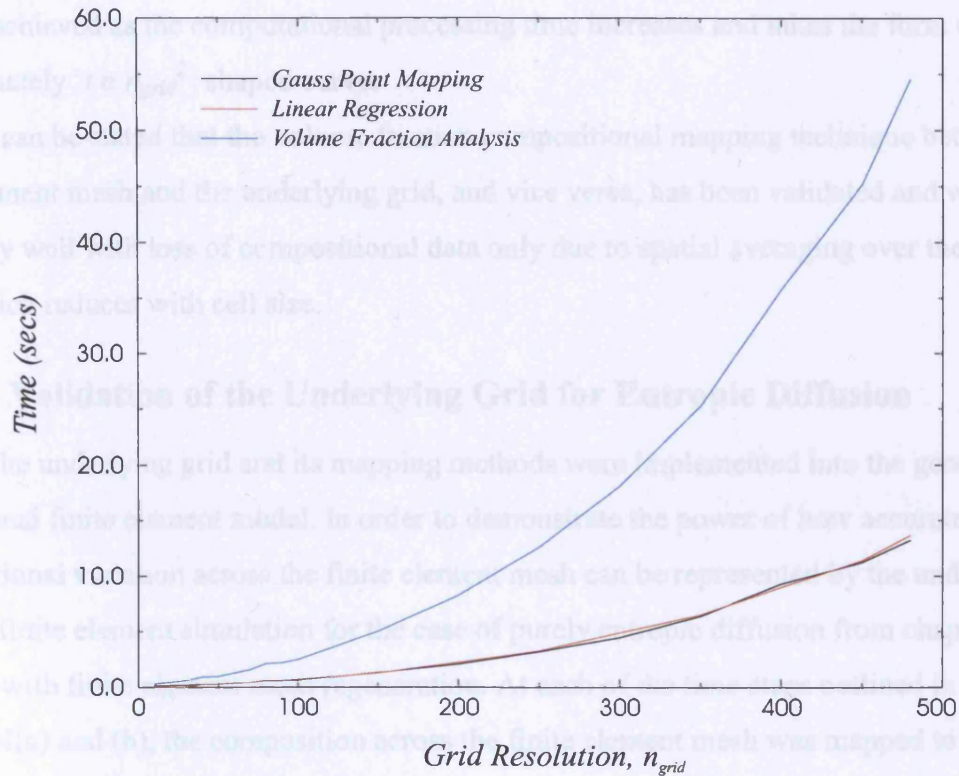


Figure 9.18 – Graph showing the computational time associated with the mapping process for increasing grid resolution for each of the different mapping techniques.

Figure 9.17 shows that, for all underlying grid to finite element mesh mapping techniques, the percentage error between the original data and the reconstructed data across the finite element mesh generally decreases as the resolution of the underlying grid increases. However, the volume fraction mapping method is shown to have a greater and more consistent reduction in error with an increase in grid resolution compared with the Gauss point mapping and linear regression mapping techniques. Figure 9.18 shows that the increase in error reduction associated with volume fraction mapping comes with a computational processing cost and requires considerably more processing time with higher grid resolutions. The processing time required for the Gauss point and linear regression mapping methods is very similar yet is considerably less than volume fraction mapping even at much higher grid densities. However, the percentage error associated with volume fraction mapping using a grid resolution of 200×200 is still an order of magnitude less than Gauss point and linear regression mapping using double this grid resolution for approximately the same processing time. For grid resolutions of over 250×250 , only a minor error reduction and little benefit is

actually achieved as the computational processing time increases and takes the form of an approximately ' $t \propto n_{grid}^2$ ' shaped curve.

It can be stated that the volume fraction compositional mapping technique between the finite element mesh and the underlying grid, and vice versa, has been validated and works efficiently well with loss of compositional data only due to spatial averaging over the grid cells, which reduces with cell size.

9.3.4 – Validation of the Underlying Grid for Entropic Diffusion

The underlying grid and its mapping methods were implemented into the general two-dimensional finite element model. In order to demonstrate the power of how accurately the compositional variation across the finite element mesh can be represented by the underlying grid, the finite element simulation for the case of purely entropic diffusion from chapter 7 was restarted with finite element mesh regeneration. At each of the time steps outlined in Figure 7.4(a) and (b), the composition across the finite element mesh was mapped to a 200×200 underlying grid, the finite element mesh was regenerated, the compositional data was then mapped back to an identical finite element geometry and the entropic finite element simulation continued. The three-noded and six-noded results for the evolution of an initial step change in carbon composition due to entropy are compared with analytical results, as before, as shown in Figure 9.19 and Figure 9.20 respectively.

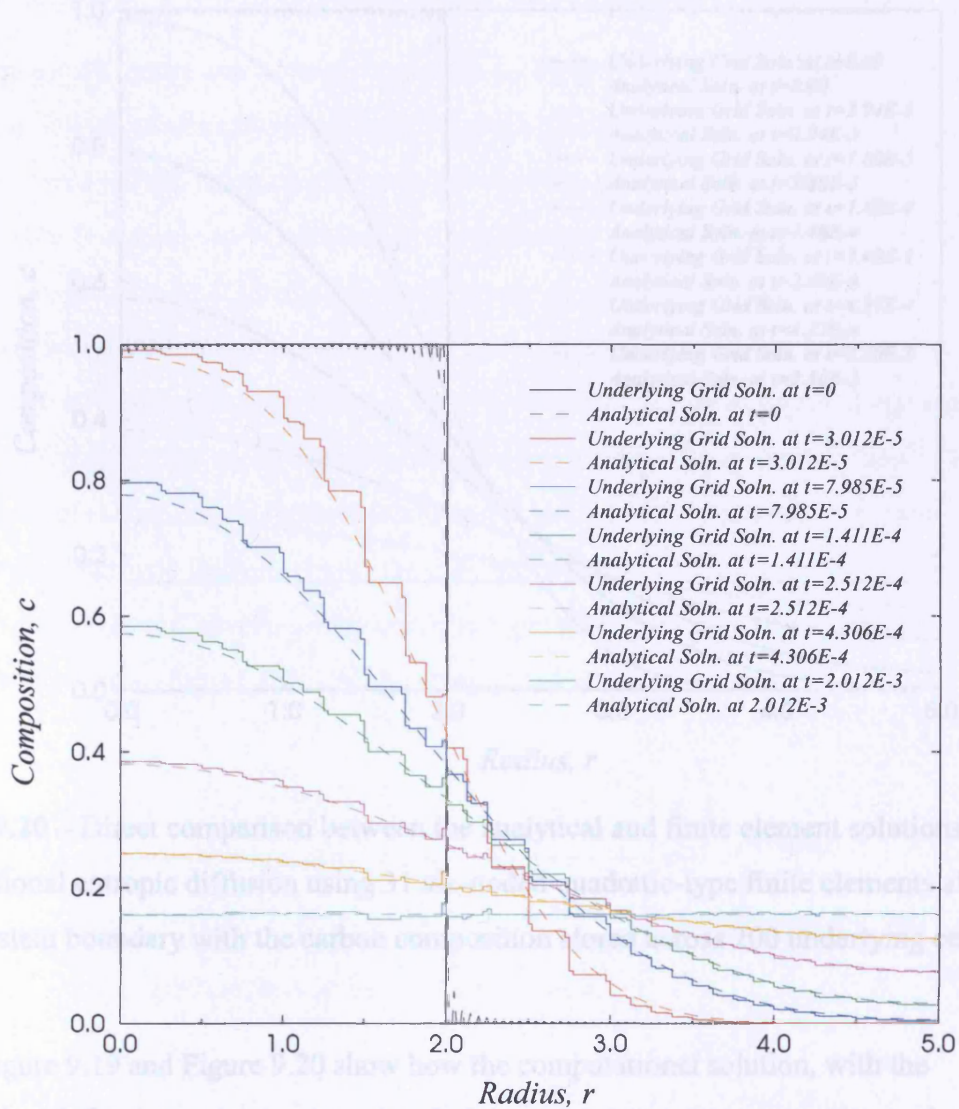


Figure 9.19 – Direct comparison between the analytical and finite element solutions for two-dimensional entropic diffusion using 31 three-noded linear-type finite elements along the system boundary with the carbon composition stored across 200 underlying cells.

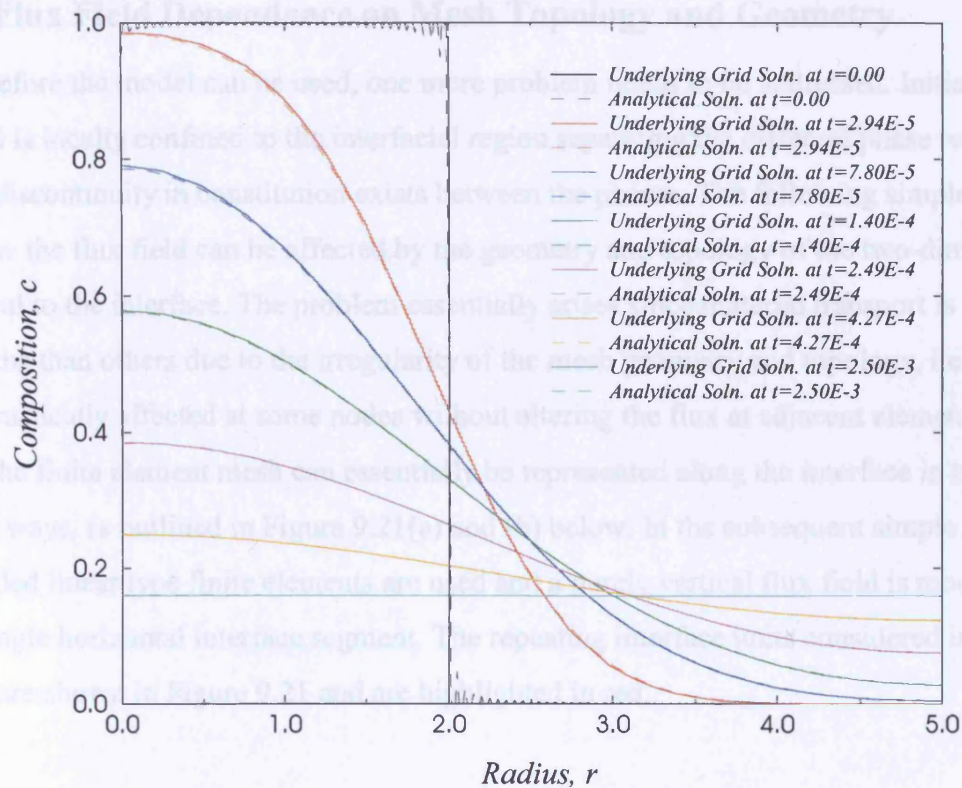


Figure 9.20 – Direct comparison between the analytical and finite element solutions for two-dimensional entropic diffusion using 31 six-noded quadratic-type finite elements along the system boundary with the carbon composition stored across 200 underlying cells.

Figure 9.19 and Figure 9.20 show how the computational solution, with the composition defined across a structured underlying grid, attempts to approximate the analytical solution by constant (Figure 9.19) and linear (Figure 9.20) elemental compositional step functions. As expected, the linear compositional step function over each element, as shown in Figure 9.20, is in excellent agreement with the analytical solution. It can be seen from these Figures that the volume fraction mapping does not significantly affect the results.

9.4 – Flux Field Dependence on Mesh Topology and Geometry

Before the model can be used, one more problem needs to be addressed. Initially the flux field is locally confined to the interfacial region separating the different phase regions if a definite discontinuity in constitution exists between the phases. The following simple cases show how the flux field can be affected by the geometry and topology of the two-dimensional mesh local to the interface. The problem essentially arises since material transport is easier by some paths than others due to the irregularity of the mesh geometry and topology, i.e. the flux can be drastically affected at some nodes without altering the flux at adjacent elemental nodes.

The finite element mesh can essentially be represented along the interface in two different ways, as outlined in Figure 9.21(a) and (b) below. In the subsequent simple models, three-noded linear type finite elements are used and a purely vertical flux field is modelled over a single horizontal interface segment. The repeating interface units considered in this analysis are shown in Figure 9.21 and are highlighted in red.

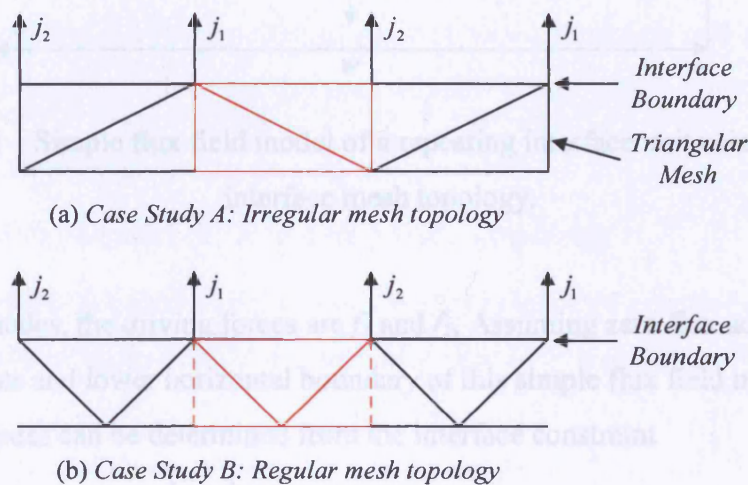


Figure 9.21 – Two different types of interface mesh topology considered in the simple flux field model.

9.4.1 – Flux Field Model A: Irregular Mesh Topology

The simplified flux field model across a repeating interface segment block of the irregular mesh shown in Figure 9.21(a) can be represented by Figure 9.22 below.

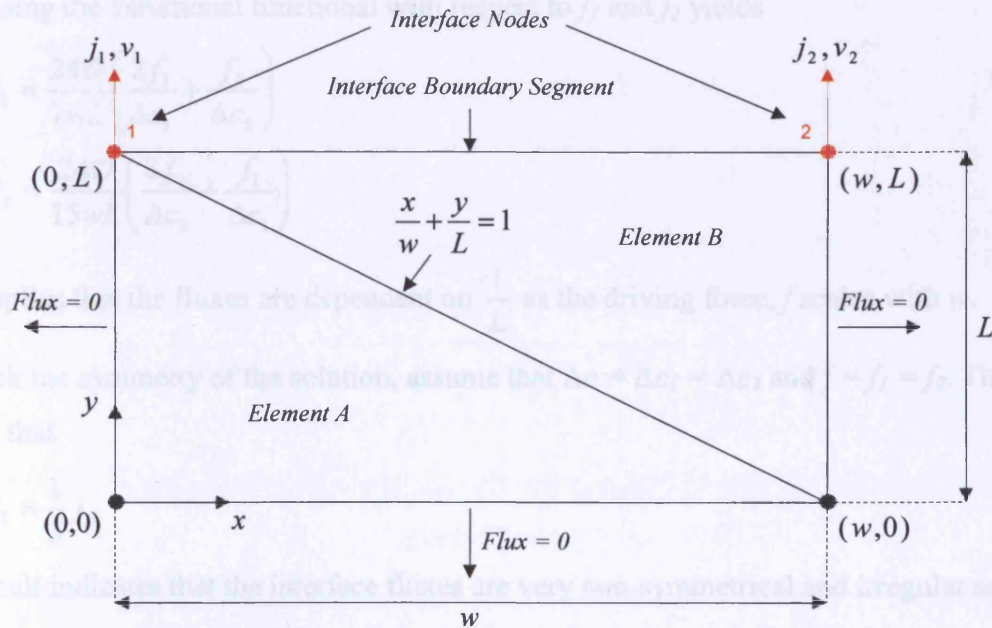


Figure 9.22 – Simple flux field model of a repeating interface unit using an irregular interface mesh topology.

At the interface nodes, the driving forces are f_1 and f_2 . Assuming zero flux across the two vertical boundaries and lower horizontal boundary of this simple flux field model, the fluxes at the interface nodes can be determined from the interface constraint

$$j_1 = \Delta c_1 v_1 \quad j_2 = \Delta c_2 v_2 \quad (9.12)$$

where Δc_1 and Δc_2 are the compositional differences across the interface segment at nodes 1 and 2 respectively. The flux field across elements *A* and *B* can each be described by a linear function of x and y as follows

$$j_A(x, y) = j_1 \frac{y}{L} \quad j_B(x, y) = j_2 \left(\frac{x}{w} + \frac{y}{L} - 1 \right) + j_1 \left(1 - \frac{x}{w} \right)$$

Ignoring the driving forces due to the rate of change of composition, one can write the variational functional as

$$\Pi = \frac{wL}{24\mathcal{D}}(4j_1^2 - j_1j_2 + j_2^2) - f_1v_1 - f_2v_2$$

Minimising the variational functional with respect to j_1 and j_2 yields

$$\begin{aligned} j_1 &= \frac{24\mathcal{D}}{7wL} \left(\frac{2f_1}{\Delta c_1} + \frac{f_2}{\Delta c_2} \right) \\ j_2 &= \frac{24\mathcal{D}}{15wL} \left(\frac{8f_2}{\Delta c_2} + \frac{f_1}{\Delta c_1} \right) \end{aligned} \tag{9.13}$$

This implies that the fluxes are dependent on $\frac{1}{L}$ as the driving force, f scales with w .

To check the symmetry of the solution, assume that $\Delta c = \Delta c_1 = \Delta c_2$ and $f = f_1 = f_2$. This implies that

$$j_1 = \frac{1}{3}j_2 \tag{9.14}$$

This result indicates that the interface fluxes are very non-symmetrical and irregular across the repeating interface segment block and that their relation to one another is independent of w and L .

9.4.2 – Flux Field Model B: Regular Mesh Topology

The simplified flux field model across a repeating interface segment block of the regular mesh shown in Figure 9.21(b) can be represented by Figure 9.23.

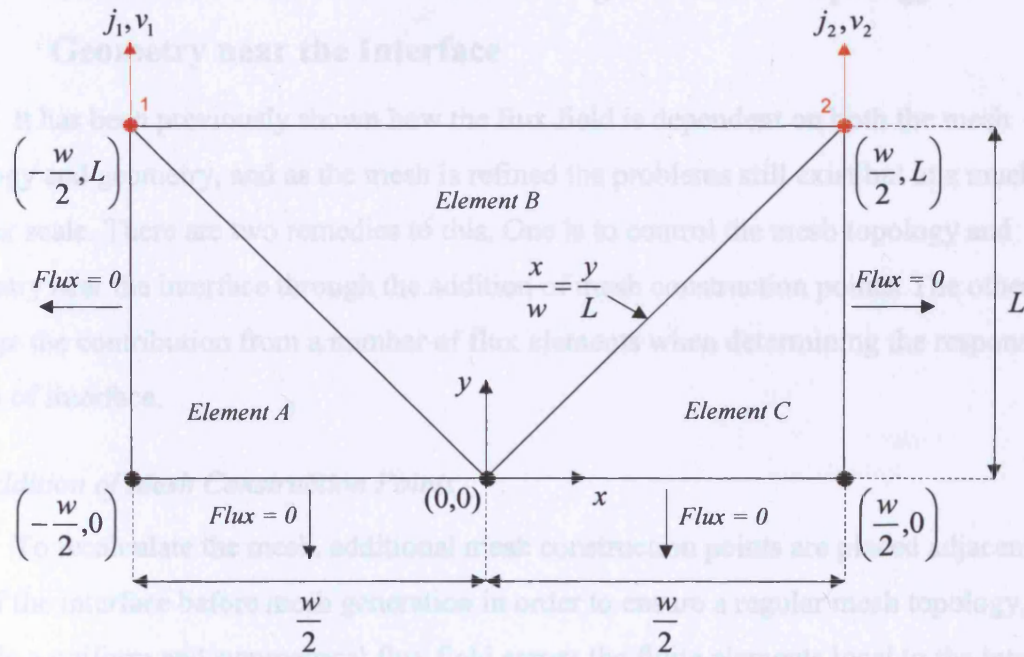


Figure 9.23 – Simple flux field model of a repeating interface unit using a regular interface mesh topology.

As considered in the previous sub-section for an irregular flux field model, the interface fluxes can be related to the interfacial velocities by equation (9.12).

Hence

$$\Pi = \frac{wL}{24\mathcal{D}} \left(\frac{5}{2} j_1^2 - j_1 j_2 + \frac{5}{2} j_2^2 \right) - f_1 v_1 - f_2 v_2$$

Minimising the variational functional with respect to j_1 and j_2 yields

$$\begin{aligned} j_1 &= \frac{\mathcal{D}}{wL} \left(\frac{5f_1}{\Delta c_1} + \frac{f_2}{\Delta c_2} \right) \\ j_2 &= \frac{\mathcal{D}}{wL} \left(\frac{5f_2}{\Delta c_2} + \frac{f_1}{\Delta c_1} \right) \end{aligned} \tag{9.15}$$

Again assuming that $\Delta c = \Delta c_1 = \Delta c_2$ and $f = f_1 = f_2$, one gets

$$j_1 = j_2 \tag{9.16}$$

This result indicates that the interface fluxes are symmetric across the repeating interface segment block for the regular mesh topology shown in Figure 9.21(b) and Figure 9.23.

9.4.3 – Mesh Construction to Ensure a Regular Mesh Topology & Geometry near the Interface

It has been previously shown how the flux field is dependent on both the mesh topology and geometry, and as the mesh is refined the problems still exist but at a much smaller scale. There are two remedies to this. One is to control the mesh topology and geometry near the interface through the addition of mesh construction points. The other is to average the contribution from a number of flux elements when determining the response of a length of interface.

(a) Addition of Mesh Construction Points

To recalculate the mesh, additional mesh construction points are placed adjacent to the line of the interface before mesh generation in order to ensure a regular mesh topology, and to provide a uniform and symmetrical flux field across the finite elements local to the interface boundary.

To improve the computed solution near the interface boundary, the finite element mesh density can be increased, if required, around the interfacial region. It is therefore possible to have more than one finite element edge per interface boundary segment, and these are referred to as interface boundary sub-segments.

Mesh construction points are created by projecting points a set distance away from the mid-point of each interface boundary sub-segment in a direction normal to each interface boundary segment. The projected points are in turn connected to the two nearest nodal points placed along the interface boundary. Careful control over the distance that the construction points are placed away from the boundary sub-segments is taken in order to maintain the regularity of the elements and to avoid sub-division due to minimum angle constraints imposed during mesh generation. If the minimum meshing angle is taken as β , no triangles can be generated within the finite element mesh that have angles smaller than this.

Consider the interface boundary sub-segment shown in Figure 9.24.

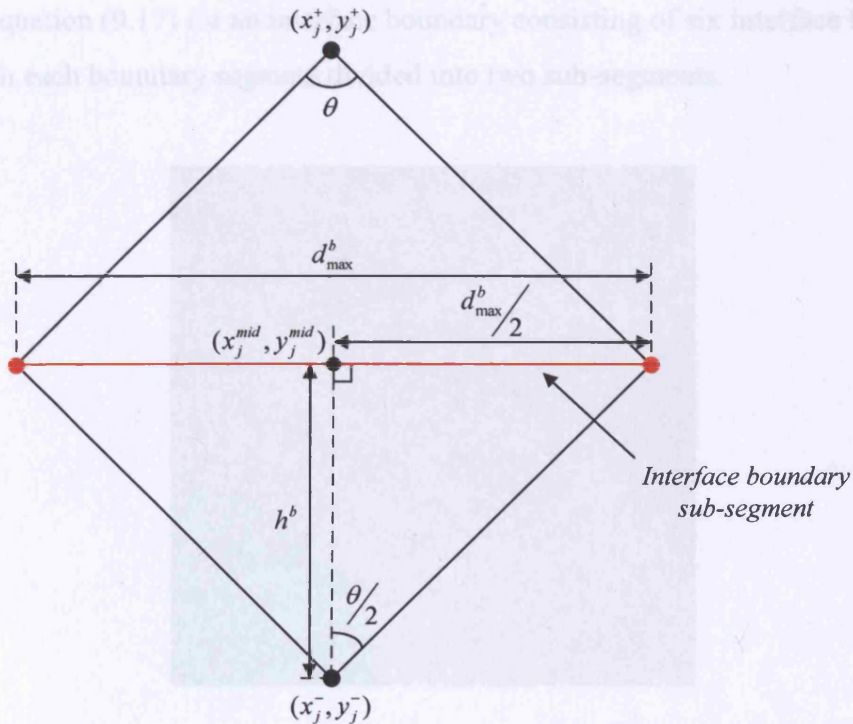


Figure 9.24 – Interface elements are constructed (by calculating the length, h^b) such that the minimum meshing angle is not violated and the finite elements cannot be sub-divided further.

If the angle, θ is selected such that $\theta = 2\beta$, the constructed interface element can be split into two further elements without violating any mesh angle constraints. However, if the angle, θ , is calculated such that $\theta < 2\beta$, the constructed interface element cannot be sub-divided any further and the distance, h^b , along interface boundary, b , can be calculated from

$$h^b = \frac{d_{\max}^b}{2} \tan\left(\frac{\theta}{2}\right) \quad (9.17)$$

where d_{\max}^b represents the maximum interface sub-segment length associated with interface boundary b . This maximum distance is considered since some interface boundary segments may grow or shrink faster than others, depending on the varying magnitude of the driving forces along the interface and on any form of external loading applied to the system.

Having calculated the mid point coordinates $(x_j^{\text{mid}}, y_j^{\text{mid}})$ of the interface boundary sub-segment, j , the inner and outer mesh construction point coordinates are set at a distance, h^b , normal to and on either side of the boundary from this point. Figure 9.25 shows an illustration

of applying equation (9.17) for an interface boundary consisting of six interface boundary segments with each boundary segment divided into two sub-segments.

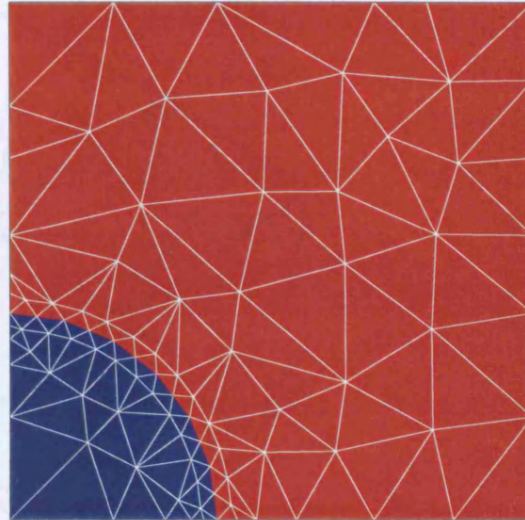


Figure 9.25 – Additional mesh construction points are added along either side of the interface boundary to ensure a regular mesh topology and geometry near the interface.

(b) Linear Velocity Field across each Interface Boundary Segment

The second remedy is achieved through linear interpolation functions, which are employed to ensure a linear velocity field across each interface boundary segment such that the velocity at any point along the segment can be related to the velocities at the outer segment nodes. This implies that the velocity degrees of freedom along the interface will be linked together.

Consider the situation described in Figure 9.26, where an interface boundary segment, t , is sub-divided into four regularly spaced boundary sub-segments. As discussed in the previous sub-section, additional mesh construction points are added along either side of the interface boundary to ensure a regular mesh topology and geometry near the interface. In order to ensure a linear velocity field across the interface segment, it is necessary to impose additional constraints at locations s_1 , s_2 and s_3 in order to ensure that the interface nodal velocities at each of these points are consistent with the nodal velocities, v'_{nA} and v'_{nB} , defined at the outer nodes of the segment.

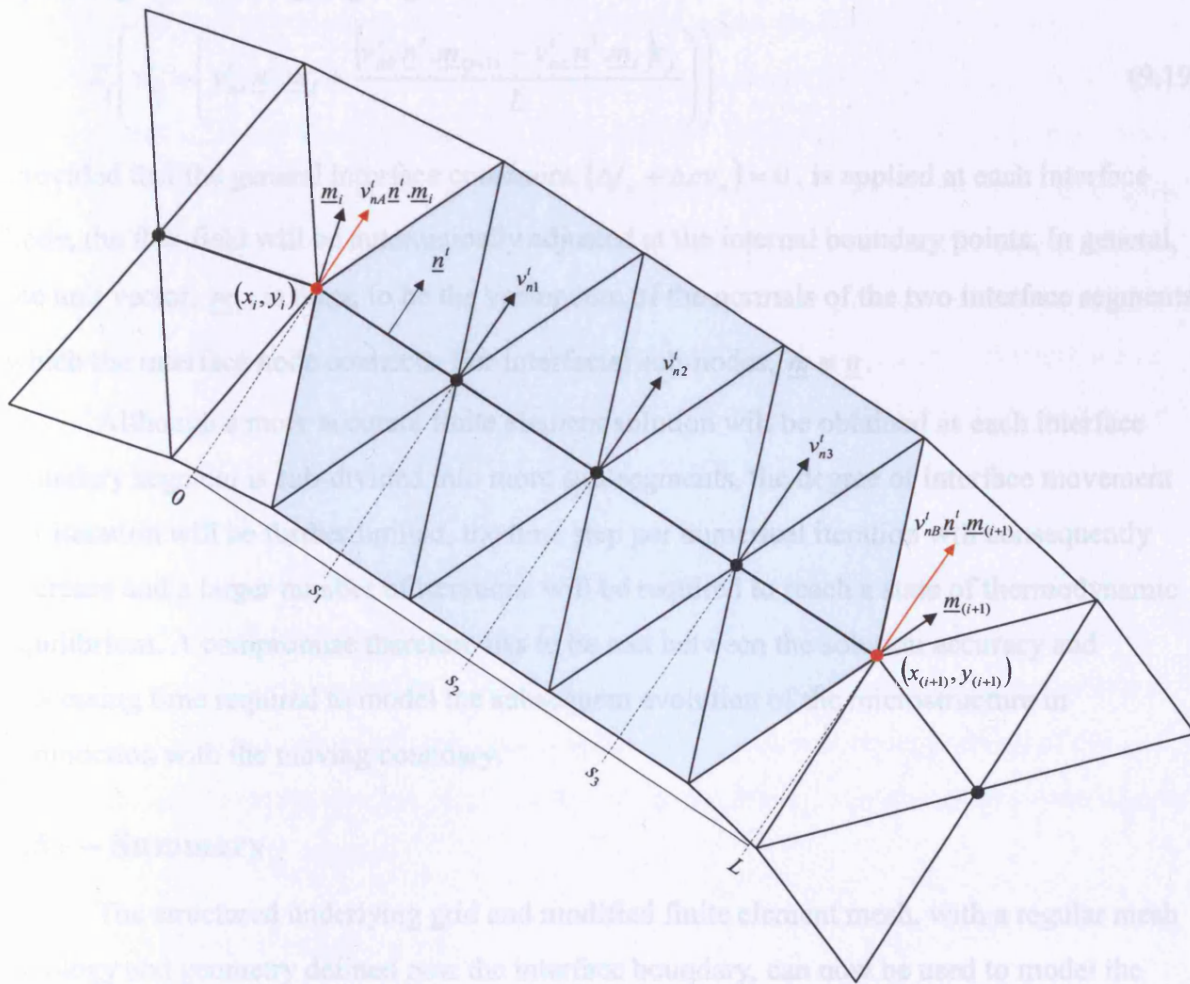


Figure 9.26 – An interface boundary segment sub-divided into a series of four regularly spaced sub-segments, where the velocities at the outer segment nodes dictate the velocity variation over the segment.

Given the unit directions of movement of the interfacial end nodes, \underline{m}_i and \underline{m}_{i+1} , the interface velocity variation over boundary segment, t , can be described by

$$v_{nj}^t = v_{nA}^t \underline{n}^t \cdot \underline{m}_i + \frac{s_j}{L} \left(v_{nB}^t \underline{n}^t \cdot \underline{m}_{(i+1)} - v_{nA}^t \underline{n}^t \cdot \underline{m}_i \right) \quad (9.18)$$

where \underline{n}^t is the unit normal to interface boundary t .

Therefore at location s_j , a constraint can be imposed on the corresponding nodal velocity, v_{nj}^t , by adding the following Lagrangian term to the variational functional

$$\lambda_j^t \left(v_{nj}^t - \left(v_{nA}^t \underline{n}^t \cdot \underline{m}_i + \frac{(v_{nB}^t \underline{n}^t \cdot \underline{m}_{(i+1)} - v_{nA}^t \underline{n}^t \cdot \underline{m}_i) s_j}{L} \right) \right) \quad (9.19)$$

Provided that the general interface constraint, $(\Delta j_n + \Delta c v_n) = 0$, is applied at each interface node, the flux field will be automatically adjusted at the internal boundary points. In general, the unit vector, \underline{m}_i , is taken to be the vector sum of the normals of the two interface segments which the interface node connects. For interfacial sub-nodes, $\underline{m} \equiv \underline{n}$.

Although a more accurate finite element solution will be obtained as each interface boundary segment is sub-divided into more sub-segments, the degree of interface movement per iteration will be further limited, the time step per numerical iteration will consequently decrease and a larger number of iterations will be required to reach a state of thermodynamic equilibrium. A compromise therefore has to be met between the solution accuracy and processing time required to model the subsequent evolution of the microstructure in conjunction with the moving boundary.

9.5 – Summary

The structured underlying grid and modified finite element mesh, with a regular mesh topology and geometry defined near the interface boundary, can now be used to model the evolution of a general microstructure within a moving boundary framework. The general model described in chapter 4 along with the modifications discussed in this chapter can now be applied to model both the kinetics and thermodynamics of microstructural evolution of a range of real material systems.

The subsequent chapter examines the implementation of the general model in order to model the growth of a nucleus of ferrite embedded in an austenite matrix. This system consists of two different phase regions with different material properties which are separated by an interface boundary with a single diffusing species. The main purpose of research in this area is to investigate the effects of elasticity on microstructure evolution within the iron-carbon dual phase system under high temperatures and stresses.

10.0 – Evolution of a Ferrite Precipitate

There is currently much research being carried out in the field of modelling microstructural phase transformations associated with precipitate strengthening in steel alloys. An overview of recent work is presented in this section, followed by an examination of how the general variational model, along with the modifications discussed in the previous chapter, can be used to model the mechanisms of morphological evolution of a ferrite precipitate embedded within an austenite matrix in plain carbon steel. Since precipitate shape and size play a major role in determining mechanical and other physical properties of materials, it is important to understand the evolution of precipitates during solid-solid phase transformations.

The situation is considered where material rearrangement occurs by interstitial diffusion driven by compositional variations, phase transformations and changes of elastic stored energy. The system consists of two different phase regions with different material properties separated by an interface boundary with a single diffusing species. The problem however contains all the ingredients for the analysis of multi-component diffusion problems. The main purpose of research in this area is to develop the current understanding of the microstructural material changes which occur within the iron-carbon dual phase system under high temperatures and stresses.

10.1 – Physical Background

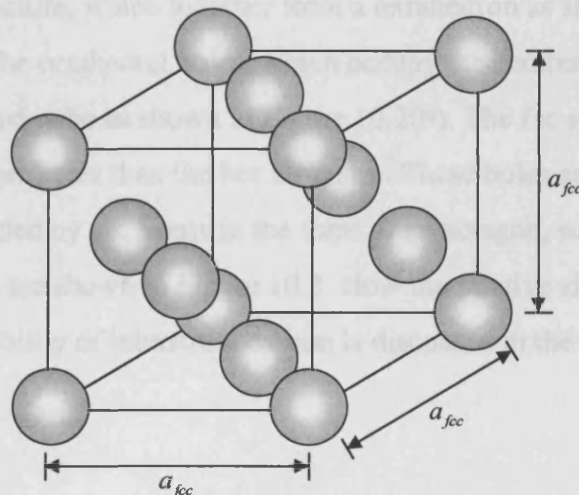
Steel is a generic name for alloys of iron and carbon that have many useful engineering properties and have widespread applications within the engineering industry. The mechanical properties of steel are strongly dependent on both the carbon content and on the type of selective heat treatment employed. Heat treatments involve the alteration of the microstructure by physical processes involving phase transformations in order to achieve the required material properties for a particular engineering application.

In its pure form, iron is soft and generally not useful as an engineering material. However, the principal method of strengthening it and converting it into steel is by adding small amounts of carbon. In solid steel, carbon is generally found in two forms, either in solid solution in austenite and ferrite, or as carbide. Iron (Fe) is a relatively dense allotropic metal with a silvery white appearance and distinctive magnetic properties. Its crystal structure either comprises the body-centred cubic (bcc) or face-centred cubic (fcc) atomic arrangement,

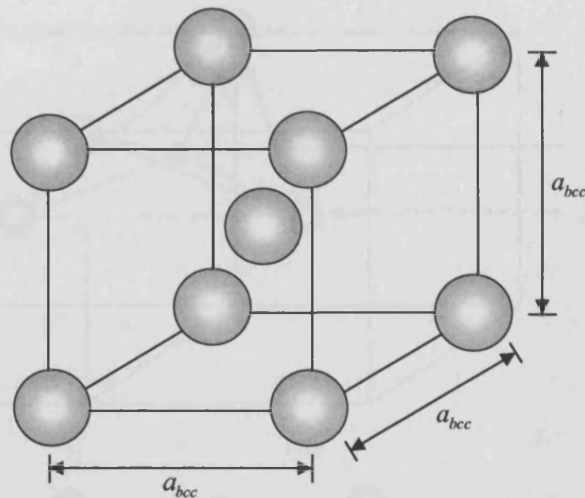
depending on both the carbon composition and temperature. At room temperature, pure iron has a bcc structure referred to as alpha-ferrite which persists until the temperature is raised to 912°C, when it transforms into an fcc arrangement known as austenite. With further heating, austenite remains until the temperature reaches 1,394°C, at which point the bcc structure reappears. This form of iron, called delta-ferrite, remains until the melting point is reached. These phase changes can be easily followed and understood by considering the iron-carbon phase diagram shown in Figure 2.3.

10.2 – The Two Phases: α - and γ -iron

The γ - to α - transformation is accompanied by an atomic volume change which can lead to the generation of internal stresses during transformation. The detailed geometry of the unit cells of α - and γ -iron crystals is particularly relevant to understanding the physics behind the generation of internal stresses during the phase transformation and to the difference in solubility of a non-metallic element such as carbon within these two phases. The atomic arrangement of the body-centred cubic (bcc) form (α -iron, ferrite) and face-centred cubic (fcc) form (γ -iron, austenite) are shown in Figure 10.1 below.



(a) Austenite (γ -phase) – The higher density, high temperature fcc form of iron contains 4 iron atoms per unit cell with a packing density of 74%.



(b) Ferrite (α -phase) – The bcc form of iron contains 2 iron atoms per unit cell with a packing density of 68%.

Figure 10.1 – The (a) face-centred-cubic unit cell of γ -phase austenite and (b) body-centred-cubic unit cell of α -phase ferrite.

The bcc structure of α -iron is more loosely packed than that of fcc γ -iron. The largest cavities in the bcc structure are the tetrahedral holes existing between the two edge and two central atoms in the structure, which together form a tetrahedron as shown in Figure 10.2(a). The second largest are the octahedral holes, which occupy the centres of the faces and the edges of the body-centred-cube as shown in Figure 10.2(b). The fcc structure, although more closely-packed, has larger holes than the bcc structure. These holes are at the centres of the cube edges and surrounded by six atoms in the form of an octagon, so are referred to as octahedral holes, which are shown in Figure 10.3. How the relative sizes of the interstitial sites influences the solubility of interstitial carbon is discussed in the following sub-section.



Figure 10.3 – The octahedral interstitial sites available within the fcc unit structure [54]

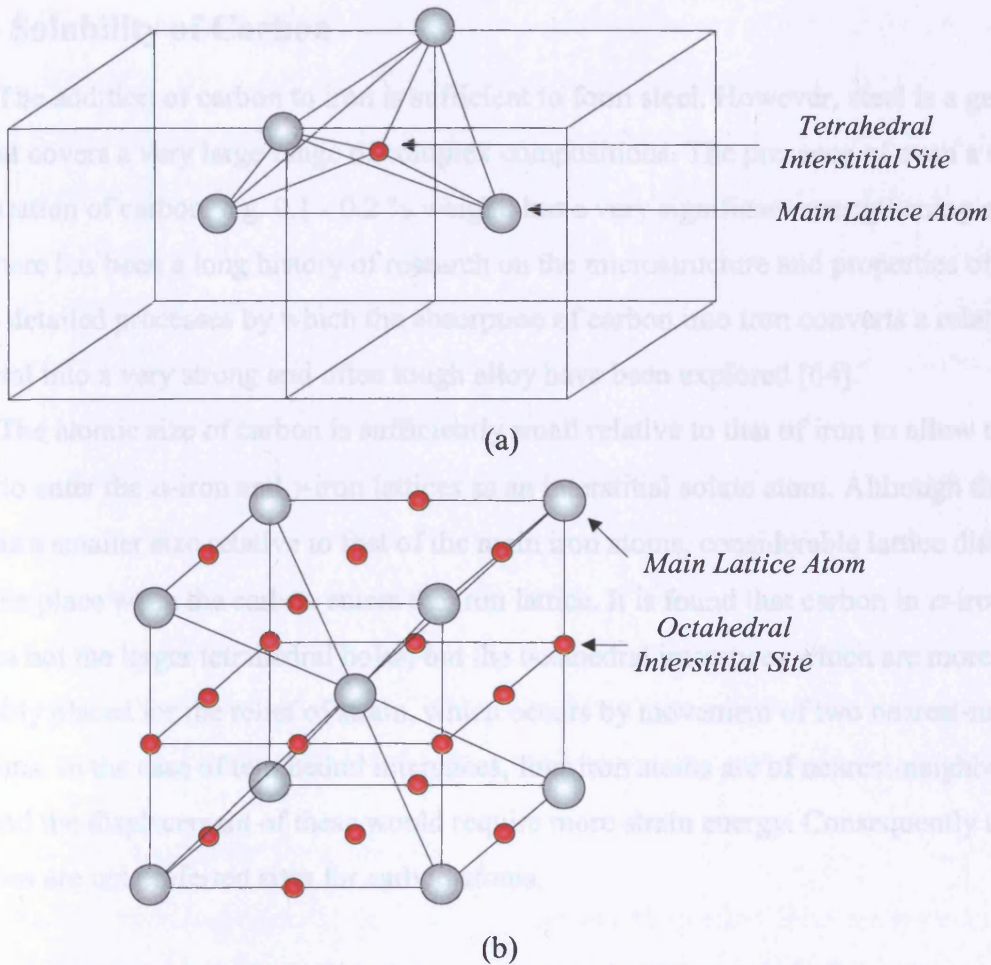


Figure 10.2 – The (a) tetrahedral and (b) octahedral interstitial sites available within the bcc unit structure [64].

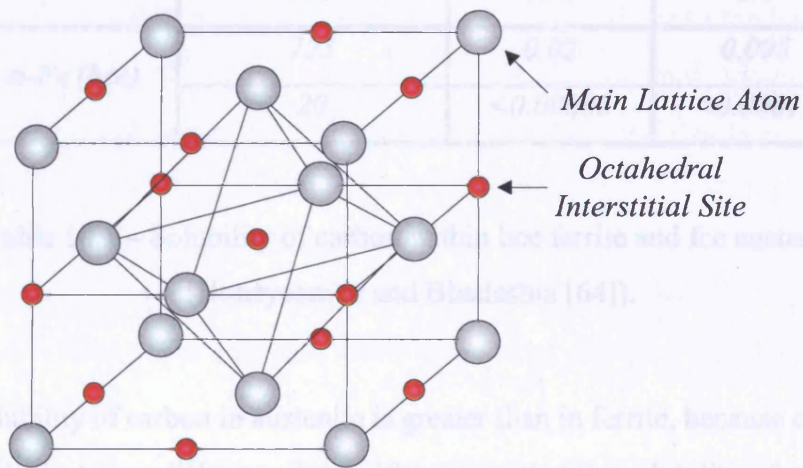


Figure 10.3 – The octahedral interstitial sites available within the fcc unit structure [64].

10.3 – Solubility of Carbon

The addition of carbon to iron is sufficient to form steel. However, steel is a generic term that covers a very large range of complex compositions. The presence of even a small concentration of carbon, e.g. 0.1 - 0.2 % weight, has a very significant strengthening effect on iron. There has been a long history of research on the microstructure and properties of steel, and the detailed processes by which the absorption of carbon into iron converts a relatively soft metal into a very strong and often tough alloy have been explored [64].

The atomic size of carbon is sufficiently small relative to that of iron to allow the carbon to enter the α -iron and γ -iron lattices as an interstitial solute atom. Although the carbon atom has a smaller size relative to that of the main iron atoms, considerable lattice distortion must take place when the carbon enters the iron lattice. It is found that carbon in α -iron occupies not the larger tetrahedral holes, but the octahedral interstices which are more favourably placed for the relief of strain, which occurs by movement of two nearest-neighbour iron atoms. In the case of tetrahedral interstices, four iron atoms are of nearest-neighbour status and the displacement of these would require more strain energy. Consequently these interstices are not preferred sites for carbon atoms.

Phase	Temperature (°C)	Carbon Solubility	
		wt%	at%
γ -Fe (fcc)	1150	2.04	8.8
	723	0.80	3.6
α -Fe (bcc)	723	0.02	0.095
	20	<0.00005	<0.00012

Table 10.1 – Solubility of carbon within bcc ferrite and fcc austenite (Honeycombe and Bhadeshia [64]).

The solubility of carbon in austenite is greater than in ferrite, because of the larger interstices available during diffusion. Table 10.1 shows that the solubility of carbon in γ -iron can be as high as 9% in contrast to the maximum solubility of carbon in α -iron of 0.1%. These

marked differences in the solubility of carbon in γ and α -iron are of profound significance in the heat treatment of steels, and are fully exploited to increase strength. It should be noted that the room temperature solubility of carbon in α -iron is extremely low and the interstitial diffusion process involved is assumed to be very slow due to the lack of thermal energy available. It is therefore reasonable to expect that during simple heat treatments, excess carbon will be precipitated as Fe_3C . This could happen during heat treatments involving quenching from the γ -state, or even after treatments entirely within the α -field, where the solubility of carbon varies by nearly three orders of magnitude between 720°C and 20°C.

At a particular temperature, diffusion of interstitial solute carbon atoms is expected to occur much more rapidly in ferrite than in austenite. This arises because γ -iron is a close-packed structure whereas α -iron, which is more loosely-packed, responds more readily to thermal activation and allows easier passage through the structure of vacancies and associated solute atoms. A consequence of this is that the activation energy is usually lower for a particular element diffusing in α -iron, than it is for the same element diffusing in γ -iron [36].

10.4 – The Transformation Strain

The volume change associated with the phase transformation from austenite to ferrite is typically small and is quite frequently ignored in theoretical analyses. The elastic strain energy arises from the effects of misfit-generated elastic stress within the bcc ferrite phase region. By investigating the effects of the elastic stress generated by the lattice mismatch between the bcc ferrite inclusion and the surrounding fcc austenite matrix it is possible to consider the effect the elastic strain energy has on the process of microstructural evolution.

The body-centred-cubic ferrite and face-centred-cubic austenite phases have different lattice spacings indicating that a change in volume will occur when one phase is transformed into another. For the bcc and fcc unit cells, the lattice parameters, a_{bcc} and a_{fcc} describe the dimension of the sides the unit cells respectively. The volumetric strain arises due to a change in volume with respect to the original volume occupied by the reference state. The fcc austenite matrix is taken as the reference phase and is assumed to be unstrained in the absence of the ferrite precipitate.

The ferrite phase has a larger volume per mole of iron than the austenite and is subjected to a volumetric strain of -1.34% (see Appendix H) so that it can be accommodated into the matrix.

Therefore, for small strains

$$\varepsilon_T \approx \frac{1}{3}\varepsilon_v = -0.445\% \quad (10.1)$$

In order to simplify the elastic analysis, coherency is assumed between the ferrite precipitate and the surrounding austenite matrix. The constraint of coherency may be a valid approximation for the treatment of small misfitting precipitates but can not generally be applied to the case of larger precipitates [7]. However, the variational model can be later modified to allow this constraint to be removed, which would permit the phases to slip or slide in a direction tangential to the interface boundary. Computationally, this would require modelling a discontinuity in the elastic displacement field at the interface boundaries.

The constraint of coherency carries with it an elastic penalty which results in elastic distortions in both the precipitate particle and the matrix material surrounding it. The elastic deformation required to accommodate this volume change contributes to the change in elastic stored energy. In order to reduce the elastic strain energy, the interface is expected to migrate in a direction such as to reduce the size of the bcc ferrite phase, if other energetic factors permit it.

10.5 – Comparison with Other Studies

The general microstructure of interest can be considered as that of a matrix material punctuated by the presence of a number of second-phase particles. If an alloy is cooled to the point where there is an overabundance of foreign atoms within the host matrix, these foreign atoms can collect and begin to form precipitates by the process of diffusion. Due to the difference in structure (e.g. atomic arrangement and chemical composition) between the matrix and precipitate, there is an energy penalty for both the interface between the matrix and precipitate as well as for elastic strains induced by the difference in atomic structure.

Consideration is given to a class of second-phase microstructures in which the phases are coherent. However, by virtue of suitable material processing techniques, the nature and distribution of precipitates may be tailored to yield desirable physical properties.

Through a thorough literature search, there appears to be a lack of ‘general’ models that are capable of modelling microstructure evolution over a range of different precipitate systems. Although it is impossible to provide an extensive literature review of all previous

studies carried out within this field, it is the purpose of this section to examine and review a range of models that have had a significant impact within this field of research.

The iron-carbon binary phase system has been investigated a number of times over the years as opposed to more complex higher-order systems, such as Fe-Cr-C, in order to avoid excessive complexity due to the diffusion of both interstitial and substitutional solutes. This is a reasonable development since one must first establish an understanding of binary phase phenomena before attempting to model more complex multi-component phenomena. When three or more components take part in the diffusion process, the situation not only becomes more computationally intensive but additional complexities arise due to the stoichiometry of the phase components, different diffusivities of diffusing species, mass balance of components at the moving interface and the formation of new phases as dispersed particles in the matrix.

As a precipitate nucleates, the interface separating the new phase region and the bulk matrix will traverse under non-equilibrium conditions, yet many previous studies assume equilibrium conditions at the interface (see [35], [38] and [66] - [73]). For a binary alloy system, local equilibrium at the interface either implies that the compositions on either side of the interface are identical (such that the interface moves via a displacive phase transformation) or more typically that the compositions within each phase adjacent to the interface are maintained at fixed equilibrium values corresponding to the selected system temperature. At a given temperature, the equilibrium concentrations on either side of the interface are usually calculated by equating chemical potentials and solving the resulting non-linear equations. In this case, local equilibrium at the interface has to satisfy a mass balance constraint for the diffusing species. In many previous analyses of precipitation kinetics, consideration of diffusion is only given within the matrix phase and the composition within the precipitate is fixed. As a result, assumed local equilibrium conditions at the interface are then used to model a moving interface not in equilibrium. Although this assumption may be applicable to a particular class of physical problems, where the precipitate has a particularly low solubility of a particular component, this assumption is not always warranted within a general class of precipitation problems. Although the assumption of local equilibrium at the interface drastically simplifies analyses, the variational model described in chapter 4 can be used to form a direct dynamical description of the moving interface under non-equilibrium conditions coupled with the redistribution of material within all phases of interest.

Many initial studies into precipitate growth concentrated on developing one-dimensional numerical models for predicting the position of the interface with respect to both space and time. The first serious study of diffusional growth during a phase transformation was by Zener [71], who investigated a spherical precipitate particle growing in an infinite solid solution of initially uniform composition. In this study, Zener solved Fick's diffusion equation by assuming that the moving interface between the parent phase (austenite) and the product phase (ferrite) is always in a state of local equilibrium. Many of such initial studies into precipitate growth ignored elastic interactions and considered only phase energy variations and capillarity (surface energy) effects [35] [38]. It has only been in recent years that the role of elasticity on precipitation kinetics has been fully considered.

Recently, Jou [59] considered the effects of elastic fields on particle morphology and kinetics during early stage precipitate growth and late stage coarsening during a diffusional phase transformation. In this case, a sharp interface model based on the boundary integral method was adopted, and a misfit strain between the precipitate and matrix and an applied stress in the matrix were considered. Although local equilibrium was assumed at the interface, with diffusion restricted to an infinite matrix, far-field fluxes were considered (as opposed to a localised flux field) and the effect of linear elasticity was integrated into the model. In this analysis, no diffusional driven elasticity was considered since it is assumed that mechanical properties equilibrate much faster than diffusional processes. The results from this analysis illustrated that elastic effects are observed to cause considerable distortion and change in shape during growth of precipitate particles and elasticity was seen to restrict the morphology of the growing precipitates. These conclusions were confirmed and seen to be consistent with compared experimental observations.

Svoboda et al. [65] considered the interface kinetics and phase transformations associated with the binary Fe-C system using a novel analytical technique and a finite difference numerical method. The model successfully couples bulk diffusion and interface migration under non-equilibrium interface conditions and takes into account both the chemical phase energy and mechanical elastic stored energy contributions to the interface driving forces. The analysis is limited to isothermal interface evolution during a diffusional phase transformation within one-dimensional space and it is assumed that both phases have the same elastic properties. Within this framework, interstitial carbon diffusion is ignored within the growing bcc ferrite phase region and the carbon distribution within the growing precipitate is

set to a corresponding equilibrium value. The carbon diffusion is therefore entirely focused within the fcc austenite matrix. Considering the simplifying assumptions introduced, the results generated provide a solid yet general insight into the evolution of the interface during a diffusional phase transformation within the binary phase alloy. However, it may be difficult to use this method to model precipitate growth where the equilibrium composition within the growing precipitate phase is unknown. In this case, the process of diffusion would have to be considered within all phases. This model may also have difficulties modelling the evolution of complex multi-phase systems where both interstitial and substitutional diffusive mechanisms need to be considered.

Gill and Cocks [30] developed a variational principle for evaluating the rate of evolution of the microstructure of a material, and have applied this approach to model a ferrite precipitate growing within an austenite matrix within plain carbon steel. They have considered the situation where material rearrangement occurs by solute and interstitial diffusion, driven by compositional variations, phase transformations and changes of elastic stored energy. Although it is assumed that both the growing precipitate and the matrix regions exhibit the same elastic properties, they have demonstrated the importance of modelling the elastic strain energy and state that it is likely that the effects of the elastic fields associated with transformed phases will be relatively long range. Although the authors have considered a situation where there is perhaps limited interface movement, they have demonstrated the power behind the variational approach and how this can be applied and incorporated within a two-dimensional finite element framework to model other such similar processes.

Generally, only isothermal simulations are usually carried out since the diffusion coefficients, energy terms (hence driving forces) and equilibrium compositions within the different phase regions are direct functions of temperature. The diffusion coefficients are usually functions of the composition with each respective phase domain, but in a study by Vandermeer [72], a quasi-static approach was introduced to model the evolution using constant diffusion coefficients (essentially integrated averaged values over the region of interest). In this study of the Fe-C binary alloy system, the austenite decomposition kinetics are modelled by calculating the time necessary to re-distribute the carbon atoms leaving the ferrite region and moving into the austenite region assuming the interface is static for an increment of time. During the transformation, a build-up of carbon ahead of the advancing interfaces occurs such that the interiors of the parent phase austenite grains become enriched

in carbon. It is often assumed that the diffusion of carbon within ferrite is negligible and is frequently ignored since the solubility of carbon within ferrite is so small relative to the much higher solubility of carbon within the austenite phase. The corresponding carbon composition within the ferrite phase region is therefore taken as an assumed equilibrium value which remains constant throughout evolution. The carbon composition within the austenite phase region therefore builds up as the size of the austenite phase region reduces and the ferrite precipitate grows.

10.6 – Description of the Precipitate Model

Many areas of current interest in the field of materials science involve the simultaneous diffusional growth and dissolution of a random dispersion of second phase particles in a matrix. Here, a small nucleus of ferrite is introduced into a matrix of austenite. The compositions and temperature of the two phases are selected so that they coincide with an area of the iron-carbon phase diagram for medium carbon steels (see Figure 2.3) in which both the austenite and the ferrite phases exist at equilibrium. The initial configuration consists of a region of body-centred cubic (bcc) ferrite surrounded by a matrix of face-centred cubic (fcc) austenite as shown in Figure 10.4(a) for a planar interface geometry and Figure 10.4(b) for a circular interface geometry.

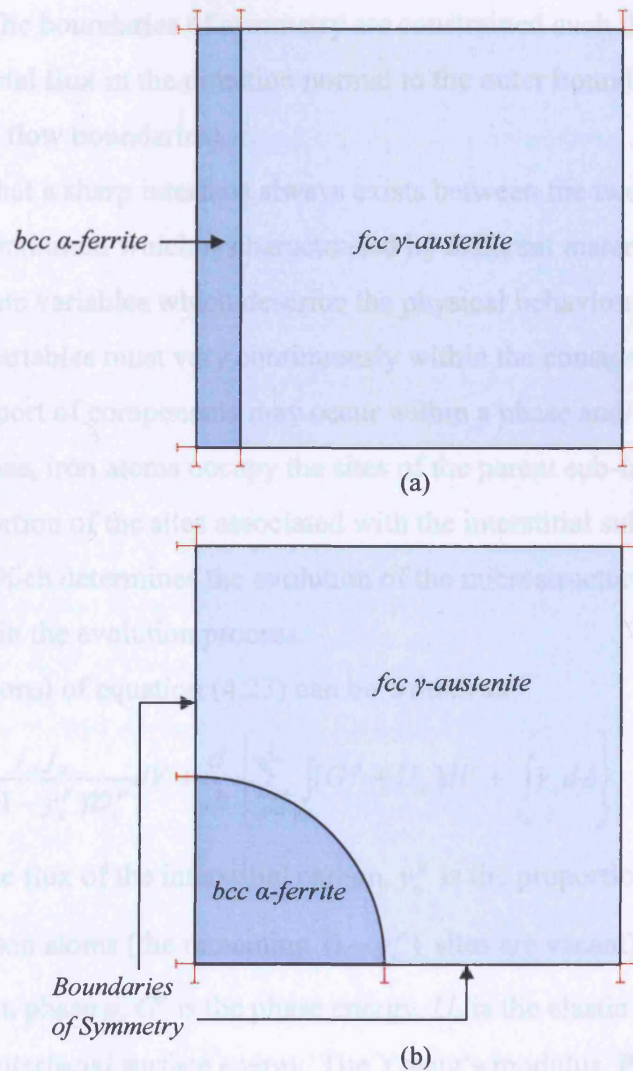


Figure 10.4 – Modelling the growth kinetics of a small nucleated ferrite phase embedded in an austenite matrix for an interface of (a) planar and (b) circular geometry (outer boundary constraints are highlighted in red).

Figure 10.4(b) shows a partially transformed austenite matrix with a circular ferrite precipitate introduced of uniform radius, \bar{r}_{in} . The region located between $0 \leq \bar{r} \leq \bar{r}_{in}$ is identified as initial region occupied by the ferrite precipitate and the remaining volume is occupied by the austenite matrix. In order to correctly set up a finite element mesh it is necessary to make use of any existing axes of symmetry in order to reduce computational time and resources. The configuration shown in Figure 10.4(b) is taken from a system which is assumed to be two-fold symmetric, which implies that only a single quadrant of the system

need be considered. The boundaries of symmetry are constrained such that there is no elastic displacement or material flux in the direction normal to the outer boundaries (i.e. all system boundaries are closed flow boundaries).

It is assumed that a sharp interface always exists between the two phases. Each phase is defined as part of a continuum which is characterised by different material properties and a well-defined set of state variables which describe the physical behaviour at all points across the phase. The state variables must vary continuously within the considered phase of a continuum. The transport of components may occur within a phase and/or across the interface boundary. In each phase, iron atoms occupy the sites of the parent sub-lattice and the carbon atoms occupy a proportion of the sites associated with the interstitial sublattice. It is the diffusion of carbon which determines the evolution of the microstructure and consideration is given to this element in the evolution process.

The variational functional of equation (4.23) can be written as

$$\Pi = \frac{1}{2} \sum_{p=1}^2 \int \frac{j_\alpha j_\alpha}{y_c^p (1 - y_c^p) \mathcal{D}_c^p} dV + \frac{d}{dt} \left\{ \sum_{p=1}^2 \int [G^p + U_e] dV + \int_{A_m} \gamma_s dA \right\} \quad (10.2)$$

where j_α represents the flux of the interstitial carbon, y_c^p is the proportion of the interstitial sites occupied by carbon atoms (the remaining $(1 - y_c^p)$ sites are vacant), \mathcal{D}_c^p is the interstitial diffusivity of carbon in phase p , G^p is the phase energy, U_e is the elastic stored energy per unit volume and γ_s is the interfacial surface energy. The Young's modulus, Poisson's ratio and the transformation strain within the two phases are assumed to be independent of the carbon content, which eliminates the need to consider the elastic driving force due to the change in elastic stored energy with change in composition. This assumption is in agreement with work published by Miodownik [74], where, for this particular class of steel, it is shown that the Young's modulus varies relatively weakly with change in carbon composition. The lattice diffusivity is assumed to be independent of the carbon concentration, although concentration dependent diffusivities can be readily incorporated into the variational model. The diffusivity of carbon in ferrite is found to be roughly 20 times that in the austenite and is assumed not to be affected by local straining of the lattice.

The thermodynamic parameters contained in the Gibbs free energy and chemical potential functions were extracted from a recent evaluation of the Fe-C-Cr system by

Andersson [75] and Hillert and Qui [76] which drew on a new assessment of the thermodynamic properties of iron and carbon.

The phase energy density can be expressed, at a specified temperature, T , in the form

$$G^p = \rho^p \left\{ A_1^p (1 - y_c) + A_2^p y_c + A_3^p y_c (1 - y_c) \right. \\ \left. + a^p RT [y_c \ln y_c + (1 - y_c) \ln(1 - y_c)] + G_{mo}^p \right\} \quad (10.3)$$

where A_i^p and G_{mo}^p are temperature dependent constants, which are listed in Appendix I for interstitial carbon in the fcc and bcc lattices, a^p is the number of interstitial sites per parent sub-lattice site ($a^{fcc} = 1$ for austenite and $a^{bcc} = 3$ for ferrite) and ρ^p is the number of mols of iron per cubic metre. With reference to equation (2.2), $c^{fcc} = c^{bcc} = 1$, and therefore this term does not appear in equation (10.3).

The flux must be continuous, apart from at the interface, such that

$$(j_\alpha^{fcc} - j_\alpha^{bcc}) n_\alpha = -(a^{fcc} y_c^{fcc} - a^{bcc} y_c^{bcc}) v_n \quad (10.4)$$

where n_α is the normal to the interface pointing into the fcc phase, v_n is the component of the velocity of the interface in the direction of n_α and the other quantities are determined on either side of the interface.

10.7 – The Phase Energy

At a given temperature, the phase energy of equation (10.3) is only a function of the concentration of carbon, and the contribution to the rate of change of Gibbs free energy can be expressed as

$$\frac{d}{dt} \sum_{p=1}^2 \int_{V^p} G^p dV = \int_{V^{bcc}} \frac{dG^{bcc}}{dy_c} \frac{dy_c}{dt} dV + \int_{V^{fcc}} \frac{dG^{fcc}}{dy_c} \frac{dy_c}{dt} dV + \int_{A_{in}} (G^{bcc} - G^{fcc}) v_n dA \quad (10.5)$$

The first two terms within equation (10.5) represent the phase energy driving force acting on the carbon at the interstitial sites due to the varying solubility of carbon in the different phases. The third term represents the change in phase energy due to the movement of the interface (i.e. the phase transformation).

The variation in the phase energy and its derivative as a function of carbon composition at a temperature of 723°C for the bcc ferrite and fcc austenite phases are shown in Figure 10.5 and Figure 10.6 respectively. It can be seen from Figure 10.5 that the Gibbs free energy of the fcc phase region changes quite strongly with a change in carbon composition relative to the Gibbs free energy of the bcc phase region.

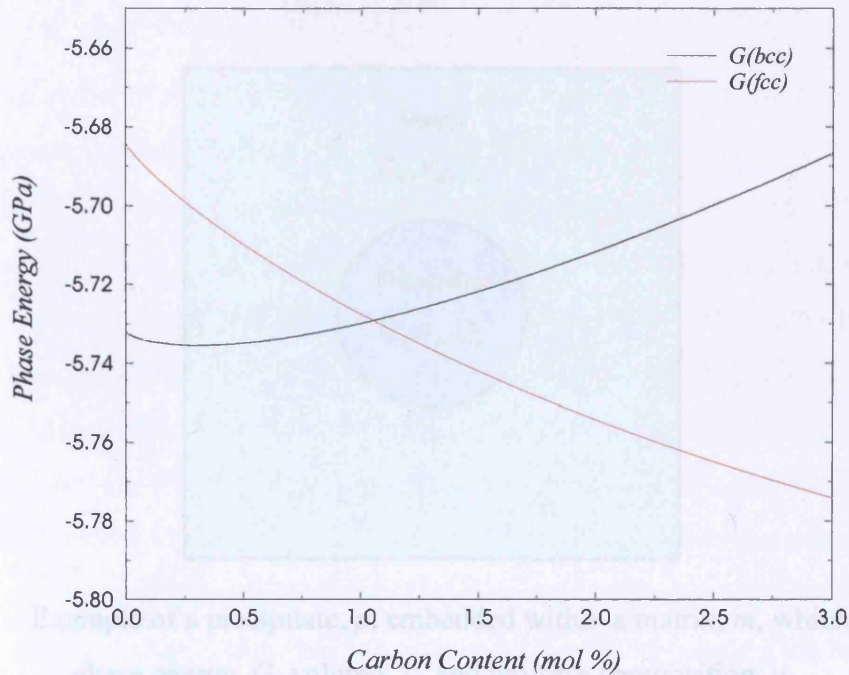


Figure 10.5 – The phase energy G^p as a function of the carbon content at 723°C.

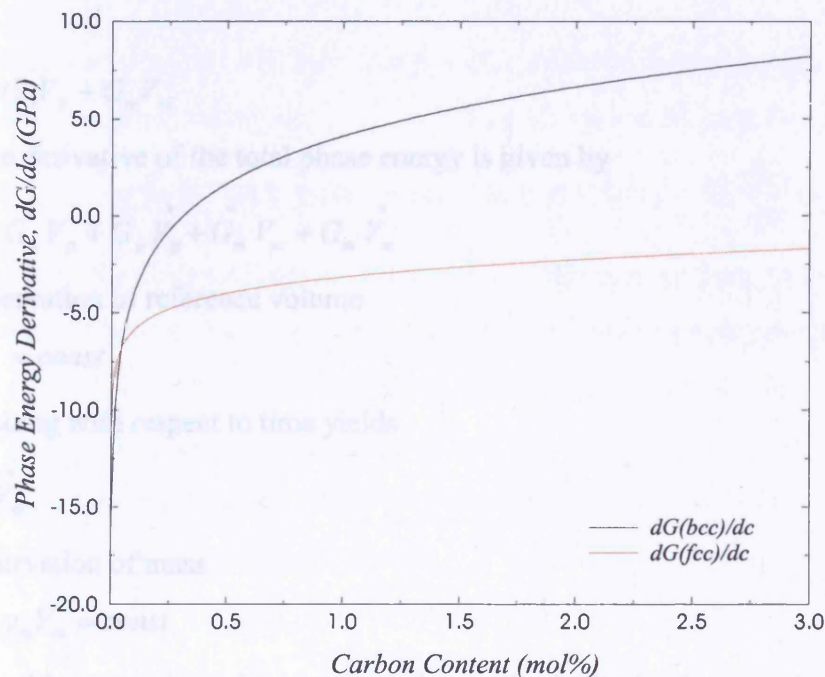


Figure 10.6 – Phase energy derivative as a function of the carbon content (mol%) at 723°C.

The following example shows that sole consideration of Figure 10.5 is not sufficient to predict the resultant evolution of the interface boundary.

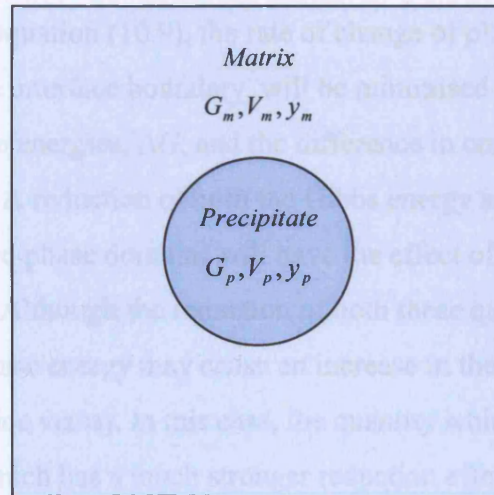


Figure 10.7 – Example of a precipitate, p , embedded within a matrix, m , which have defined phase energy, G , volume, V , and uniform composition, y .

Considering the situation described in Figure 10.7, the total phase energy, G_{total} , can be described by

$$G_{total} = G_p V_p + G_m V_m$$

where the time derivative of the total phase energy is given by

$$\dot{G}_{total} = \dot{G}_p V_p + G_p \dot{V}_p + \dot{G}_m V_m + G_m \dot{V}_m \quad (10.6)$$

Through conservation of reference volume

$$V_p + V_m = const$$

and differentiating with respect to time yields

$$\dot{V}_p = -\dot{V}_m \quad (10.7)$$

Through conservation of mass

$$y_p V_p + y_m V_m = const$$

Differentiating this expression with respect to time and substituting in equation (10.7) gives

$$\dot{y}_m V_m = -\dot{y}_p V_p + \dot{V}_p (y_m - y_p) \quad (10.8)$$

Substituting equations (10.7) and (10.8) into equation (10.6) gives the expression

$$\dot{G}_{total} = \dot{V}_p \left[(G_p - G_m) + \frac{\partial G_m}{\partial y_m} (y_m - y_p) \right] + \dot{y}_p V_p \left(\frac{\partial G_p}{\partial y_p} - \frac{\partial G_m}{\partial y_m} \right) \quad (10.9)$$

Through consideration of equation (10.9), the rate of change of phase energy, with respect to the rate of migration of the interface boundary, will be minimised by reducing both the difference in the Gibbs free energies, ΔG , and the difference in composition, Δy , between the precipitate and the matrix. A reduction of both the Gibbs energy and compositional differences between the two phase domains will have the effect of decreasing the rate of migration of the interface. Although the reduction of both these quantities is theoretically ideal, a reduction in the phase energy may cause an increase in the compositional difference between the phases (and vice versa). In this case, the quantity which is reduced, at the expense of the other, will be that which has a much stronger reduction effect on the overall free energy.

It can also be seen from equation (10.9) that the rate of change of phase energy, with respect to the rate of change of composition, will be minimised by altering the composition within each phase domain in order to reduce the difference between the phase energy

derivatives, i.e. $\left(\frac{\partial G_p}{\partial y_p} - \frac{\partial G_m}{\partial y_m} \right)$. A reduction in the difference in phase energy derivatives

between the two phase domains will therefore have the effect of decreasing the rate of change of composition across the microstructure. From Figure 10.6 it can be seen that as the carbon

composition approaches its lowest compositional state (i.e. when $y = 0$), $\frac{\partial G}{\partial y} \rightarrow -\infty$, providing

a large driving force for the interstitial carbon atoms to diffuse away from this compositional state. This provides a barrier to ensure that the composition remains between the physically relevant values of $y_c = 0$ and $y_c = 1$. It can be seen that the variation of the first derivative of the phase energy with increase in carbon composition within the bcc region is much stronger than that within the fcc phase region, which reinforces the fact that the bcc phase has a lower solubility for carbon compared to the fcc phase.

10.8 – Results and Discussion

The nucleation process is assumed to have already occurred and the ferrite phase precipitate is initially given with an assumed shape. The initial ferrite phase is taken to contain 0.5% molar fraction of carbon and the austenite is taken to contain 1.0% molar fraction of carbon at a temperature of 723°C. The ferrite phase is found to have a maximum carbon solubility of 0.0075 mol% at 723°C. The thermodynamic driving forces arise from variations in the elastic strain energy density, interface surface energy and compositional phase energy density. The elastic strain energy and compositional phase energy densities both depend on the volume and scale with the cube of the characteristic unit length. The interfacial terms scale as the unit length squared, and hence the non-dimensionalised problem is not completely independent of the chosen length scale.

An isotropic interfacial surface energy of $\gamma_s = 0.8 \text{ Jm}^{-2}$ was used in the computations, which is an experimental value from the work of Yang and Johnson [77]. The interfacial surface energy driving forces were considered at the selected characteristic length scale of $\{L\} = 10 \text{ }\mu\text{m}$. The surface energy driving force is included into the model in order to consider the effect of this driving force in the later stages of the precipitation sequence.

(a) Planar Precipitate Morphology

Figure 10.8 shows the evolution and phase morphology of a planar interface over non-dimensional time using six-noded quadratic type finite elements with the elastic stored energy contribution included in the model. The interface is constructed as a single interface boundary segment and is sub-divided into 25 boundary sub-segments. Figure 10.9 shows the variation of the non-dimensionalised interface position during migration of the planar interface over non-dimensional time both with and without elasticity effects included in the model.

The results from this simulation initially indicate that the interface motion is both smooth and continuous in conjunction with excellent conservation of mass of carbon. The interface also remains relatively flat during evolution of the ferrite precipitate. These results imply that issues relating to re-meshing and the flux field dependence on the mesh have been successfully implemented and addressed. The physical significance of these results is discussed in full detail in the following sub-section, which considers the morphology of the circular ferrite precipitate.

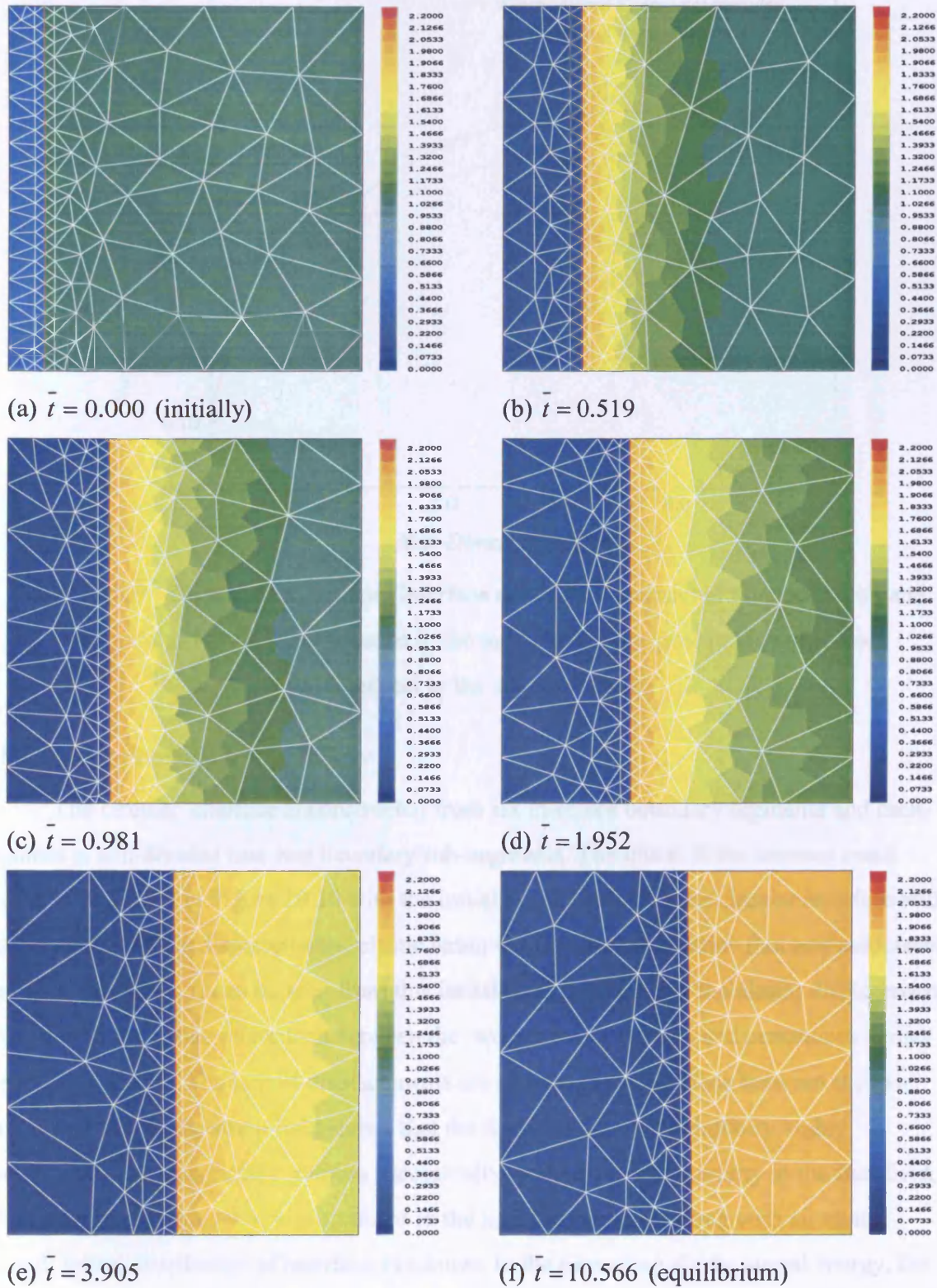


Figure 10.8 – Compositional contours (mol%) and phase morphology at 723°C for a planar interface with elasticity effects included in the model.

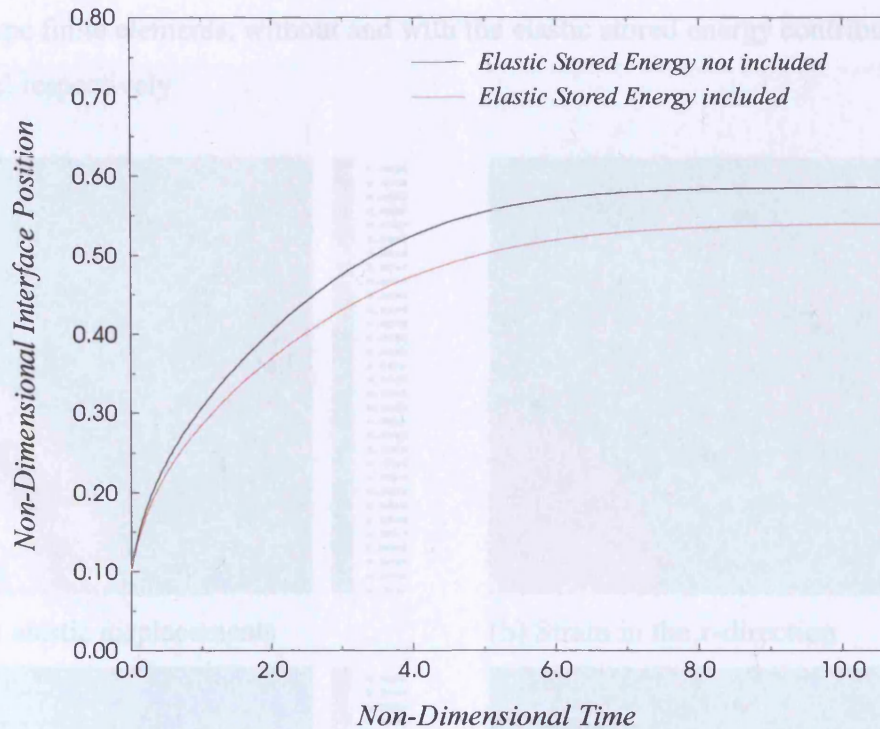


Figure 10.9 – Migration of a planar interface over non-dimensional time both with and without elasticity effects included in the model (interface position is normalised with respect to the system length).

(b) Circular Precipitate Morphology

The circular interface is constructed from six interface boundary segments and each segment is sub-divided into two boundary sub-segments. The initial finite element mesh geometry is shown in Figure 10.10 with the initial configuration of the circular interface with respect to the elastic displacements, elastic strain field, volumetric lattice flux and associated interface velocities. It can be seen from this initial configuration that the elastic displacement field, due to the lattice mis-match between the two phases, is smooth and continuous across the sharp interface. The largest displacements are located at the interface between the two phases and the elastic strain field shows that the ferrite precipitate is initially highly constrained. The interfacial condition successfully models the discontinuity in the flux field, which is initially symmetric and confined to the interfacial region, along with an almost smooth initial distribution of interface velocities. In the case of no elastic stored energy, the interface velocities are initially identical at all interface nodes.

Figure 10.11 and Figure 10.12 show the resulting compositional contours and phase morphology of an initially circular interface over non-dimensional time using six-noded

quadratic type finite elements, without and with the elastic stored energy contribution included in the model respectively.

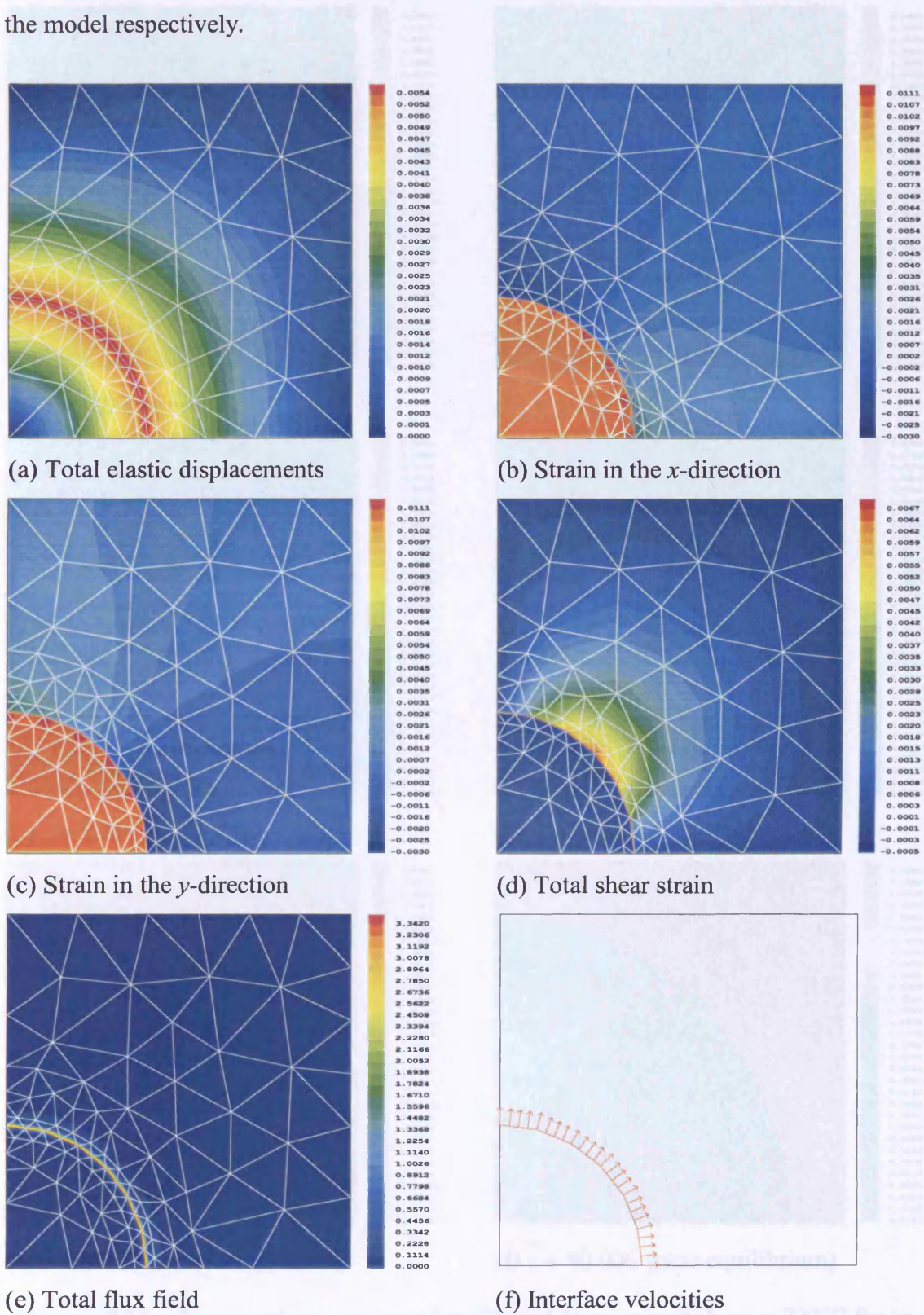


Figure 10.10 – The initial configuration of an initially circular interface with elastic interaction effects included in the model.

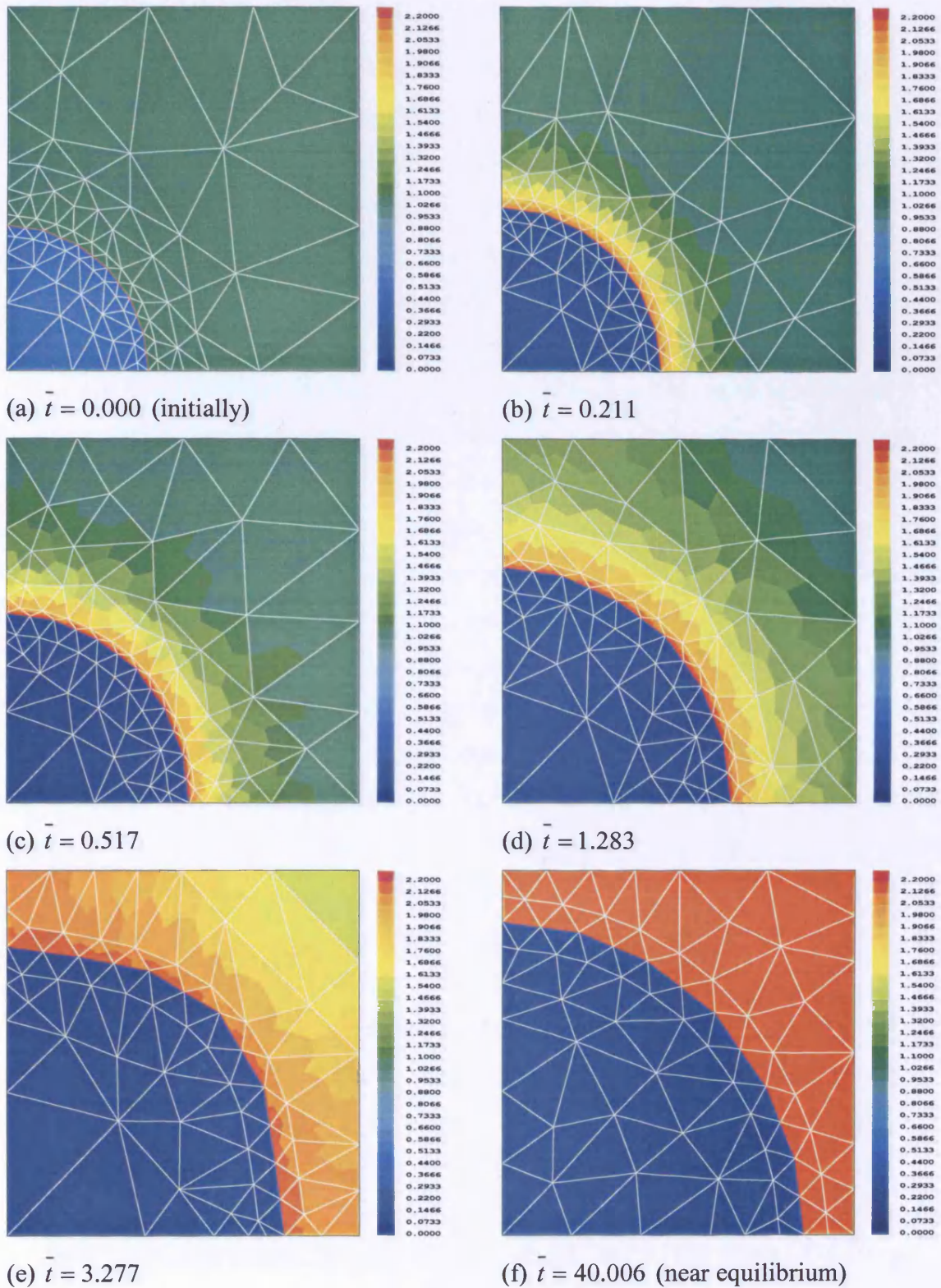


Figure 10.11 – Compositional contours (mol%) and phase morphology at 723°C for an initially circular interface without elasticity effects included in the model.

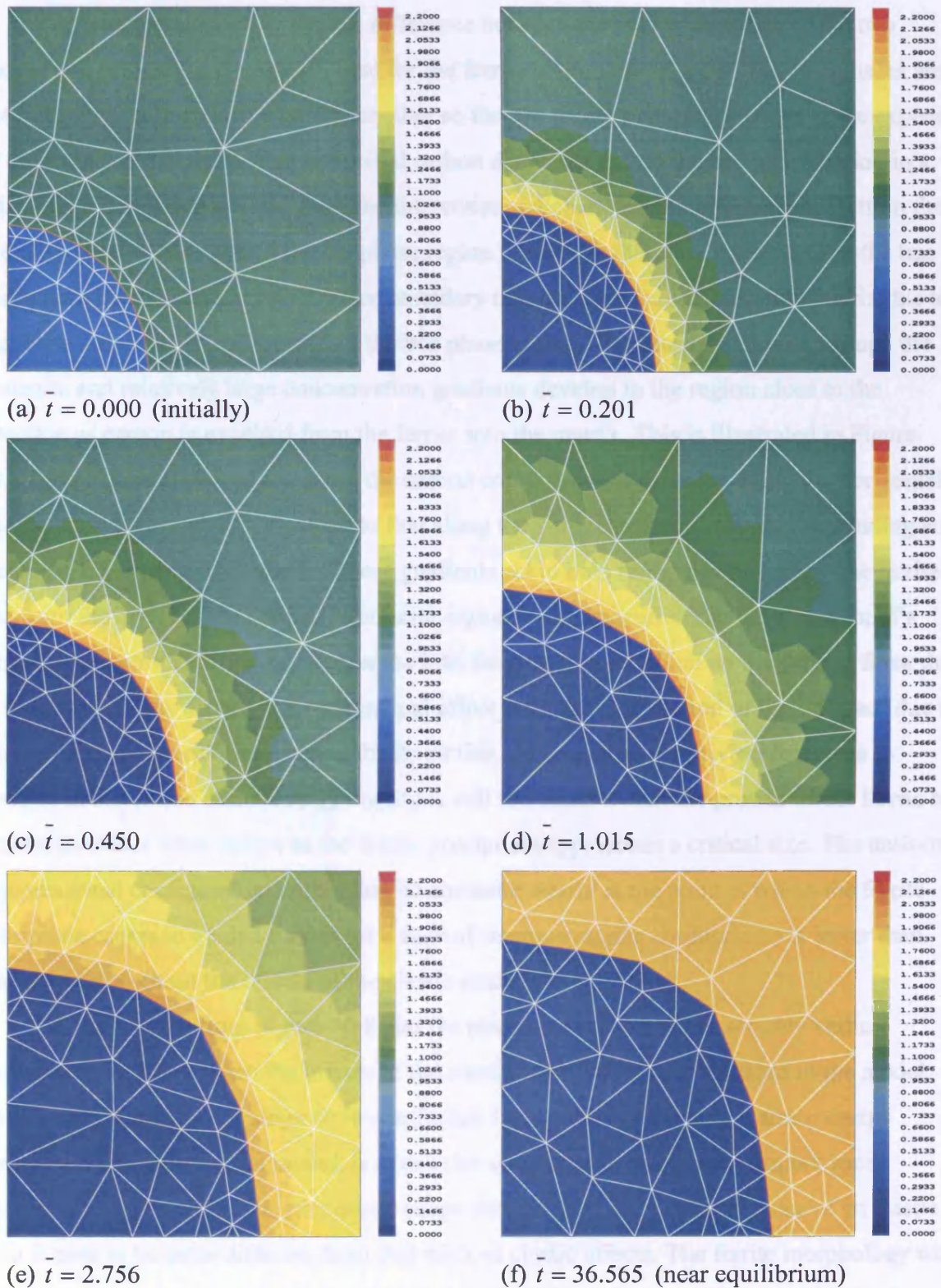


Figure 10.12 – Compositional contours (mol%) and phase morphology at 723°C for an initially circular interface with elasticity effects included in the model.

At a temperature of 723°C the difference between the energy densities of the two phases is significant and it is sufficient for the ferrite precipitate to grow. The two phases are not initially in equilibrium with one another so the bcc ferrite precipitate grows at the expense of the fcc austenite phase. The interstitial carbon decreases within the bcc phase region in a relatively short period of time since the interstitial carbon atoms can diffuse faster within the bcc phase region than within the fcc phase region. Carbon is therefore rejected from the bcc phase ahead of the advancing interface boundary into the surrounding austenite matrix due to the lower solubility of carbon within the bcc phase region. The interface moves through the austenite and relatively large concentration gradients develop in the region close to the interface as carbon is expelled from the ferrite into the matrix. This is illustrated in Figure 10.13 and Figure 10.14, which show the carbon compositional variation along the horizontal system boundary (which is identical to that along the vertical system boundary) excluding and including the effects of elasticity. These gradients act to help remove carbon from the ferrite and from the high carbon content interfacial region in the austenite. The development of a larger compositional difference across the interface has a small effect on the driving force due to the phase energy density but its principal effect is to slow the motion of the interface due to the increase in material flux needed for its motion. At this stage the driving force due to changes in the elastic strain energy density is still too small to halt the growth of the ferrite but eventually this is what occurs as the ferrite precipitate approaches a critical size. The uniform compositional configuration within the fcc austenite matrix at the point at which the ferrite precipitate ceases to evolve further (at a state of thermodynamic equilibrium) is lower than that obtained without the effects of the elastic strain energy density.

It can be seen from Figure 10.8 that the planar interface remains roughly vertical throughout evolution when the effects of the elastic strain energy are included in the model. The circular ferrite morphology shown in Figure 10.11, without the elastic strain energy contribution included in the model, is seen to be symmetrical, stable and adopts a more circular shape over time. The precipitate shape change observed in the presence of an elastic field is seen to be quite different from that without elastic effects. The ferrite morphology with the elastic strain energy contribution included in the model (shown in Figure 10.12) is also stable but evolves towards a slightly more distorted circular shape over time.

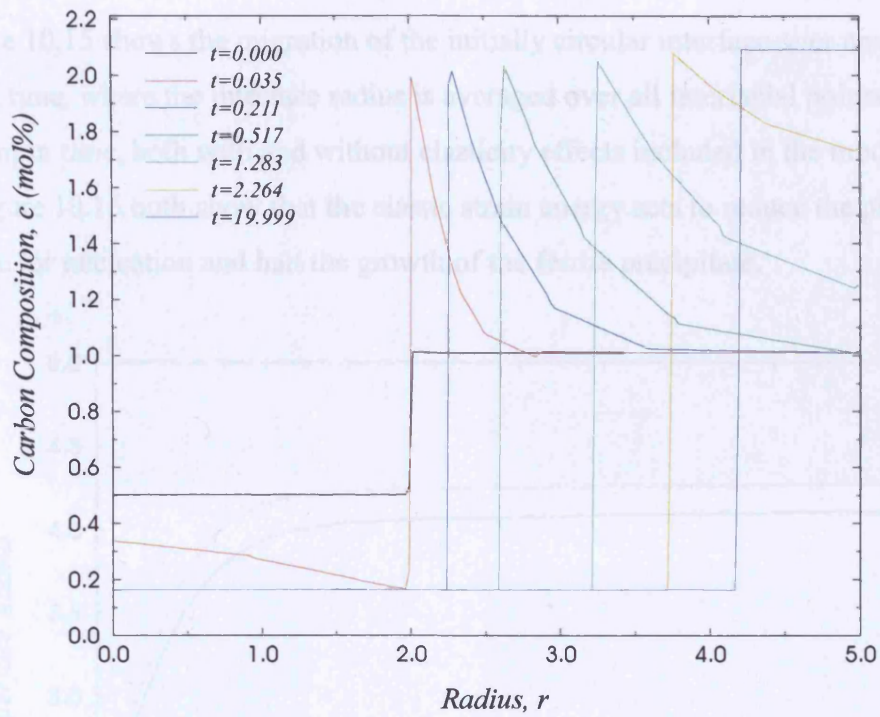


Figure 10.13 – Compositional contours (mol%) along the system boundary without elasticity effects included in the model.

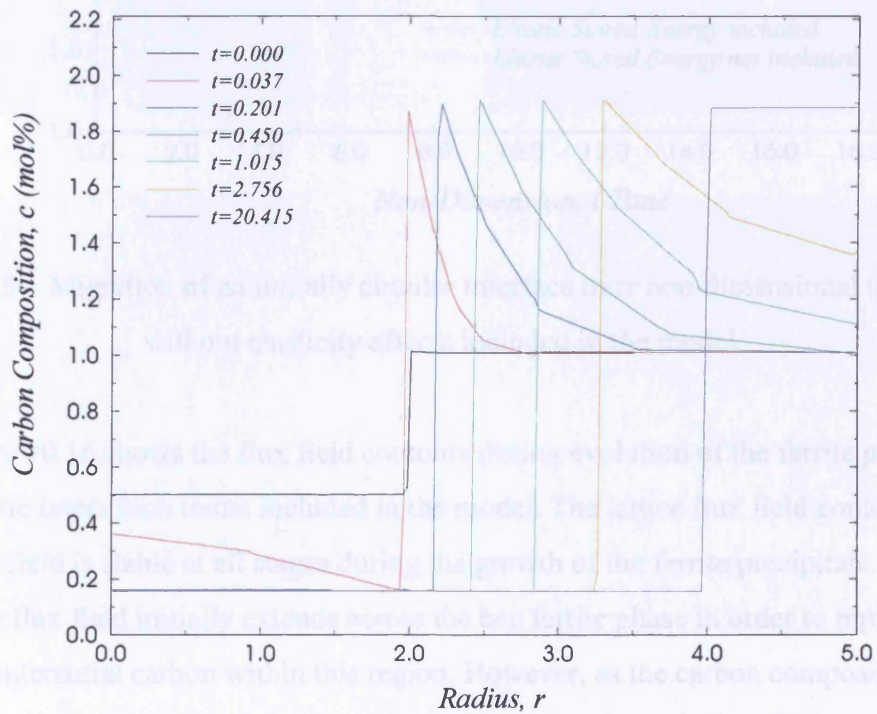


Figure 10.14 – Compositional contours (mol%) along the system boundary with elasticity effects included in the model.

Figure 10.15 shows the migration of the initially circular interface over non-dimensional time, where the interface radius is averaged over all interfacial points at each selected point in time, both with and without elasticity effects included in the model. Figure 10.9 and Figure 10.15 both show that the elastic strain energy acts to reduce the phase energy driving force for nucleation and halt the growth of the ferrite precipitate.

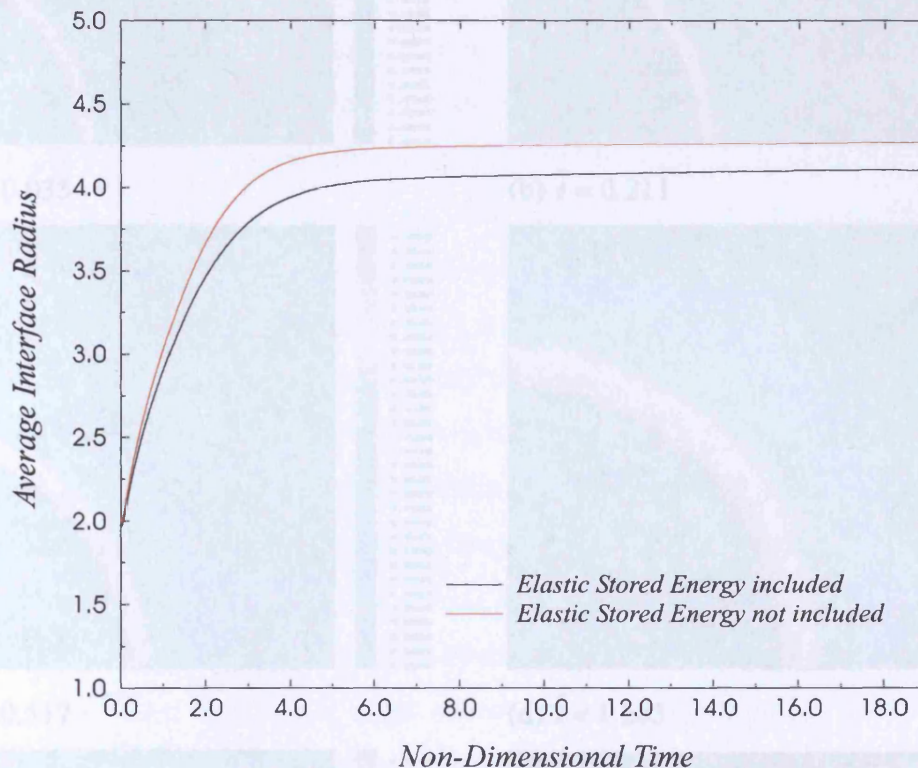


Figure 10.15 – Migration of an initially circular interface over non-dimensional time with and without elasticity effects included in the model.

Figure 10.16 shows the flux field contours during evolution of the ferrite precipitate with no elastic interaction terms included in the model. The lattice flux field contours show that the flux field is stable at all stages during the growth of the ferrite precipitate. It can be seen that the flux field initially extends across the bcc ferrite phase in order to rapidly reduce the level of interstitial carbon within this region. However, as the carbon composition within the bcc ferrite precipitate approaches its near equilibrium value, the flux field, and hence all diffusion of carbon becomes principally confined to the austenite matrix region.

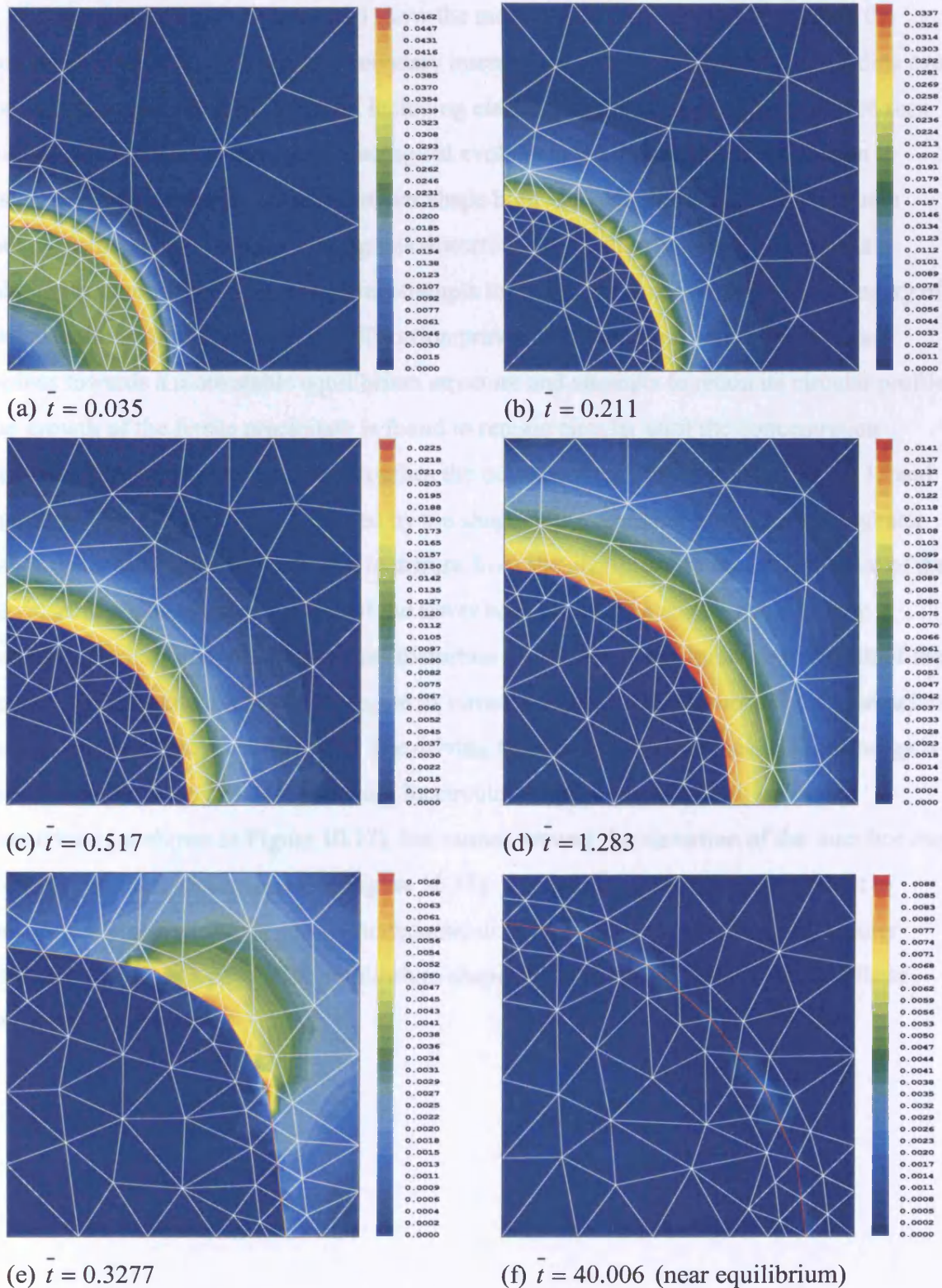


Figure 10.16 – Flux field contours and phase morphology at 723°C for an initially circular interface without elasticity effects included in the model.

Figure 10.17 and Figure 10.18 show the motion of two different points along the circular interface (centre and outer boundary intersection points) with the average radius over non-dimensional time excluding and including elasticity effects respectively. It can be seen from these Figures that during morphological evolution, the ferrite precipitate is seen to distort somewhat from its initially circular shape both with and without the elastic strain energy included in the model. During this distortion, the bcc ferrite precipitate adopts a cuboidal square-like configuration and attempts to mimic the shape of the outer boundary of the austenite matrix. However, this distortion proves to be temporary as the precipitate evolves towards a more stable equilibrium structure and attempts to retain its circular profile. The growth of the ferrite precipitate is found to remain circular until the concentration gradient within the austenite matrix reaches the outer boundary (shown in Figure 10.13 and Figure 10.14). The distortion is caused by the shape of the austenite matrix, since a greater distance exists for interstitial carbon to diffuse from the precipitate to the upper corner of the matrix as opposed to along the line of the lower boundaries. The elastic strain energy is observed to contribute to the temporary distortion of the ferrite precipitate. As a result of this, the ferrite precipitate doesn't quite regain its circular shape as the microstructure approaches a state of thermodynamic equilibrium. The driving force due to the interface surface energy is seen to assist the precipitate in retaining its circular shape, especially with no elastic interactions (as shown in Figure 10.17), but cannot prevent the distortion of the interface due to elastic interactions (as shown in Figure 10.18). The elastic strain energy is thought to constitute relatively long range thermodynamic driving forces and the shape of the outer boundary still plays a part in the equilibrium shape of the ferrite precipitate through these elastic driving forces.

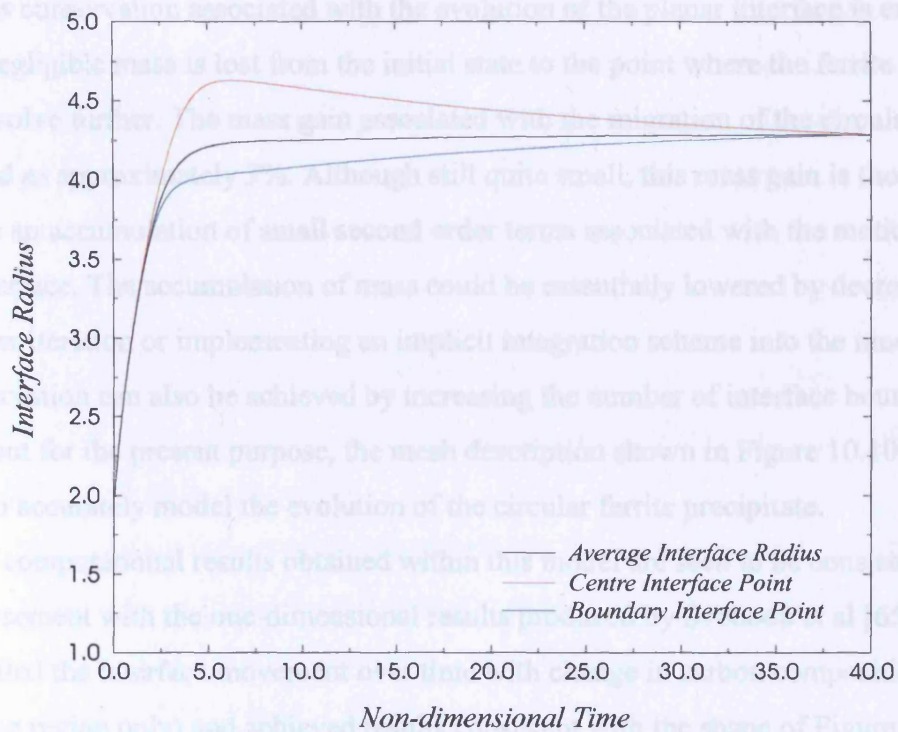


Figure 10.17 – Migration of two different interface points with the average non-dimensional radius of an initially circular interface without elasticity effects included in the model.

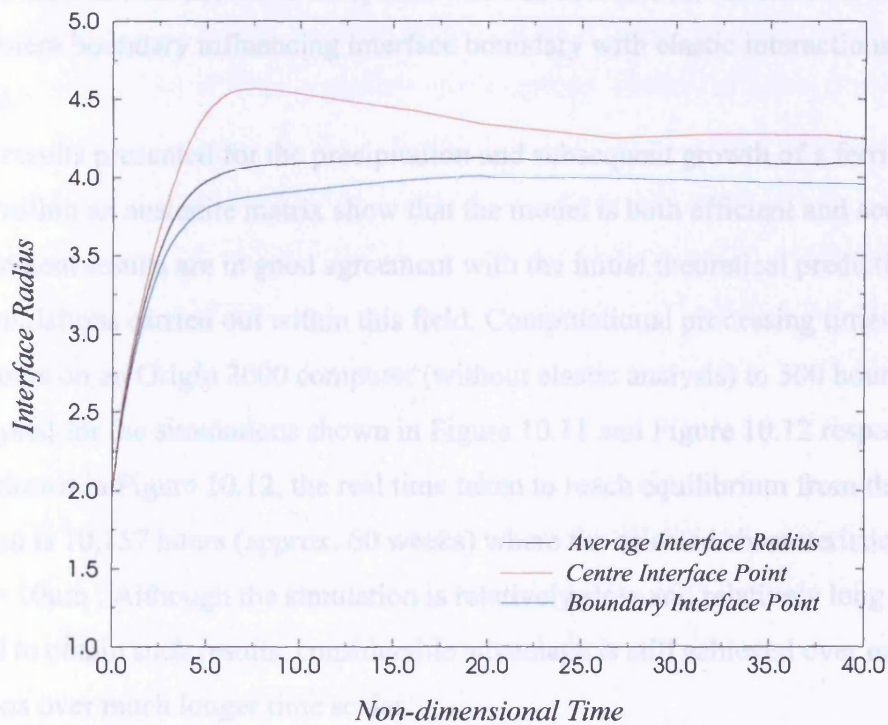


Figure 10.18 – Migration of two different interface points with the average non-dimensional radius of an initially circular interface with elasticity effects included in the model.

Mass conservation associated with the evolution of the planar interface is extremely good and negligible mass is lost from the initial state to the point where the ferrite precipitate ceases to evolve further. The mass gain associated with the migration of the circular interface is calculated as approximately 3%. Although still quite small, this mass gain is thought to arise due to an accumulation of small second order terms associated with the motion of the circular interface. The accumulation of mass could be essentially lowered by decreasing the time step per iteration or implementing an implicit integration scheme into the model. Better mass conservation can also be achieved by increasing the number of interface boundary sub-segments, but for the present purpose, the mesh description shown in Figure 10.10 is sufficient to accurately model the evolution of the circular ferrite precipitate.

The computational results obtained within this model are seen to be consistent and are in good agreement with the one-dimensional results produced by Svoboda et al [65]. Svoboda et al. modelled the interface movement over time with change in carbon composition (within the fcc phase region only) and achieved results consistent with the shape of Figure 10.9 and Figure 10.15. Their analysis included the effects of elastic distortions but no direct comparison was made with and without the effects of elasticity in the model. Due to the limiting one-dimensional nature of the system that was considered, the effect of the shape of the outer system boundary influencing interface boundary with elastic interactions could not be modelled.

The results presented for the precipitation and subsequent growth of a ferrite precipitate within an austenite matrix show that the model is both efficient and accurate, and the finite element results are in good agreement with the initial theoretical predictions and previous simulations carried out within this field. Computational processing times ranged from 300 hours on an Origin 2000 computer (without elastic analysis) to 500 hours (with elastic analysis) for the simulations shown in Figure 10.11 and Figure 10.12 respectively. For the results shown in Figure 10.12, the real time taken to reach equilibrium from the initial configuration is 10,157 hours (approx. 60 weeks) where the selected characteristic length scale, $\{L\} = 10\mu\text{m}$. Although the simulation is relatively slow and relatively long processing are required to obtain such results, considerable advantage is still achieved over experimental investigations over much longer time scales.

The results seen in this analysis with elastic interactions are consistent with the sphere-to-cube transition observed in several cubic systems possessing a dilatational misfit and an

approximately isotropic interfacial energy [88] [89]. From the work of Johnson and Voorhees [104] it was shown that as the precipitate particle size increases, the shape becomes progressively more square-like, indicating the increasing importance of the elastic stored energy at larger length scales. The elastic energy of a cubical-like particle has been found to be less than that of a spherical particle of equal volume when the particle has a smaller modulus than the matrix in an elastically isotropic system [90].

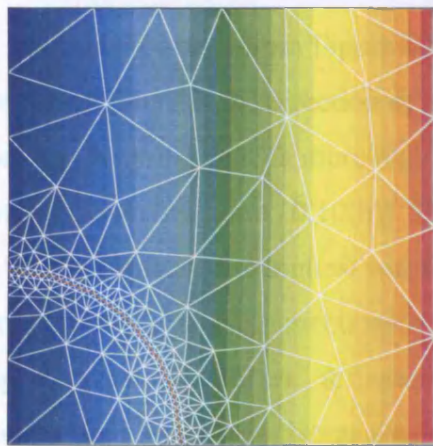
(c) Circular Precipitate Morphology with Applied Uniaxial Tensile Loading

The effect of external loading can be numerically implemented into the general model and is described in detail in Appendix F.

The resulting morphology of the phases will depend upon the sign of the applied traction, i.e. whether the tractions are either tensile or compressive in nature. For simplicity, consideration is limited to the application of a tensile traction along only one direction, such that the system is loaded uniaxially. The effect of applied loading in both x and y directions serves little purpose and is not expected to greatly influence the change in shape of the moving boundary during the resulting phase morphology.

The finite element mesh used to study the influence of applied uniaxial tensile loading on ferrite precipitate morphology is constructed from six interface boundary segments, with each segment sub-divided into six boundary sub-segments. The initial finite element mesh geometry for uniaxial loading is shown in Figure 10.19, along with the initial configuration with respect to the elastic displacements, elastic strain and elastic stress fields. The uniaxial loading is applied to the far vertical boundary of the matrix phase in the x -direction with the effect of the transformation strain also included in the model. The loading was applied such as to strain the system, in the absence of the ferrite precipitate, such that $\varepsilon_x = 2.5\%$ and $\varepsilon_y = -1.2\%$. The bcc ferrite precipitate has a Young's modulus which is less than that of the austenite matrix (i.e. $E^{bcc} < E^{fcc}$).

The number of sub-segments per interface segment was naturally increased to allow for expected distortions and change in precipitate shape from its initially circular profile. The increase in interface sub-segments is a requirement to ensure that the local interface mesh topology remains regular. This invoked an immediate computational processing cost and a long processing time-frame was required to generate results relating to the evolution of the precipitate.



(a) Elastic displacements in the x -direction



(b) Elastic displacements in the y -direction



(c) Strain in the x -direction



(d) Strain in the y -direction



(e) Stress in the x -direction



(f) Stress in the y -direction

Figure 10.19 – The initial configuration of an initially circular interface with an applied uniaxial load applied to the outer vertical system boundary such that

$$\varepsilon_x = 2.5\% \text{ and } \varepsilon_y = -1.2\%.$$

It can be seen from Figure 10.19(a) and (b) that, as expected, the elastic displacements are concentrated in the direction of applied uniaxial loading. As a result of the applied loading, the precipitate is more highly strained than with only the effects of the transformation strain (shown in Figure 10.10(b)). Since the system is inhomogeneous, the stress field is seen to be non-uniform and highest within the austenite matrix region at the point where the junction of the interface meets with the vertical system boundary (see Figure 10.19(e)). It is expected that material will diffuse away from regions of high stress into regions of low stress and the precipitate will change shape in order to accommodate this. The system will therefore evolve in order to reduce the regions of high elastic stored energy, if there is a means by which it can do so.

The results in Figure 10.20 show the influence of the applied uniaxial load on the morphological evolution of the ferrite precipitate over non-dimensional time. From these results it can be seen that the elastic field, as a result of the application of an external load, dictates the resulting evolution of the precipitate. The ferrite precipitate is observed to experience considerable distortion and shape change in order to elongate and align itself parallel with the principal direction of applied uniaxial loading. The growing precipitate is seen to break its symmetrical shape in a relatively short space of time and extend into a plate-like structure. As a result of the rapid change in precipitate shape, only a small redistribution of carbon is observed local to the interface boundary. Interstitial carbon is seen to diffuse away from the region of high stress concentration and into the region of low stress concentration (where the junction of the interface meets with the horizontal system boundary) in order to lower the elastic stored energy. The change in precipitate shape can occur via rapid redistribution of carbon through the loosely-packed bcc phase avoiding the slower path through the fcc phase. In addition, the large elastic contribution to the chemical potential creates a strong driving force for this process. This allows the precipitate to change shape over a very short time scale. Hence almost no growth of the precipitate occurs during this part of the evolution process. It is expected that the precipitate will continue to branch itself along the direction of applied loading with local redistribution of carbon around the interfacial region until a state of equilibrium is attained.

Due to the required increase in mesh density around the interfacial region, the solution provides excellent conservation of mass, but processing times in excess of 700 hours were required to carry out the simulation shown in Figure 10.20. This illustrates the processing demand on modelling precipitate growth under the influence of an externally applied elastic field.

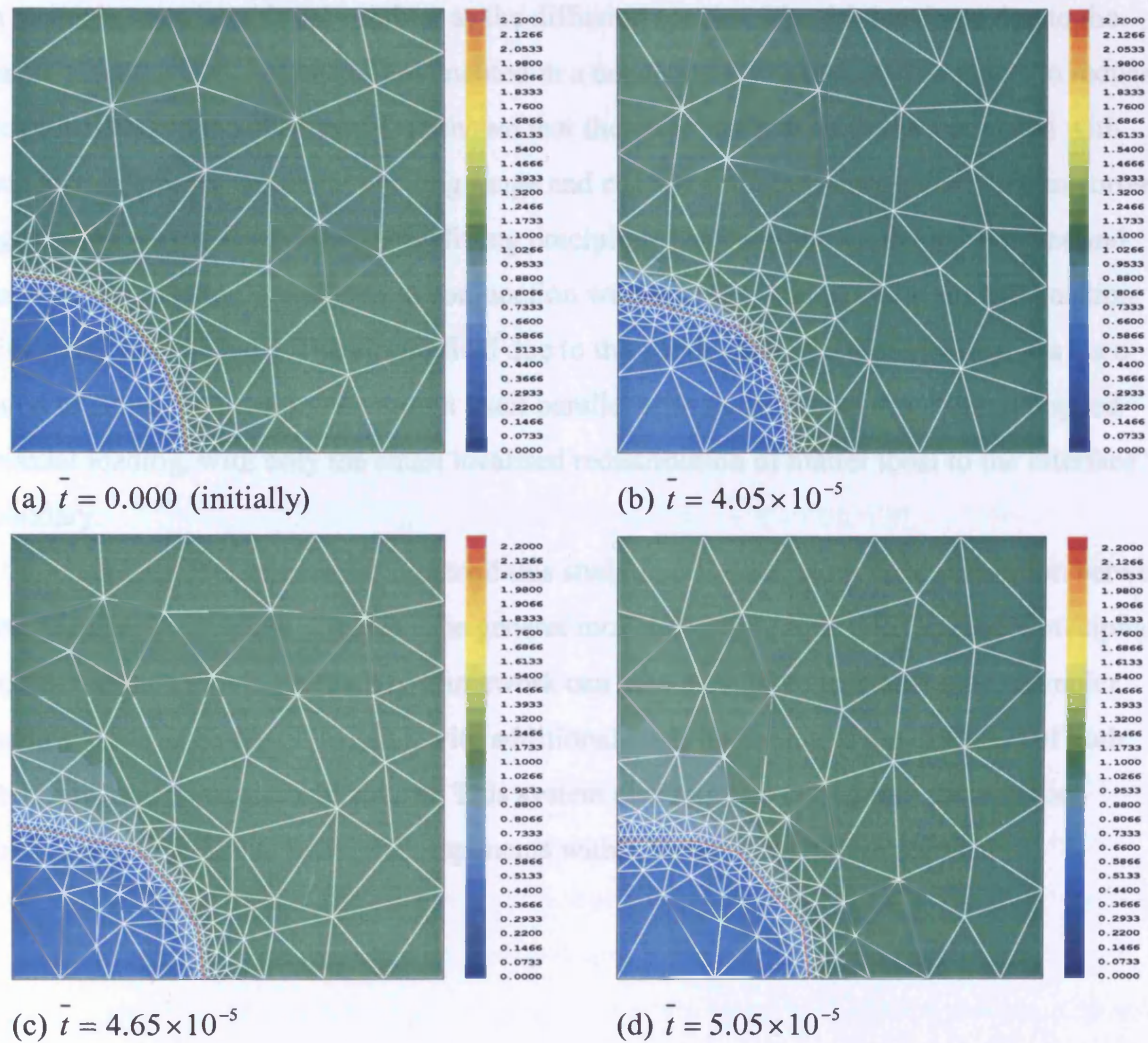


Figure 10.20 – Compositional contours (mol%) and phase morphology at 723°C for an initially circular interface subject to an applied uniaxial load in the x -direction (such that, in the absence of the ferrite precipitate, $\epsilon_x = 2.5\%$ and $\epsilon_y = -1.2\%$).

10.9 – Summary and Conclusions

The numerical model based on the variational principle has been successfully applied to model the kinetics and thermodynamics of microstructural evolution in a simple multi-component, multi-phase system under the influence of elastic stored energy variations. The model has been implemented in a simple two phase system of a ferrite precipitate growing in an austenite matrix with only carbon as the diffusing species. The driving force due to the elastic stored energy has been implemented in a consistent manner such that it acts to reduce the global elastic strain energy. It is shown that the effects of elastic fields associated with transformed phases are relatively long range and can cause distortions around the transformed region. The elastic field due to a misfitting precipitate has been shown to alter the size and shape of the growing precipitate in conjunction with changing the equilibrium composition within the matrix phase. The elastic field due to the application of a uniaxial load has been found to cause the precipitate to align itself parallel with the principal direction of applied uniaxial loading, with only the small localised redistribution of matter local to the interface boundary.

It is therefore of interest to extend this study into investigating the competition between simultaneously nucleating phases. The general model and technique used to model precipitate growth within a moving boundary framework can now be applied to model more complex systems, such as Fe-Cr-C ($M_{23}C_6$), with additional complexity due to the diffusion of both interstitial and substitutional solutes. This system also requires taking into account the stoichiometric relations between components within the different phase regions.

11.0 – Coarsening of $M_{23}C_6$ Precipitates

This chapter considers the application of the general model, along with the modifications discussed in chapter 9, to simulate the coarsening kinetics of two misfitting spherical $M_{23}C_6$ carbide precipitates embedded within a ferrite matrix. The $M_{23}C_6$ phase is found to precipitate in high chromium steels, where M represents a combination of iron (Fe) and chromium (Cr) atoms which exist on the main sublattice and the carbon (C) atoms exist on the interstitial sublattice. The stoichiometric relation between the components within $M_{23}C_6$ must always be maintained and this adds some additional complexity to the model (see section 3.5.4). The influence of elasticity during the resulting phase morphology and coarsening kinetics of the $M_{23}C_6$ carbide precipitate particles is investigated.

11.1 – Background into Coarsening

Many physical engineering problems can be associated with a large number of moving boundaries, and one can expect that within a particular range of microstructures, a number of phases can co-exist within close proximity to one another. The properties of multi-phase materials depend strongly on the morphology and spatial distribution of minority precipitate phases within a majority matrix phase. The morphologies and spatial distribution of these precipitates are in many cases governed by the dynamics of a phase transformation process.

Many two-phase mixtures undergo a coarsening effect (also termed Ostwald ripening) and it is widely known that this process plays a major role in determining the mean precipitate size within many multi-component multi-phase systems. Coarsening usually occurs in the later stages of precipitation where the volume fraction of the precipitates has almost reached its equilibrium value, and likewise the composition of the matrix phase is close to its equilibrium value. This coarsening is known as Ostwald ripening and is the process whereby larger particles within the matrix grow at the expense of the smaller particles. As a result, the microstructure consists of large widely spaced precipitate particles. The principal thermodynamic driving force for Ostwald ripening is the reduction in the total interfacial energy between the matrix and precipitate. It can be seen from Figure 11.1 that smaller particles have a higher free energy than that of the larger particles. It follows from Figure 11.1 that the equilibrium compositions will be altered so that there will be a diffusional flux of material from the smaller particles to the larger particles. This has the effect of reducing the

total free energy of the system with larger precipitate particles growing at the expense of the smaller ones.

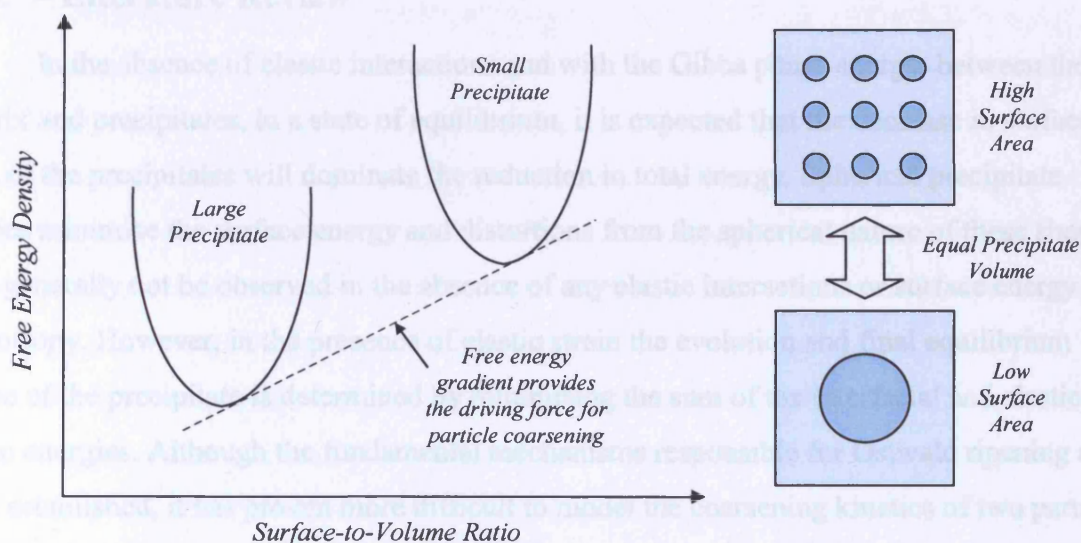


Figure 11.1 – The origin of particle coarsening: particles with a smaller radius of curvature have a higher free energy than particles with a higher radius of curvature.

A result of coarsening is that the average radius of particles within the microstructure will increase with time because a shrinking small particle will eventually disappear at which point the number of precipitates decreases by one (and the average particle size increases). Therefore, as the average particle size increases, the particle density distribution will continuously reduce. The rate at which coarsening occurs is clearly proportional to the temperature, driving force and the kinetic factors. Thus higher coarsening rates should therefore be associated with higher interfacial energies, higher diffusion coefficients and higher solubilities.

As a result of coarsening, the low number density of precipitates can, in some cases, lead to the eventual failure of the material. For example, the high temperatures and stresses experienced by turbine blades within jet engines can lead to material coarsening, which as a result can lead to the catastrophic failure of the component. Such an event is to be avoided if possible, so it is important to understand the factors and mechanisms that influence the rate of coarsening and study the role of elasticity. To clarify the mechanisms by which precipitates coarsen, it is necessary to investigate the details of the local arrangements of the precipitates,

their subsequent evolution and the diffusion of solute from the smaller precipitate to the larger precipitate particle.

11.2 – Literature Review

In the absence of elastic interactions and with the Gibbs phase energy, between the matrix and precipitates, in a state of equilibrium, it is expected that the decrease in surface area of the precipitates will dominate the reduction in total energy. Spherical precipitate shapes minimise the surface energy and distortions from the spherical nature of these shapes will generally not be observed in the absence of any elastic interactions or surface energy anisotropy. However, in the presence of elastic strain the evolution and final equilibrium shape of the precipitate is determined by minimising the sum of the interfacial and elastic strain energies. Although the fundamental mechanisms responsible for Ostwald ripening are well established, it has proven more difficult to model the coarsening kinetics of two particles along with the effects of elasticity as compared to that of a single precipitate particle. The treatment of interacting precipitates requires consideration of factors such as precipitate alignment, orientation and distance of separation (i.e. spatial correlations), which are absent within a single precipitate system.

The simplest models of coarsening omit any influence of elasticity and are usually only applicable to systems in which there is negligible misfit strain. A good review of some of the methods that have been previously used to model the process of coarsening is provided by Che and Hoyt [78]. Many of these previous attempts to model coarsening are extensions and modifications to the classical theory of Ostwald ripening due to Lifshitz and Slyozov [8] and Wagner [9] (LSW theory). Here, the precipitates are assumed to be spherical and fixed in space, and the analysis is limited to binary alloys where the coarsening proceeds by the diffusional transport of a single independent chemical component. The LSW theory basically states that the mean particle radius tends to change in proportion to the power law of $t^{1/3}$, and that the particle size distribution, when scaled by the average particle size, approaches a time independent form as $t \rightarrow \infty$. From this power law, it can be seen that the rate of coarsening decreases rapidly with time. The situation changes radically when a difference in lattice spacing between the matrix and precipitate is introduced (i.e. a lattice misfit), which gives rise to long-range elastic interactions. In this case, precipitate shapes have been seen to be non-spherical (more cuboidal or plate-like) and tend to align themselves into almost regular arrays

in order to minimise the total elastic energy [79] [80]. The theoretical studies of Enomoto and Kawasaki [81], Nishimori and Onuki [82] [83], Leo et al. [84] and Abinandanan [85] and the experiments of Miyazaki et al. [86] and Miyazaki and Doi [87] show that elastic deformation can alter the temporal power law for the average particle size during coarsening.

Enomoto and Kawasaki [81] (and some of the references therein) have shown that modelling the effect of elasticity on coarsening are not always simple, affecting both the local equilibrium concentration near the precipitate interface boundaries and the diffusion processes in the bulk phases. Johnson and Voorhees [3] have shown that elastically-induced shape transitions can occur during precipitate growth and coarsening when the shape that minimises the elastic energy is different from that which minimises the interfacial energy. Jou [59] applied the boundary integral method to model the effects of elastic fields on the process of coarsening between two particles. The results from this analysis found that considerable precipitate shape change occurs in the presence of elastic strain. It was found that if the particles are softer than the matrix, they mutually attract each other due to the elastic interactions, while if the precipitates are harder than the matrix, they repel one another. Due to the distorted shape changes associated with the particles, the surface energy was observed to increase as the elastic energy dominated the decrease of total energy. It was concluded that the overall shape behaviour of the precipitates will depend on the details of the misfit and the elastic constants of both the precipitate and matrix phases, along with the initial geometric configuration relating to the separation and orientation of the particles.

Gurtin and Voorhees [91] have shown that precipitate particles, subject to an internal misfit strain, have been found to take shapes which are spherical at small sizes, cuboidal at intermediate sizes and plate-like at large sizes. However, in any analysis, the geometry and characteristic length scale of interest has to be carefully characterised since the surface energy scales with the surface area of the precipitate and the elastic stored energy scales with the volume of the precipitate. The particle shape should evolve towards a spherical shape which minimises the isotropic interfacial energy at small volumes and towards a shape that minimises the elastic stored energy at large volumes. The definitions of “small” and “large” depend on the physical and geometric properties of the system under consideration.

11.3 – Physical Background of $M_{23}C_6$

The complex cubic crystallographic structure of $M_{23}C_6$ was first determined by Westgren [92] in 1933, which consists of 116 atoms [92] with a lattice parameter of 10.621 [94]. Snapshots taken from different angles of the complex cubic structure of $M_{23}C_6$ are shown in Figure 11.2, and a full three-dimensional rotational atomic model (developed by Simon Gill) can be viewed at <http://www.le.ac.uk/eg/spg3/atomic.html>.

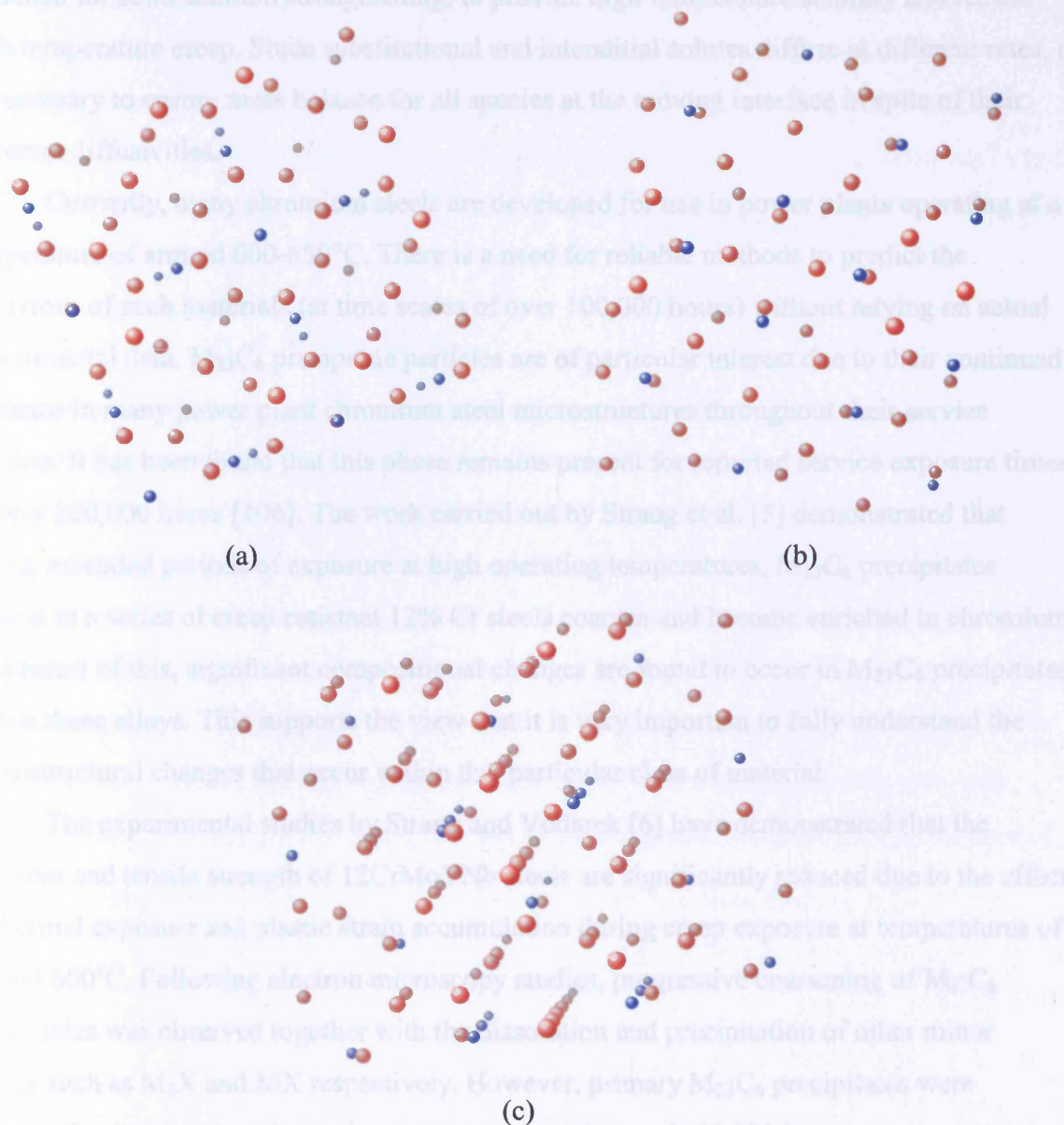


Figure 11.2 – Snapshots taken from different angles of the $M_{23}C_6$ complex cubic atomic structure. The red atoms represent M (iron / chromium) and smaller blue atoms are interstitial carbon.

Naturally, the formation of $M_{23}C_6$ mainly involves the substitutional diffusion of iron and chromium and the interstitial diffusion of carbon. Other substitutional alloying elements such as Nickel (Ni), Tungsten (W), Molybdenum (Mo), Vanadium (V) and Niobium (Nb) are also found to substitute partially for chromium. It is well known that the addition of chromium provides oxidation resistance and other elements such as tungsten and molybdenum can also be added for solid solution strengthening, to provide high-temperature stability and reduce high temperature creep. Since substitutional and interstitial solutes diffuse at different rates, it is necessary to ensure mass balance for all species at the moving interface in spite of their different diffusivities.

Currently, many chromium steels are developed for use in power plants operating at a temperature of around 600-650°C. There is a need for reliable methods to predict the behaviour of such materials (at time scales of over 100,000 hours) without relying on actual experimental data. $M_{23}C_6$ precipitate particles are of particular interest due to their continued presence in many power plant chromium steel microstructures throughout their service lifetime. It has been found that this phase remains present for reported service exposure times of over 200,000 hours [106]. The work carried out by Strang et al. [5] demonstrated that during extended periods of exposure at high operating temperatures, $M_{23}C_6$ precipitates present in a series of creep resistant 12% Cr steels coarsen and become enriched in chromium. As a result of this, significant compositional changes are found to occur in $M_{23}C_6$ precipitates within these alloys. This supports the view that it is very important to fully understand the microstructural changes that occur within this particular class of material.

The experimental studies by Strang and Vodarek [6] have demonstrated that the hardness and tensile strength of 12CrMoVNb steels are significantly reduced due to the effects of thermal exposure and plastic strain accumulation during creep exposure at temperatures of around 600°C. Following electron microscopy studies, progressive coarsening of $M_{23}C_6$ precipitates was observed together with the dissolution and precipitation of other minor phases such as M_2X and MX respectively. However, primary $M_{23}C_6$ precipitates were continually observed to exist during creep exposure times of 100,000 hours at a temperature of 600°C. Within this analysis, $M_{23}C_6$ precipitate growth was seen to initially increase at an approximately linear rate with exposure time, but after prolonged exposure, an abrupt

reduction in the coarsening rate is observed suggesting a tendency towards a limiting particle size and an equilibrium condition.

It can be seen that the coarsening of $M_{23}C_6$ carbide precipitates is an important phenomenon within creep resistant steels used for high temperature components within aircraft jet engines and industrial power plants. This chapter discusses the application of the variational model to simulate the coarsening of $M_{23}C_6$ carbide precipitates and to study the complex role of elasticity on the coarsening process. The model has the potential for use as a residual life assessment of high temperature service exposed components where the coarsening of $M_{23}C_6$ precipitates plays a major role. The model also has the potential for simulating the effect of applied loading on the process of coarsening of these precipitates and to investigate whether external elastic fields can be used to stabilise or hinder the coarsening process within these steel alloys.

11.4 – Description of the Problem

Consideration is given to a regularly spaced periodic dispersion of $M_{23}C_6$ iron / chromium carbide precipitates located within a bcc ferrite matrix as shown in Figure 11.3. The repeating unit of Figure 11.3 (highlighted in red) is shown in Figure 11.4, where two $M_{23}C_6$ precipitate quadrants are aligned in the x -direction and consist of radii r_1 and r_2 , where $r_1 \neq r_2$. The two precipitates are initially taken to be circular (although the computer code can accommodate any initial shape), and are arranged within two-dimensional space such that they occupy volumes, $V_1^{M_{23}C_6}$ and $V_2^{M_{23}C_6}$ respectively. In the following analysis, consideration is given to the carbon / vacancy interstitial sublattice, and within each precipitate a uniform molar carbon composition of $y_c^{M_{23}C_6}$ is defined by stoichiometric constraints. The volume of the ferrite matrix, V^{bcc} , is taken to consist of a uniform carbon composition, y_c^{bcc} .

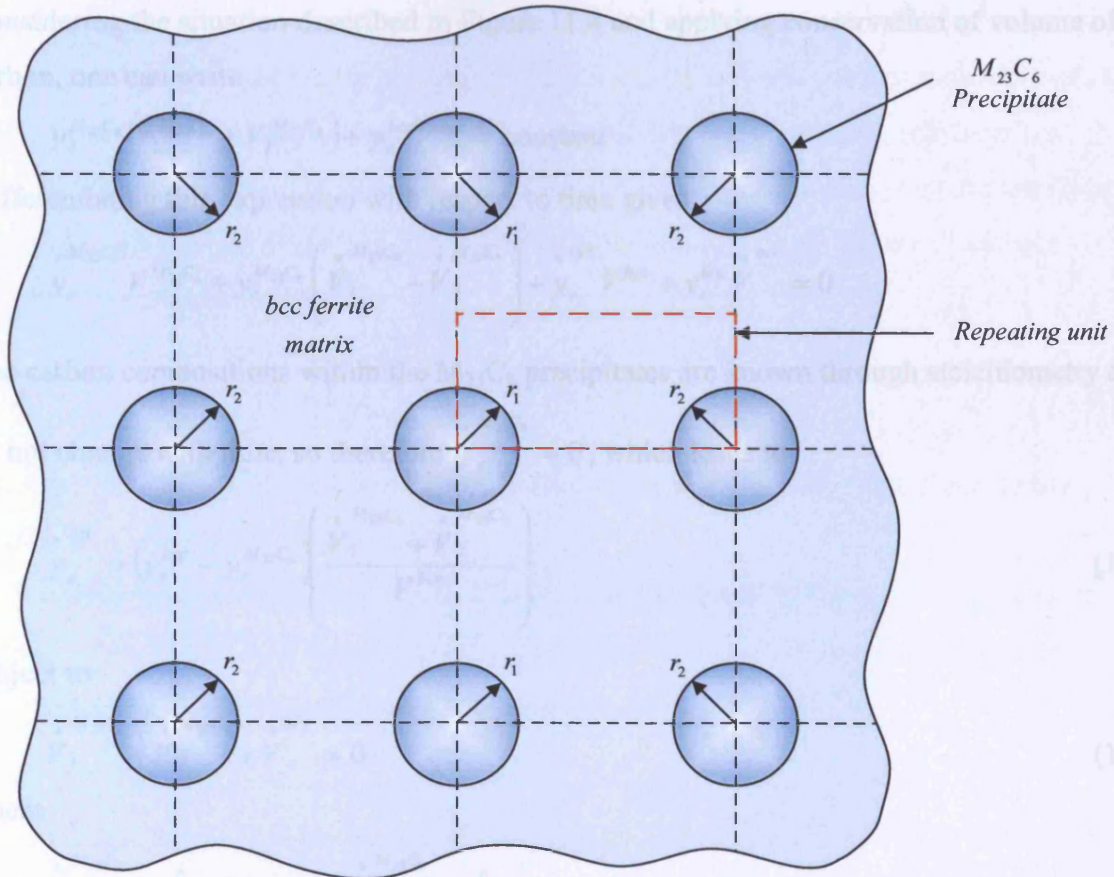


Figure 11.3 – A regularly spaced dispersion of $M_{23}C_6$ iron / chromium carbide precipitates located within a bcc ferrite matrix.

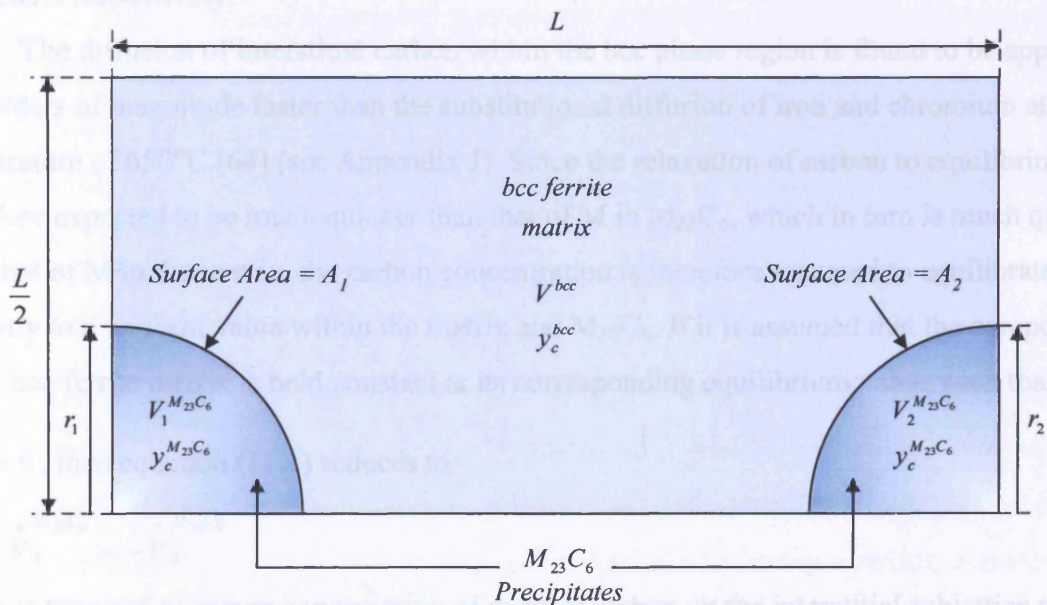


Figure 11.4 – The repeating unit consisting of two $M_{23}C_6$ precipitate quadrants, of radii r_1 and r_2 , embedded within a bcc ferrite matrix.

Considering the situation described in Figure 11.4 and applying conservation of volume of carbon, one can write

$$y_c^{M_{23}C_6} (V_1^{M_{23}C_6} + V_2^{M_{23}C_6}) + y_c^{bcc} V^{bcc} = \text{constant}$$

Differentiating this expression with respect to time gives

$$y_c^{M_{23}C_6} \dot{V}^{M_{23}C_6} + y_c^{M_{23}C_6} \left(\dot{V}_1^{M_{23}C_6} + \dot{V}_2^{M_{23}C_6} \right) + y_c^{bcc} \dot{V}^{bcc} + y_c^{bcc} \dot{V}^{bcc} = 0$$

The carbon compositions within the $M_{23}C_6$ precipitates are known through stoichiometry and do not change with time, so therefore $\dot{y}_c^{M_{23}C_6} = 0$, which leads to

$$y_c^{bcc} = \left(y_c^{bcc} - y_c^{M_{23}C_6} \right) \left(\frac{\dot{V}_1^{M_{23}C_6} + \dot{V}_2^{M_{23}C_6}}{V^{bcc}} \right) \quad (11.1)$$

subject to

$$\dot{V}_1^{M_{23}C_6} + \dot{V}_2^{M_{23}C_6} + \dot{V}^{bcc} = 0 \quad (11.2)$$

where

$$\dot{V}_1^{M_{23}C_6} = \int_{A_1} v_{ni} dA \quad \dot{V}_2^{M_{23}C_6} = \int_{A_2} v_{ni} dA$$

where the integrals are performed over the interfacial surface areas, A_1 and A_2 , of each precipitate respectively.

The diffusion of interstitial carbon within the bcc phase region is found to be approx. 7 to 8 orders of magnitude faster than the substitutional diffusion of iron and chromium at a temperature of 650°C [64] (see Appendix J). Since the relaxation of carbon to equilibrium is therefore expected to be much quicker than that of M in $M_{23}C_6$, which in turn is much quicker than that of M in the matrix, the carbon concentration is therefore assumed to equilibrate instantly to a uniform value within the matrix and $M_{23}C_6$. If it is assumed that the composition in the bcc ferrite matrix is held constant at its corresponding equilibrium value, such that

$y_c^{bcc} = 0$, then equation (11.1) reduces to

$$\dot{V}_1^{M_{23}C_6} = -\dot{V}_2^{M_{23}C_6} \quad (11.3)$$

which is required to ensure conservation of mass of carbon on the interstitial sublattice and implies constant volume of precipitate. Equation (11.3) dictates (through mass conservation)

that if one particle grows then the other particle in the system must shrink. This equation essentially decouples the metal and interstitial sublattices and ensures that the volume of the matrix and the $M_{23}C_6$ precipitates remain unchanged respectively. The linear interface velocity relation of equation (5.10) is integrated over the area of each precipitate interface boundary, and equation (11.3) is computationally enforced through the use of a single Lagrangian constraint such that

$$\lambda \left(\sum_t \int_{-s'_o}^{+s'_i} v_n^t(s) ds \right) = \lambda \left(\sum_t \left(\frac{v_{n1}^t + v_{n(i+1)}^t}{2} \right) 2s_o^t \right) = 0 \quad (11.4)$$

where the summation is performed over each interface boundary segment, t , across the interfacial surface areas of each precipitate.

Since the total volume of the $M_{23}C_6$ precipitates shown in Figure 11.4 is conserved during coarsening (through equation (11.4)), the final radius, R , of the resulting single precipitate can be determined through the relation

$$R = \sqrt{(r_1^2 + r_2^2)} \quad (11.5)$$

provided that the precipitates remain circular and the interface radii, r_1 and r_2 , are initially given. However, during coarsening, the curvature of the smaller precipitate will approach infinity as its radius approaches zero, which implies that the surface energy driving force will also approach an infinite value. Therefore, as the radius of the smaller precipitate reaches a critical size, the coarsening kinetics and interface velocity of the smaller precipitate will increase dramatically.

If consideration is given to the diffusion of the components on both sublattices, the flux of carbon can be calculated through the stoichiometric relation between the sublattice components such that

$$j_c^p = \frac{c^p}{a^p} (j_{Fe}^p + j_{Cr}^p)$$

where a^p and c^p are given in Appendix J. However, since the iron / chromium sublattice is independent of the carbon / vacancy sublattice and the composition of carbon is fixed within each phase (no compositional gradients exist for interstitial carbon to diffuse), the evolution of the microstructure can be described in terms of the diffusion of one component, chromium, such that

$$j = j_{Cr} = -j_{Fe}$$

The interface condition is applied to the diffusion of chromium on the main sublattice such as to ensure mass conservation as the interface moves. The flux of chromium must be continuous, apart from at the interface, such that

$$(j_{\alpha}^{bcc} - j_{\alpha}^{M_{23}C_6})n_{\alpha} = -(a^{bcc} y_{Cr}^{bcc} - a^{M_{23}C_6} y_{Cr}^{M_{23}C_6})v_n \quad (11.6)$$

where n_{α} is the normal to the interface pointing into the bcc phase, v_n is the component of the velocity of the interface in the direction of n_{α} and the other quantities are determined on either side of the interface. The velocity of the interface is therefore given by the diffusion of chromium.

It is the diffusion of chromium which determines the evolution of the microstructure and consideration is therefore only given to this element. The variational functional of equation (4.23) can be written as

$$\Pi = \frac{1}{2} \sum_{p=1}^2 \int \frac{j_{\alpha} j_{\alpha}}{y_{Cr}^p (1 - y_{Cr}^p) \mathcal{D}^p} dV + \frac{d}{dt} \left\{ \sum_{p=1}^2 \int [G^p + U_e] dV + \int_{A_1+A_2} \gamma_s dA \right\} \quad (11.7)$$

where j_{α} represents the flux of chromium, y_{Cr}^p is the proportion of sites occupied by chromium atoms (the remaining sites are occupied by iron atoms), \mathcal{D}^p is the combined lattice diffusivity of chromium and iron in phase, p (see Appendix J), G^p is the phase energy, U_e is the elastic stored energy per unit volume and γ_s is the interfacial surface energy. The material properties within the two phases, such as Young's modulus, Poisson's ratio and the transformation strain, are weakly dependent on the chromium content but are included within this analysis. An extensive literature search found no specific data relating to the diffusivity of iron or chromium in $M_{23}C_6$, so from talks with experts in this field [94], it was assumed to be twice that of iron and chromium in ferrite respectively (see Appendix J). It is assumed not to be affected by local straining of the lattice. There was also found to be a lack of data relating to the Young's modulus and Poisson's ratio of $M_{23}C_6$, so it was assumed that these properties were independent of the chromium content but similar to that of bcc ferrite (see section 11.6 for details relating to the elastic analysis).

11.5 – The Phase Energy

The thermodynamic parameters contained in the Gibbs free energy and chemical potential functions were extracted (as in the previous chapter) from a recent evaluation of the Fe-C-Cr system [75] [76]. The $M_{23}C_6$ carbide is considered as a stoichiometric two-sublattice compound, where the first sublattice is occupied by the metal elements iron (Fe) and chromium (Cr) and the second sublattice is completely filled by interstitial carbon. In the work by Andersson [75], this phase was modelled as a stoichiometric compound with three-sublattices in order to incorporate experimental information from higher order systems such as Fe-Cr-W-C and Fe-Cr-Mo-C. Since higher order systems are not considered in the current analysis and substitutional components (such as tungsten and molybdenum) apart from iron and chromium are ignored, this thermodynamic assessment was changed to a two-sublattice model.

The lattice site fraction of carbon, y_c , is related to the carbon molar fraction, x_c , through equation (2.2), where a^p and c^p (used to denote the numbers of sites on each sublattice in a formula unit) are defined in Appendix J. The lattice site fraction of iron, y_{Fe} , is related to the molar fraction of iron, x_{Fe} , through the relation

$$y_{Fe} = \frac{x_{Fe}}{(1-x_c)}$$

and the site fraction of chromium, y_{Cr} , is simply

$$y_{Cr} = 1 - y_{Fe}$$

The molar fraction of chromium, x_{Cr} , can be calculated from

$$x_{Cr} = 1 - x_{Fe} - x_c$$

The phase energy density of bcc α -iron can be expressed, at a specified temperature, T , in the form of

$$G^{bcc} = \rho^{bcc} \left\{ \begin{aligned} & y_{Cr}(1-y_c)B_1^{bcc} + y_{Cr}y_cB_3^{bcc} + y_{Fe}(1-y_c)B_2^{bcc} + y_{Fe}y_cB_4^{bcc} \\ & + RT \left[a^{bcc} (y_{Cr} \ln y_{Cr} + y_{Fe} \ln y_{Fe}) + c^{bcc} (y_c \ln y_c + (1-y_c) \ln(1-y_c)) \right] \\ & + y_c(1-y_c)(y_{Cr} + y_{Fe})B_5^{bcc} + y_{Cr}y_{Fe} \left((1-y_c)B_6^{bcc} + y_cB_7^{bcc} \right) + G_{mo}^{bcc} \end{aligned} \right\} \quad (11.8)$$

where B_i^{bcc} and G_{mo}^{bcc} are temperature dependent constants associated with the bcc lattice, which are listed in Appendix J, and ρ^{bcc} is the number of mols of iron per cubic metre.

The phase energy density of $M_{23}C_6$ can be expressed, at a specified temperature, T , in the form

$$G^{M_{23}C_6} = \rho^{M_{23}C_6} \left\{ y_{Cr} B_1^{M_{23}C_6} + y_{Fe} B_2^{M_{23}C_6} + a^{M_{23}C_6} RT (y_{Cr} \ln y_{Cr} + y_{Fe} \ln y_{Fe}) \right\} + y_{Cr}^2 y_{Fe}^2 (B_3^{M_{23}C_6} + 2B_4^{M_{23}C_6} (y_{Cr} - y_{Fe})) \quad (11.9)$$

where $B_i^{M_{23}C_6}$ are temperature dependent constants also listed in Appendix J. The derivatives of the phase energy density with respect to the chromium composition for both bcc ferrite and $M_{23}C_6$ can be easily calculated from equations (11.8) and (11.9) respectively.

11.5.1 – Phase Energy Dependence on Carbon Composition

The graph outlined in Figure 11.5 shows the variation in phase energy with chromium content for different carbon compositions within a bcc ferrite matrix at a temperature of 650°C. This graph shows the low sensitivity of the phase energy with increase in carbon composition with no distinct variation in phase energy observed as the carbon content is increased from zero to over the maximum solubility (0.0075 mol%) within this phase. If it is therefore assumed that the carbon composition within the bcc ferrite matrix is constant then this will have little effect on the overall phase energy, which is more strongly dependent on the composition of chromium.

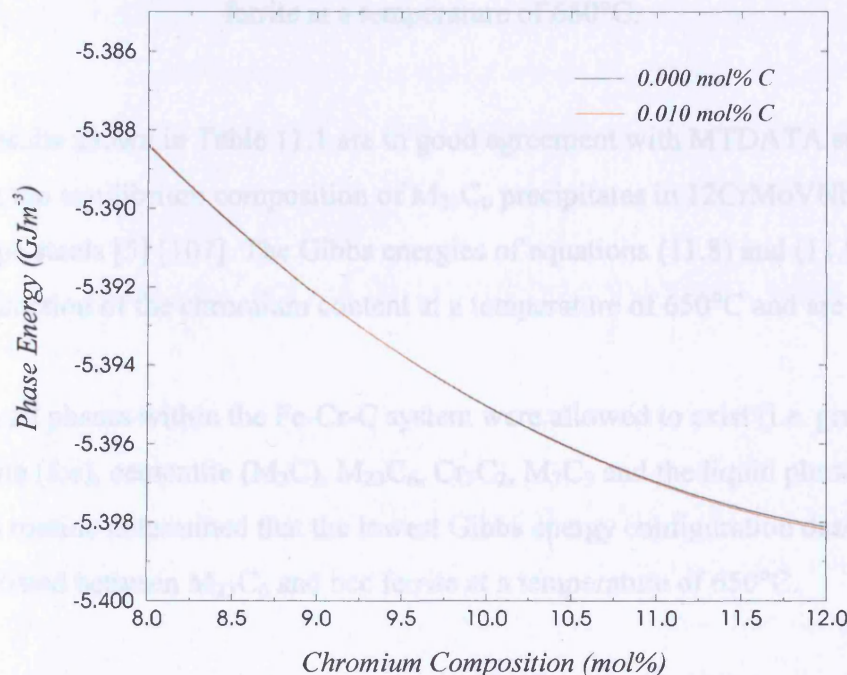


Figure 11.5 – Graph showing the variation in phase energy with chromium content for different carbon compositions within a bcc ferrite matrix at a temperature of 650°C.

11.5.2 – Phase Energy Equilibrium Solution

In order to calculate the Gibbs free energy thermodynamic equilibrium configuration (in the absence of any capillarity and elastic effects) between the $M_{23}C_6$ precipitate and the ferrite matrix, the Gibbs free energy expressed in equations (11.8) and (11.9) was minimised. The minimisation was constrained such that the stoichiometry of the phases (i.e. the number of moles of each sublattice are in the correct ratio) was preserved as was conservation of mass (i.e. the number of moles of each component is correct). The Gibbs free energy minimisation was carried out at a temperature of 650°C and yielded the configuration described in Table 11.1 below.

<i>Phase</i>	<i>Sublattice 1</i>		<i>Sublattice 2</i>
	c_{Fe} (mol%)	c_{Cr} (mol%)	c_c (mol%)
<i>bcc ferrite</i>	86.97	13.03	1.5×10^{-3}
$M_{23}C_6$	18.20	61.11	20.69

Table 11.1 – Calculated lowest Gibbs phase energy configuration between $M_{23}C_6$ and bcc ferrite at a temperature of 650°C.

The results shown in Table 11.1 are in good agreement with MTDATA studies carried out to predict the equilibrium composition of $M_{23}C_6$ precipitates in 12CrMoVNb and 12CrMoV type steels [5] [107]. The Gibbs energies of equations (11.8) and (11.9) were plotted as a function of the chromium content at a temperature of 650°C and are shown in Figure 11.6.

When all phases within the Fe-Cr-C system were allowed to exist (i.e. graphite, ferrite (bcc), austenite (fcc), cementite (M_3C), $M_{23}C_6$, Cr_3C_2 , M_7C_3 and the liquid phase), the minimisation routine determined that the lowest Gibbs energy configuration described in Table 11.1 existed between $M_{23}C_6$ and bcc ferrite at a temperature of 650°C.

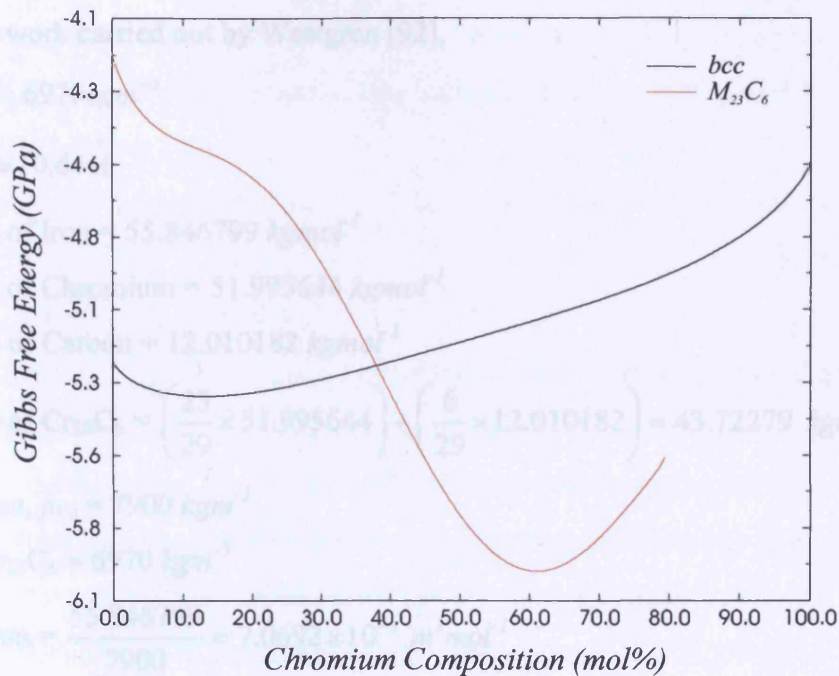


Figure 11.6 – Gibbs free energy variation with chromium content at a temperature of 650°C.

11.6 – Elastic Analysis

In the following analysis, consideration is given to the misfit strain arising from the difference in lattice spacings between the $M_{23}C_6$ precipitate and the surrounding bcc ferrite matrix. It is assumed that the precipitates and matrix are elastically isotropic, so inhomogeneity provides the elastic driving force for particle motion and morphology change.

11.6.1 – The Transformation Strain

The lattice parameters of iron and chromium at room temperature within a bcc unit cell [36] can be defined as

$$a_{Cr} = 0.2884$$

$$a_{Fe} = 0.2866$$

indicating that there is only approximately 0.6% difference between the lattice spacings of iron and chromium. This small difference implies only a small strain energy contribution within the α -iron matrix due to the substitutional diffusion of iron and chromium within this phase. Carbon occupies the interstitial sites and therefore does not significantly affect the lattice spacing of iron and chromium atoms within a bcc unit cell. The strain energy contribution from the $M_{23}C_6$ precipitate is therefore only considered in this analysis.

According to work carried out by Westgren [92],

$$\rho_{Cr_{23}C_6} = 6970 \text{ kgm}^{-3}$$

$$a_{Cr_{23}C_6} = 10.64 \text{ \AA}$$

Atomic mass of Iron = $55.846799 \text{ kgmol}^{-1}$

Atomic mass of Chromium = $51.995644 \text{ kgmol}^{-1}$

Atomic mass of Carbon = $12.010182 \text{ kgmol}^{-1}$

$$\text{Atomic mass of } Cr_{23}C_6 = \left(\frac{23}{29} \times 51.995644 \right) + \left(\frac{6}{29} \times 12.010182 \right) = 43.72279 \text{ kgmol}^{-1}$$

Density of Iron, $\rho_{Fe} = 7900 \text{ kgm}^{-3}$

Density of $Cr_{23}C_6 = 6970 \text{ kgm}^{-3}$

$$\text{Volume of Iron} = \frac{55.846799}{7900} = 7.0692 \times 10^{-3} \text{ m}^3 \text{ mol}^{-1}$$

$$\text{Volume of } Cr_{23}C_6 = \frac{43.72279}{6970} = 6.2730 \times 10^{-3} \text{ m}^3 \text{ mol}^{-1}$$

$$\text{Volume per mol} = N \bar{a}^3$$

where \bar{a} is the average lattice spacing and N is Avogadro's number ($6.02 \times 10^{23} \text{ mol}^{-1}$)

So,

$$\bar{a}_{Fe} = \left(\frac{7.0692 \times 10^{-3}}{N} \right)^{\frac{1}{3}} = \frac{0.19192}{N^{\frac{1}{3}}}$$

$$\bar{a}_{Cr_{23}C_6} = \left(\frac{6.2730 \times 10^{-3}}{N} \right)^{\frac{1}{3}} = \frac{0.18443}{N^{\frac{1}{3}}}$$

Therefore the mis-match strain, ϵ_o , between these structures is calculated as

$$\epsilon_o = \frac{\bar{a}_{Fe}}{\bar{a}_{Cr_{23}C_6}} - 1 = 0.04064 \approx 4\%$$

As the lattice spacing of chromium and iron are similar, it is assumed that

$\bar{a}_{Cr_{23}C_6} = \bar{a}_{Fe_{23}C_6} = \bar{a}_{M_{23}C_6}$, such that the mis-match strain is independent of the choice of M.

11.6.2 – Material Property Variation with Chromium Composition

Data detailing changes in elastic constants with the chromium content within bcc α -iron was extrapolated from work carried out by Leslie [93]. The data provided in this paper allowed linear elastic relations to be obtained for the Young's modulus and Poisson's ratio

dependence on the chromium content within bcc ferrite. Although the data within this paper only considers chromium contents up to 11%, higher chromium content data was obtained from www.WebElements.com.

The linear elastic relations extrapolated from these sources can be expressed as

$$\begin{aligned} E^{bcc}(x_{Cr}^{bcc}) &= 68.0x_{Cr}^{bcc} + 208.2 \\ \nu^{bcc}(x_{Cr}^{bcc}) &= -0.080x_{Cr}^{bcc} + 0.291 \end{aligned} \quad (11.10)$$

where E^{bcc} is expressed in GPa . It can be seen from these relations that both the Young's modulus and Poisson's ratio vary weakly with variation in the molar fraction of chromium, with a Young's modulus variation of only $8.8 GPa$ as the chromium content is increased from zero to 13%. Therefore, the global elastic driving force due to the change in elastic stored energy with chromium content is relatively weak but is nevertheless included into the variational functional. Due to the lack of experimental data on $M_{23}C_6$, the material properties of this phase are assumed to be independent of chromium composition and are defined as $E^{M_{23}C_6} = 210.0 GPa$ and $\nu^{M_{23}C_6} = 0.291$.

11.7 – Interfacial Surface Energy

From work by Strang, Vodarek and Bhadeshia [5], the surface energy of an $M_{23}C_6$ precipitate can be considered as, $\gamma_s = 0.25 Jm^{-2}$. The elastic strain energy and compositional phase energy densities both depend on the volume and scale with the cube of the unit length. The interfacial terms scale as the unit length squared, and hence the non-dimensionalised problem is not completely independent of the chosen length scale. The non-dimensionalised surface energy can therefore be described by

$$\overline{\gamma}_s = \frac{\gamma_s}{\{w\} \{L\}} \quad (11.11)$$

where $\{w\}$ is the unit of volumetric energy density and $\{L\}$ is the unit of length. The importance of surface energy contributions with respect to the bulk energy contributions clearly depends on the length scale. The contribution due to surface energy is more important at small length scales than at larger length scales.

It is expected that a $M_{23}C_6$ precipitate typically has a radius of the order of $50nm - 100nm$ [94], so computational simulations are therefore performed within this range of characteristic length scales. Although Okamoto and Suehiro [95] change the interfacial energy as the particles grow, Miyazaki [96] has shown that a single value for the interfacial energy

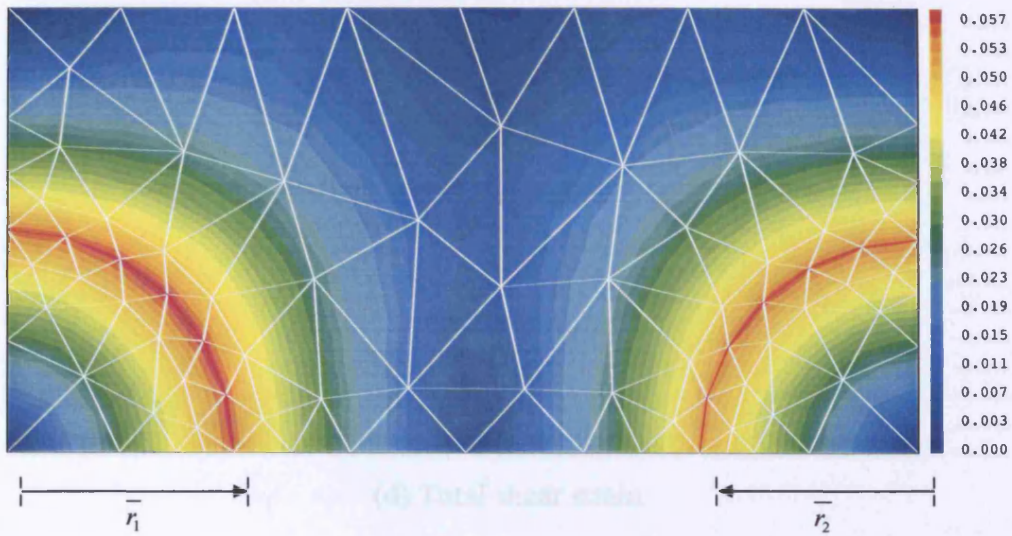
can describe the entire range of particle sizes. Therefore, in this analysis it was assumed that the interfacial surface energy, γ_s , was constant during the coarsening and evolution of the precipitate particles. We choose $\{w\} = 1 \text{ GJm}^{-3}$ such that $\bar{\gamma}_s = 0.25\{L\}$ where $\{L\}$ is in nanometres.

11.8 – Results and Discussion

The precipitation sequence is assumed to have already occurred and the $M_{23}C_6$ precipitates are initially given a circular shape. The non-dimensionalised precipitate particle radii are chosen such that $\bar{r}_1 = 2.5$ and $\bar{r}_2 = 2.4$ (see Figure 11.4), indicating that the size of the right-hand particle is approximately 8% smaller by area than that of the left-hand particle. From equation (11.5) it can be expected that the system will evolve, in the absence of any elastic effects, such that the smaller particle will be consumed by the larger particle until a single $M_{23}C_6$ precipitate exists of non-dimensional radius, $\bar{R} = 3.47$.

The circular interfaces are constructed from six interface boundary segments, which are not sub-divided into any boundary sub-segments in order to reduce computational processing costs associated with large mesh densities around the interfacial regions. The initial finite element mesh geometry is shown in Figure 11.7 along with the initial configuration with respect to the elastic displacements, elastic strain field, elastic stored energy distribution, lattice flux field and associated interface velocities. It can be seen from this initial configuration that the elastic displacement field, due to the lattice mis-match between the two phases, is smooth and continuous across the sharp interface boundaries. The largest displacements are located at the interface between the two phases and the elastic strain fields show that the precipitates are initially highly constrained. The system is initially symmetrical so there is little difference between the vertical and horizontal strain fields around the precipitates. In order to minimise the elastic strain energy, the elastic driving force acts in a direction such that it attempts to minimise the size of both precipitates.

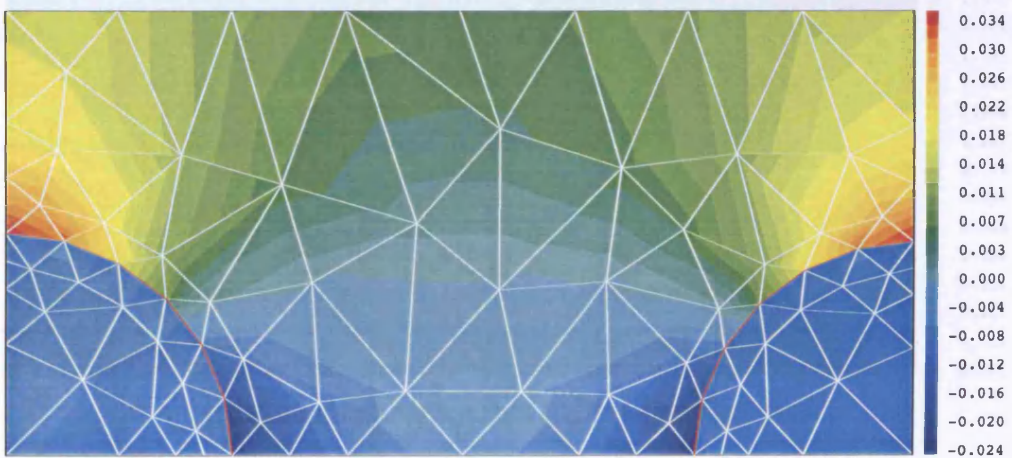
The interfacial condition models the discontinuity in the flux field which is initially seen to be non-uniform but confined to the interfacial regions. The initial distribution of interface velocities indicates that elasticity is likely to induce considerable precipitate shape change during particle coarsening. In the case of no elastic effects, the initial flux field is seen to be completely uniform and symmetric along each interface with a smooth uniform distribution of interface velocities.



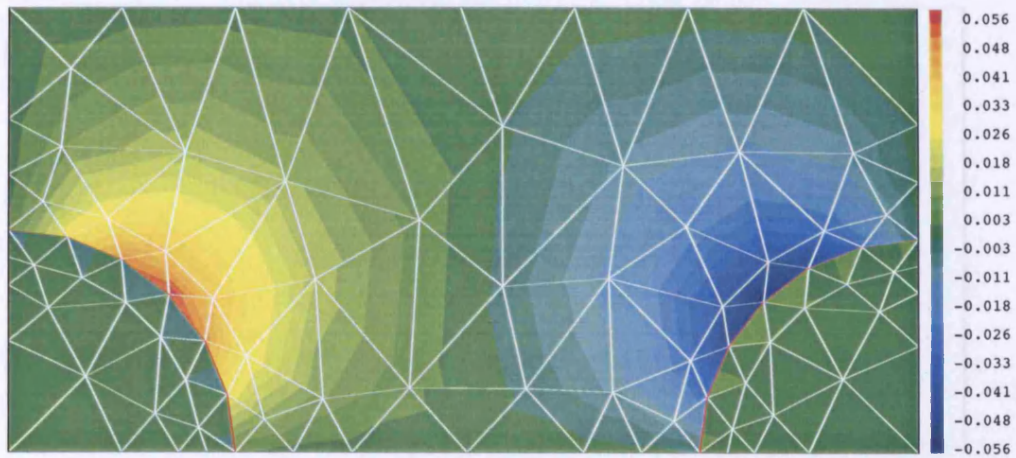
(a) Elastic displacements



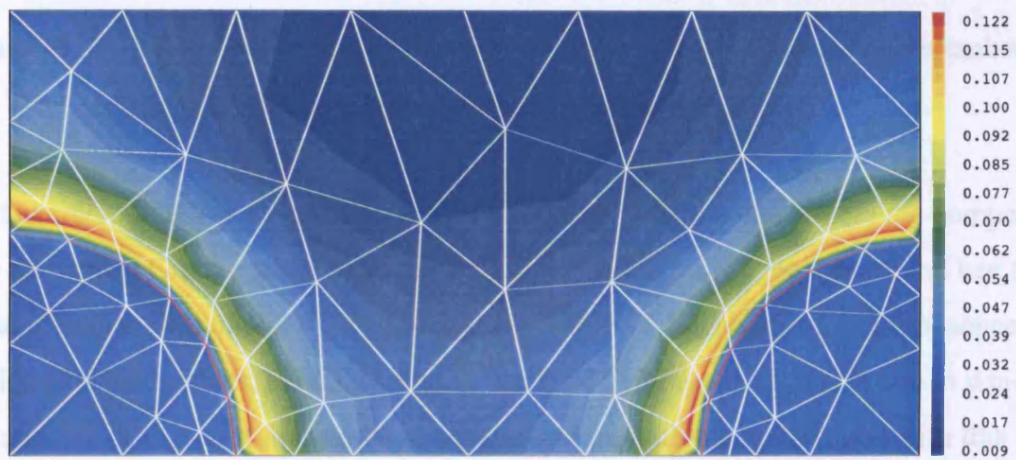
(b) Strain in the x -direction



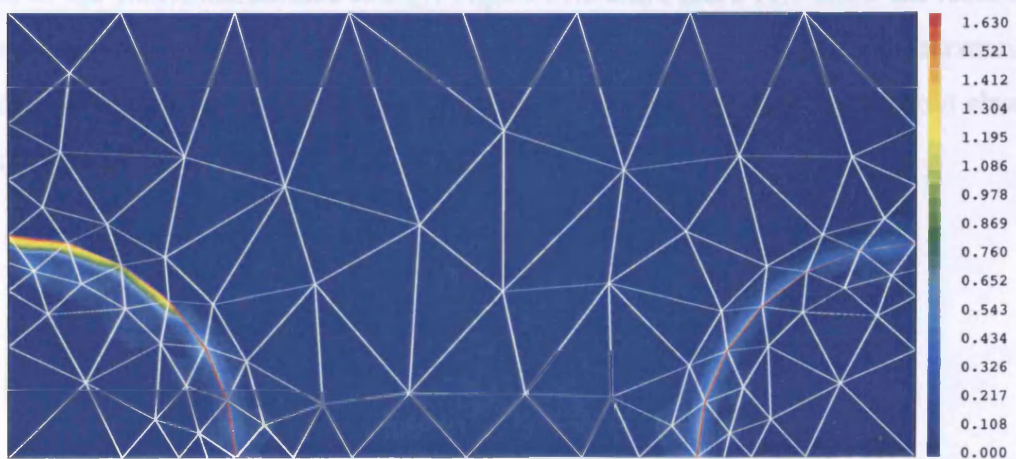
(c) Strain in the y -direction



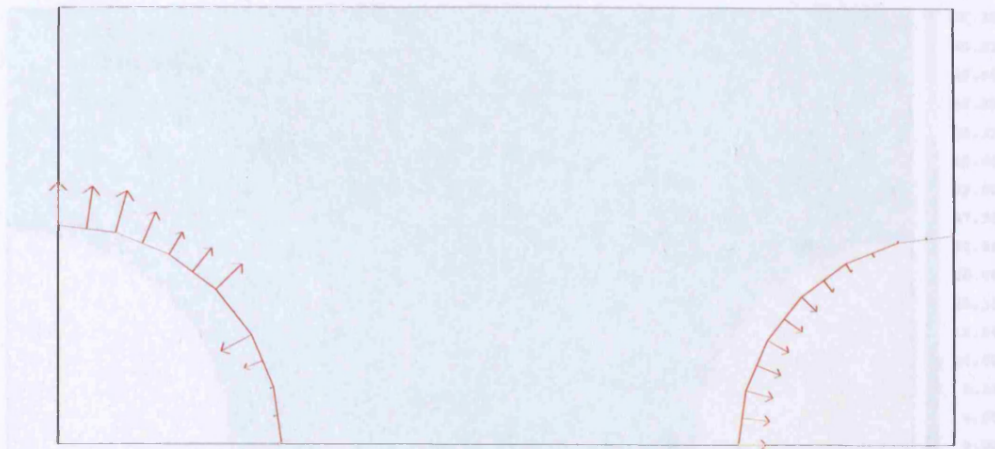
(d) Total shear strain



(e) Continuous elastic stored energy distribution



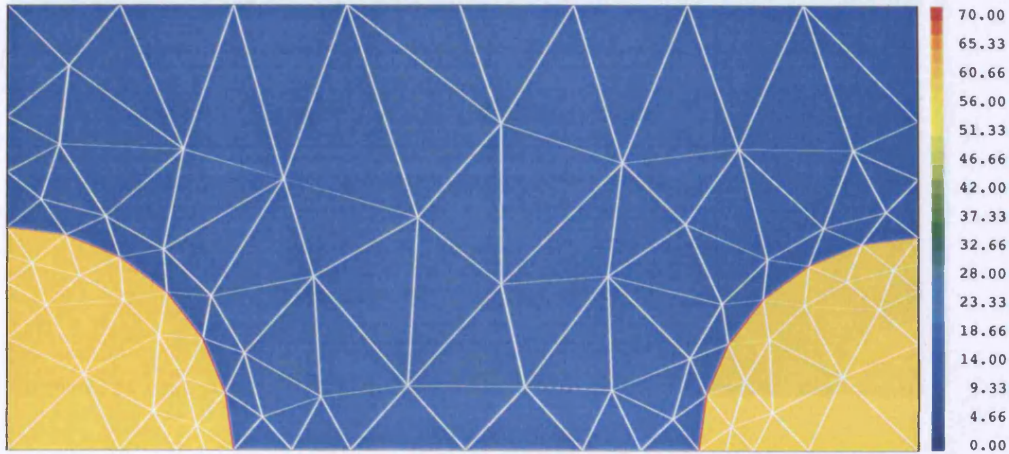
(f) Volumetric lattice flux field (with elasticity)



(e) Interface velocity distribution (with elasticity)

Figure 11.7 – Initial configuration of two initially circular $M_{23}C_6$ precipitates embedded within a ferrite matrix.

The microstructure description shown in Figure 11.8(a) is that where the compositions provide the lowest Gibbs energy configuration between the $M_{23}C_6$ precipitate and bcc ferrite matrix at a temperature of 650°C, as described in Table 11.1. Therefore, in the absence of any capillarity or elastic effects, the configuration described in Figure 11.8(a) is one in which the precipitates are in a state of thermodynamic equilibrium with the matrix, and with this configuration no form of microstructure evolution or particle coarsening will occur. With the inclusion of the interfacial surface energy, Figure 11.8 and Figure 11.9 show the resulting chromium compositional contours and phase morphology during two particle coarsening over non-dimensional time using six-noded triangular finite elements, with and without elasticity included in the model.



(a) $\bar{t} = 0.000$



(b) $\bar{t} = 87.040$

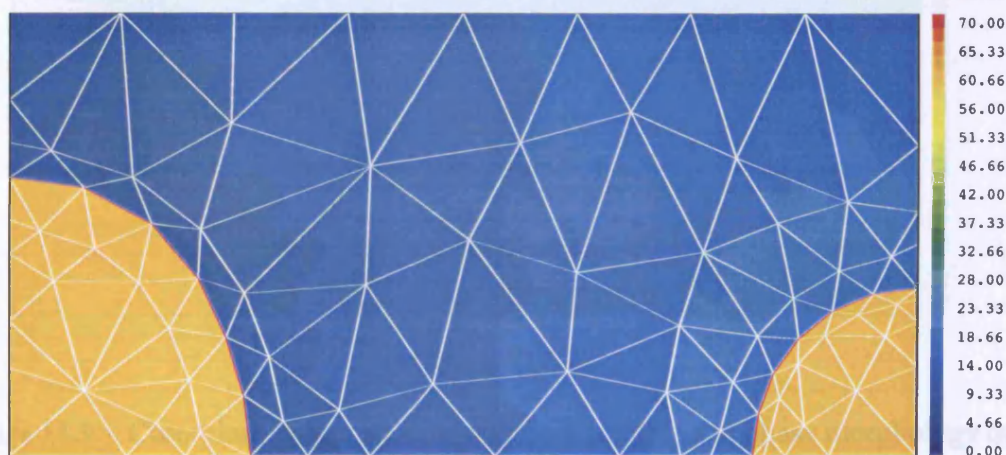


(c) $\bar{t} = 94.879$



(d) $\bar{t} = 97.661$

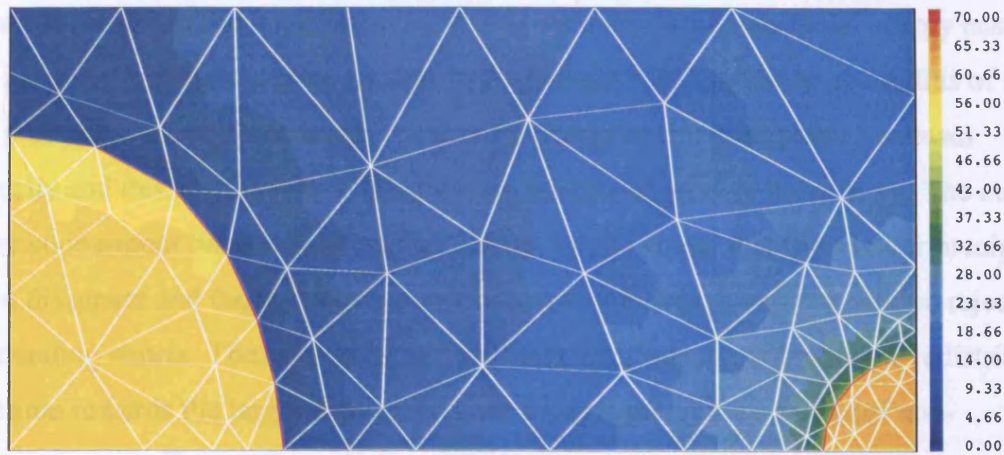
Figure 11.8 – Chromium compositional contours (mol%) and phase morphology during coarsening at 650°C without elasticity effects included in the model.



(a) $\bar{t} = 56.191$



(b) $\bar{t} = 67.063$



(c) $\bar{t} = 70.751$



(d) $\bar{t} = 71.328$

Figure 11.9 – Chromium compositional contours (mol%) and phase morphology during coarsening at 650°C with elasticity effects included in the model.

From Figure 11.8 it can be seen that, in the absence of elastic effects, the smaller right-hand particle shrinks and rejects chromium into the surrounding ferrite matrix, while the larger left-hand particle grows by taking in chromium from the surrounding matrix. Chromium compositional gradients soon develop and a steady diffusional flux exists to transport chromium from the smaller particle to that of the larger particle. The coarsening process is initially quite slow since the matrix contains a relatively low amount of chromium for the growth of the larger particle, and the diffusion of chromium in the ferrite matrix is slower than that within the $M_{23}C_6$ precipitates. However, large compositional gradients soon develop between the two precipitates and chromium is transported down these gradients to

allow for the growth of the larger particle. The dominance of the interfacial energy ensures that the interface boundaries do not distort from their circular shapes. As the radius of the smaller precipitate particle decreases, the surface energy of this precipitate increases dramatically and this has the effect of increasing the rate of particle coarsening. The current computer code cannot handle disappearing phases, but it is clear that the smaller precipitate will soon disappear and the high chromium content within this precipitate will be rejected into the surrounding matrix. The microstructure will then continue to evolve by the redistribution of chromium towards the larger precipitate until a single precipitate exists (of non-dimensional radius, $\bar{R} = 3.47$) and a state of thermodynamic equilibrium is attained.

It can be seen from Figure 11.9 that a similar process occurs when the effect of elasticity is included into the model. In this case, considerable shape change is observed to occur primarily within the growing precipitate. The larger precipitate is seen to experience some repulsion from the shrinking precipitate during coarsening and long range elastic interactions between the particles cause the larger precipitate to extend into a vertical plate-like structure. This result is confirmed by Figure 11.10, which shows the motion of two points, located where each precipitate interface intersects the horizontal and vertical system boundaries, along with the average interface radius of each precipitate over non-dimensional time with the effects of elasticity. From this Figure, the outer interface boundary points of the growing precipitate show that this precipitate distorts from its initially circular shape within a relatively short space of time. Although this distortion does not appear to either increase or decrease over time, the square-like cuboidal configuration appears to be that which minimises the elastic stored energy. Contrary to the shape change and distortion experienced by the larger precipitate, the smaller precipitate experiences very little shape change and remains circular as it decreases in size.

Figure 11.11 shows the variation of each precipitate radius over non-dimensional time, where the interfacial radii are calculated by averaging over all points located along each interface boundary at each selected point in time, both with and without elasticity. It can be seen from this Figure that elasticity has the effect of speeding up the coarsening process, which can be substantiated by the fact that there is more energy available within the system and this provides a larger driving force for the microstructure to evolve. This finding has been confirmed by experimental investigations carried out by Hättestrand and Andrén [97] (and

some of the references contained therein), who confirmed that the coarsening of $M_{23}C_6$ carbides was found to be accelerated through the influence of elastic strain.

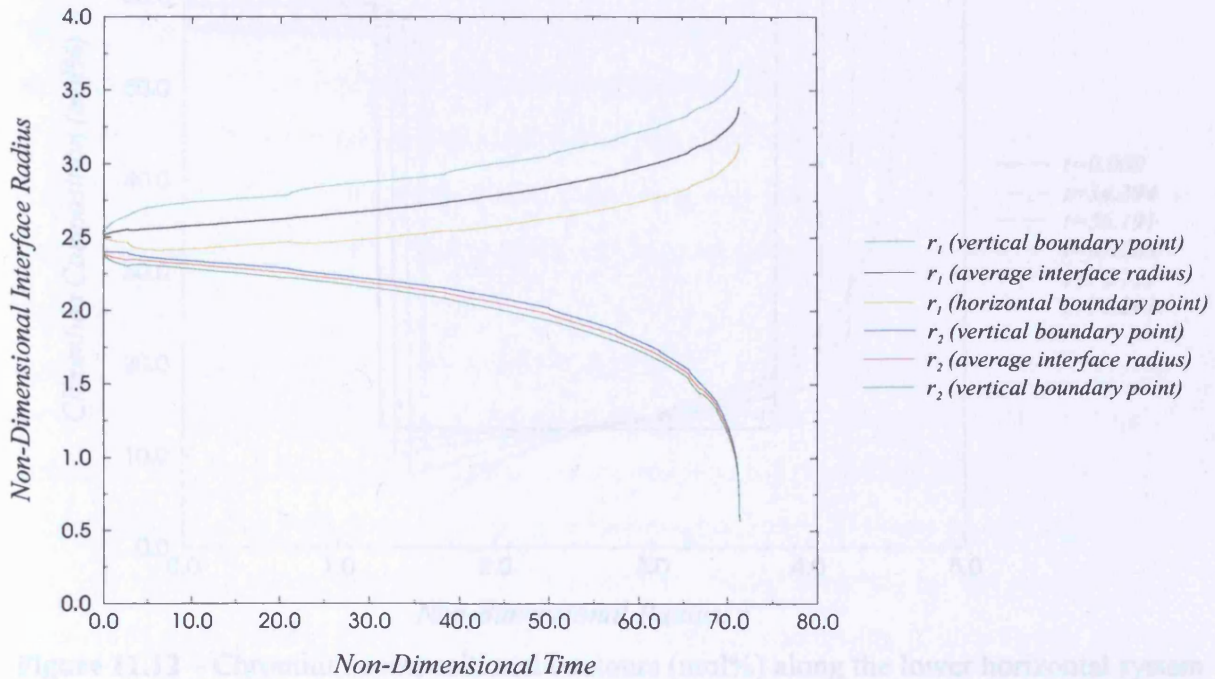


Figure 11.10 – Migration of two interface boundary points and the average radius for each initially circular precipitate particle during coarsening with the effect of elasticity.

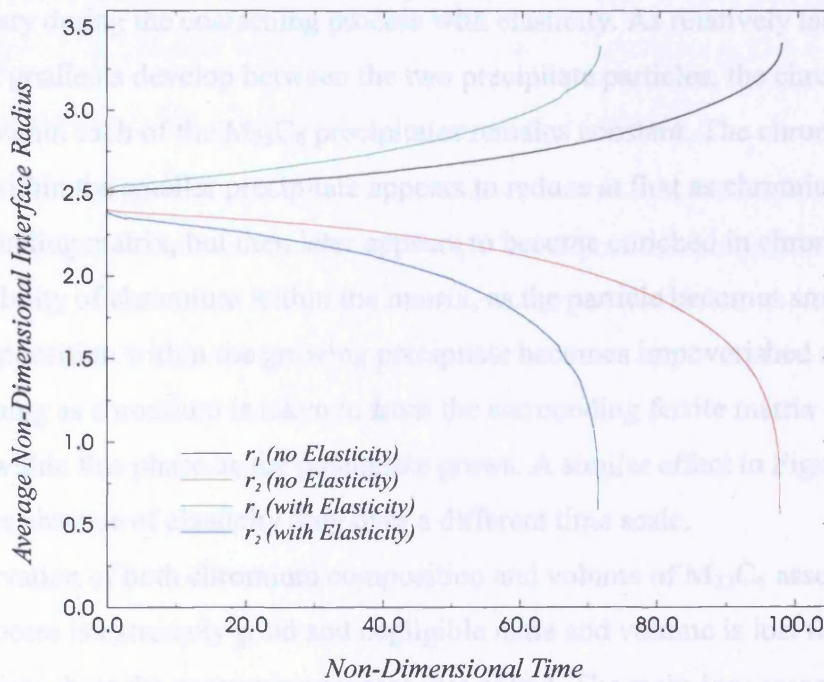


Figure 11.11 – Variation of the average interface radii of two initially circular $M_{23}C_6$ precipitates over non-dimensional time during coarsening both with and without elasticity.

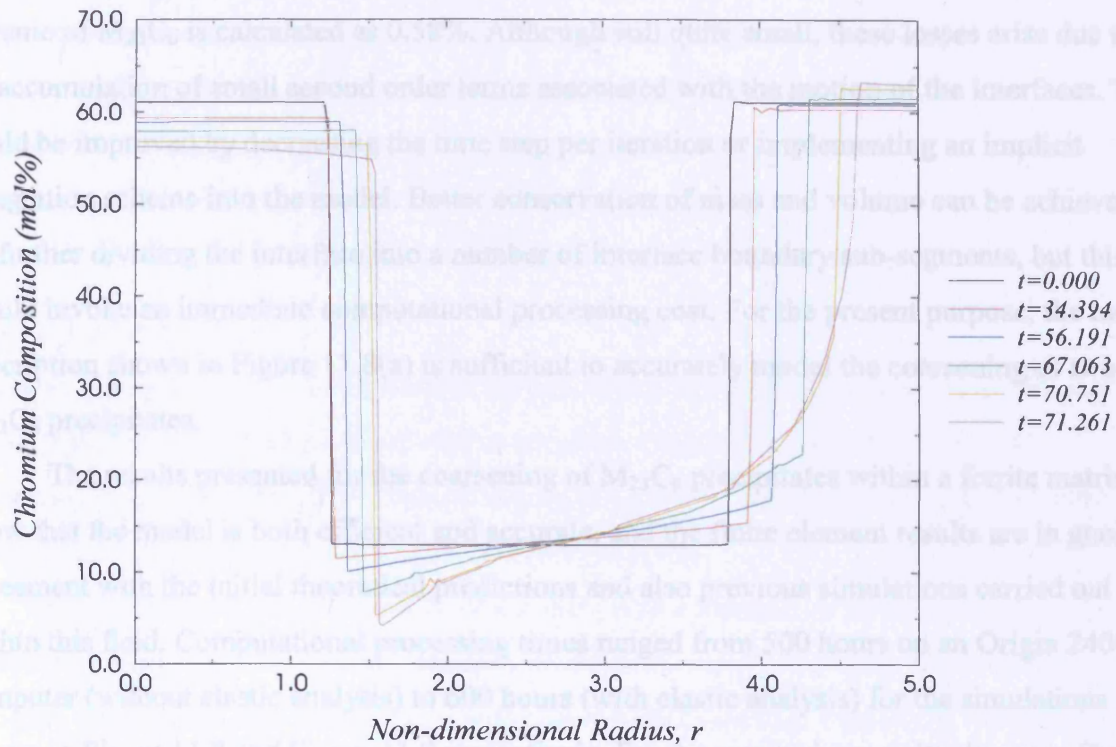


Figure 11.12 – Chromium compositional contours (mol%) along the lower horizontal system boundary with elasticity effects included into the model.

Figure 11.12 shows how the chromium composition varies along the lower horizontal system boundary during the coarsening process with elasticity. As relatively large compositional gradients develop between the two precipitate particles, the chromium composition within each of the $M_{23}C_6$ precipitates remains constant. The chromium composition within the smaller precipitate appears to reduce at first as chromium is rejected into the surrounding matrix, but then later appears to become enriched in chromium, due to the lower solubility of chromium within the matrix, as the particle becomes smaller. The chromium composition within the growing precipitate becomes impoverished and reduces during coarsening as chromium is taken in from the surrounding ferrite matrix and redistributed within this phase as the precipitate grows. A similar effect to Figure 11.12 is also observed in the absence of elasticity only over a different time scale.

Conservation of both chromium composition and volume of $M_{23}C_6$ associated with the coarsening process is extremely good and negligible mass and volume is lost from the initial state to the point where the coarsening process was halted. The mass loss associated with two particle coarsening with elasticity is calculated as approximately 0.064%, while the loss of

volume of $M_{23}C_6$ is calculated as 0.58%. Although still quite small, these losses arise due to an accumulation of small second order terms associated with the motion of the interfaces. This could be improved by decreasing the time step per iteration or implementing an implicit integration scheme into the model. Better conservation of mass and volume can be achieved by further dividing the interface into a number of interface boundary sub-segments, but this would invoke an immediate computational processing cost. For the present purpose, the mesh description shown in Figure 11.8(a) is sufficient to accurately model the coarsening of two $M_{23}C_6$ precipitates.

The results presented for the coarsening of $M_{23}C_6$ precipitates within a ferrite matrix show that the model is both efficient and accurate, and the finite element results are in good agreement with the initial theoretical predictions and also previous simulations carried out within this field. Computational processing times ranged from 500 hours on an Origin 2400 computer (without elastic analysis) to 600 hours (with elastic analysis) for the simulations shown in Figure 11.8 and Figure 11.9 respectively. For the coarsening results shown in Figure 11.9, the real time taken from the initial configuration to reach the point where the simulation was halted (shown in Figure 11.9(d)) is 141,435 hours (approx. 842 weeks) where the selected characteristic length scale, $\{L\} = 10nm$. Although the simulation is relatively slow and relatively long processing times are required to obtain such results, considerable advantage is still achieved over experimental investigations over much longer time scales.

11.9 – Comparison with Classical Coarsening Models

To obtain an insight into the expected coarsening behaviour, a simplified variational analysis of two interacting precipitates is conducted. To achieve an analytical result it is assumed that the reduction in interfacial surface energy is the only thermodynamic driving force and the concentration of the diffusing species does not change with time. Both elastic and compositional phase energies are consequently ignored. The simplified variational analysis is presented in Appendix K, from which the following two-particle coarsening relationships are derived

$$\frac{dr_1}{dt} = \frac{A}{r_1} \left(\frac{1}{r_2} - \frac{1}{r_1} \right) \quad (11.12a)$$

$$\frac{dr_2}{dt} = \frac{A}{r_2} \left(\frac{1}{r_1} - \frac{1}{r_2} \right) \quad (11.12b)$$

where A is defined as a constant. These expressions are identical to the classical Ostwald ripening equation for the growth rate of a precipitate [99], which is the basis of the mean-field theory for Ostwald ripening [7] [98]. This assumes that a scaling state exists in which the particle size distribution keeps the same shape although the scale may change. The conclusion of this argument is the widely used growth law for particle coarsening

$$\bar{r}^{-3}(t) - \bar{r}^{-3}(0) = kt$$

as derived in Appendix K. The assumptions introduced in the classical theory all vary in their validity and depend on the physical system which one is attempting to describe [19].

However, the predictions of the classical theory of Ostwald ripening are often found to be in good agreement with experimental observations [98] [99].

The non-dimensional interface radii variation as a function of non-dimensional time is plotted in Figure 11.13 for the two particles shown in Figure 11.4 in order to compare classical coarsening (equation (11.12)) with that obtained from the variational model without elasticity. For the classical model, the value of A was selected so that the smaller particle disappears at the same time as in the variational model (the value of A does not alter the general shape of the curve). When elasticity is included in the analysis the variational results are similar, but the evolution occurs more rapidly.

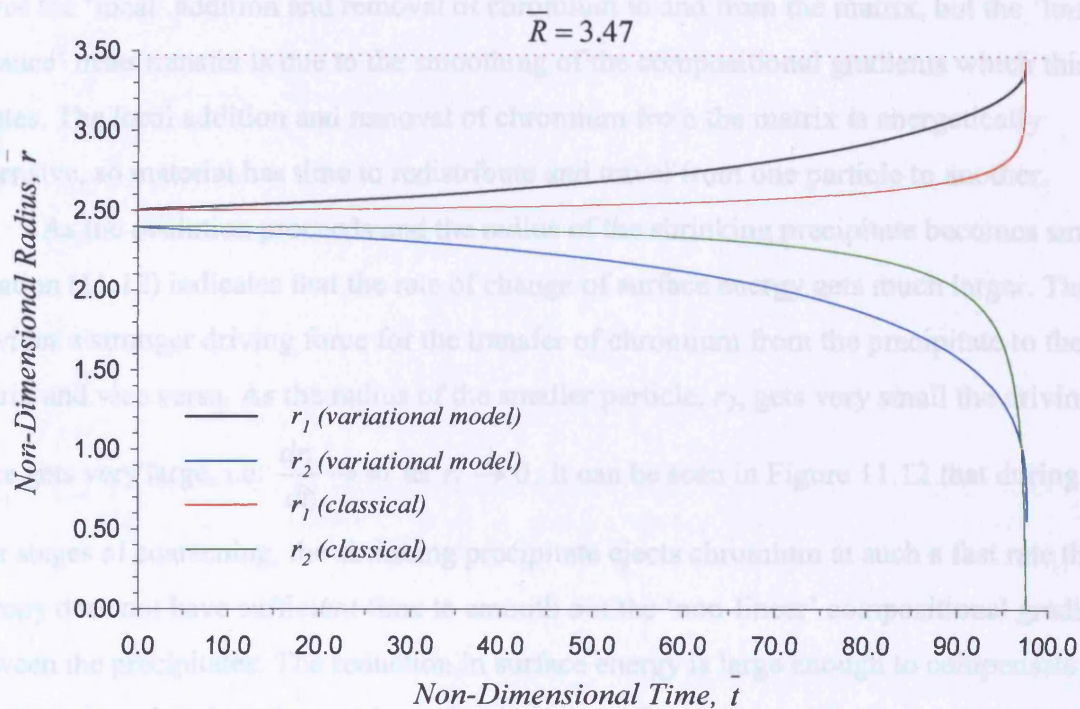


Figure 11.13 – Variation of non-dimensional interface radii as a function of non-dimensional time for two particle coarsening comparing classical Ostwald ripening with that obtained from the variational model (without elasticity).

Figure 11.13 shows that the classical coarsening curves do not match the shape of the curves from the variational model very closely, and that the behaviour of the interface radii, r_1 and r_2 , appears to be more complex compared to that of classical coarsening. This is expected since the variational model considers the contribution from the compositional phase energy and elastic stored energy, which is not addressed in the classical theory of Ostwald ripening.

Mass rearrangement during coarsening is initially local, i.e. no chromium is transferred between the precipitate particles. Chromium leaves the matrix and diffuses into the growing precipitate and chromium leaves the shrinking precipitate and is rejected into the surrounding matrix. The surface energy driving force in the early stages is quite small since the precipitate radii are initially very similar, i.e. $\bar{r}_1 \approx \bar{r}_2$. Chromium is therefore added / removed from the matrix at a relatively slow rate and entropy has time to smooth out the localised non-linear compositional fields. Hence linear concentration gradients develop between the two particles and chromium is transferred from the shrinking precipitate to that of the larger precipitate. This is illustrated in the early evolution of Figure 11.12. The surface energy driving force

drives the ‘local’ addition and removal of chromium to and from the matrix, but the ‘long distance’ mass transfer is due to the smoothing of the compositional gradients which this creates. The local addition and removal of chromium from the matrix is energetically expensive, so material has time to redistribute and travel from one particle to another.

As the evolution proceeds and the radius of the shrinking precipitate becomes smaller, equation (11.12) indicates that the rate of change of surface energy gets much larger. This provides a stronger driving force for the transfer of chromium from the precipitate to the matrix and vice versa. As the radius of the smaller particle, r_2 , gets very small the driving force gets very large, i.e. $\frac{dr_1}{dt} \rightarrow \infty$ as $r_2 \rightarrow 0$. It can be seen in Figure 11.12 that during the later stages of coarsening, the shrinking precipitate ejects chromium at such a fast rate that the entropy does not have sufficient time to smooth out the ‘non-linear’ compositional gradients between the precipitates. The reduction in surface energy is large enough to compensate for rejecting chromium into the matrix so that it does not have to travel from one precipitate to another for the precipitates to grow / shrink.

Figure 11.14 shows the variation of the average rate of change of interface radius of the growing precipitate, $\frac{d\bar{r}_1}{dt}$ (from the variational model) against the right hand side of equation

(11.12a), i.e. $\frac{1}{r_1} \left(\frac{1}{r_2} - \frac{1}{r_1} \right)$, for two particles coarsening without elasticity. Figure 11.15 shows

the equivalent log-log graph of Figure 11.14 and compares the rate of classical coarsening with the data obtained from the variational model without the effects of elasticity. It can be seen that the interface velocity field of the growing precipitate is seen to fluctuate somewhat, particularly in the later stages of coarsening, as the chromium is rapidly ejected and then removed from the interface before further transfer can take place.

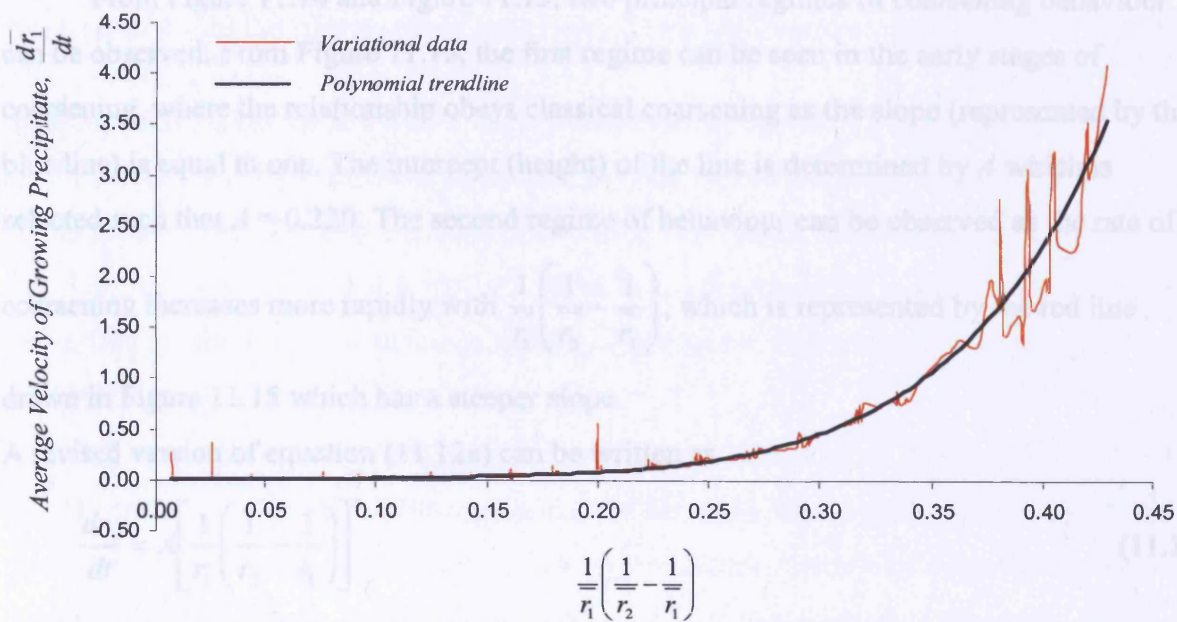


Figure 11.14 – Variation of the average interface velocity of the growing precipitate against the right hand side of equation (11.12a) for two particle coarsening without elasticity. If the evolution obeyed the classical coarsening relationship of equation (11.12a) the curve would be a straight line of slope A through the origin.

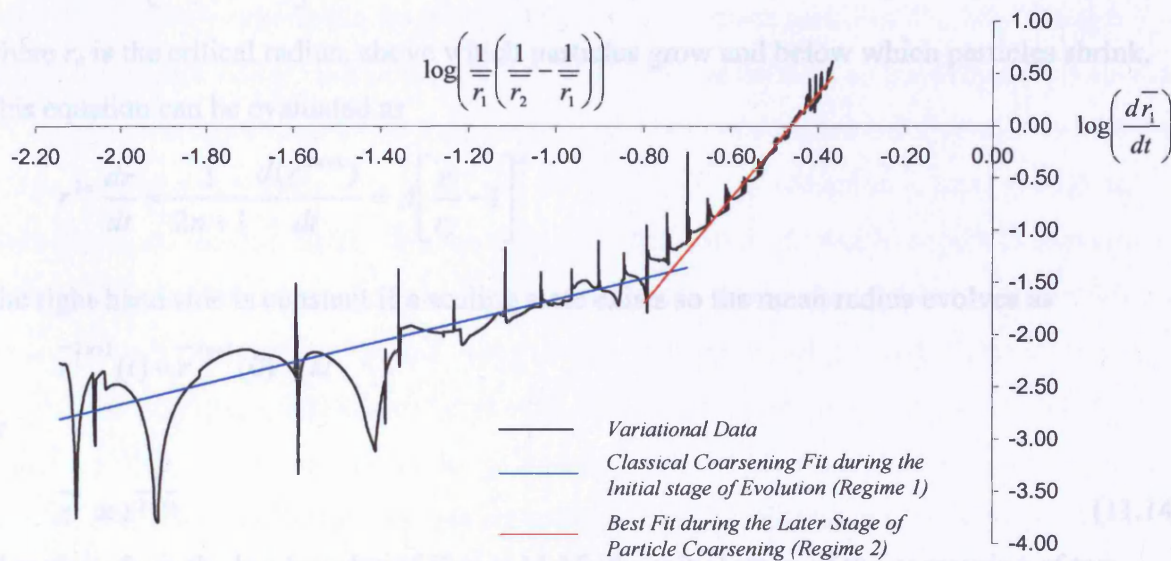


Figure 11.15 – Equivalent log-log graph of Figure 11.14 comparing the rate of classical coarsening of equation (11.12a) with the data obtained from the variational model without elasticity.

From Figure 11.14 and Figure 11.15, two principal regimes of coarsening behaviour can be observed. From Figure 11.15, the first regime can be seen in the early stages of coarsening, where the relationship obeys classical coarsening as the slope (represented by the blue line) is equal to one. The intercept (height) of the line is determined by A which is selected such that $A = 0.220$. The second regime of behaviour can be observed as the rate of coarsening increases more rapidly with $\frac{1}{r_1} \left(\frac{1}{r_2} - \frac{1}{r_1} \right)$, which is represented by the red line

drawn in Figure 11.15 which has a steeper slope.

A revised version of equation (11.12a) can be written as

$$\frac{dr_1}{dt} = A \left[\frac{1}{r_1} \left(\frac{1}{r_2} - \frac{1}{r_1} \right) \right]^n \quad (11.13)$$

where n is the slope of the log-log fit shown in Figure 11.15. Clearly $n = 1$ is the classical result and this is the slope at the beginning of particle coarsening (during the first regime). Near the end of particle coarsening (i.e. within the second regime), the slope changes to $n = 5$. In a mean field theory, equation (11.13) can be written as

$$\frac{dr}{dt} = A \left[\frac{1}{r} \left(\frac{1}{r_c} - \frac{1}{r} \right) \right]^n$$

where r_c is the critical radius, above which particles grow and below which particles shrink.

This equation can be evaluated as

$$r^{2n} \frac{dr}{dt} = \frac{1}{2n+1} \frac{d(r^{2n+1})}{dt} = A \left[\frac{r}{r_c} - 1 \right]^n$$

The right-hand side is constant if a scaling state exists so the mean radius evolves as

$$r^{-2n+1}(t) - r^{-2n+1}(0) = kt$$

or

$$r^{-3} \propto t^{\frac{3}{2n+1}} \quad (11.14)$$

Therefore, from the log-log plot of Figure 11.15, the initial stage of the coarsening of two $M_{23}C_6$ particles (regime 1) follows the classical growth law of $r^{-3} \propto t$. Near the end of particle coarsening (regime 2), equation (11.14) dictates that the mean field precipitate radius varies according to $r^{-3} \propto t^{\frac{3}{11}}$. In this case, the transition from the classical coarsening behaviour of

regime 1 to that of the later stages of coarsening of regime 2 occurs when $\frac{1}{r_1} \left(\frac{1}{r_2} - \frac{1}{r_1} \right) \approx 0.2$

(determined from the intersection of the fitted coarsening curves of Figure 11.15).

When elasticity is included in the analysis, the value of n (slope of the log-log fit) within each regime of coarsening behaviour remains unaltered, but the value of A (intercept) was found to change such that $A = 0.350$. Therefore, when elasticity is considered, the same coarsening growth laws are obeyed as without elasticity but coarsening is found to be accelerated by approximately 37%.

The overall evolution depends on which process dominates. In this simulation the time spent in each regime appears to be approximately the same. The second regime only occurs near the end of evolution when the surface energy reduction rate is very large. Hence the dominance of this regime depends on the length scale. In this simulation the length scale considered is relatively small ($\{L\} = 10\text{nm}$). Hence the surface energy (which depends on area and scales with the square of the unit length) has a large contribution compared to the compositional phase energy (which depends on the volume and scales with the cube of the unit length), i.e. $area / volume = 1 / length$, so as the length scale decreases the surface energy is more important. The influence from the compositional phase energy and elastic stored energy is therefore expected to be greater for larger precipitate particles. For larger length scales, the surface energy contribution is less significant at the start so the evolution is slower, i.e. regime 1 occupies most of the time and regime 2 only occurs in a brief period towards the end as the particles become very small and the surface energy reduction is large enough to eject chromium into the matrix. Hence, at large length scales one would expect to see classical Ostwald ripening but not at smaller length scales. As the coarsening initially occurs rapidly to remove the very small particles, this is perhaps not detected experimentally. This effect could however be important in nanoparticle systems. Nevertheless, an interesting effect has been discovered that occurs near the demise of a particle which only becomes significant once the particle is below a certain size and merely accelerates its already rapid end. Hence for large particles the significant part of the evolution is expected to be classical.

For reasons already mentioned, experimental investigations into coarsening do not always show such localised compositional changes between precipitates [6]. The variational model assumes that the rate of coarsening is primarily governed by volumetric diffusion between precipitate particles. This assumption may be criticised somewhat since some

particles form on lath or sub-grain boundaries and one would expect that coarsening would be enhanced by a more rapid diffusion along these boundaries. It has been reported that $M_{23}C_6$ particles often form on boundaries, and also to some extent within laths or sub-grains [111]. However, there currently appears to be a lack of available experimental data concerning the evolution of $M_{23}C_6$ precipitates to allow for direct comparison with the results obtained from the variational model. The majority of available experimental data is typically obtained from long-term creep exposure during in-service operating conditions [5]. Due to the lack of experimental data, the classical theory of Ostwald ripening has been used as a basis for comparison due to its reported good agreement with previous experimental observations. The effect of grain boundaries and creep relaxation could be incorporated into the variational principle but it is beyond the scope of the work presented in this thesis.

The classical coarsening theory is useful in describing the mean field coarsening effect of a large number of precipitate particles within a general microstructure. This is based on a simple constitutive relation. These simulations have been shown to be useful in deriving more accurate relations on which more advanced mean field theories can be developed. They have also shown that the variational model is a practical method for modelling the small scale coarsening features of precipitate particles under the influence of elasticity within a particular microstructure.

11.10 – Summary and Conclusions

The numerical model based on the variational principle has been successfully applied to model the kinetics and thermodynamics of the coarsening of two $M_{23}C_6$ precipitate particles embedded within a ferrite matrix under the influence of elastic strain. Simplifications were introduced such that the metal and interstitial sublattices can be decoupled, subject to the constraint of conservation of volume, whilst maintaining the stoichiometry of components within the phases. With the carbon compositions held constant within each phase, two particle coarsening was accurately simulated with chromium as the diffusing species.

It is shown that the effects of elastic fields can induce considerable particle distortion and shape change in order to minimise the global elastic strain energy. Elasticity was observed to alter the circular symmetric geometry of the growing precipitate to that of a cuboidal plate-like configuration and was also shown to speed up the process of particle coarsening. These

general findings are in good agreement with previous studies carried out within this field of research (see section 11.2).

The early stages of coarsening of the $M_{23}C_6$ precipitate particles has been found to follow the classical growth law of Ostwald ripening, i.e. $r^{-3} \propto t$. The later stages of two particles coarsening was found to obey the growth law of $r^{-3} \propto t^{11/3}$. Within the simulation presented in this chapter, a significant part of the evolution of $M_{23}C_6$ precipitate particles was found to obey that of classical coarsening. The dominance of each regime of coarsening behaviour has been found to be dependent on the length scale of the simulation.

12.0 – General Conclusions and Further Work

12.1 – Summary and Conclusions

A general numerical model based on a fundamental variational principle has been developed to model the kinetics and thermodynamics of microstructural evolution in multi-component multi-phase systems within which elastic strain plays a significant role. The variational framework readily allows for the incorporation of a number of different competing kinetic processes and thermodynamic driving forces into a numerical model without geometrical restrictions.

The variational model has been successfully applied to model the evolution of a class of moving boundary precipitate systems subject to a number of thermodynamic driving forces and compositional variations in the presence of deformation due to either a misfit or an applied strain field. The driving force due to the elastic stored energy has been implemented in a consistent manner such that it acts to reduce the global elastic strain energy. The general model places no restrictions on the geometry and number of components or phases that take part in the calculations, provided that the necessary thermodynamic and kinetic data are available.

A static underlying structured grid has been successfully coupled with a dynamic unstructured finite element mesh which is adapted to fit the line of the moving boundary. The transfer of data from one finite element geometry to another using the structured underlying grid has been validated and proved to give excellent accuracy with negligible loss of compositional data. The method for transferring information across finite element geometries can be readily applied to model other phase transformation moving boundary type phenomena within the fields of solid mechanics and also fluid dynamics.

The general model was applied to study the precipitation kinetics in steels with particular reference to the evolution of a ferrite precipitate embedded within an austenite matrix and the coarsening of $M_{23}C_6$ precipitate particles. Long range elastic effects were considered in both these cases and observed to cause considerable distortion on the growth morphology of the precipitate particle(s). On the growth of a ferrite precipitate embedded within an austenite matrix, elastic distortions were observed to halt the growth of the ferrite precipitate and alter the equilibrium shape such that the particle distorts from its initially

circular shape. On the coarsening of $M_{23}C_6$ precipitate particles embedded within a ferrite matrix, elasticity was observed to induce considerable shape change within the growing precipitate and also speed up the coarsening process. During coarsening of $M_{23}C_6$ precipitates, the shrinking precipitate became enriched in chromium and the growing precipitate became impoverished. In each of these two simulations, elastic effects were observed to alter the circular symmetric geometry of the precipitate(s) to that of almost cuboidal square-like configuration. This is accepted as the geometric configuration that minimised the elastic stored energy in each of these cases.

The variational approach presented in this thesis is shown to be a powerful technique for modelling microstructural changes which occur within engineering service components over time, without having to resort to long-term experimental investigations. The variational model has wide applicability to a number of complex microstructural processes involving phase transformations and can be used as a valuable life prediction tool for many in-service engineering components.

12.2 – Future Work

Proposed further work and extensions to this field of research:

1. The general variational method described in this thesis contains all the ingredients for simulating the microstructure evolution of more complex multi-phase multi-component systems. This variational method can therefore be used to study the effect of other interstitial and substitutional alloying elements on the precipitation and coarsening kinetics (considered by Voorhees and Glicksman [102] [103]) over a range of material systems. In the case of modelling multi-component systems, the same underlying grid may be used to transfer the compositions of each component across finite element geometries.
2. The elastic analysis within this thesis is currently limited to linear elasticity, but the finite element method has the distinct ability to model more complex non-linear elasticity, plasticity and creep phenomena. Modelling such complex processes would be fundamental to further understanding material behaviour during processing and in service conditions.
3. The elastic effects considered within this thesis are an important step to understanding more realistic microstructures. However, the complex crystallographic structure of real

- alloys is still missing. Consideration can therefore be given to elastic anisotropies (e.g. an anisotropic misfit strain) and anisotropic surface energies.
4. Consideration can also be given to modelling the evolution of initially distorted and perturbed precipitate shapes. This will invoke a computational processing cost due to the larger number of interface sub-segments required to ensure a regular mesh topology local to the interface and to model more complex interface shapes.
 5. The current model can be theoretically extended into three-dimensional space, based on the availability of a three dimensional tetrahedral finite element mesh generator, although the topological changes that occur are more complex in comparison to those within two-dimensional space. Extension of the current variational model into three-dimensional space will also invoke a large computational processing cost, but speed increase may be achieved through the use of parallel code optimisation.
 6. The current model can be extended to simulate the effects of prescribed defects and dislocations within the microstructure and the effect these have during microstructure evolution.
 7. It would be interesting to consider the case where a uniaxial strain field is applied to a matrix / precipitate system where the Young's modulus of the precipitate is considered to be much higher than that of the surrounding matrix, i.e. a hard precipitate. This is contrary to the applied loading simulations within chapter 10, where the Young's modulus of the precipitate was less than that of the matrix and the precipitate is considered soft.
 8. The current variational model assumes coherency between the precipitate and the surrounding lattice, which may be a valid approximation for the treatment of small misfitting precipitates but can not generally be applied to the case of larger precipitates. The variational model can be modified to allow this constraint to be removed, which would permit the phases to slip or slide in a direction tangential to the interface boundary. Computationally, this would require modelling a discontinuity in the elastic displacement field at the interface boundaries.
 9. The variational model can be used to investigate if the effect of coarsening of particles can be halted or stabilised by the influence of applied elastic fields. It is expected that the influence of such external fields will substantially alter the particle morphologies and coarsening kinetics. Through the use of the variational model and careful choice of applied directional fields, it may prove to be possible to dynamically stabilise the

coarsening effect, such that finer microstructures can be achieved. This concept has been studied by Johnson [108] who considered the stability against coarsening of two misfitting spherical precipitates both in the absence and presence of an applied uniaxial stress field using a bifurcation approach. From this analysis it was found that under an applied stress, the precipitate stability can be either enhanced or diminished depending of the relative orientation of the precipitates and the magnitude of the applied stress.

10. The current computational code can be modified to handle disappearing phases such that the full process of particle coarsening can be modelled from the initial configuration until a state of equilibrium has been attained. A precipitate phase can be removed from the simulation once its volume reduces below that of a pre-defined critical size, and the volume and mass previously occupied by the precipitate then becomes integrated into that of the bulk matrix.
11. The model presented here can also be applied to model the enrichment process for $M_{23}C_6$ carbide precipitates within high temperature chromium steels. This process occurs due to the fact that the service temperature is lower than that associated with the initial tempering heat treatment given to the steel. As a result, chromium enrichment is observed within this phase [5] until the phase finally attains its equilibrium composition corresponding to the service temperature. The model presented here has the ability to accurately model the role of elasticity on the enrichment process.
12. It has been observed that within 12CrMoVNb steels containing raised levels of nickel, coarsening of $M_{23}C_6$ precipitates occurs at a faster rate leading to quicker microstructural degradation and poorer creep rupture strength [6]. The coarsening rate due to creep exposure at 600°C has been observed to be approximately three times greater in the highest nickel (1.15 wt%) material compared with the steel with the lowest nickel (0.52 wt%) content [6]. It would therefore be beneficial to study the role of nickel on the coarsening kinetics of $M_{23}C_6$ precipitates, since thermodynamic data is currently available on the Fe-Cr-Ni-C system [76].
13. An alloying strategy that has proven to be very effective for increased creep strength in chromium steels is the addition of small amounts of boron. In a recent study by Hättestrand and Andrén [110], it was found that only very small amounts of boron remain dissolved in the matrix after completed heat treatment. Instead almost all of the boron ended up in the $M_{23}C_6$ precipitate particles, and this was thought to decrease the

coarsening rate of these precipitates. The effect of substitutional stabilising alloying elements, such as Mo, Ti, V and Nb, on the coarsening kinetics of $M_{23}C_6$ precipitate particles can also be investigated using the variational model.

14. It would be interesting to model the effect of inverse coarsening, a process where a smaller particle can grow at the expense of a larger one. This process usually occurs under the influence of strong elastic fields and has been studied by Johnson et al. [104] for fixed morphologies, Su and Voorhees [105] for elastically homogeneous isotropic materials and by Jou [59] for elastically inhomogeneous isotropic materials. During inverse coarsening, the elastic fields enhance the growth of the smaller particle at the expense of the larger one. However, inverse coarsening may be prevented by increasing the applied strain field such that only classical coarsening can be observed.
15. The variational model can be used and applied to model the precipitation and coarsening kinetics between multiple particles embedded within a matrix. The particles can be arranged in such a manner such that their shapes are non-symmetric, in order to model the complex long-range elastic interactions between particles. However, such a simulation would invoke a huge computational processing cost (due to non-symmetries and a corresponding high finite element mesh density) and a long simulation time-frame would be required. However, it is predicted that, with current computational resources, simulations can be carried out for up to four precipitate particles within an acceptable and realistic time frame.
16. Many of the model modifications and extensions discussed above will no doubt require more computer processing time, but such simulations can be shortened through the parallelisation of computational code. It is calculated that approximately 80% of the time per iterative cycle is spent solving the general linear system equation (equation (5.42)) in section 5.4 for both the elasticity and coupled diffusion and moving boundary problem. Considerable speed advancement can be achieved through the use of a parallel solver. Through the use of improved numerical techniques, parallelisation of computer code and increase in computer processing power, longer-time and larger-scale simulations of microstructure evolution will hopefully become feasible.
17. The variational model developed within this thesis assumes that the rate of coarsening is primarily governed by volumetric diffusion between precipitate particles. However, precipitate particles often form on lath or sub-grain boundaries and one would expect that

coarsening would be enhanced by a more rapid diffusion along these boundaries. Cocks, Gill and Pan have developed models for grain boundary diffusion, surface diffusion, interface reactions and grain boundary migration within the variational framework [23]. These phenomena can be readily incorporated into the variational model presented in this thesis.

Appendix

A. – Elastic Finite Element Derivations

A.1. – The Stress-Strain Relationship

The stresses are related to the strains through the linear elastic relation

$$[\sigma] = [D][\varepsilon] \quad (\text{A.1})$$

where $[D]$ is the material stiffness matrix, and $[\sigma]$ and $[\varepsilon]$ are the stress and strain matrices respectively, defined by

$$[\sigma] = \begin{bmatrix} \sigma_x \\ \sigma_y \\ \tau_{xy} \end{bmatrix} \quad [\varepsilon] = \begin{bmatrix} \varepsilon_x \\ \varepsilon_y \\ \gamma_{xy} \end{bmatrix} \quad (\text{A.2})$$

If loading and geometrical changes of a three-dimensional problem lie within a plane then one can use a representative two-dimensional problem to find approximate solutions to the three-dimensional problem. Plane stress or plane strain assumptions can therefore be introduced in order to simplify the elastic analysis and can be invoked depending on the geometric features of the system under consideration.

For plane stress conditions ($\sigma_z = 0$),

$$[D] = \frac{E}{(1-\nu^2)} \begin{bmatrix} 1 & \nu & 0 \\ \nu & 1 & 0 \\ 0 & 0 & \frac{1}{2}(1-\nu) \end{bmatrix} \quad (\text{A.3})$$

where E is Young's modulus and ν is Poisson's ratio.

For plain strain ($\varepsilon_z = 0$), Young's modulus and Poisson's ratio can be substituted by \bar{E} and $\bar{\nu}$, defined by

$$\bar{E} = \frac{E}{(1-\nu^2)} \quad \bar{\nu} = \frac{\nu}{(1-\nu)}$$

Since these are simply material parameters, a plane stress analysis can be carried out and can then be converted to plane strain by making the above substitutions.

A.2. – The Relationship between Strain and Displacement

The strains can be related to the elastic displacements through the relation

$$[\varepsilon] = [B^e][u^e] \quad (\text{A.4})$$

where

$$\begin{aligned} [u^e]^T &= [u_1^e \quad u_2^e \quad u_3^e \quad u_4^e \quad u_5^e \quad u_6^e] \\ [u_i^e]^T &= [u_i \quad v_i] \end{aligned}$$

The longitudinal strain within an element brought about by a displacement in the x -direction is given by

$$\varepsilon_{xx} = \frac{\partial u}{\partial x} \quad (\text{A.5})$$

The first suffix in the symbol for the strain represents the direction in which the strain measuring gauge length is oriented (in this case the x direction). The second suffix represents the direction of the displacements at the end of the gauge length (which in this case is also x). Since the suffices are identical, the strain is a direct or tensile strain.

A similar relation can be obtained by considering the vertical strain within an element brought about by a displacement in the y -direction

$$\varepsilon_{yy} = \frac{\partial v}{\partial y} \quad (\text{A.6})$$

It is now necessary to consider the shear strains within the element, where the particle displacement is perpendicular to the gauge length

$$\gamma_{xy} = \frac{\partial u}{\partial y} + \frac{\partial v}{\partial x}$$

where γ_{xy} represents the total shear strain (engineering shear strain). Differentiating the terms in equation (5.3) gives

$$\begin{aligned} \varepsilon_{xx} &= \frac{\partial}{\partial x} (n_i(\xi, \eta) u_i) = \frac{\partial n_i(\xi, \eta)}{\partial x} u_i \\ \varepsilon_{yy} &= \frac{\partial n_i(\xi, \eta)}{\partial y} v_i \\ \gamma_{xy} &= \frac{\partial n_i(\xi, \eta)}{\partial y} u_i + \frac{\partial n_i(\xi, \eta)}{\partial x} v_i \end{aligned}$$

Thus

$$[B^e] = [B_1^e \quad B_2^e \quad B_3^e \quad B_4^e \quad B_5^e \quad B_6^e]$$

with

$$[B_i^e] = \begin{bmatrix} \frac{\partial n_i(\xi, \eta)}{\partial x} & 0 \\ 0 & \frac{\partial n_i(\xi, \eta)}{\partial y} \\ \frac{\partial n_i(\xi, \eta)}{\partial y} & \frac{\partial n_i(\xi, \eta)}{\partial x} \end{bmatrix} \quad (A.7)$$

To explicitly calculate the derivatives of the shape functions we use the chain rule to write

$$\begin{bmatrix} \frac{\partial}{\partial \xi} \\ \frac{\partial}{\partial \eta} \end{bmatrix} = \begin{bmatrix} \frac{\partial x}{\partial \xi} & \frac{\partial y}{\partial \xi} \\ \frac{\partial x}{\partial \eta} & \frac{\partial y}{\partial \eta} \end{bmatrix} \begin{bmatrix} \frac{\partial}{\partial x} \\ \frac{\partial}{\partial y} \end{bmatrix} \quad (A.8)$$

The 2×2 matrix in equation (A.8) plays an important role in the mapping process and is referred to as the 'Jacobian' matrix. It can be presented in a simplified form as

$$[J] = \begin{bmatrix} \frac{\partial x}{\partial \xi} & \frac{\partial y}{\partial \xi} \\ \frac{\partial x}{\partial \eta} & \frac{\partial y}{\partial \eta} \end{bmatrix} = \begin{bmatrix} n_{i,\xi}(\xi, \eta)x_i & n_{i,\xi}(\xi, \eta)y_i \\ n_{i,\eta}(\xi, \eta)x_i & n_{i,\eta}(\xi, \eta)y_i \end{bmatrix}$$

where $n_{i,\xi}(\xi, \eta) = \frac{\partial n_i(\xi, \eta)}{\partial \xi}$. The derivatives $\frac{\partial}{\partial x}$ and $\frac{\partial}{\partial y}$, which are needed to determine the

$[B^e]$ matrix, can now be obtained by inverting equation (A.8)

$$\begin{bmatrix} \frac{\partial}{\partial x} \\ \frac{\partial}{\partial y} \end{bmatrix} = \frac{1}{J} \begin{bmatrix} n_{i,\eta}y_i & -n_{i,\xi}y_i \\ -n_{i,\eta}x_i & n_{i,\xi}x_i \end{bmatrix} \begin{bmatrix} \frac{\partial}{\partial \xi} \\ \frac{\partial}{\partial \eta} \end{bmatrix} \quad (A.9)$$

where

$$J = (n_{i,\xi}n_{j,\eta} - n_{i,\eta}n_{j,\xi})x_i y_j = N_{ij}x_i y_j \quad (A.10)$$

is the determinant of the Jacobian.

Equation (A.7) can therefore be written as

$$[B_i^e] = \frac{1}{J^e} \begin{bmatrix} N_{ij}y_j & 0 \\ 0 & -N_{ij}x_j \\ -N_{ij}x_j & N_{ij}y_j \end{bmatrix} = \frac{1}{J^e} [b_i^e] \quad (A.11)$$

Equation (A.4) relates the elastic strains to the nodal displacements within an isoparametric triangular finite element. The terms in this matrix equation contain only the derivatives of the shape functions (which are known), the nodal coordinates of the real element (which are

known) and the nodal displacements, which are the unknowns. Once the elemental nodal displacements are known, the elastic strain within each element can be numerically calculated.

A.3. – Elemental Elasticity Matrices

The elemental stiffness matrix integrals of equation (5.5) can be evaluated over (ξ, η) space.

One can write

$$[C^e] = \int \int [B^e]^T [D] [B^e] dx dy = \int_0^{1-\eta} \int_0^{\eta} \frac{[b^e]^T}{J^e} [D] \frac{[b^e]}{J^e} J^e d\xi d\eta = \int_0^{1-\eta} \int_0^{\eta} [c^e] d\xi d\eta \quad (A.12)$$

where $[c^e] = \frac{[b^e]^T [D] [b^e]}{J^e} = [c^e(\xi, \eta)]$

Similarly

$$\begin{aligned} [R^e] &= \int \int [\varepsilon_T]^T [D] [B^e] dx dy = \int_0^{1-\eta} \int_0^{\eta} [\varepsilon_T]^T [D] \frac{[b^e]}{J^e} J^e d\xi d\eta = \int_0^{1-\eta} \int_0^{\eta} [r^e] d\xi d\eta \\ U_o^e &= \int \int [\varepsilon_T]^T [D] [\varepsilon_T] dx dy = \int_0^{1-\eta} \int_0^{\eta} [\varepsilon_T]^T [D] [\varepsilon_T] J^e d\xi d\eta = \int_0^{1-\eta} \int_0^{\eta} u_o^e d\xi d\eta \end{aligned} \quad (A.13)$$

where $[r^e] = [\varepsilon_T]^T [D] [b^e] = [r^e(\xi, \eta)]$ and $u_o^e = [\varepsilon_T]^T [D] [\varepsilon_T] J^e$

These integrals can be numerically evaluated using Gaussian quadrature (see Appendix B), such that

$$[C^e] = \frac{1}{2} w \sum_i [c^e(\xi_i, \eta_i)]$$

where w , ξ_i and η_i are given in Appendix B.

A.4. – Stiffness and Transformation Matrix Differentials

In order to evaluate equation (5.24) it is necessary to determine the differentials of the stiffness and transformation matrices with respect to the positions of the nodes, x_{in}^t , that lie on interfacial boundary, t . These are defined by

$$\begin{aligned} \left[\frac{\partial C^e}{\partial x_{in}^t} \right] &= \int_0^{1-\eta} \int_0^{\eta} 2[b^e]^T [D] \left[\frac{\partial b^e}{\partial x_{in}^t} \right] J^{e-1} d\xi d\eta - \int_0^{1-\eta} \int_0^{\eta} [b^e]^T [D] [b^e] J^{e-2} \frac{\partial J^e}{\partial x_{in}^t} d\xi d\eta \\ \left[\frac{\partial R^e}{\partial x_{in}^t} \right] &= \int_0^{1-\eta} \int_0^{\eta} [\varepsilon_T]^T [D] \left[\frac{\partial b^e}{\partial x_{in}^t} \right] d\xi d\eta \\ \frac{\partial U_o^e}{\partial x_{in}^t} &= \int_0^{1-\eta} \int_0^{\eta} [\varepsilon_T]^T [D] [\varepsilon_T] \frac{\partial J^e}{\partial x_{in}^t} d\xi d\eta \end{aligned} \quad (A.14)$$

Appendix

Analytical expressions for these differential matrices can be readily evaluated for isoparametric finite elements in terms of the mapping from the parent (reference) element to the mapped (physical) element within two-dimensional space

$$\begin{bmatrix} \frac{\partial b^e}{\partial x_j} \end{bmatrix} = \begin{bmatrix} 0 & 0 \\ 0 & -N_{i,j} \\ -N_{i,j} & 0 \end{bmatrix} \quad \begin{bmatrix} \frac{\partial b^e}{\partial y_j} \end{bmatrix} = \begin{bmatrix} N_{i,j} & 0 \\ 0 & 0 \\ 0 & N_{i,j} \end{bmatrix}$$

$$\frac{\partial J^e}{\partial x_j} = N_{ij} y_j$$

$$\frac{\partial J^e}{\partial y_j} = N_{ij} x_i = -N_{ij} x_j$$

B. – Numerical Integration: Gaussian Quadrature

Gaussian quadrature is a very powerful and widely used technique in numerical integration. For convenience, the following section provides details regarding the one-dimensional and two-dimensional shape functions along with Gauss point coordinates and weighting factors used in the computational analysis. The reader is referred to other literature sources (such as [109]) for a fully descriptive insight into Gaussian quadrature.

B.1. – One-Dimensional Gaussian Quadrature

The shape functions across a one-dimensional two-noded linear-type finite element can be described by

$$\begin{aligned}n_1(\xi) &= \frac{1}{2}(1 + \xi) \\n_2(\xi) &= \frac{1}{2}(1 - \xi)\end{aligned}\tag{B.1}$$

For a linear interpolation function, the position of the Gauss point and the weighting factor are

$$\begin{aligned}\xi_1 &= 0 \\w_1 &= 2\end{aligned}$$

The shape functions across a one-dimensional three-noded quadratic-type finite element can be described by

$$\begin{aligned}n_1(\xi) &= -\frac{1}{2}(1 - \xi)\xi \\n_2(\xi) &= (1 - \xi)(1 + \xi) \\n_3(\xi) &= \frac{1}{2}(1 + \xi)\xi\end{aligned}\tag{B.2}$$

For a quadratic interpolation function, the positions of the Gauss points and the weighting factors are

$$\begin{aligned}\xi_1 &= +\frac{1}{\sqrt{3}} \\ \xi_2 &= -\frac{1}{\sqrt{3}} \\ w_1 &= w_2 = 1\end{aligned}$$

The shape functions across a one-dimensional four-noded cubic-type finite element can be described by

$$\begin{aligned}n_1(\xi) &= -\frac{9}{16}(\xi + \frac{1}{3})(\xi - \frac{1}{3})(\xi - 1) \\n_2(\xi) &= \frac{27}{16}(\xi + 1)(\xi - \frac{1}{3})(\xi - 1) \\n_3(\xi) &= -\frac{27}{16}(\xi + 1)(\xi + \frac{1}{3})(\xi - 1) \\n_4(\xi) &= \frac{9}{16}(\xi + 1)(\xi + \frac{1}{3})(\xi - \frac{1}{3})\end{aligned}\tag{B.3}$$

For a cubic interpolation function, the positions of the Gauss points and the weighting factors are

$$\xi_1 = -0.7746$$

$$\xi_2 = 0.0000$$

$$\xi_3 = 0.7746$$

$$w_1 = 0.5556$$

$$w_2 = 0.8889$$

$$w_3 = 0.5556$$

B.2. – Two-Dimensional Gaussian Quadrature

The variation of a function can be described over a two-dimensional three-noded linear or six-noded quadratic type finite element as shown in Figure B.1(a) and (b) respectively.

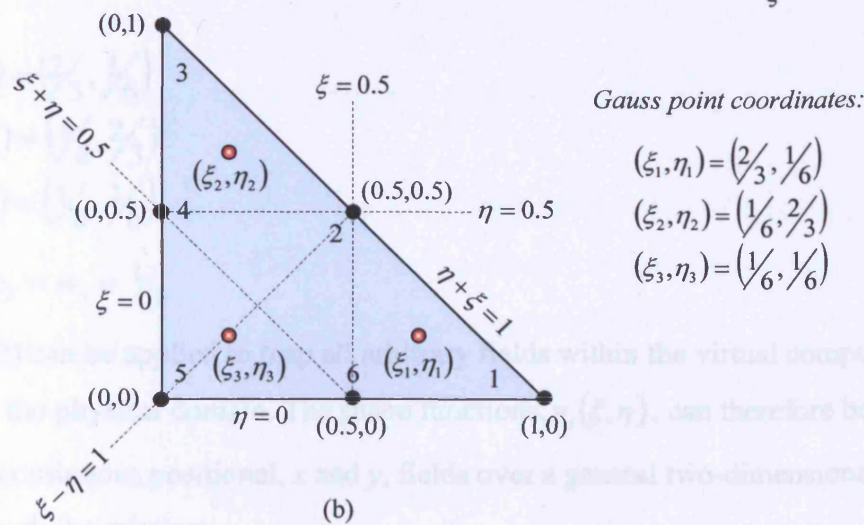
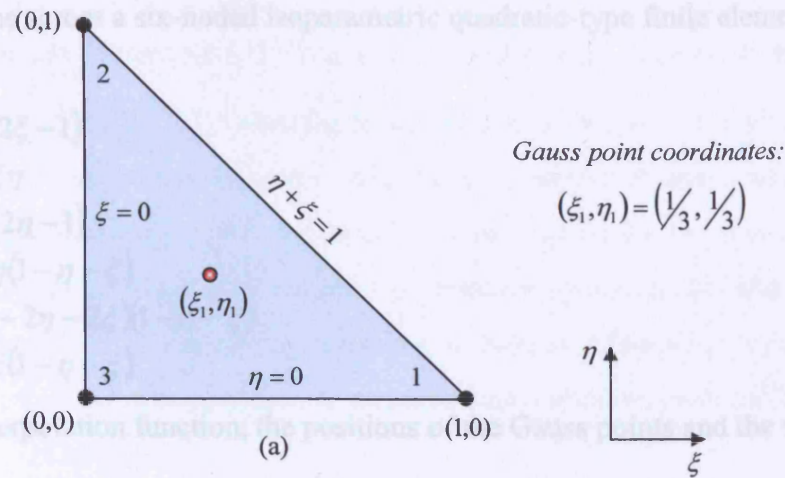


Figure B.1 – A two-dimensional (a) three-noded linear (b) six-noded quadratic type finite element.

The shape functions across a two-dimensional three-noded linear-type isoparametric finite element can be described by

$$\begin{aligned} n_1(\xi, \eta) &= \xi \\ n_2(\xi, \eta) &= \eta \\ n_3(\xi, \eta) &= 1 - \xi - \eta \end{aligned} \tag{B.4}$$

For a linear interpolation function, the position of the Gauss point and the weighting factor are

$$\begin{aligned} (\xi_1, \eta_1) &= \left(\frac{1}{3}, \frac{1}{3}\right) \\ w_1 &= 1 \end{aligned}$$

The shape functions across a six-noded isoparametric quadratic-type finite element can be described by

$$\begin{aligned}
 n_1(\xi, \eta) &= \xi(2\xi - 1) \\
 n_2(\xi, \eta) &= 4\xi\eta \\
 n_3(\xi, \eta) &= \eta(2\eta - 1) \\
 n_4(\xi, \eta) &= 4\eta(1 - \eta - \xi) \\
 n_5(\xi, \eta) &= (1 - 2\eta - 2\xi)(1 - \eta - \xi) \\
 n_6(\xi, \eta) &= 4\xi(1 - \eta - \xi)
 \end{aligned} \tag{B.5}$$

For a quadratic interpolation function, the positions of the Gauss points and the weighting factors are

$$\begin{aligned}
 (\xi_1, \eta_1) &= \left(\frac{2}{3}, \frac{1}{6}\right) \\
 (\xi_2, \eta_2) &= \left(\frac{1}{6}, \frac{2}{3}\right) \\
 (\xi_3, \eta_3) &= \left(\frac{1}{6}, \frac{1}{6}\right) \\
 w_1 = w_2 = w_3 &= \frac{1}{3}
 \end{aligned}$$

Equation (5.2) can be applied to map all arbitrary fields within the virtual computational domain onto the physical domain. The shape functions, $n_i(\xi, \eta)$, can therefore be used to describe the continuous positional, x and y , fields over a general two-dimensional finite element through the relations

$$\begin{aligned}
 x &= n_i(\xi, \eta)x_i \\
 y &= n_i(\xi, \eta)y_i
 \end{aligned} \tag{B.6}$$

where suffix notation has been used so that the occurrence of the index, i twice implies a summation over each node, i .

C. – General Input Data for 2D Finite Element Mesh Generation

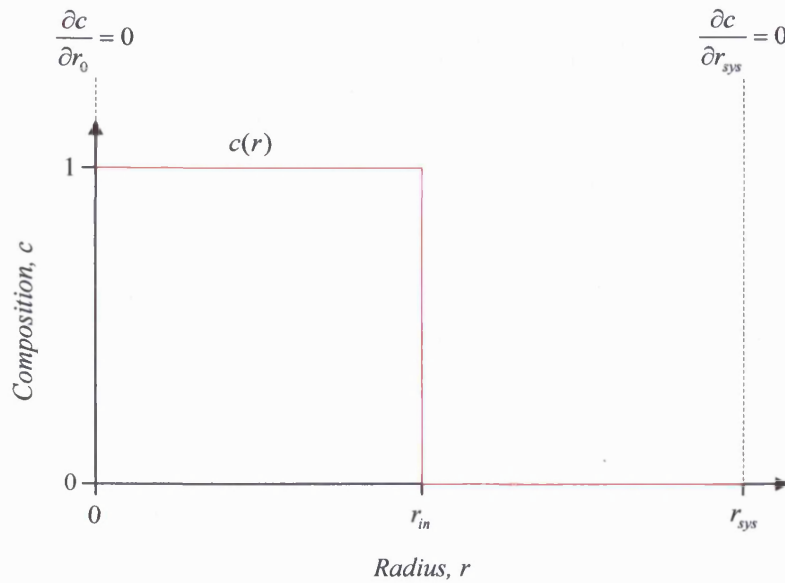
The program 'Triangle' [1] is used for two-dimensional quality finite element mesh generation and is fast, memory-efficient, robust and can compute Delaunay and conforming Delaunay triangulations exactly. The two-dimensional mesh generator requires an input file (.poly file), which by definition is a collection of geometrical system points and connecting system boundary segments. The input file also can also contain information regarding holes and concavities, as well as regional attributes and area constraints imposed on the finite element mesh being generated.

The general layout of the input (.poly file) file is represented as follows:

First line: [# of points] [dimension] [# of attributes] [# of boundary markers]
Following lines: [point #] [x-coordinate] [y-coordinate] [attributes] [boundary marker]
One line: [# of segments] [# of boundary markers]
Following lines: [segment #] [end-point] [end-point] [boundary marker]
One line: [# of holes]
Following lines: [hole #] [x-coord] [y-coord]
Optional line: [# of regional attributes and/or area constraints]
Following lines: [region #] [x-coordinate] [y-coordinate] [attribute] [maximum area]

D. – Derivation and Analysis of the Analytical Solution

A one-dimensional analytical solution can be calculated for the initial compositional distribution of Figure 7.3(a), shown in Figure D.1, in terms of both space and time assuming zero boundary surface flux [43]. The analytical solution can be compared and validated against the finite element solution generated by the computational model for purely entropic diffusion.



$$c(r) = \begin{cases} 1 & \text{when } 0 \leq r \leq r_{in} \\ 0 & \text{when } r_{in} \leq r \leq r_{sys} \end{cases}$$

Figure D.1 – Initial compositional distribution represented by an analytical function.

For a cylindrical system, the analytical solution can be expressed as

$$c(r, t) = \frac{2}{r_{sys}^2} \int_0^{r_{sys}} rc(r) dr + \frac{2}{r_{sys}^2} \sum_{n=1}^{\infty} e^{\left(\frac{-D\alpha_n^2 t}{r_{sys}^2}\right)} \cdot \frac{J_0(r\alpha_n / r_{sys})}{J_0^2(\alpha_n)} \int_0^{r_{sys}} rc(r) J_0(r\alpha_n / r_{sys}) dr \quad (D.1)$$

where J_0 and J_1 are Bessel functions of the first kind of zero and first order respectively, α_n are the roots of $J_1(\alpha) = 0$ and \mathcal{D} is the non-dimensional diffusivity.

Equation (D.1) can be broken down into its constituent parts and simplified as follows

$$\frac{2}{r_{sys}^2} \int_0^{r_{sys}} rc(r) dx = \frac{2}{r_{sys}^2} \int_0^{r_{in}} r dr = \frac{2}{r_{sys}^2} \left[\frac{r^2}{2} \right]_0^{r_{in}} = \frac{r_{in}^2}{r_{sys}^2}$$

$$\begin{aligned} \frac{2}{r_{\text{sys}}^2} r \int_0^{r_{\text{sys}}} r c(r) J_0\left(\frac{r \alpha_n}{r_{\text{sys}}}\right) dr &= \frac{2}{r_{\text{sys}}^2} \int_0^{r_{\text{in}}} r J_0\left(\frac{r \alpha_n}{r_{\text{sys}}}\right) dr \\ &= \frac{2}{r_{\text{sys}}^2} \left[r J_1\left(\frac{r \alpha_n}{r_{\text{sys}}}\right) \cdot \frac{r_{\text{sys}}}{\alpha_n} \right]_0^{r_{\text{in}}} \\ &= \frac{2 r_{\text{in}}}{r_{\text{sys}} \alpha_n} J_1\left(\frac{r_{\text{in}} \alpha_n}{r_{\text{sys}}}\right) \end{aligned}$$

To give

$$c(r, t) = \frac{r_{\text{in}}^2}{r_{\text{sys}}^2} + \frac{2 r_{\text{in}}}{r_{\text{sys}}} \sum_{n=1}^{\infty} e^{\left(\frac{-D \alpha_n^2 t}{r_{\text{sys}}^2}\right)} \left(\frac{J_0\left(\frac{r \alpha_n}{r_{\text{sys}}}\right) J_1\left(\frac{r_{\text{in}} \alpha_n}{r_{\text{sys}}}\right)}{\alpha_n J_0^2(\alpha_n)} \right) \quad (\text{D.2})$$

The Bessel functions, J_0 and J_1 can be calculated using Fortran library NAG subroutines. The analytical solution can be used to calculate the evolution of the microstructure and solve for the composition in terms of both space and time.

E. – Material Constants for InGaAs

The phase energy density ($Jmol^{-1}$) can be expressed as a function of the Indium concentration, c and the temperature, T through the relation

$$G_c(c, T) = (1 - c)G_{GaAs}(T) + cG_{InAs}(T) + \Delta G_{internal}(c) + \Delta G_{entropy}(c, T) \quad (E.1)$$

where the energy is relative to the enthalpy of the Standard Element Reference (HSER) at 298.15K (20°C) [100], and

$$G_p(T) = a_p + b_p T + c_p T \log(T) + d_p T^2 + e_p T^{-1} + f_p T^3$$

$$\Delta G_{internal}(c) = \rho \sum_{m=0}^4 v_m(c)(1 - 2c)^m$$

$$\Delta G_{entropy}(c, T) = \frac{1}{2} RT [c \log(c) + (1 - c) \log(1 - c)]$$

where G_p is the chemical phase energy of the pure GaAs and InAs compounds obtained via empirical measurements [100], $\Delta G_{internal}$ is the change in the energy associated with combining atoms of different sizes into the regular face-centred-cubic lattice, obtained from first principles calculations [40] and which can reasonably be assumed to be independent of temperature, $\Delta G_{entropy}$ is the change in energy due entropic mixing (the factor of a half arises because mixing only occurs on the InGa fcc lattice, which represents only half of the molar fraction). For the calculation of the phase energy, G^p of the pure GaAs and InAs compounds the constants in Table E.1 were used.

Phase, p	a^p	b^p	c^p	d^p	e^p	f^p
<i>GaAs</i>	-52176	132.716	-24.3406	-5.579×10^{-4}	63835	-3.5689×10^{-7}
<i>InAs</i>	-36528	115.459	-22.5939	-3.865×10^{-3}	34719	7.09×10^{-8}

Table E.1 – Constants used for the calculation of the phase energy, G^p of the pure GaAs and InAs compounds.

Appendix

From the first principle calculations of Mohri [40], the combinational internal energy of the $In_cGa_{1-c}As$ alloy is defined in terms of the functions

$$v_m(c) = \frac{v_{m1}}{r^7} - \frac{v_{m2}}{r^{3.5}} + v_{m3} \quad (E.2)$$

where $r = 10.684(1-c) + 11.449c$ is the lattice spacing in Bohr radii and the fitting parameters are given in Table E.2 below. The constant $\rho = 1.641 \times 10^5$ converts the units from *Ryds (unit cell)⁻¹* to *Jmol⁻¹*.

<i>m</i>	0	1	2	3	4
v_{m1}	4.624×10^7	-9.972×10^6	-6.557×10^4	6.019×10^4	-2.311×10^3
v_{m2}	2.037×10^4	-1.962×10^3	-2.242×10^2	1.359×10^1	-1.949×10^{-1}
v_{m3}	2.253	5.347×10^{-2}	-2.481×10^{-2}	1.026×10^{-5}	2.423×10^{-5}

Table E.2 – Fitting parameters used to determine the combinational internal energy of the $In_cGa_{1-c}As$ alloy (defined by equation (E.2)).

The driving force due to the phase energy density can be expressed as

$$F^e_{phase} = G_{GaAs}(T) - G_{InAs}(T) - \frac{\partial \Delta G_{internal}(c)}{\partial c} - \frac{\partial \Delta G_{entropy}(c, T)}{\partial c} \quad (E.3)$$

For the $In_cGa_{1-c}As$ alloy, the volumetric transformation strain, ε_T (%) with reference to the unstrained state (GaAs, i.e. when $c = 0$) is defined as

$$\varepsilon_T = 6.7c \quad (E.4)$$

The Young's modulus, E (GPa), and Poisson's ratio, ν , are linearly related to the Indium composition, c , through the expressions

$$\begin{aligned} E &= 51.44(1-c) + 85.26c \\ \nu &= 0.3520(1-c) + 0.3177c \end{aligned} \quad (E.5)$$

F. – Modelling the Effect of External Loading

The effect of external loading can be modelled and investigated with respect to the subsequent evolution of the microstructure and movement of the interface boundary. In order to implement the effect of external loading, there are two principal methods which can be implemented into the general model and these are described as follows.

F.1. – Modelling an Applied Displacement along the System Boundary

If a displacement is applied to the outer system boundaries, as shown in Figure F.1, then one can define

$[u_f^*]$ – Free displacements

$[u_d]$ – Defined displacement

$[R_f]$ – Free forces (due to the transformation strain, ε_T)

$[R_d^*]$ – Defined force

where the asterisk (*) is used to identify the system unknowns.

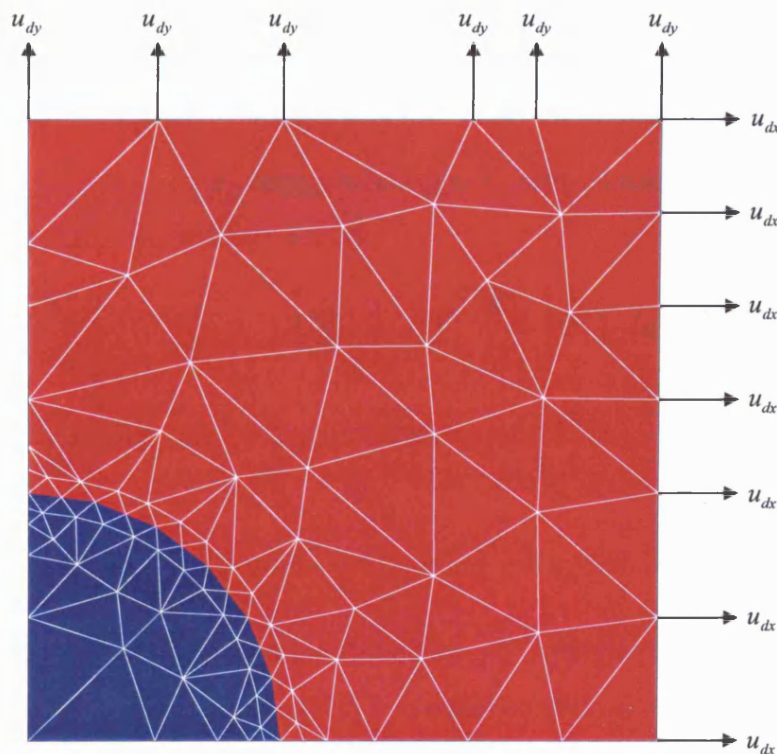


Figure F.1 – Displacements are applied along the outer system boundaries to model the effect of external loading.

From equation (5.7), one can write

$$\begin{bmatrix} C_{ff} & C_{fd} \\ C_{df} & C_{dd} \end{bmatrix} \begin{bmatrix} u_f^* \\ u_d \end{bmatrix} = \begin{bmatrix} R_f \\ R_d^* \end{bmatrix}$$

Expanding this gives

$$[C_{ff}][u_f^*] + [C_{fd}][u_d] = [R_f] \quad (F.1)$$

$$[C_{fd}]^T [u_f^*] + [C_{dd}][u_d] = [R_d^*] \quad (F.2)$$

Re-arranging equation (F.1) gives

$$[u_f^*] = [C_{ff}]^{-1} ([R_f] - [C_{fd}][u_d])$$

The elastic stored energy can be represented as

$$\begin{aligned} U_{elastic} &= \frac{1}{2} [u]^T [C][u] - [u]^T [R] + \frac{1}{2} U_o \\ &= \frac{1}{2} [u_f^*]^T [C_{ff}][u_f^*] - [u_f^*]^T [R_f] + [u_f^*]^T [C_{fd}][u_d] - [u_d]^T [R_d^*] \\ &\quad + \frac{1}{2} [u_d]^T [C_{dd}][u_d] + \frac{1}{2} U_o \end{aligned}$$

Multiplying equation (F.2) by $[u_d]^T$ and substituting this into the above expression for the elastic stored energy

$$U_{elastic} = \frac{1}{2} [u_f^*]^T [C_{ff}][u_f^*] - [u_f^*]^T [R_f] - \frac{1}{2} [u_d]^T [C_{dd}][u_d] + \frac{1}{2} U_o \quad (F.3)$$

The derivative of the elastic strain energy with respect to the positions of the nodes that lie on the interfacial boundary can be described by

$$\begin{aligned} \frac{\partial U_{elastic}}{\partial x_{in}'} &= \left[\frac{\partial u_f^*}{\partial x_{in}'} \right]^T \left([C_{ff}][u_f^*] - [R_f] \right) + \frac{1}{2} [u_f^*]^T \left[\frac{\partial C_{ff}}{\partial x_{in}'} \right] [u_f^*] - [u_f^*]^T \left[\frac{\partial R_f}{\partial x_{in}'} \right] \\ &\quad - \left[\frac{\partial u_d}{\partial x_{in}'} \right]^T [C_{dd}][u_d] - \frac{1}{2} [u_d]^T \left[\frac{\partial C_{dd}}{\partial x_{in}'} \right] [u_d] + \frac{1}{2} \frac{\partial U_o}{\partial x_{in}'} \end{aligned} \quad (F.4)$$

but, $\left[\frac{\partial u_d}{\partial x_{in}'} \right]^T = 0$ and $\left[\frac{\partial C_{dd}}{\partial x_{in}'} \right] = 0$ unless the interface and system boundary (where the

displacement is applied) share a common finite element. Applying these simplifying assumptions and substituting equation (F.1) into equation (F.4) gives

$$\frac{\partial U_{elastic}}{\partial x_{in}'} = \frac{1}{2} [u_f^*]^T \left[\frac{\partial C_{ff}}{\partial x_{in}'} \right] [u_f^*] - [u_f^*]^T \left[\frac{\partial R_f}{\partial x_{in}'} \right] + \left[\frac{\partial u_f^*}{\partial x_{in}'} \right]^T [C_{fd}][u_d] + \frac{1}{2} \frac{\partial U_o}{\partial x_{in}'}$$

where $\left[\frac{\partial u_f^*}{\partial x_{in}^t} \right]^T$ is very expensive to calculate computationally, but can be obtained by

differentiating equation (F.1) to give

$$\left[\frac{\partial u_f^*}{\partial x_{in}^t} \right] = [C_{ff}]^{-1} \left(\left[\frac{\partial R_f}{\partial x_{in}^t} \right] - \left[\frac{\partial C_{ff}}{\partial x_{in}^t} \right] [u_f^*] - \left[\frac{\partial C_{fd}}{\partial x_{in}^t} \right] [u_d] \right) \quad (\text{F.5})$$

It can be seen that the calculation of $\left[\frac{\partial u_f^*}{\partial x_{in}^t} \right]^T$ involves the solution of an equation similar to

that for the elastic displacements defined by equation (5.7).

F.2. – Modelling an Applied Force along the System Boundary

If an external force is applied to the outer system boundaries, as shown in Figure F.2, then one can define

$[u_f^*]$ – Free displacements

$[u_d^*]$ – Displacements due to applied forces (F_{dx} and F_{dy} respectively)

$[R_f]$ – Free forces (due to the transformation strain, ϵ_T)

$[R_d]$ – Applied (defined) forces

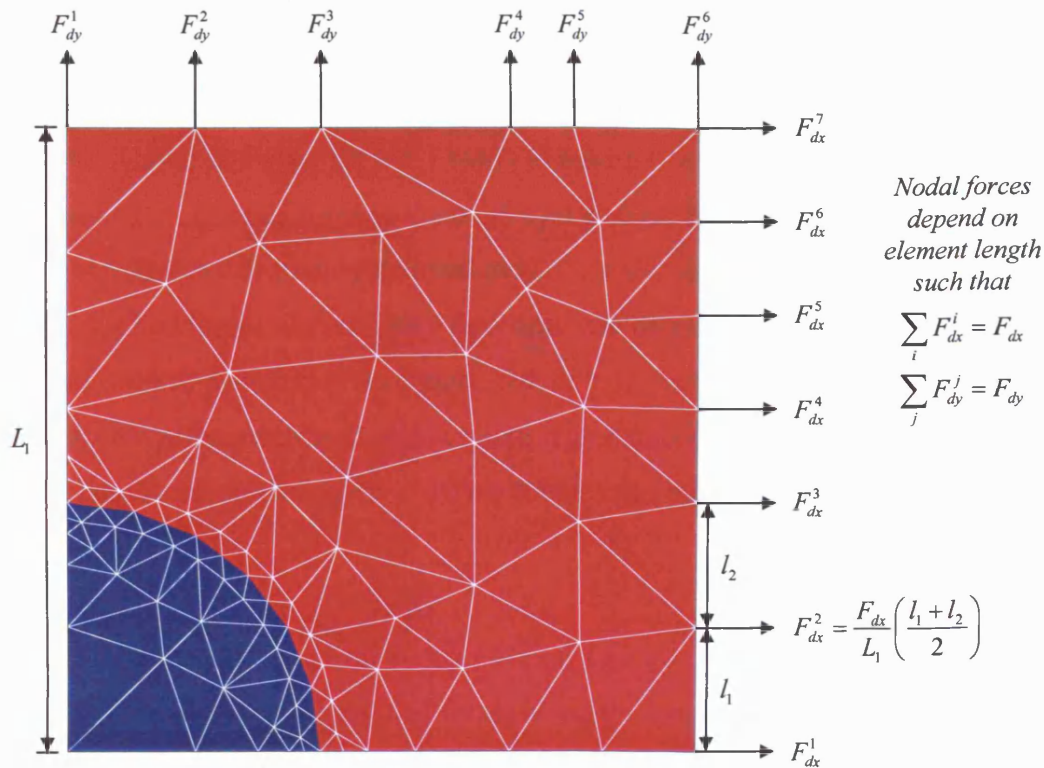


Figure F.2 – Forces are applied along the outer system boundaries to model the effect of external loading.

From equation (5.7), one can write

$$\begin{bmatrix} u_f^* \\ u_d^* \end{bmatrix} = \begin{bmatrix} C_{ff} & C_{fd} \\ C_{df} & C_{dd} \end{bmatrix}^{-1} \begin{bmatrix} R_f \\ R_d \end{bmatrix}$$

which implies a trivial matrix inversion and multiplication in order to calculate the unknown nodal displacements. The application of an external boundary force can be easily implemented

into the general model by simply adding two extra degrees of freedom (one for each boundary subject to an applied force).

The elastic strain energy can then be expressed in the form

$$U_{elastic} = \frac{1}{2} \int_V \sigma_{ij} \varepsilon_{ij} dV - \int (F_{dx} u_{dx} + F_{dy} u_{dy}) dA \quad (F.6)$$

In the case of no applied loading, all external boundaries are constrained to move in both the x and y directions. For the case of applied loading, these constraints are relaxed such that the two outer system boundaries are free to move in a direction normal to the direction of applied loading. However, it is necessary to set the condition of zero flux across these outer boundaries such that no material can flow across the boundaries and to ensure that the system is thermodynamically 'closed'. The flux boundary condition can be enforced through the use of two extra Lagrange multipliers applied across the vertical boundary (at $x = XMAX$) and across the horizontal boundary (at $y = YMAX$) to ensure that mass is conserved.

Applying an external force to the outer system boundaries also requires no extensive modification to the existing computational model in order to calculate the elastic driving forces. The applied forces in the x and y directions can be calculated such as to strain the system by an amount which may be greater than or comparable with that of the transformation strain. Considering the unstrained matrix phase region only (shown in Figure F.3) and assuming plane strain conditions ($\varepsilon_z = 0$), the stresses can be related to the applied forces through

$$\sigma_x = \frac{F_{dx}}{L_1} \quad \sigma_y = \frac{F_{dy}}{L_2}$$

where F_{dx} and F_{dy} represent the applied forces along the length of the vertical and horizontal boundaries, L_1 and L_2 , respectively.

The strains in the x , y and z directions can be related to the stresses through

$$\begin{aligned} \varepsilon_x &= \frac{\sigma_x}{E} - \frac{\nu}{E} (\sigma_y + \nu(\sigma_x + \sigma_y)) \\ \varepsilon_y &= \frac{\sigma_y}{E} - \frac{\nu}{E} (\sigma_x + \nu(\sigma_x - \sigma_y)) \\ E\varepsilon_z = 0 &\Rightarrow \sigma_z = \nu(\sigma_x + \sigma_y) \end{aligned}$$

Substituting the stress relations into the strain expressions and re-arranging for the applied forces along the length of the outer boundaries gives

$$F_{dx} = \frac{EL_1}{(1-2\nu)(1+\nu)} [(1-\nu)\epsilon_x + \nu\epsilon_y]$$

$$F_{dy} = \frac{EL_2}{(1-2\nu)(1+\nu)} [(1-\nu)\epsilon_y + \nu\epsilon_x]$$
(F.7)

The applied forces can therefore be calculated for a particular material system given values for Young's modulus, Poisson's ratio, the system dimensions and the required strain.

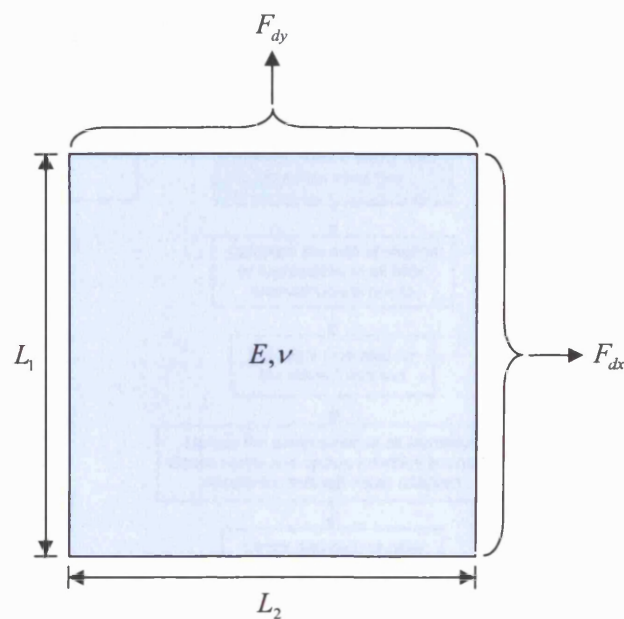


Figure F.3 – The boundary forces are applied such as to strain the system (in the absence of the precipitate) by a pre-determined value.

G. – Flowcharts for Modelling Microstructure Evolution

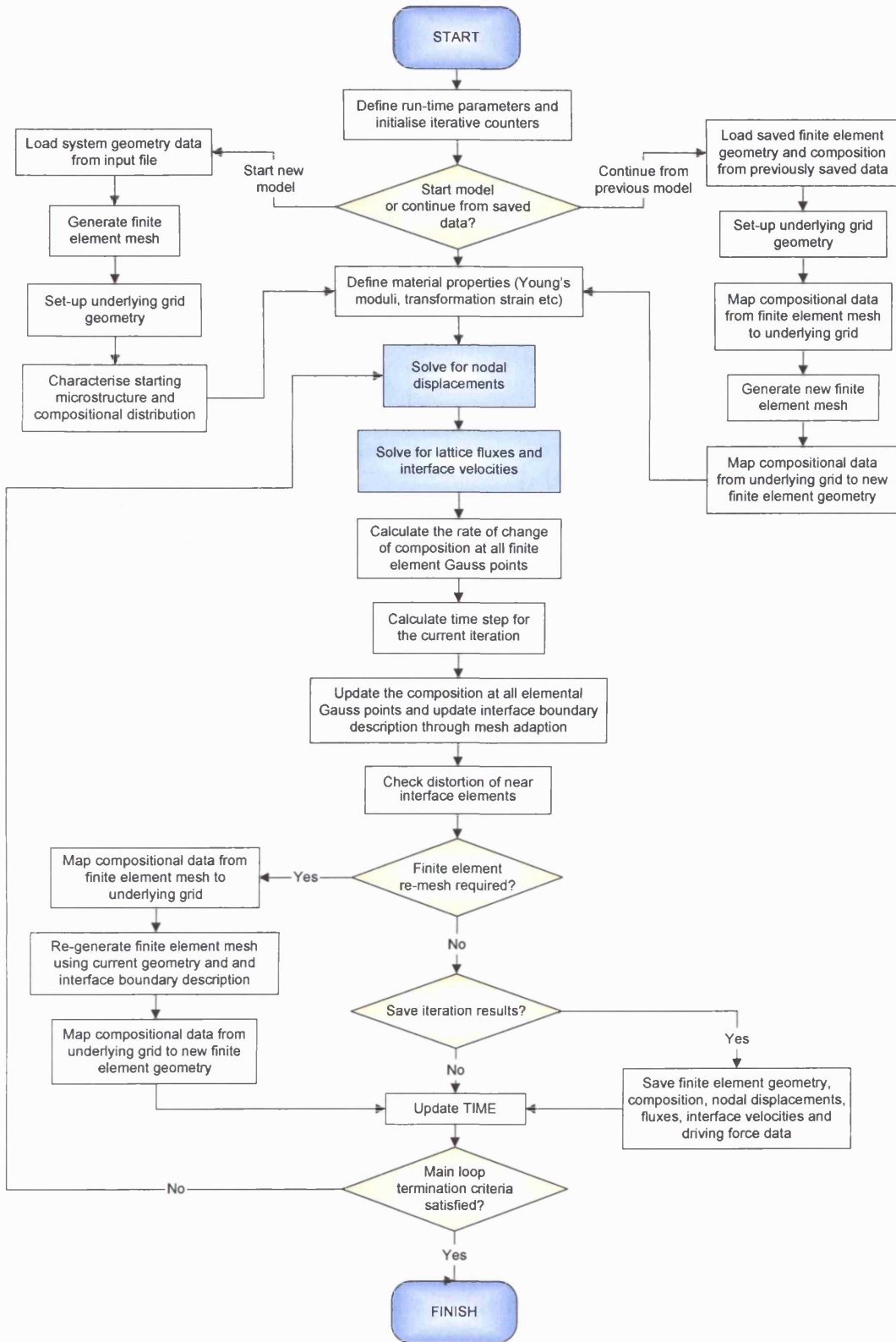


Figure G.1 – Main computational flowchart to model general microstructure evolution.

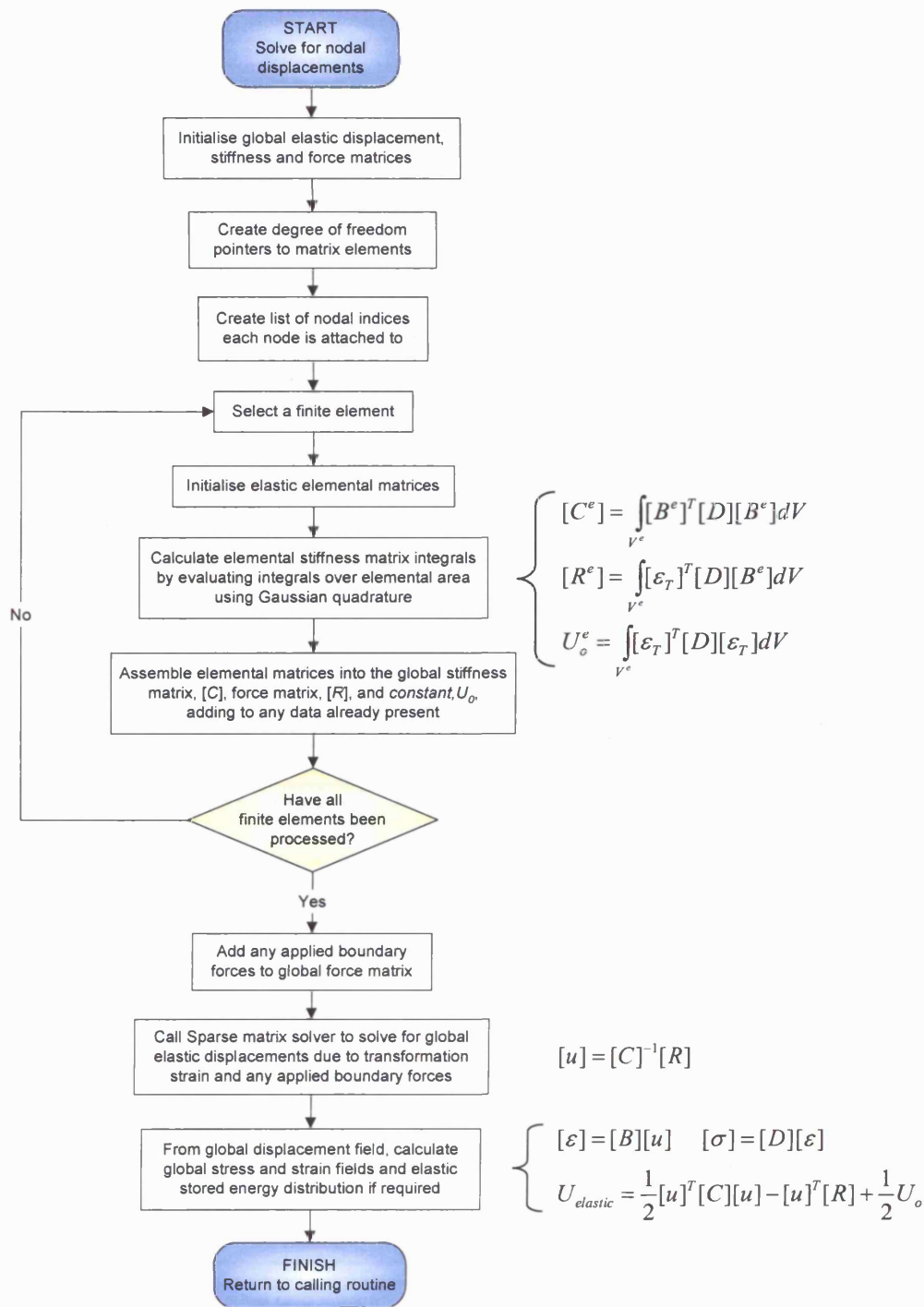


Figure G.2 – Computational flowchart to solve for the elastic nodal displacements (static problem).

Appendix

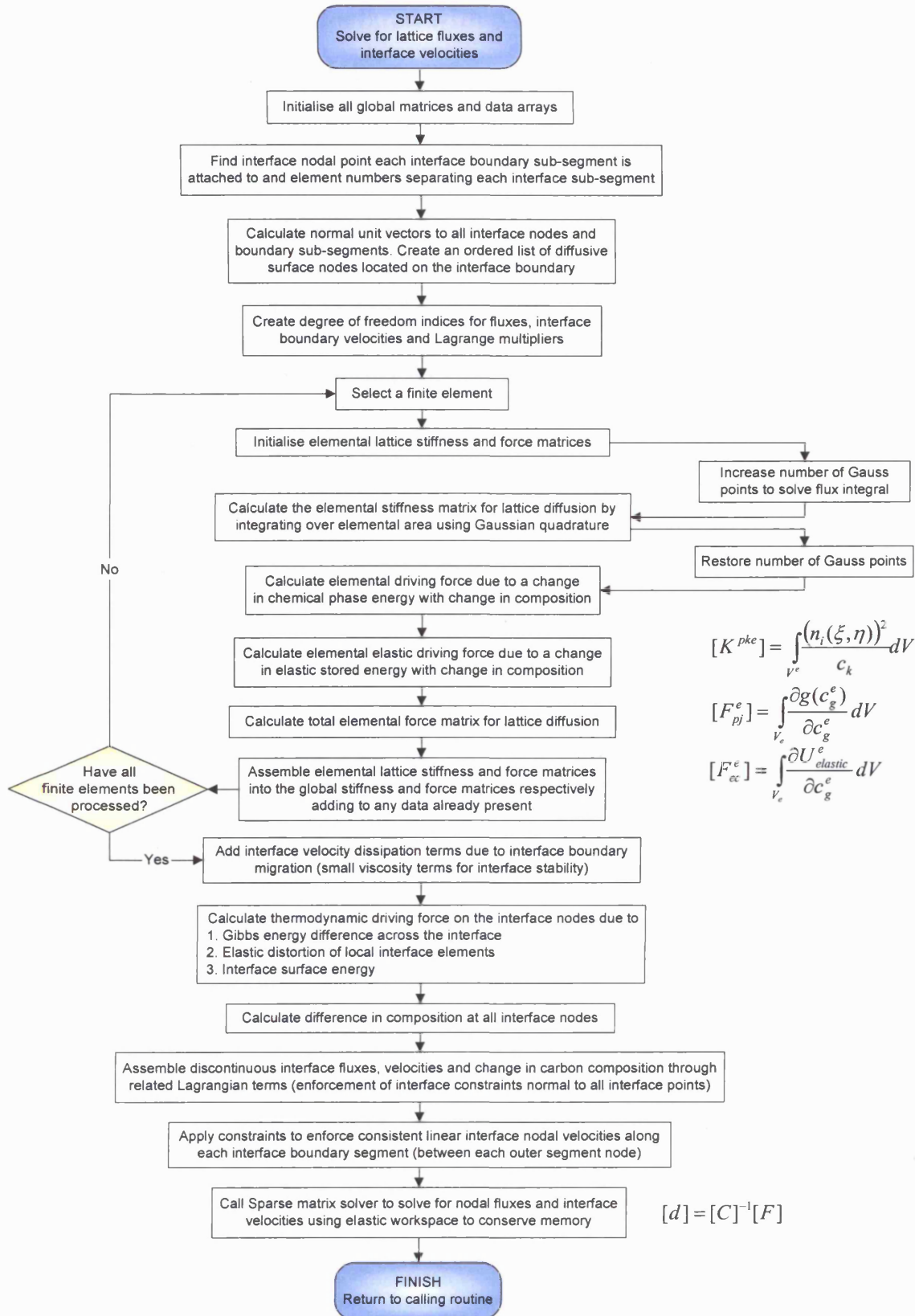


Figure G.3 – Computational flowchart to solve for the lattice fluxes and interface velocities (kinetic problem).

H. – Volumetric Strain Associated with a Ferrite Precipitate Embedded within an Austenite Matrix

For the bcc ferrite unit cell:

$$\text{Lattice spacing, } a_{bcc} = 2.863 \text{ \AA} \quad [36]$$

$$\text{Volume, } V_{bcc} = (a_{bcc})^3 = 23.467 \text{ \AA}^3$$

$$\text{Number of atoms within bcc unit cell, } N_{bcc} = \left(\frac{1}{8} \times 8\right) + 1 = 2$$

$$\text{Volume per atom} = \frac{V_{bcc}}{N_{bcc}} = \frac{23.467 \text{ \AA}^3}{2} = 11.7335 \text{ \AA}^3$$

For the fcc austenite unit cell:

$$\text{Lattice spacing, } a_{fcc} = 3.591 \text{ \AA} \quad [36]$$

$$\text{Volume, } V_{fcc} = (a_{fcc})^3 = 46.307 \text{ \AA}^3$$

$$\text{Number of atoms within fcc unit cell, } N_{fcc} = \left(\frac{1}{8} \times 8\right) + \left(\frac{1}{2} \times 6\right) + 1 = 4$$

$$\text{Volume per atom} = \frac{V_{fcc}}{N_{fcc}} = \frac{46.307 \text{ \AA}^3}{4} = 11.5768 \text{ \AA}^3$$

The volumetric strain can therefore be expressed as

$$\varepsilon_v = -\frac{dV_{bcc}}{V_{bcc}} = -\frac{\left(11.7335 \text{ \AA}^3 - 11.57675 \text{ \AA}^3\right)}{11.7335 \text{ \AA}^3} = -0.01336 = -1.336\% \quad (\text{H.1})$$

I. – Data used in the Fe-C Computations

Full expressions for the temperature dependent constants of equation (10.3) are provided by Andersson [75] and Hillert and Qiu [76]. Appropriate activation energies and diffusion constants for carbon in fcc and bcc iron are given by Askeland [36] and the values of the variation of Young's Modulus with temperature are given by Frost and Ashby [101]. The values of the appropriate constants used in the Fe-C computations are listed in Table I.1 at a temperature of 723°C.

<i>Constant</i>	<i>bcc (α) iron</i>	<i>fcc (γ) iron</i>
$A_1 (J mol^{-1})$	-41178.72	-41664.84
$A_2 (J mol^{-1})$	318550.44	7160.78
$A_3 (J mol^{-1})$	-189268.0	-34671.0
$G_{mo} (J mol^{-1})$	-837.24	-2.582×10^{-4}
α^p	3	1
c^p	1	1
$E (GPa)$	117.5	140.4
ν	0.33	0.33
$D_c (m^2 s^{-1})$	2.81×10^{-11}	1.36×10^{-12}

Table I.1 – Data and constants used in the Fe-C computations.

Here D_c is the diffusion coefficient for carbon at a temperature of 723°C [36]. All Gibbs energy values are given relative to the enthalpy of selected reference states for the elements at 298.15K.

J. – Data used in the Fe-Cr-C Computations

Full expressions for the temperature dependent constants of equations (11.8) and (11.9) are provided by Andersson [75] and Hillert and Qiu [76]. The values of the appropriate constants used in the Fe-Cr-C computations are listed in Table J.1 at a temperature of 650°C.

<i>Constant</i>	<i>bcc (α) iron</i>	<i>M₂₃C₆</i>
<i>B₁ (J mol⁻¹)</i>	<i>-32,474.21</i>	<i>-1,149,777.72</i>
<i>B₂ (J mol⁻¹)</i>	<i>-36,103.44</i>	<i>-865,145.69</i>
<i>B₃ (J mol⁻¹)</i>	<i>350,988.41</i>	<i>458,422.32</i>
<i>B₄ (J mol⁻¹)</i>	<i>323,270.00</i>	<i>-1,814,930.00</i>
<i>B₅ (J mol⁻¹)</i>	<i>-175,398.50</i>	<i>N/A</i>
<i>B₆ (J mol⁻¹)</i>	<i>11,563.91</i>	<i>N/A</i>
<i>B₇ (J mol⁻¹)</i>	<i>-699,804.50</i>	<i>N/A</i>
<i>G_{mo} (J mol⁻¹)</i>	<i>-872.76</i>	<i>N/A</i>
<i>a^p</i>	<i>1</i>	<i>23</i>
<i>c^p</i>	<i>3</i>	<i>6</i>
<i>D_C (m² s⁻¹)</i>	<i>1.220 × 10⁻¹¹</i>	<i>N/A</i>
<i>D_{Cr} (m² s⁻¹)</i>	<i>1.171 × 10⁻¹⁹</i>	<i>2.342 × 10⁻¹⁹</i>
<i>D_{Fe} (m² s⁻¹)</i>	<i>1.314 × 10⁻¹⁸</i>	<i>2.628 × 10⁻¹⁸</i>

Table J.1 – Data and constants used in the Fe-Cr-C computations.

Here D_C , D_{Cr} and D_{Fe} are the diffusion coefficients for carbon, chromium and iron respectively at a temperature of 650°C. All Gibbs energy values are given relative to the enthalpy of selected reference states for the elements at 298.15K. Diffusion coefficient data was obtained from Honeycombe & Bhadeshia [64].

K. – A Simplified Ostwald Ripening Model

Consider two general precipitate particles connected by a ‘flux channel’ of width, d , as illustrated in Figure K.1 below.

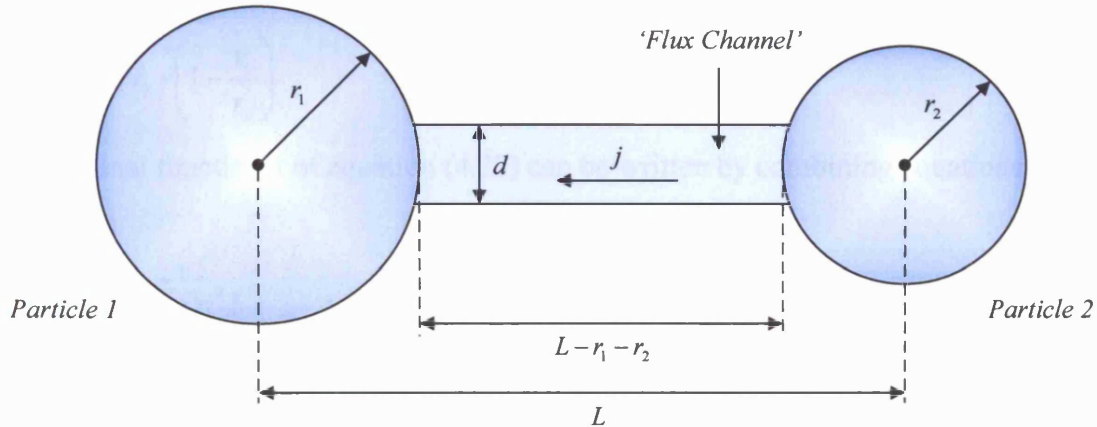


Figure K.1 – A simplified Ostwald ripening model.

In order to simplify the coarsening analysis, a single degree of freedom model is assumed where the rate of change of radius of particle 1, \dot{r}_1 is the unknown variable to be determined (\dot{r}_2 can then be calculated through conservation of mass given the radii, r_1 and r_2). The model assumes that the concentration of the single diffusing species does not change with time.

The rate of increase of mass of the larger precipitate (particle 1) is equal to the rate of decrease of mass of the smaller precipitate (particle 2), which can be expressed as

$$jd = \frac{d}{dt}(\pi r_1^2) = -\frac{d}{dt}(\pi r_2^2)$$

Hence, in order to satisfy mass conservation, one must have

$$\dot{r}_2 = -\frac{r_1}{r_2} \dot{r}_1$$

The dissipation due to a lattice flux through the flux channel is

$$\psi_{flux} = \frac{j^2 d}{2D} (L - r_1 - r_2)$$

If $L \gg r_1 + r_2$, then this can be simplified to

$$\psi = \frac{j^2 dL}{2D} = \frac{2\pi^2 \dot{r}_1^2 r_1^2 L}{Dd} \quad (\text{K.1})$$

Ignoring elastic and compositional phase energies, the rate of change of Gibbs free energy can be expressed as

$$\dot{G} = 2\pi \dot{r}_1 \gamma \left(1 - \frac{r_1}{r_2}\right) \quad (\text{K.2})$$

The variational functional of equation (4.23) can be written by combining equations (K.1) and (K.2) to give

$$\Pi = \frac{2\pi^2 \dot{r}_1^2 r_1^2 L}{Dd} + 2\pi \dot{r}_1 \gamma \left(1 - \frac{r_1}{r_2}\right)$$

which can be minimised with respect to \dot{r}_1 to give

$$\dot{r}_1 = \frac{A}{r_1} \left(\frac{1}{r_2} - \frac{1}{r_1}\right) \quad (\text{K.3})$$

where $A = \frac{\gamma D d^2}{2\pi L}$.

From the conservation of mass, the rate of change of r_2 can be expressed as

$$\dot{r}_2 = \frac{A}{r_2} \left(\frac{1}{r_1} - \frac{1}{r_2}\right) \quad (\text{K.4})$$

When we have a large number of precipitates, equations (K.3) and (K.4) can be written as

$$\frac{dr}{dt} = \frac{A}{r} \left(\frac{1}{r_{cr}} - \frac{1}{r}\right) \quad (\text{K.5})$$

for the evolution of a precipitate of radius r , where r_{cr} is a critical radius, above which the particle grows and below which the particle shrinks. This is usually the mean particle radius, i.e. $r_{cr} = \bar{r}$. To derive the temporal evolution law, it is assumed that the size distribution of particles remains the same shape but just scales in magnitude over time (as the particles get bigger), i.e. the distribution of r/r_{cr} remains constant. A plot of the distribution of number of particles of radius, r against r/\bar{r} for spherical particles undergoing coarsening can be seen in Lifshitz and Slyozov [8] and Shewmon [7]. Since the mean particle radius, \bar{r} increases with

time, the system will continually coarsen as particles of radius $r < \bar{r}$ will tend to lose solute to the matrix and particles of radius $r > \bar{r}$ will gain solute from the matrix and grow.

Equation (K.5) can be re-written such that

$$r^2 \frac{dr}{dt} = \frac{1}{3} \frac{dr^3}{dt} = A \left(\frac{r}{r_{cr}} - 1 \right)$$

The right hand side can be assumed to be constant if a scaling state exists. If this is the case

$$\frac{dr^3}{dt} = \text{constant}$$

which implies that

$$\frac{dr_{cr}^3}{dt} = \frac{d\bar{r}^3}{dt} = \text{constant} = k$$

This leads to the classical power law theory for Ostwald ripening

$$\bar{r}^3(t) - \bar{r}^3(0) = kt \tag{K.6}$$

which predicts that the mean particle volume increases linearly with time.

L. – Accompanying PC CD-ROM

A full chapter-by-chapter version of this thesis is also provided on computer CD-ROM which also includes animations of:

1. Planar and circular ferrite precipitate morphology (with and without effects of elasticity) as described in chapter 10.
2. The coarsening of two $M_{23}C_6$ precipitates (with and without effects of elasticity) as described in chapter 11.

Minimum PC system requirements:

OS: Windows '9X, 2000, XP
CPU: PII or later recommended
RAM: 32 MB or more recommended
CD ROM: 8 speed or faster
No sound card or hard-drive space required.

To launch the menu selection screen:

1. Insert CD ROM into your CD-ROM drive.
2. The CD should start the interactive menu automatically. If this does not happen, then select 'autorun.exe' from the CD within windows explorer.
3. When prompted, select the required option(s) from the menu selection screen.

References

- [1]. Triangle: A Two-Dimensional Quality Mesh Generator and Delaunay Triangulator, Jonathan Richard Shewchuk, Computer Science Division, University of California at Berkeley, Berkeley, California 94720-1776.
Web Reference: <http://www.cs.cmu.edu/~quake/triangle.html>
- [2]. Gill, S.P.A., Cornforth, M.G. & Cocks, A.C.F. (2001), Modelling Microstructure Evolution in Engineering Materials, *Int. J. Plast.*, 17, pp669-690.
- [3]. Johnson, W.C. and Voorhees, P.W. (1992), Elastically-Induced Precipitate Shape Transitions in Coherent Solids, *Solid State Phenomena*, Vol. 23 & 24, pp87-104.
- [4]. Matan, N., Winand, H.M.A., Bogdanoff, P.D. and Reed, R.C. (1998), A Coupled Thermodynamic/Kinetic Modelling of Diffusion Reactions in Superalloys, *Acta Mater.*, 46 (13), pp4587-4600.
- [5]. Strang, A., Vodarek, V. and Bhadeshia, H.K.D.H. (1998), Modelling of Microstructural Evolution in Creep Resistant Materials, A. Strang and M. McLean, eds, Institute of Materials, pp129-150.
- [6]. Strang, A. and Vodarek, V. (1998), Microstructural Stability of Creep Resistant Alloys for High Temperature Plant Applications, A. Strang, J. Cawley and G.W. Greenwood, eds, Institute of Materials, pp117-133.
- [7]. Shewmon, P.G. (1969), *Transformations in Metals*, McGraw-Hill, New York.
- [8]. Lifshitz, I.M. and Slyozov, V.V. (1961), The Kinetics of Precipitation from Supersaturated Solid Solutions, *J. Phys. Chem. Solids*, 19, pp35-50.
- [9]. Wagner, C. (1961), Theory of Precipitate Aging via Dissolution / Reprecipitation; Ostwald Ripening, *Z. Electrochem.* 65, pp581-591.
- [10]. Fichthorn, K.A. and Weinberg, W.H. (1991), Theoretical Foundations of Dynamical Monte Carlo Simulations, *J. Chem. Phys.*, Vol. 95 (2), pp1090-1095.
- [11]. Sutton, A.P., Mason, D. and Cerezo, A., Modelling Diffusional Phase Transformations in the Presence of Elastic Interactions.
Web Reference: <http://users.oc.ac.uk/~masondr/research/theory.htm>
- [12]. Krauth, W. (1996), *Introduction to Monte Carlo Algorithms*.
Web Reference: <http://lps.ens.fr/~krauth>

References

- [13]. Chen, L.-Q. and Wang, Y. (1996), The Continuum Field Approach to Modelling Microstructural Evolution, *JOM* 48, pp11-18.
- [14]. Wang, Y., Chen, L. and Khachaturyan, A.G. (1994), Computer Simulation of Microstructure Evolution in Coherent Solids. W.C. Johnson, J.M. Howe, D.E. Laughlin, and W.A. Soffia eds., Solid-solid Phase Transformations, The Minerals, Metals and Materials Society, p245.
- [15]. Provatas, N., Goldenfeld, N. & Dantzig, J. (1998), Efficient Refinement of Dendritic Microstructures Using Adaptive Mesh Refinement, *Phys. Rev. Lett.*, 80, p3308.
- [16]. Venkitachalam, M., Chen, L. Q., Khachaturyan, A. G., and Messing, G. L. (1997), Multicomponent Order Parameter Phase-Field Model for Anisotropic Grain Growth, *Materials Science and Engineering, A* 238, p94.
- [17]. Kazanyan, A., Wang, Y., Dregia, S.A. and Patton, B.P. (2000), Generalised Phase-Field Model for Computer Simulation of Grain Growth in Anisotropic Systems, *Phys. Rev.* B61, pp14275-14278.
- [18]. Sagui, C., Orlikowski, D., Somoza, A.M. & Roland, C. (1998), Three-Dimensional Simulations of Ostwald Ripening with Elastic Effects, *Phys. Rev.*, E58, R4092.
- [19]. Warren, J.A. and Murray, B.T. (1996), Ostwald Ripening and Coalescence of a Binary Alloy in Two Dimensions using a Phase-Field Model, *Modelling Simul. Mater. Sci. Eng.* 4, pp215-229.
- [20]. Lu, W. and Suo, Z. (2000), Dynamics of Nanoscale Pattern Formation of an Epitaxial Monolayer, *J. Mech. Phys. Solids.*, pp1-19.
- [21]. Zhu, J. (2002), Phase-Field Modelling of Microstructural Evolution and Properties, PhD Thesis, Pennsylvania State University.
- [22]. Suo, Z. (1996), Motions of Microscopic Surfaces in Materials, *Adv. Appl. Mech.*, 33, p193.
- [23]. Cocks, A.C.F., Gill, S.P.A. & Pan, J. (1999), Modelling Microstructure Evolution in Engineering Materials, *Adv. Appl. Mech.*, 36, pp81-162.
- [24]. Sun, B., Suo Z. & Cocks, A.C.F. (1996), A Global Analysis of Structural Evolution in a Row of Grains, *J. Mech. Phys. Solids*, Vol. 44, No. 4, pp559-581.
- [25]. Cocks, A.C.F. and Gill, S.P.A. (1996), A Variational Approach to Two Dimensional Grain Growth – I. Theory, *Acta. Mater.*, Vol. 44, No. 12, pp4765-4775.

References

- [26]. Pan, J., Cocks, A.C.F. & Kucherenko, S. (1997), Finite Element Formulation of Coupled Grain-Boundary and Surface Diffusion with Grain-Boundary Migration, *Proc. Roy. Soc. London Ser. A*, 453, 2161.
- [27]. Cocks, A.C.F. and Gill, S.P.A. (1996), A Variational Approach to Two Dimensional Grain Growth – II. Numerical Results, *Acta. Mater.*, Vol. 44, No. 12, pp4777-4789.
- [28]. Cocks, A.C.F and Pan, J. (1993), Void Growth ahead of a Dominant Crack in a Material which Deforms by Coble Creep, *Int. J. Fracture* 60, pp249-265.
- [29]. Gill, S.P.A. and Cocks, A.C.F. (1999), The Relaxation of Epitaxial Islands, *J. Phys. IV France*, 9, pp83-94.
- [30]. Gill, S.P.A. and Cocks, A.C.F. (1998), Microstructure Evolution in Precipitate Strengthened Materials, Proceedings of the International Conference on Modelling of Microstructural Evolution in Creep Resistant Materials (Imperial College, London).
- [31]. Suo, Z. and Lu, W. (2000), Self-Organizing Nanophases on a Solid Surface, in Multi-Scale Deformation and Fracture in Materials and Structures-The James R. Rice 60th Anniversary Volume, edited by T.-J. Chuang and J. W. Rudnicki, Kluwer Academic Publishers, The Netherlands, pp107-122.
- [32]. Sundman, B. & Agren, J. (1981), A Regular Solution Model for Phases with Several Components and Sublattices Suitable for Computer Applications, *J. Phys. Chem. Solids*, 42, pp297-301.
- [33]. Clyne, T.W. and Withers, P.J. (1993), An Introduction to Metal Matrix Composites, Cambridge Solid Science Series, p44.
- [34]. Ashby, M.F. & Jones, D.R.H. (1986), Engineering Materials 2: An Introduction to Microstructures, Processing and Design, Pergamon Press, International Series on Materials Science and Technology, Vol. 39.
- [35]. Jost W. (1960), Diffusion in Solids, Liquids and Gases, Academic Press Inc., 3rd Edition, New York.
- [36]. Askeland, D.R. (1989), The Science and Engineering of Materials, Second Edition, Chapman and Hall.
- [37]. Newey, C. & Weaver, G. (1990), Materials Principles and Practice, Butterworths, The Open University.
- [38]. Shewmon, P.G. (1963), Diffusion in Solids, McGraw-Hill, New York.

References

- [39]. Babuska, I. and Aziz, A.K. (1976), On the Angle Condition in the Finite Element Method, *SIAM Journal of Numerical Analysis*, 13, pp214-226.
- [40]. Mohri, T. (1994), Theoretical Study of the Phase Stability of a III-IV Semiconductor Alloy, *Progress of Theoretical Physics Supplement*, No. 115, pp147-163.
- [41]. Ockendon, J.R. & Hodgkins, W.R. (1975), Moving Boundary Problems in Heat Flow and Diffusion (Proceedings of the Conference held at the University of Oxford, 25-27th March 1974), Clarendon Press, Oxford.
- [42]. Wilson, D.G., Soloman, A.D. & Boggs P.T. (1978), Moving Boundary Problems, Academic Press, New York.
- [43]. Carslaw, H.S. & Jaeger, J.C. (1986), Conduction of Heat in Solids (2nd Edition), Oxford University Press, p204.
- [44]. Stefan, J. (1889), Über einige Probleme der Theorie der Wärmeleitung, *Sber. Akad. Wiss. Wien., Math.Cl.*, 98, pp473-484.
- [45]. Stefan, J. (1891), Ueber die theorie der eisbildung, insbesondere ueber die eisbildung im polarmeere, *Ann. Chem. Phys.*, 42, pp269-286.
- [46]. Crank, J. (1984), Free and Moving Boundary Problems, Oxford Science Publications, Oxford, p163.
- [47]. Bonnerot, R. and Jamet, P. (1981), A Conservative Finite Element Method for One-Dimensional Stefan Problems with Appearing and Disappearing Phases, *J. Comput. Phys.* 41, p357.
- [48]. Bonnerot, R. and Jamet, P. (1979), A Third Order Accurate Discontinuous Finite Element Method for the One-Dimensional Stefan Problem, *J. Comput. Phys.* 32, p145.
- [49]. Furzeland, R.M. (1980), A Comparative Study of Numerical Methods for Moving Boundary Problems, *J. Inst. Maths. Appl.*, 26, pp411-429.
- [50]. Poirer, D. and Salcuden, M. (1988), *Trans. ASME J. Heat Transfer* 110, pp333-340.
- [51]. Zerroukat, M. (1993), Numerical Computation of Moving Boundary Phenomena, PhD Thesis, Glasgow University.
- [52]. Johnson, A.A. and Tezduyar, T.E. (1994), Mesh Update Strategies in Parallel Finite Element Computations of Flow Problems with Moving Boundaries and Interfaces, *Comp. Meth. Appl. Mech. Eng.*, 119, pp73-94.
- [53]. Johnson, A.A. and Tezduyar, T.E. (1996), Simulation of Multiple Spheres Falling in a Liquid-Filled Tube, *Comp. Meth. Appl. Mech. Eng.*, 134, p351.

References

- [54]. Mittal, S. and Tezduyar, T.E. (1995), Parallel Finite Element Simulation of 3D Incompressible Flows: Fluid-Structure Interactions, *Int. J. Num. Meth. Fluids*, 21, pp933-953.
- [55]. Tezduyar, T.E., Behr, M., Mittal, S. and Liou, J. (1992), A New Strategy for Finite Element Computations Involving Moving Boundaries and Interfaces – the DSD/ST Procedure: 1. The Concept and the Preliminary Numerical Tests, *Comp. Meth. Appl. Mech. Eng.*, 94, pp339-351.
- [56]. Hu, H.H., Joseph, D.D. and Crochet, M.J. (1992), Direct Simulation of Fluid Particle Motions, *Theoret. Comp. Fluid Dynam.*, 3, pp285-306.
- [57]. Unverdi, S.O. and Tryggvason, G. (1992), A Front-Tracking Method for Viscous, Incompressible, Multi-Fluid Flows, *J. Comp. Phys.*, 100, pp25-37.
- [58]. Brebbia, C. A., Telles, J. C. F. and Wrobel L. C. (1984), Boundary Element Techniques: Theory and Application in Engineering (Springer-Verlag, Berlin).
- [59]. Jou, Heng-Jeng (1995), Analytic and Numerical Studies of the Role of Elasticity on Microstructural Evolution during Diffusional Phase Transformations, Ph.D. Thesis, University of Minnesota, Minneapolis, Minnesota.
- [60]. Jou, H.-J., Leo, P. and Lowengrub, J. (1994), Numerical Calculations of Precipitate Shape Evolution, Solid-Solid Phase Transformation, eds. W.C. Johnson, J.M. Howe, D.E. Laughlin and W.A. Soffa, The Minerals, Metals & Materials Society, Pennsylvania.
- [61]. Jou, H.-J., Leo, P. and Lowengrub, J. (1997), Microstructural Evolution In Inhomogeneous Elastic Media, *J. Comp. Phys.*, Vol. 131, No. 1, pp109-148.
- [62]. Heinlein, M., Mukherjee, S. and Richmond, O. (1986), A Boundary Element Method Analysis of Temperature Fields and Stress during Solidification, *Acta Mechanica* 59, pp59-81.
- [63]. Zabaras, N. and Mukherjee, S. (1987), An Analysis of Solidification Problems by the Boundary Element Method, *Int. J. Numer. Methods Eng.* 24, p1879.
- [64]. Honeycombe, R.W.K. & Bhadeshia H.K.D.H. (1995), Steels – Microstructure and Properties, Edward Arnold.
- [65]. Svoboda J., Fischer F.D., Fratzl P., Gamsjäger E. and Simha N.K. (2001), Kinetics of Interfaces during Diffusional Transformations, *Acta Mater.*, 49, pp1249-1259.
- [66]. Crank J. (1975), The Mathematics of Diffusion, Clarendon Press, Oxford, p286.

References

- [67]. Judd R.R. and Paxton H.W. (1968), Kinetics of Austenite Formation from a Spheroidised Ferrite-Carbide Aggregate, *Trans. Metall. Soc. AIME*, 242, pp206-215.
- [68]. Kirkaldy J.S. and Young D.J. (1987), Diffusion in the Condensed State, The Institute of Metals, London, pp.42,36.
- [69]. Purdy G.R. and Kirkaldy J.S. (1963), *Trans. Metall. Soc. AIME*, 227, p1255.
- [70]. Tanzilli R.A. and Heckel R.W. (1968), *Trans. Metall. Soc. AIME*, 242, p2313.
- [71]. Zener C. (1949), Theory of Growth of Spherical Precipitates from Solid Solution, *J. App. Phys.*, 20, pp950-953.
- [72]. Vandermeer R.A. (1990), Modelling Diffusional Growth during Austenite Decomposition to Ferrite in Polycrystalline Fe-C Alloys, *Acta Metall. Mater.*, 38, No. 12, pp2461-2470.
- [73]. Atkinson, C. and Akbay, T. (1996), The Effect of the Concentration-Dependent Diffusivity of Carbon in Austenite on a Model of Reaustenitisation from Ferrite / Cementite Mixtures in Fe-C Steels, *Acta Mater.*, vol. 44, No. 7, pp2861-2868.
- [74]. Miodownik, A.P. (1994), Young's Modulus for Carbides of 3D Elements (with particular reference to Fe₃C), *Materials Science and Technology*, Vol. 10, pp190-192.
- [75]. Andersson J-O. (1988), A Thermodynamic Evaluation of the Fe-Cr-C System, *Metall. Trans. A.*, 19A, pp627-636.
- [76]. Hillert, M. and Qiu, C. (1990), A Thermodynamic Assessment of the Fe-Cr-Ni System, *Metall. Trans. A*, 21A, 1990, pp1673.
- [77]. Yang, Z. and Johnson, R.A. (1993), An EAM Simulation of the α - γ Iron Interface, *Modelling Simul. Mater. Sci. Eng.*, 1, pp707-716.
- [78]. Che, D.Z. and Hoyt, J.J. (1995), Spatial Correlations during Ostwald Ripening – A Simplified Approach, *Acta Mater.*, 43 (7), pp2551-2561.
- [79]. Fratzl, P., Penrose, O. and Lebowitz, J.L. (1999), Modeling of Phase Separation in Alloys with Coherent Elastic Misfit, *J. Stat. Phys.* 95, pp1429-1503.
- [80]. Orlikowski, D., Sagui, C., Somoza, A. and Roland, C. (2000), Phase Separation and Elastic Fields: Three Dimensional Simulations of a Phase Field Model, *Materials Research Society Symposium - Proceedings*, v 580, pp21-26.
- [81]. Enomoto, Y. and Kawasaki, K. (1989), Computer Simulations of Ostwald Ripening with Elastic Field Interactions, *Acta Metall.*, Vol. 37, No. 5, pp1399-1406.

References

- [82]. Nishimori, H. and Onuki, A. (1990), Pattern Formation in Phase Separating Alloys with Cubic Symmetry, *Phys. Rev. B* 42, pp980-983.
- [83]. Nishimori, H. and Onuki, A. (1991), Freezing of Domain Growth in Cubic Solids with Elastic Misfit, *J. Phys. Soc. Japan*, 60, pp1208-1211.
- [84]. Leo, P.H., Mullins W.W., Sekerka, R.F. and Vinals, J. (1990), Effects of Elasticity on Late Stage Coarsening, *Acta Metall. Mater.*, 38, pp1573-1580.
- [85]. Abinandanan, T.A. (1991), Coarsening of Elastically Interacting Particles, Ph.D. Thesis, Carnegie Mellon University, U.S.A.
- [86]. Miyazaki, T., Doi, M. and Kozakai, T. (1988), Shape Bifurcations in the Coarsening of Precipitates in Elastically Constrained Systems, *Solid State Phenomena* 3, pp227-236.
- [87]. Miyazaki, T. and Doi, M. (1989), Shape Bifurcations in the Coarsening of Precipitates in Elastically Constrained Systems, *Mater. Sci. Engng A* 110, pp175-185.
- [88]. Doi, M., Miyazaki, T. and Wakatsuki, T. (1985), The Effects of Elastic Interaction Energy on the γ Precipitate Morphology of Continuously Cooled Nickel Base Alloys, *Mater. Sci. Eng.*, 74, pp139-145.
- [89]. Johnson, W.C. and Cahn, J.W. (1984), Elastically Induced Shape Bifurcations in Inclusions, *Acta Metall.*, 32, pp1925-1933.
- [90]. Johnson, W.C. and Voorhees, P.W. (1987), Elastic Interaction and Stability of Misfitting Cuboidal Inhomogeneities, *J. Appl. Phys.*, Vol. 61, pp1610-1619.
- [91]. Gurtin, M.E. and Voorhies, P.W. (1993), The Continuum Mechanics of Coherent Two-Phase Elastic Solids with Mass Transport, *Proc. R. Soc. Lond. A*, 440, pp323-343.
- [92]. Westgren, A. (1933), Complex Chromium and Iron Carbides, *Nature*, Vol. 133, p480.
- [93]. Leslie, W.C. (1972), Iron and its Dilute Substitutional Solid Solutions, *Metall. Trans.*, Vol. 3, pp5-26.
- [94]. Strang, A., verbal communication.
- [95]. Okamoto, R. and Suehiro, M. (1998), *Tetsu-to-Hagane* (J. Iron Steel Inst. Jpn.), Vol. 84, pp650-657.
- [96]. Miyazaki, T., *Solid-Solid Phase Transformations '99* (1999), (ed. M. Koiwa et al.), The Japan Institute of Metals, pp15-22.
- [97]. Hättestrand, M. and Andrén, H.-O. (2001), Influence of Strain on Precipitation Reactions during Creep of an Advanced 9% Chromium Steel, *Acta Mater.* 49, pp2123 -2128.

References

- [98]. Ardell, A.J. (1969), Experimental Confirmation of the Lifshitz-Wagner Theory of Particle Coarsening, Institute of Metals Report Series, No. 33, The Mechanism of Phase Transformations in Solids, pp111-116.
- [99]. Greenwood, G.W. (1969), Session III – Particle Coarsening, Institute of Metals Report Series, No. 33, The Mechanism of Phase Transformations in Solids, pp103-110.
- [100]. Ankara, I., Chatillon, C., Lukas, H.L., Nishizawa, T., Ohtani, H., Ishida, K., Hillert, M., Sundman, B., Argent, B.B., Watson, A., Chart, T.G. and Anderson, T. (1994), A Thermodynamic Assessment of the III-IV Semiconductor System, *Calphad*, 18, pp177-222.
- [101]. Frost, H.J. and Ashby M.F. (1982), Deformation-Mechanism Maps – The Plasticity and Creep of Metals and Ceramics, Pergamon Press.
- [102]. Voorhees, P.W. and Glicksman, M.E. (1984), Solution to the Multi-Particle Diffusion Problem with Applications to Ostwald Ripening – I. Theory, *Acta Metall.*, Vol. 32, No. 11, pp2001-2011.
- [103]. Voorhees, P.W. and Glicksman, M.E. (1984), Solution to the Multi-Particle Diffusion Problem with Applications to Ostwald Ripening – II. Computer Simulations, *Acta Metall.*, Vol. 32, No. 11, pp2013-2030.
- [104]. Johnson, W.C., Voorhees, P.W. and Zupon, D.E. (1989), The Effects of Elastic Stress on the Kinetics of Ostwald Ripening: The Two-Particle Problem, *Metall. Trans.*, 20A, p1175.
- [105]. Su, C.H. and Voorhees, P.W. (1996), The Dynamics of Precipitate Evolution in Elastically Stressed Solids – I. Inverse Coarsening, *Acta Mater.*, 44, pp1987-1999.
- [106]. Hald, J. (1998), Microstructural Stability of Creep Resistant Alloys for High Temperature Plan Applications, A. Strang, J. Cawley and G.W. Greenwood eds., Institute of Materials, p173-184.
- [107]. Thomson, R.C. and Bhadeshia, H.K.D.H. (1992), Carbide Precipitation in 12Cr1MoV Power Plant Steel, *Metall. Trans. A.*, 23A, pp1171-1179.
- [108]. Johnson, W.C. (1984), On the Elastic Stabilisation of Precipitates against Coarsening under Applied Load, *Acta Metall.*, Vol. 32, No. 3, pp465-475.
- [109]. Davis, P.J. and Rabinowitz, P. (1984), Methods of Numerical Integration. Academic Press, California.

References

- [110]. Hättestrand, M. and Andrén, H.-O. (1999), Boron Distribution in 9–12% Chromium Steels, *Mat. Sci. and Eng. A270*, pp33–37.
- [111]. Hald, J. (1995), New Steels for Advanced Plant up to 620°C, EPRI / National Power, London, 1995, p152.

